# DESIGN AND CONTROL OF ULTRA-HIGH SPEED SWITCHED RELUCTANCE MACHINES OVER 1 MILLION RPM

A Dissertation
Presented to
The Academic Faculty

by

Cheng Gong

In Partial Fulfillment
of the Requirements for the Degree
Doctor of Philosophy in the
School of Electrical and Computer Engineering

Georgia Institute of Technology
May 2019

# DESIGN AND CONTROL OF ULTRA-HIGH SPEED SWITCHED RELUCTANCE MACHINES OVER 1 MILLION RPM

Approved by:

Dr. Thomas G. Habetler, Advisor
School of Electrical and Computer Engineering
*Georgia Institute of Technology*

Dr. Maryam Saeedifard
School of Electrical and Computer Engineering
*Georgia Institute of Technology*

Dr. Lukas Graber
School of Electrical and Computer Engineering
*Georgia Institute of Technology*

Dr. Daniel Molzahn
School of Electrical and Computer Engineering
*Georgia Institute of Technology*

Dr. J. Rhett Mayor
The George W. Woodruff School of Mechanical Engineering
*Georgia Institute of Technology*

Date Approved: March 27, 2019

*To*

*my dear father in heaven, Hai Gong*

*my dear mother, Jinling Yang*

*and my dear wife, Xiao Liu*

# ACKNOWLEDGEMENTS

It would not have been possible for me to finish this doctoral dissertation without the guidance from my advisor, help from my friends, and support from my family.

First of all, I would like to give my deepest gratitude to my advisor, Dr. Thomas G. Habetler. He is the kindest person in the world and the most knowledgeable professor in my life. He is always open-minded to listen to me, patient to advise me, and supportive behind my back. He has always made himself available to provide insightful discussions about my research despite his busy schedules. Most of all, he is always encouraging me to challenge the most difficult topics in my research area. I feel so privileged to be his PhD student, and I cannot imagine having a better advisor and mentor in my life.

I would also like to take this opportunity to express my gratitude to Dr. Ronald G. Harley and Dr. J. Rhett Mayor. Their invaluable guidance and constant encouragement help me overcome great challenges throughout the course of my research. They have always been willing to share their wisdom and experience to me. I would never forget their support and caring. I would also like to thank Dr. Lukas Graber, Dr. Maryam Saeedifard and Dr. Daniel Molzahn to serve as my PhD committee members and provide valuable feedback.

I owe a great debt of gratitude to Mr. Steve Sprague from Proto Lam, a talented, reliable, and selfless mentor throughout my PhD study. He is an expert in magnetic materials. He knows everything about laminations from mechanical to magnetic properties. I have enjoyed much from the discussions with him, and I have learned much from his

experience and rich knowledge. All the high quality laminations were kindly provided by him and Proto Lam for free.

I would give my deep thanks to one of my senior lab mate, Dr. Jie Dang. His innovative work on high speed SRM inspired me a lot for my PhD work. All my work is based on the results of his work. Also, he behaved as my elder brother. He has given me many advice throughout my PhD work in both academic research and career planning.

I also appreciate Dr. Jose Restrepo for his selfless help in my research. He has played a crucial role in the completion of my research work. I have learned so much from his joy and enthusiasm in research.

My roommate Dr. Peiyan Yang is another important person I would like to thank. He provided me much insightful opinion in mechanical engineering in the early stage of my PhD study. And in those days I suffered, he always helped me get out of sadness.

My time at Georgia Tech is unforgettable thanks to the many friends that have become a part of my life. I would give my deep thanks to my lab mates, Hao Chen, Heng Yang, Jie Dang, Yi Deng, Lijun He, Nan Liu, Chen Jiang, Sufei Li, Shen Zhang, Hang Shao, Genyi Luo, Xiangyu Han, Qichen Yang, Liyao Wu, Liran Zheng, Chunmeng Xu, Zheng An who have helped me and provided collaborative efforts in the past few years. The lab has been a source of friendships, love and support. I feel grateful and wish them all the best. I also appreciate the help from Dr. Deepak Divan, Dr. A.P. Meliopoulos, and Dr. Santiago Grijalva. I will never forget them.

I would like to acknowledge my supervisor Prof. Johann W. Kolar, Dr. Arda Tüysüz, and my dear fellow colleges Mr. Tibor Stolz, Dr. Michael Flankl and Dr. Spasoje Miric, during my summer internship at PES lab at ETH-Zürich in 2017. I learnt a lot from them. I also would like to thank Dr. Ping Zhou, Dr. Bo He, Dr. Dingsheng Lin, Dr. Yumin Xiao, Dr. Chuan Lu, Dr. Ningning Chen, Dr. Yang Hu, Dr. Yanpu Zhao and Dr. Ozgur Tuncer for their help during my internship in 2018.

There are numerous names of faculty, family, and friends that I should mention here. But most of all, I owe my greatest debt of gratitude to my father in heaven, he had always wanted me to make some contributions to the world. My earning a PhD degree had always been his wish when he was alive. Now I can proudly present my work to him. I wish him rest in peace in heaven. I also want to thank my dear mother, who has always been a strong woman, standing by me through the good times and bad. Whenever I feel depressed, she is always the first to support me. Last but not least, I would like to thank my dear wife Dr. Xiao Liu. She has always been by my side no matter what happens. We took care of each other in our PhD life in Georgia Tech and grew up together. Thank you all.

# TABLE OF CONTENTS


**ACKNOWLEDGEMENTS** iv

**LIST OF TABLES** xii

**LIST OF FIGURES** xiii

**LIST OF SYMBOLS AND ABBREVIATIONS** xix

**SUMMARY** xxii

**CHAPTER 1. INTRODUCTION** 1
**1.1 Background** 1
**1.2 Literature Survey** 1
1.2.1 Ultra-High Speed Electric Machine Applications 1
1.2.2 High Speed Electric Machines below 100,000 rpm 6
1.2.3 Ultra-high speed Electric Machines beyond 100,000 rpm 7
**1.3 Objective** 10
**1.4 Difference of Regular Speed Machine and Ultra-High Speed Machine** 10
1.4.1 Mechanical Strength of Rotor 11
1.4.2 Air Gap Length 11
1.4.3 Magnetic Loading and Core Losses 11
1.4.4 Electric Loading and Copper Losses 12
1.4.5 Machine Size and Length 13
**1.5 Challenges** 13
1.5.1 Challenges in Design 13
1.5.2 Challenges in Control 14
1.5.3 Challenges in Manufacture 14
**1.6 Dissertation Outline** 15

**CHAPTER 2. ROTOR MECHANICAL DESIGN** 17
**2.1 Introduction** 17
**2.2 Stress Analysis of a Coaxial Cylinder** 17
2.2.1 Analytical Analysis 18
2.2.2 Finite Element Analysis 18
2.2.3 Validation of the Finite Element Model 19
**2.3 Problem of Conventional Rotor Designs** 20
2.3.1 Localized Stress Concentration 20
2.3.2 Too Small Space for the Shaft 21
2.3.3 Too Much Windage Loss 21
**2.4 Possible Solutions in the Literature** 22
2.4.1 Using Bolts Rather Than a Shaft 22
2.4.2 Using Rotor Sleeves 23
2.4.3 Design with “Flux Bridges” 23
**2.5 Design of a Novel Rotor Geometry for Ultra-High Speed Applications** 24

2.5.1 Design Details 25
2.5.2 Advantages 26
2.5.3 Disadvantages 27
**2.6 Stress Analysis of the Proposed Rotor 29**
2.6.1 Theoretical Stress Analysis of the Shaft 29
2.6.2 3D Finite Element Analysis of the Shaft 31
2.6.3 3D Finite Element Analysis of the Rotor Stack 35
**2.7 Chapter Summary 35**

**CHAPTER 3. ROTOR ROBUSTNESS ANALYSIS 37**
**3.1 Introduction 37**
**3.2 Problem of Small Gaps and Stress Concentration 38**
**3.3 Improved Design with Adhesives 39**
**3.4 Cohesive Zone Model 40**
3.4.1 General Description 40
3.4.2 Traction-Separation Law and Important Parameters 41
**3.5 Modeling and Simulation 44**
3.5.1 Interface Delamination v.s. Contact Debonding 44
3.5.2 Meshing 45
3.5.3 Separation-Distance Based v.s. Fracture-Energy Based 46
3.5.4 Mode I v.s. Mode II Separation 46
**3.6 Adhesive Selection 46**
**3.7 Parametric Study Results 49**
**3.8 Chapter Summary 51**

**CHAPTER 4. ROTOR DYNAMICS ANALYSIS AND PROTOTYPING 52**
**4.1 Introduction 52**
**4.2 Bearing Selection 52**
4.2.1 Category 52
4.2.2 Ball Bearing 53
4.2.3 Magnetic Bearing 54
4.2.4 Air Bearing 54
**4.3 Analytical Analysis of Rotor Dynamics 55**
**4.4 Finite Element Analysis of Rotor Dynamics 59**
4.4.1 Modal Analysis of the Basic Geometry 59
4.4.2 Solid and Laminated Stack 61
4.4.3 Two Alternative Geometries 63
**4.5 Rotor Stack Prototype 67**
4.5.1 Lamination Selection 67
4.5.2 Stacking 68
**4.6 Shaft Prototype 69**
4.6.1 Titanium Alloy Shaft 69
4.6.2 Carbon Fiber Shaft 70
**4.7 Manufacturing Tolerance 72**
4.7.1 Surface Joint Issues 72
4.7.2 Roundness and Straightness 73
4.7.3 Temperature 73

**4.8 Chapter Summary** **73**

**CHAPTER 5. ELECTROMAGNETIC DESIGN** **75**
**5.1 Introduction** **75**
**5.2 Pole Pair Selection** **75**
**5.3 Air Gap Design** **75**
**5.4 Stator Winding Design** **76**
5.4.1 Winding Type Selection 76
5.4.2 Winding Area Calculation 77
**5.5 Stator Design** **78**
5.5.1 Material 78
5.5.2 Dimension 78
**5.6 Windage Torque Estimation** **79**
**5.7 Complete Design** **81**
**5.8 Chapter Summary** **82**

**CHAPTER 6. ELECTRICAL MODELLING AND SIMULATION** **83**
**6.1 Introduction** **83**
**6.2 2D Finite Element Modelling** **83**
6.2.1 Model Description 83
6.2.2 Simulation Results 84
**6.3 Maxwell/Simplorer Co-Simulation Model** **86**
**6.4 Fast Equivalent Model in Simulink** **87**
6.4.1 Equivalent model using lookup tables 87
6.4.2 Hysteresis Current Control for Steady State Simulation 88
6.4.3 Speed Feedback Control for Dynamic Simulation 90
**6.5 Chapter Summary** **92**

**CHAPTER 7. CONSTANT V/F CONTROL FOR UHSSRM** **94**
**7.1 Introduction** **94**
**7.2 Analysis of the Current Profile** **95**
7.2.1 Stage I: Low inductance stage (0, $\theta_1$). 96
7.2.2 Stage II: Inductance increasing stage ($\theta_1$, $\theta_{sat}$). 96
7.2.3 Stage III: Saturation stage ($\theta_{sat}$, $\theta_{off}$) 99
7.2.4 Stage IV: Freewheel stage ($\theta_{off}$ to $\theta_2$) 99
**7.3 Constant Volts per Herts Control** **99**
7.3.1 Stage I: Current increasing stage (0, $\theta_1$) 99
7.3.2 Stage II: Current constant stage ($\theta$1, $\theta$sat) 100
7.3.3 Stage III: Skipped 101
7.3.4 Stage IV: Freewheel stage ($\theta_{off}$ to $\theta_2$) 101
**7.4 Simulation Results** **103**
7.4.1 Validation of the Constant Volts/Hertz Control 103
7.4.2 Find the Suitable Value of V/$\omega$ 105
**7.5 Chapter Summary** **107**

**CHAPTER 8. DIRECT POSITION CONTROL FOR UHSSRM** **108**
**8.1 Introduction** **108**

**8.2 Limitation of Conventional Sensing Methods for UHSSRMs 110**
8.2.1 Optical Encoder 110
8.2.2 Hall-Effect Sensor 112
8.2.3 Resolver 112
8.2.4 Sensorless Control 113
**8.3 Non-intrusive Direct Position Control for UHSSRMs 114**
8.3.1 Non-intrusive Reflective Position Sensor 114
8.3.2 Direct Positoin Control for Ultra-high speed SRMs 115
8.3.3 Advantages 118
8.3.4 Disadvantages 118
**8.4 Modeling and Optimization 120**
8.4.1 Finite Element Model 121
8.4.2 Simulink Equivalent Model 122
8.4.3 Output Torque Optimization 123
**8.5 Experimental Results 125**
8.5.1 Experimental Setup 125
8.5.2 Model Validation 128
8.5.3 Experimental Results at 100,000 rpm 129
**8.6 Chapter Summary 130**

**CHAPTER 9. MULTI-PHYSICS ACOUSTIC ANALYSIS OF UHSSRM 131**
**9.1 Introduction 131**
**9.2 Electromagnetic Modeling and Analysis 132**
9.2.1 Electromagnetic Finite Element Analysis 132
**9.3 Radial Force Calculation 133**
**9.4 Modal and Vibration Analysis 136**
9.4.1 Modal Analysis 137
9.4.2 Harmonic Response Analysis 140
**9.5 Acoustic Analysis and Prediction 142**
9.5.1 Modeling 142
9.5.2 Model Setup 143
9.5.3 A-weighted Sound Pressure Level 143
**9.6 Experimental Verification 145**
9.6.1 Experimental Setup 145
9.6.2 Verification of Natural Frequencies 146
9.6.3 Verification of Acoustic Prediction 148
**9.7 Conclusion 150**

**CHAPTER 10. SYSTEM INTEGRATION AND TEST RESULTS 151**
**10.1 Introduction 151**
**10.2 Stator Prototype 151**
**10.3 Machine Assembly 152**
10.3.1 Bearing Housing and Face Collars 152
10.3.2 Sensor Tables 153
10.3.3 Final Assembly 154
10.3.4 Alignment Issues 155
**10.4 Fitting and Tubing 157**

**10.5 Air Compression System Setup 158**
**10.6 Experimental Results 160**
10.6.1 Inductance Measurement 160
10.6.2 Current Comparison 163
10.6.3 Torque Estimation 164
**10.7 Freewheeling Test 166**
10.7.1 Speed below 40,000 rpm 167
10.7.2 Speed beyond 40,000 rpm 168
**10.8 Possible Reasons for Too Much Windage Torque 169**
10.8.1 Unsmooth Surface Finish 169
10.8.2 Radial Force 170
**10.9 Conclusion 171**

**CHAPTER 11. CONCLUSION AND FUTURE WORKS 172**
**11.1 Conclusion 172**
**11.2 Recommendations for Future Work 174**
11.2.1 Exploring More New Applications with the New Rotor Design 174
11.2.2 Fatigue Analysis 175
11.2.3 Investigation of the Influence of Temperature on Shaft 175
11.2.4 New Shaft with High-Accuracy Surface Finish 175
11.2.5 Using Thin Sleeves outside the Existing Shaft 176
11.2.6 Hysteresis Control at Low Speed 176
11.2.7 Loss Estimation 177
11.2.8 Loss and Torque Measurement 178
11.2.9 Thermal Analysis 179
11.2.10 Noise Reduction 179
**11.3 Contributions 179**

**APPENDIX A. DRAWINGS OF MOTOR PARTS 185**

**REFERENCES 189**

**VITA 200**

# LIST OF TABLES


| | | |
|---|---|---|
| Table 2.1 | Properties of the cylinder | 19 |
| Table 2.2 | Comparison of Different Rotor Geometries | 28 |
| Table 2.3 | Mechanical Properties of Different Materials | 32 |
| Table 3.1 | Adhesive Strength of DP 420 Black for Different Materials [63] | 48 |
| Table 3.2 | Maximum Gap Length under Different Adhesive Strength | 50 |
| Table 4.1 | Comparison of Different Bearing Technologies [67] | 53 |
| Table 4.2 | Comparison of DN Number of Different Bearing Technologies [68] | 53 |
| Table 4.3 | Analytical and Numerical Calculation of the First Three Natural Frequencies of Titanium Alloy and Carbon Fiber | 58 |
| Table 4.4 | Mechanical Properties of Different Materials | 58 |
| Table 4.5 | Comparison between the Three Different Designs | 67 |
| Table 5.1 | The Characteristic of Different Types of Litz-wires | 77 |
| Table 5.2 | The Characteristic of Different Types of Litz-wires | 82 |
| Table 8.1 | Different Sensor Types for High-speed SRMs | 110 |
| Table 8.2 | Comparison of Different Sensing Methods | 120 |
| Table 8.3 | List of the Machine Parameters | 122 |
| Table 9.1 | Comparison of natural frequencies between FEA and experiment | 148 |

# LIST OF FIGURES


| | | |
|---|---|---|
| Figure 1.1 | High speed PCB spindle from Westwind [11] | 2 |
| Figure 1.2 | (a) Dental hand piece with a low-speed motor and several stages of mechanical transmission. (b) Direct-driven dental hand piece proposed in [12] | 3 |
| Figure 1.3 | 70 W, 300,000 rpm turbo compressor from Celeroton [14] | 4 |
| Figure 1.4 | NASA G2 3 kW, 40,000 rpm flywheel energy storage system [16] | 5 |
| Figure 1.5 | 30 kW, 100,000 rpm homopolar machine rotor [17] | 6 |
| Figure 1.6 | High speed machine examples in the literature | 6 |
| Figure 1.7 | The hollow shaft and magnet (left), housing, two caps, and the integrated rotor (right) of the 2kw, 200,000 rpm PM machine in [23]. | 7 |
| Figure 1.8 | Another 2kw, 200,000 rpm PM machine proposed in [24]. | 8 |
| Figure 1.9 | The 100w, 1,000,000 rpm PM machine proposed in [20]. | 8 |
| Figure 1.10 | Valeo's 70,000 rpm SRM turbocharger [30] | 9 |
| Figure 2.1 | Von-Mises stress distribution of the coaxial cylinder at 1000 rad/s. | 19 |
| Figure 2.2 | Comparison of the Von-Mises Stress between analytical and FEM of the coaxial cylinder. | 20 |
| Figure 2.3 | Stress distribution of the regular rotor geometry. | 21 |
| Figure 2.4 | High speed rotor lamination with no shaft bore (left) and rotor assembly with end plates (right) [38] | 22 |
| Figure 2.5 | High speed SRM with rotor sleeves. | 23 |
| Figure 2.6 | Stress distribution of the rotor with "flux bridges". | 24 |
| Figure 2.7 | Three view drawing and 3D view of the proposed design. | 26 |
| Figure 2.8 | Theoretical analysis of the proposed design using principle of the lever. | 29 |

| | | |
|---|---|---|
| Figure 2.9 | Stress distribution of a short rotor with 2 mm rotor stack. | 31 |
| Figure 2.10 | Stress distribution of a long rotor with 5 mm rotor stack. | 32 |
| Figure 2.11 | Zoom-in plot of the area with maximum stress. | 33 |
| Figure 2.12 | Total deformation of the short rotor. | 34 |
| Figure 2.13 | Total deformation of the long rotor. | 34 |
| Figure 2.14 | Stress distribution of the rotor stack. | 35 |
| Figure 3.1 | Mechanical finite element analysis of the shaft at 1.2 million rpm | 39 |
| Figure 3.2 | Mode I and Mode II separation. | 41 |
| Figure 3.3 | Traction-seperation curve and illustration of the adhesive region. The length of the arrows represents the value of the stress. | 42 |
| Figure 3.4 | Highlighted contact region. | 45 |
| Figure 3.5 | Meshing of the proposed model. | 45 |
| Figure 3.6 | Comparison of different adhesives for different adherends [61]. | 47 |
| Figure 3.7 | Parametric study results of total deformation of the shaft at 1.2 Mrpm. | 49 |
| Figure 3.8 | Strength analysis of the shaft with 2.3 mm rotor stack using adhesives. | 51 |
| Figure 4.1 | A pair of air bearings from OAV air bearing company. | 55 |
| Figure 4.2 | Side view of the ultra-high speed SRM. | 56 |
| Figure 4.3 | Strees analysis of the carbon fiber shaft at 1.2 million rpm. | 59 |
| Figure 4.4 | Shaft model with two bearings. | 60 |
| Figure 4.5 | First five vibration modes. | 61 |
| Figure 4.6 | Comparison of the Campbell diagram of the shaft with solid and laminated rotor stack. The third critical speeds are near the rated speed of 1 million rpm | 62 |
| Figure 4.7 | Shaft with tandem rotors in the middle. | 64 |

| | | |
|---|---|---|
| Figure 4.8 | Stress analysis of the shaft with tandem rotors. | 64 |
| Figure 4.9 | Shaft with bilateral rotors at both ends. | 65 |
| Figure 4.10 | Campbell diagram of the three different shaft geometries: single (red), tandem (blue) and bilateral (green). | 65 |
| Figure 4.11 | 0.006'' Hiperco 50 lamination in comparison with a | 68 |
| Figure 4.12 | Left: prototype of the rotor stack in comparison with a US quarter Right: zoom-in look of the rotor stack | 68 |
| Figure 4.13 | Construction of the shaft using interference fit. | 69 |
| Figure 4.14 | Procedure of the 3D printed shaft. | 70 |
| Figure 4.15 | Illustration of the process of manufacturing a carbon fiber shaft | 71 |
| Figure 4.16 | Comparison of three prototypes of carbon fiber shafts. | 72 |
| Figure 5.1 | CAD model of the machine with 50 turns of Litz-wire. | 79 |
| Figure 6.1 | External drive circuit. | 84 |
| Figure 6.2 | Flux density at the position of the maximum value. | 84 |
| Figure 6.3 | Current profile at 1 million rpm. | 85 |
| Figure 6.4 | Torque profile at 1 million rpm. | 85 |
| Figure 6.5 | Current profile at 1.2 million rpm. | 86 |
| Figure 6.6 | Torque profile at 1.2 million rpm. | 86 |
| Figure 6.7 | Simulation diagram. | 87 |
| Figure 6.8 | Flux against rotor position | 88 |
| Figure 6.9 | Torque against rotor position | 88 |
| Figure 6.10 | Closed loop hysteresis current control model in Simulink | 89 |
| Figure 6.11 | Comparison of current curves between Simplorer and Simulink model. | 90 |
| Figure 6.12 | Comparison of torque curves between Simplorer and Simulink model. | 90 |

| | | |
|---|---|---|
| Figure 6.13 | Reference speed and real speed profile. | 91 |
| Figure 6.14 | Output torque profile. | 91 |
| Figure 6.15 | DC supply voltage profile. | 92 |
| Figure 6.16 | Phase current profile. | 92 |
| Figure 7.1 | Typical profile of current, inductance and flux considering saturation. | 95 |
| Figure 7.2 | Typical current profiles of case b and c. | 98 |
| Figure 7.3 | Block diagram of the proposed constant volts per hertz control. | 102 |
| Figure 7.4 | Typical profiles of the three situations. | 103 |
| Figure 7.5 | Current profile under different speeds. | 104 |
| Figure 7.6 | Simulation results from 0 to 1 million rpm. | 105 |
| Figure 7.7 | Curve of $d\psi/dt$ at 1 million rpm. | 106 |
| Figure 8.1 | Working mechanism and typical appearance of conventional rotary encoders. | 111 |
| Figure 8.2 | Setup of the proposed sensor. | 115 |
| Figure 8.3 | Proposed direct position control. | 117 |
| Figure 8.4 | PWM current control with the optical sensors. | 117 |
| Figure 8.5 | FEM of the SRM. | 121 |
| Figure 8.6 | Flux linkage against rotor position under various excitation currents. | 122 |
| Figure 8.7 | Torque against rotor position under various excitation currents. | 123 |
| Figure 8.8 | Torque optimization under 140 $V_{dc}$ at 100,000 rpm. | 124 |
| Figure 8.9 | Torque optimization when switching-on angle is 0°. | 124 |
| Figure 8.10 | Picture of the 4/2 SRM and the optical sensor setup. | 126 |
| Figure 8.11 | Picture of the drive circuit | 127 |
| Figure 8.12 | Block diagram of the closed loop control | 128 |

| | | |
|---|---|---|
| Figure 8.13 | Comparison of the current profiles at 50,000 rpm. | 128 |
| Figure 8.14 | Experimental result at 100,000 rpm. | 129 |
| Figure 9.1 | 3D FEA of the 4/2 SRM. | 133 |
| Figure 9.2 | Air gap flux density distribution at 300 μs (one half cycle) at 100,000 rpm. | 134 |
| Figure 9.3 | Radial force and winding current of each phase at 100,000 rpm. | 135 |
| Figure 9.4 | Total radial force on the stator at 100,000 rpm. | 135 |
| Figure 9.5 | FFT of the total radial force on the stator at 100,000 rpm. | 136 |
| Figure 9.6 | Workflow of the proposed acoustic prediction process. | 137 |
| Figure 9.7 | Model with meshing of the modal and harmonic analysis. | 139 |
| Figure 9.8 | First 6 modes and natural frequencies. | 139 |
| Figure 9.9 | Mapping of the radial force imported from electromagnetic FEA. | 141 |
| Figure 9.10 | Frequency response of velocity of the surface of aluminum case. | 141 |
| Figure 9.11 | Modeling of the acoustic analysis. | 143 |
| Figure 9.12 | A-weighted SPL of the acoustic FEA at 100,000 rpm. | 145 |
| Figure 9.13 | Experimental setup of the 4/2 ultra-high speed SRM. | 146 |
| Figure 9.14 | Measured frequency response at 100,000 rpm. | 147 |
| Figure 9.15 | Measured A-weighted SPL at 100,000 rpm. | 149 |
| Figure 10.1 | Stator lamination and prototype. | 151 |
| Figure 10.2 | Stator prototype with windings. | 152 |
| Figure 10.3 | Air bearing, bearing housing and face collars. | 153 |
| Figure 10.4 | Adjustable sensor tables. | 154 |
| Figure 10.5 | Final assembly of the proposed ultra-high speed SRM. | 154 |
| Figure 10.6 | Prototype of the 1 million rpm SRM. | 155 |

| | | |
|---|---|---|
| Figure 10.7 | Alignment of the shaft with the stator half by half. | 156 |
| Figure 10.8 | Motor with carbon fiber face collars. | 157 |
| Figure 10.11 | Air filters from RTI. | 159 |
| Figure 10.12 | Air regulator. | 159 |
| Figure 10.13 | Air pressure gauge. | 159 |
| Figure 10.14 | Setup of the air compression system. | 160 |
| Figure 10.15 | Inductance measurement of phase A at the aligned position. | 161 |
| Figure 10.16 | 3D FEA of the motor. | 162 |
| Figure 10.17 | Comparison of inductance of 2D FEA, 3D FEA and experiment. | 163 |
| Figure 10.18 | Current comparison between 2D FEA and experiment at 78,000 rpm under 18 Vdc. | 163 |
| Figure 10.19 | Torque estimation from 2D FEA at 78,000 rpm. | 164 |
| Figure 10.20 | Variable resistors for changing the current limit. | 165 |
| Figure 10.21 | Test results at 90,000 rpm. | 166 |
| Figure 10.22 | Freewheeling test at 30,000 rpm. | 167 |
| Figure 10.23 | Freewheeling test results at different speeds. | 169 |
| Figure 10.24 | Estimated radial force at 78,000 rpm. | 170 |
| Figure 11.1 | Air bearing (blue) and shaft (gray) with high-accuracy thin sleeves (red) | 176 |

# LIST OF SYMBOLS AND ABBREVIATIONS

Abbreviation:

| | |
|---|---|
| SRM | Switched Reluctance Machine |
| UHSSRM | Ultra-High Speed Switched Reluctance Machine |
| IM | Induction Machine |
| PM | Permanent Magnet |
| SynRM | Synchronous Reluctance Machine |
| FEA | Finite Element Analysis |
| FEM | Finite Element Model |
| mph | mile per hour |
| rps | revolution per second |
| VCCT | Virtual Crack Closure Technique |
| CZM | Cohesive Zone Model |
| SPL | Sound Pressure Level |
| rms | Root Mean Square |

Symbol:

| | |
|---|---|
| $D$ | Stator bore diameter (m) |
| $L$ | Machine active length (m) |
| $n$ | Rotational speed (rpm) |
| $\sigma_V$ | "Von-Mises" stress (Pa) |
| $\sigma_\theta$ | Tangential stress component (Pa) |
| $\sigma_r$ | Radial stress component (Pa) |
| $v_p$ | Poisson's ratio |
| $m_V$ | Mass per unit volume (kg/m$^3$) |
| $\omega$ | Angular velocity (rad/s) |
| $R$ | Radius (m) |
| $R_1$ | Inner radius (m) |
| $R_2$ | Outer radius (m) |
| $r$ | Radius of the point of interest (m) |
| $N_r$ | Number of rotor poles |
| $N_{rpm}$ | Rated speed in rpm |
| $m$ | Mass (kg) |
| $\delta_c$ | critical crack opening displacement (m) |
| $\sigma$ | cohesive stress (Pa) |
| $\delta$ | interfacial separation displacement (m) |
| $G$ | fracture energy release rate (J/m$^2$) |
| $G_c$ | critical fracture energy release rate (J/m$^2$) |
| $\Gamma_c$ | interface toughness (J·m$^{-3}$) |
| $\sigma_c$ | critical (peak) opening stress (Pa) |

| | |
|---|---|
| $\omega_n$ | $n^{th}$ natural frequency (rad/s) |
| $E$ | Young's modulus (MPa) |
| $\mu_l$ | Mass per unit length (kg/m) |
| $I$ | Moment of inertia ($kg \cdot m^2$) |
| $l$ | Rotor Length (m) |
| $[M]$ | Mass matrix |
| $[K]$ | Stiffness matrix |
| $[C]$ | Damping matrix |
| $[C_{gyr}]$ | Gyroscopic matrix |
| $I_p$ | Polar moment of inertia ($kg \cdot m^2$) |
| $I_d$ | Diametral moment of inertia ($kg \cdot m^2$) |
| $\theta$ | Angular displacement (rad) |
| $f_rA$ | Phase A radial force (N) |
| $f_rB$ | Phase B radial force (N) |
| $\rho_{air}$ | Density of the air ($kg/m^3$) |
| $Ta$ | Taylor number |
| $v$ | Kinematic viscosity of the air (Pa·s) |
| $\delta$ | Air gap length (m) |
| $c_f$ | Friction coefficient |
| $Re$ | Reynolds number |
| $L_d$ | d-axis inductance (H) |
| $L_q$ | q-axis inductance (H) |
| $J$ | Moment of inertia ($kg \cdot m^2$) |
| $T_f$ | Air friction torque (N.m) |

# SUMMARY

The objective of this dissertation is to design, manufacture and control an ultra-high speed switched reluctance machine (UHSSRM) for applications requiring speeds of over 1 million rpm. First, a literature survey is conducted to investigate ultra-high speed electric machines and their applications. Then a novel rotor design is proposed for an ultra-high speed SRM to be capable of running at over 1 million rpm. The rotor stack has a unique, smooth shape, without any holes in the middle. The design calls for a shaft with the same outer diameter to surround the rotor stack in the middle, with rotor poles facing directly from the stator poles across the air gap without going through any additional sleeves. Compared with the conventional design, the proposed design has many advantages, such as high strength, high power density, high efficiency and high reliability. The new geometry is validated with 3D finite element analysis (FEA). High-strength adhesives need to be applied properly to increase the mechanical bonding between the rotor stack and the shaft. The final length of the rotor stack is optimized using the cohesive zone model (CZM). A detailed rotor dynamics analysis of the proposed rotor structure is conducted.

After the rotor mechanical design, a detailed electromagnetic design of the whole UHSSRM is proposed, which includes pole pair number selection, air gap design, dimension calculation, material selection, winding selection and windage torque calculation. The final design is a 4/2 SRM, which has an outer diameter of 30 mm. It has 50 turns of gauge 42/24 Litz-wire in each stator pole. The air gap is 0.3 mm. Both of the stator and rotor poles are made from 0.006'' Hiperco 50 laminations. The machine is able to produce a maximum torque of 0.7 mN·m and 1 mN·m at 1 million and 1.2 million rpm,

respectively, in order to overcome the high windage torque. The design is validated by a detailed 2D FEA.

Next, a constant volts per hertz (*V*/*f*) control and an optical-based direct position control for UHSSRMs are proposed. The constant *V*/*f* control minimized the switching frequency over the entire speed range from 0 to 1,000,000 rpm. The shape of the current profile is analyzed in detail. In order to break the mechanical speed limit of commercial rotary encoders, a non-intrusive, low-cost optical-sensor-based direct position control for UHSSRMs is proposed. The idea is to use non-contact optical sensors to detect the relative rotor and stator position so as to reach one pulse control for each phase. The switching on and off angles are optimized to generate the maximum output torque. The method is verified on a 4/2 SRM at 100,000 rpm.

After that, a multi-physics acoustic analysis of UHSSRMs is proposed based on FEA. First, a 3D electromagnetic FEA is conducted to calculate the radial force on the stator teeth, which is the origin of the noise. Then, a modal analysis and a harmonic response analysis are conducted to estimate the surface vibration of the entire motor, using the radial force as input in the frequency domain. Finally, an acoustic response analysis is conducted to estimate the sound pressure level using the superstition of the motor surface vibration information from the harmonic response analysis. The model is proven to be very accurate in predicting the noise level of UHSSRMs at 100,000 rpm by experiment. The bearing noise is shown to be negligible compared with the noise generated by radial force.

Finally, for the first time in the literature, the proposed design is integrated with aerostatic bearings. The machine is built but has not achieved its target speed due to the

manufacture of the bearings. A detailed analysis is conducted according to the test results. The suggestions and improvements for the future work have been proposed.

# CHAPTER 1. INTRODUCTION

## 1.1 Background

Electric machines are one of the fundamental energy conversion devices in both industrial applications and everyday use. They consume a large amount of the world's total electrical energy all around the world [1, 2]. The benefit of using an electric machine is its high efficiency and high power density. Recently, there has been a trend towards the electrification of modern vehicles, brought about by the success of Tesla's first full-sized all-electric luxury car, the Model S. It has a range of over 300 miles, and it is able to accelerate from zero to sixty miles per hour in 2.5 seconds, thanks to the state-of-the-art induction motor, and new techniques in battery management. After that, more and more research emphasis has been put towards the development of electric motors by both academia and automotive companies [3-9]. The ultimate goal is to develop electric machines with high power and torque density, high efficiency, high speed and low cost.

## 1.2 Literature Survey

### *1.2.1 Ultra-High Speed Electric Machine Applications*

High-speed electric machines have been a hot topic in recent years. The most attractive feature of the machine's high speed is the dramatic decrease of the size of the machine, which roughly decreases in direct proportion to the speed for a given rating.

With the development of modern power electronics, the top speed of electric motors has increased significantly. Many new applications that were not previously possible have

been proposed, with the increasing upper limit of rotational speed. In the following sections some key applications of ultra-high speed electric machines are listed [10].

#### 1.2.1.1 Micro-Machining Spindle

One of the major applications of ultra-high speed electric machines is in micro-hole drilling. For example, in the micro-electronics industry, the trend is always towards reducing the size of electronic packages, which means an increase in the total pin number on a chip over a smaller area. These pins have to be connected to the rest of the circuit through multiple layers. These layers are then connected to each other by microvias. The smaller these microvias are, the more connections between the layers, resulting in a more compact package with more pins. State-of-the-art PCB mechanical drilling spindles from Westwind have the highest speed in excess of 370,000 rpm, enabling microvia production down to holes with a diameter of less than 75 μm diameter holes [11] (see Figure 1.1). For even smaller microvias only laser drilling is the only option, which is very expensive compared to mechanical spindles. Some research shows that for 10 μm holes, the drilling speed has to be over 1 million rpm [10].


Figure 1.1 High speed PCB spindle from Westwind [11]

Another example is its use in the dental drill industry. Currently, most dental drills are powered by air turbines driven by compressed air. The problem with using air turbines is that only a single speed can be reached by a single piece of drill, while a typical dental operation can require up to five different speeds. However, with the adjustable high-speed electrical drive with feedback control, speed and torque can be accurately controlled at several different speeds. The biggest challenge of the electrical drive is to increase the maximum speed so as to eliminate the use of gear stages, and to reduce the size of the drive to fit into a typical small handpiece. For example, the regular 10 W, 200,000 rpm dental drill is powered by a 40,000 rpm electric motor, with a triple-gear system stepping to its maximum speed [10]. With the new, direct-driven dental drill shown in Figure 1.2 [12], the size of the electric drive can be significantly reduced.

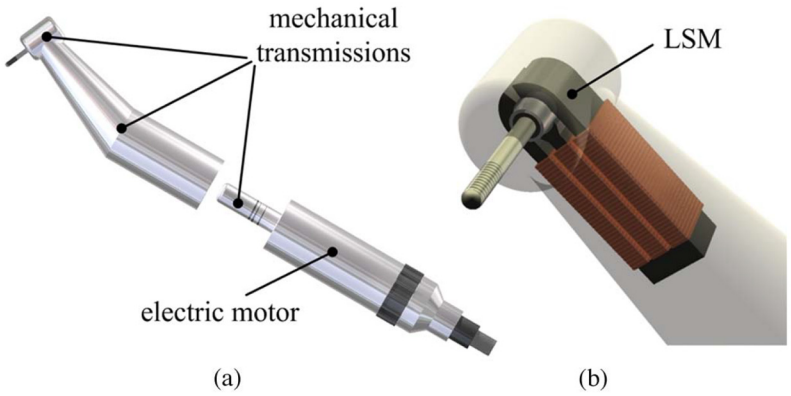


Figure 1.2 (a) Dental hand piece with a low-speed motor and several stages of mechanical transmission. (b) Direct-driven dental hand piece proposed in [12]

1.2.1.2 Turbo-Compressor/Generator

Turbo-compressors/generators are another important application for ultra-high speed electric machines. If an electric machine is working in the motor mode, it becomes a turbo-air compressor that compress the air into a useful place with electric energy. On the other

hand if it is working in the generator mode, the air rotates the rotor in a turbine, and electrical energy is generated. For example, to increase the fuel economy of an internal combustion engine, a turbocharger is often used to compress the ambient air into the combustion chamber, which burns the fuel more efficiently. Turbochargers have been reported to run at speeds up to 280,000 rpm [13]. However, normal turbochargers typically have poor performance at low engine speeds, which is known as turbo lag. With the application of an electrically assisted turbocharger (often known as "e-charger"), this problem can be easily solved. But the electrical motor has to operate at the same ultra-high speed as the turbocharger, since they are both mounted on the same shaft. Figure 1.3 shows a 70 W 300,000 rpm turbo compressor developed by Celeroton [14].

Figure 1.3 70 W, 300,000 rpm turbo compressor from Celeroton [14]

For the turbo-generator, there are emerging applications for a low power, portable, gas-turbine-based power supply, such as in a power generation system for electrical equipment (up to 100 W) of a modern soldier. For such applications, low weight is the primary concern, which results in a need for ultra-high speed turbo-generators. It is

reported that at these power levels, the gas turbine system would only occupy a very small size and weight if the rotational speed can be increased to over 500,000 rpm [15].

#### 1.2.1.3 Flywheel

Flywheels use rotational energy as a means of energy storage. They are often operated in a vacuum environment, and uses magnetic or air bearings to reduce friction losses. To increase stored energy, one can either increase the mass of the machine, and run at a low speed (<10,000 rpm), or increase the rotational speed (>10,000 rpm) with a machine with a lower mass. Obviously the latter is a better choice in terms of conserving space and resources. For example, a 3 kW, 40,000 rpm G2 flywheel was tested by NASA on Sep. 2, 2004 for space craft energy storage (Figure 1.4) [16]. Another 30 kW, 100,000 rpm homopolar machine was designed in [17] (Figure 1.5). For reduced power aerospace applications a 100 W, 300,000 rpm permanent magnet flywheel was investigated although in its experimental testing it reached only 30,000 rpm [18].

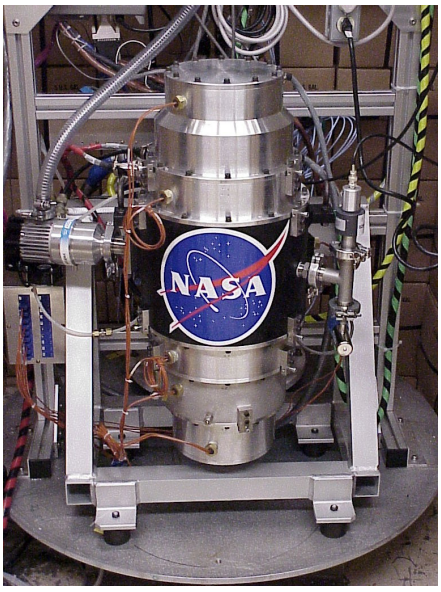


Figure 1.4 NASA G2 3 kW, 40,000 rpm flywheel energy storage system [16]

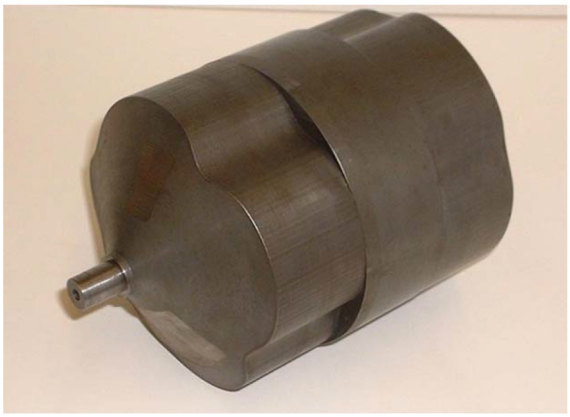

Figure 1.5 30 kW, 100,000 rpm homopolar machine rotor [17]

### *1.2.2 High Speed Electric Machines below 100,000 rpm*

Figure 1.6 shows the progress of high speed electric machines in the literature [1]. The horizontal axis denotes the rotational speed and the vertical axis denotes the power level. From the figure, it can be seen that below 100,000 rpm there are multiple types of electric machines such as induction machines (IMs), permanent magnet (PM) machines, switched reluctance machines (SRMs), synchronous reluctance machines (SynRMs) and homopolar machines. IMs and PM machines tend to have higher power levels than SRMs. Reference [19] gives a good review of different types of high-speed electric machines.

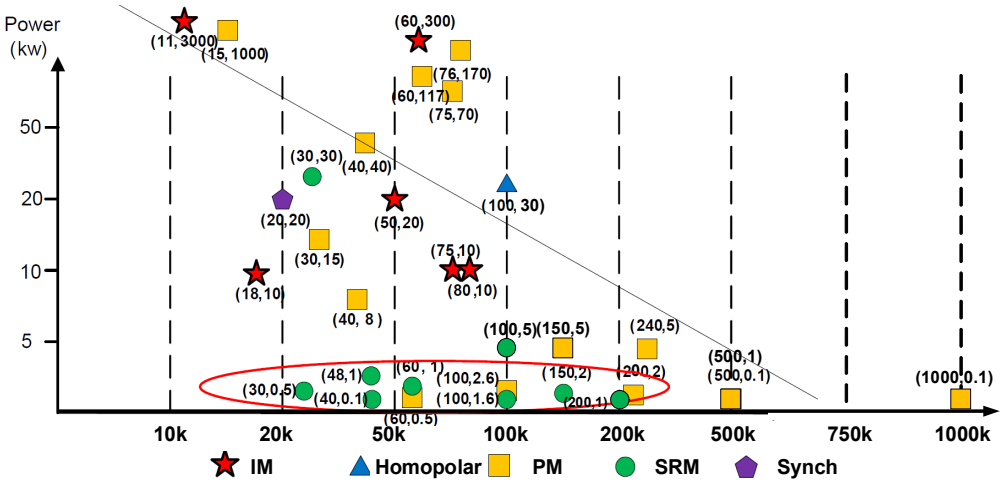


Figure 1.6 High speed machine examples in the literature [1]

### *1.2.3 Ultra-high speed Electric Machines beyond 100,000 rpm*

The most challenging element of research concerns when the operating speed is in excess of 100,000 rpm [20]. For ultra-high speed electric machines that run beyond 100,000 rpm, only a handful of research projects have been conducted [1]. There are only two major categories of machines run at this level: PM machines and SRMs.

#### 1.2.3.1 Permanent Magnet Machines

PM machines are the most popular choice for situations requiring speeds beyond 100,000 rpm. The first ultra-high speed PM motor was built by a group of scientists from Japan in 1994. The motor was a surface mounted PM type that has a power of 5 kW and a rotational speed of 150,000 rpm [21]. A 5 kW, 240,000 rpm PM machine was targeted and currently it has achieved 180,000 rpm with no load [22]. Reference [23] and [24] proposed two 2kW, 200,000 rpm PM motors separately with similar design specifications (shown in Figure 1.7 and Figure 1.8). For the commercial uses, 200,000 rpm PM machines are available from ATE, which are able to run at power levels between 200 and 900 W [25]. Machines running at speeds up to 450,000 rpm is available from Calnetix although little information on these machines can be found [26].

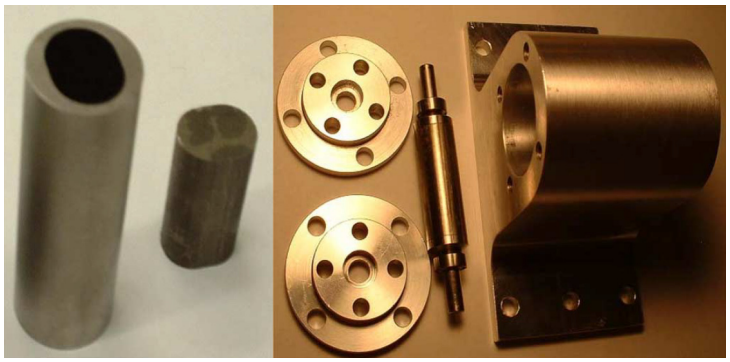

Figure 1.7 The hollow shaft and magnet (left), housing, two caps, and the integrated rotor (right) of the 2kw, 200,000 rpm PM machine in [23].

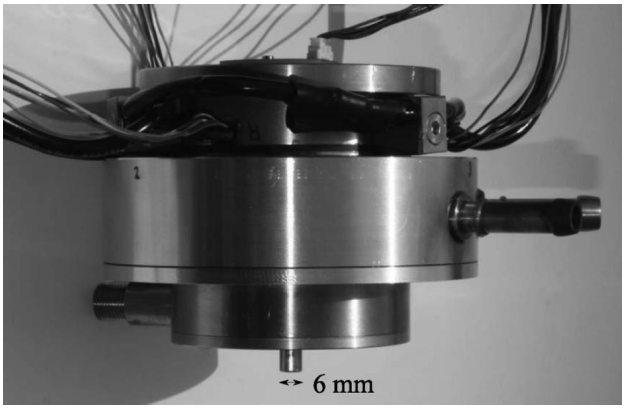


Figure 1.8 Another 2kw, 200,000 rpm PM machine proposed in [24].

Since 2004, the PES lab at ETH-Zurich and its spin-off company Celeroton have been working on ultra-high speed PM machines over 500,000 rpm. Several 500,000 rpm, 100 W [27] and 1 kW [28] PM drive systems have been developed. In 2009, a 1 million rpm, 100 W drive system was developed, which holds the current world speed record (Figure 1.9) [20]. All of these PM machines that run over 200,000 rpm share similar geometries, such as two-pole rotors with sleeves and slot-less stators.


Figure 1.9 The 100w, 1,000,000 rpm PM machine proposed in [20].

The benefit of PM machines is obvious: it can achieve a higher torque density with a comparatively simple rotor geometry. However, it has all the drawbacks of PM machines, such as the demagnetization characteristics of the PMs in the rotor due to high temperature, which could be more prominent in ultra-high speed applications, like an extended period

of grinding or drilling, or in turbocharging in a very high ambient temperature. Once the PM is irreversibly demagnetized, the motor is no longer usefull. It is reported that the exhaust temperature of a turbocharger can be as high as 1050 °C [29], which makes it impossible for any PM machines to realistically operate. Another drawback is the brittleness of a PM. This could cause problems, especially at ultra-high speeds when the rotor is under an extremely high centrifugal forces, especially if the mechanical fit between the PMs and the rotor sleeve is not properly designed or manufactured.

#### 1.2.3.2 Switched Reluctance Machines

Compared with PM machines, SRMs are also good candidates for ultra-high speed applications, due to their intrinsically simple and robust rotor geometry. Also, because there is no PM in the rotor, SRMs are more suitable in harsh environments, such as in applications where turbocharging is required. For example, Valeo developed an SRM turbocharger with a rated speed of 70,000 rpm from 1 kW to 7kW (Figure 1.10). Besides the good thermal performance, it also has very high dynamic performance. It is able to go from idle speeds to the maximum speed in less than 350 ms, thanks to the very low inertia of the SRM rotor [30].

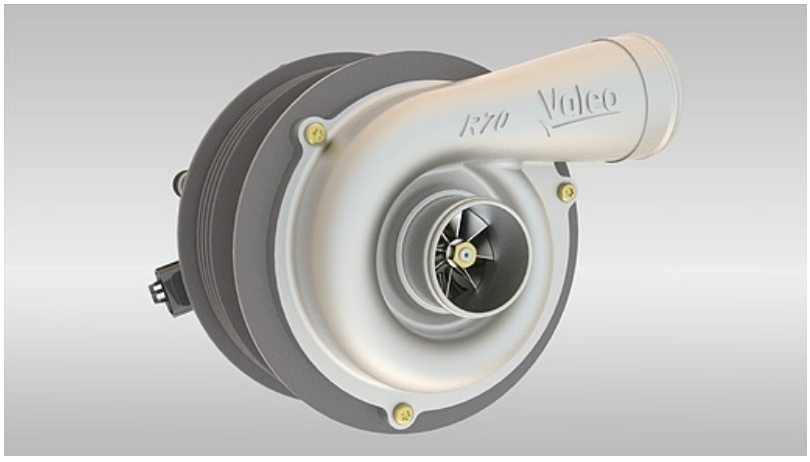


Figure 1.10 Valeo's 70,000 rpm SRM turbocharger [30]

Reference [31] gives a good review of the state-of-the-art high-speed SRMs. For ultra-high speeds over 100,000 rpm, there are only four SRMs have been reported, although several more have been designed without being implemented. For machines operating at 100,000 rpm, there are SRMs running at 1.6 kW [32] and 5 kW [33] reported in the literature. They have 4/2 and 6/4 geometries for the applications in air blowers and automotive turbo-generators, respectively. Another 2 kW, 150,000 rpm SRM was built and tested by Prof. Akira Chiba in 2008, which is the highest speed an SRM has achieved while possessing detailed experimental results. There was another SRM designed for 1 kW, 200,000 rpm applications in [34]. However, the only data from this SRM was revealed while it was running at 110,000 rpm in the paper.

## 1.3 Objective

In conclusion, the highest speed achieved by an SRM is 150,000 rpm in the literature. From the above discussion, although there are multiple applications for machines running at speeds over 500,000 rpm, no research has been done to design an SRM for those ultra-high speed applications wherein a PM machine is not suitable. This is the driving force of this thesis.

The objective of this thesis is to design, manufacture and control an ultra-high speed SRM for applications requiring speeds of over 1 million rpm. To achieve this goal, multiple challenges must be overcome in many details of the design, control and manufacturing.

## 1.4 Difference of Regular Speed Machine and Ultra-High Speed Machine

For regular speed machines, the traditional design is usually based on rules of thumb. One assumption is that the electrical frequency is either 60 Hz or 50 Hz. However, for ultra-high speed machine design, because the fundamental frequency is in the range of 10 kHz or beyond, the expertise, assumptions and design equations for regular speed machines

are no longer applicable. One must explore a totally new path to find the optimal design of ultra-high speed machines, regarding the following design parameters.

### *1.4.1 Mechanical Strength of Rotor*

For regular speed machines, the mechanical strength of the rotor is almost never a problem. However, for ultra-high speed machine design, the first thing to consider is the size of the rotor, which is limited by the high centrifugal force at ultra-high speeds. Because of this, the power rating of ultra-high speed machines is also limited. Furthermore, due to the severe limitation on the size of the rotor, the power density of the machine must be significantly higher than conventional machines.

### *1.4.2 Air Gap Length*

The choice of the air gap length in regular speed machine design is often based on empirical equations, which is proportional to the power rating. Usually the larger the machine is, the larger the air gap length is. For high speed machines, the air gap length must be smaller. However, this may not necessarily the case for ultra-high speed machines over 1 million rpm. At such high speeds, inevitably, the rotor passes through several critical resonant speeds that can easily result in catastrophic damage. If the air gap is too small, this resonance will lead to a contact of the rotor with the stator and thus a failure of operation.

### *1.4.3 Magnetic Loading and Core Losses*

The magnetic loading, or the flux density in the air gap and stator/rotor laminations, is generally selected based on empirical relationships in “normal” (50 or 60 Hz) machine design. Usually the peak flux density in the air gap is between 0.5 T to 1 T and under 1.5 T in the laminations for a normal machine in order to avoid saturation. However, this rule

of thumb does not hold for ultra-high speed machines. Because of the tiny size and the need for a sufficiently large air gap, the flux density in the air gap is necessarily lower. In order to increase the power density, new lamination materials with higher saturation are required. This is even more exasperated for UHSSRMs because SRMs usually require a smaller air gap and must be operated at a higher saturation level, to achieve the requisite power density.

With higher flux density, and a much higher fundamental frequency at ultra-high speeds, the core losses in the stator laminations (hysteresis loss, eddy current loss and excess loss) are much higher than in the regular speed machines. The well-known Steinmetz's equation clearly shows the nonlinear relationship between the frequency, flux density and the core losses. That is,

$$P_{avg} = k \cdot f^{a} \cdot B^{b} \tag{1.1}$$

where the coefficient *a* is usually between 1 and 2, and *b* is between 2 and 3 [35]. Because the size of ultra-high speed machines is actually smaller than regular speed machines, the cooling of the stator can be challenging.

### *1.4.4 Electric Loading and Copper Losses*

The electric loading, or the current density, is also usually chosen based on a rule of thumb for regular speed machines. However, for ultra-high speed machines, because of the need of a sufficiently large air gap, the electric loading needs to be larger to achieve the same flux density in the air gap, to achieve the required high power density.

For nomal speed machines, the copper loss in the stator windings is strictly ohmic. However, for ultra-high speed machines, because of the high frequency, the skin effect [36] and proximity effect [37] in the stator windings become very significant and obviously result in increased power loss in the stator coils. There are non-trivial challenges reducing these losses in ultra-high speed machines.

### *1.4.5 Machine Size and Length*

For regular speed machines, the power rating can be easily scaled up/down by increasing/decreasing the size and length of the machine without any practical limitations, from several watts up to several megawatts. However, for ultra-high speed machines, the outer diameter of the rotor is limited by the centrifugal force and the mechanical strength of the lamination in the rotor. The total rotor length must be relatively short as well in order to avoid several critical speeds before the rated speed. Therefore, the outer diameter, active length and power rating of ultra-high speed machines are limited by the speed.

## 1.5 Challenges

### *1.5.1 Challenges in Design*

The biggest challenge is in the design of the rotor. At such high speeds, the centrifugal force on the rotor laminations is huge, especially at the sharp corners and the shaft hole [38]. The similar solution of using a sleeve as in PM rotors may be applied in SRM rotors, such as in [34] and [39]. However, this will lead to an increase of the equivalent air gap by about twice [39], which should be actually avoided in the design of SRMs due to the lack of PMs in the rotor.

Another challenge in the design is to reduce the losses in both rotor and stator. Although the SRM rotor is intrinsically very robust, the double-saliency characteristic will lead to high windage loss. For ultra-high speeds as high as 1 million rpm, this problem will be a disaster since the air drag force is proportional to the third power of the rotational speed. For the stator, due to the high fundamental frequency, the switching frequency will be several hundreds of kilohertz if a PWM control is applied. This will lead to very high

switching loss and core loss. The skin effect will also provide additional losses in the stator windings.

### *1.5.2 Challenges in Control*

The challenges in control at such high speeds are obvious. The biggest one is in the speed sensor. The fastest commercial rotary encoder available on the market has the highest speed of only 60,000 rpm [1]. The reason for that is due to the mechanical stability issues. One possible solution is to use sensorless control. However, this topic itself is under research. The fasted sensorless SRM that has ever been achieved is reported in [32], with a target speed of 100,000 rpm. However, only 80,000 rpm was achieved due to some unknown reasons, which indicates that it will be extremely difficult to use sensorless control at 1 million rpm, especially without the help and comparison of commercial encoders. Also, as indicated above, the normal PWM control is not suitable for ultra-high speeds over 1 million rpm. New control method should be proposed to reduce the switching losses as well as to reduce the difficulty in the design of the drive circuits.

### *1.5.3 Challenges in Manufacture*

The manufacture of the SRM at such high speed is not trivial. At this small scale, the rotor has to be properly designed and carefully manufactured in order to ensure a safe operation under a very small air gap length. Also, the rotor has to be balanced correctly before the final assembly of the machine.

The selection of the bearings is also critical. Basically there are three kinds of different bearing technologies: ball bearing, air bearing and magnetic bearing. The first has

the highest stability but will introduce much more friction losses at ultra-high speed than the other two. The 1 million rpm PM motor developed in [20] uses ceramic ball bearings, however, they disintegrated after reaching its maximum speed. This leads to the follow-up research in magnetic bearings [40] and air-magnetic combined bearings [41]. However, the magnetic bearing technology is very complex and will increase the difficulty and reduce the reliability of the system.

Rotor dynamics is another problem to consider during the design. For such high speeds it is inevitable to pass through the first several natural frequencies [20]. How to design the rotor so that the natural frequencies can be as high as possible but not coincide with the rated speed has to be considered and estimated carefully.

## 1.6 Dissertation Outline

This dissertation is organized as follows:

Chapter 2, 3 and 4 focus on the mechanical design and analysis of the rotor. In Chapter 2, a novel rotor geometry for ultra-high speed SRMs over 1 million rpm is proposed with detailed theoretical and numerical stress analysis; then, an improved design with the analysis of the rotor robustness of the new geometry is proposed using the cohesive zone model in Chapter 3; next, the rotor dynamics analysis is conducted and a prototype of the rotor is built.

Chapter 5 and 6 focus on the electromagnetic design and modelling of the machine. In Chapter 5, a complete electromagnetic design of the 1 million rpm SRM is proposed; various models of the machine are proposed to verify the design including a Finite Element

Model (FEM) and a Simulink equivalent model, which are introduced in Chapter 6. The target is to generate enough torque at 1 million rpm.

Chapter 7 and 8 focus on the control of the machine. In Chapter 7, a constant volts per hertz control for ultra-high speed SRMs over an entire range of speeds from 0 to 1 million rpm is proposed, in order to reduce the switching losses; then a direct position control based on low-cost non-intrusive reflective sensors is proposed in Chapter 8 for ultra-high speed SRMs to break the speed limit of commercial encoders.

Chapter 9 proposed a multi-physics FEA to estimate the acoustic performance of ultra-high speed SRMs over 100,000 rpm. The model is very accurate and verified by experiments.

Chapter 10 shows the final assembly of the 1 million rpm SRM and the corresponding test results. Chapter 11 discuses about the conclusions and future works.

# CHAPTER 2. ROTOR MECHANICAL DESIGN

## 2.1 Introduction

For ultra-high speed electric machines that run at speeds over 1 million rpm, one needs to follow a totally different design procedure from "regular" or what is commonly referred to as a "high-speed" machine design. The first thing to be considered is the rotor structure, because the conventional rotor geometries are not suitable for ultra-high speed applications over 1 million rpm. In this section, a novel rotor design is proposed for ultra-high speed SRMs over 1 million rpm. The rotor stack has a unique smooth shape without any holes in the middle. A shaft that has the same outer diameter contains the rotor stack in the middle with two clamping arms. Compared to the conventional design, the proposed design has many advantages, such as high strength, high torque density, high efficiency and high reliability. Theoretical and 3D finite element stress studies are used to analyze the new geometry.

## 2.2 Stress Analysis of a Coaxial Cylinder

At ultra-high speeds, the high centrifugal force will induce significant stress on the rotor, which may lead to disintegration/failure of the rotor laminations. In order to analyse the mechanical stress of any rotor geometry under ultra-high speed conditions, a simple benchmark modelling of a coaxial cylinder is conducted in the first place to get an accurate finite element model (FEM). Usually the "Von-Mises" stress, $\sigma_V$, is used as the criteria of the likelihood of yield or fracture, which can be calculated from (2.1),

$$\sigma_V = \sqrt{\sigma_r^2 + \sigma_\theta^2 - \sigma_r \sigma_\theta} \tag{2.1}$$

where $\sigma_\theta$ denotes the tangential stress component and $\sigma_r$ denotes the radial stress component [33].

### *2.2.1 Analytical Analysis*

For regular geometries such as cylinders, there exist analytical equations to estimate the centrifugal stress distribution. Equation (2.2) and (2.3) give the exact analytical centrifugal stress distribution of a coaxial cylindrical rotor in the radial and tangential directions [33]:

$$\sigma_r = \frac{(3+\nu_p)}{8} m_V \omega^2 \left( R_1^2 + R_2^2 - \frac{R_1^2 R_2^2}{r^2} - r^2 \right) \tag{2.2}$$

$$\sigma_\theta = \frac{(3+\nu_p)}{8} m_V \omega^2 \left( R_1^2 + R_2^2 + \frac{R_1^2 R_2^2}{r^2} - \frac{1+3\nu_p}{3+\nu_p} r^2 \right) \tag{2.3}$$

where $\nu_p$ is the Poisson's ratio of the material; $m_V$ is the mass per unit volume; $\omega$ is the angular velocity; $R_1$ and $R_2$ are the inner and outer radii of the cylinder, respectively; $r$ is the radius of the point whose stress is to be calculated.

### *2.2.2 Finite Element Analysis*

In order to calculate the stress distribution of any shape under high-speed conditions, the commercial finite element analysis (FEA) software ANSYS is used. The rotational velocity is added as a load under steady state speed conditions. The "revolute-ground to solid" joint is applied to the inner radius as a boundary condition. Figure 2.1 shows the Von-Mieses stress distribution of a coaxial cylinder at 1000 rad/s. The mesh size is set to be 30 mm (shown on the figure). The properties of the cylinder is shown in Table 2.1.

Table 2.1 Properties of the cylinder

| $v$ | $m_V$ | $R_1$ | $R_2$ | $\omega$ |
|---|---|---|---|---|
| 0.3 | 7610 kg/m$^3$ | 0.5 m | 1 m | 1000 rad/s |

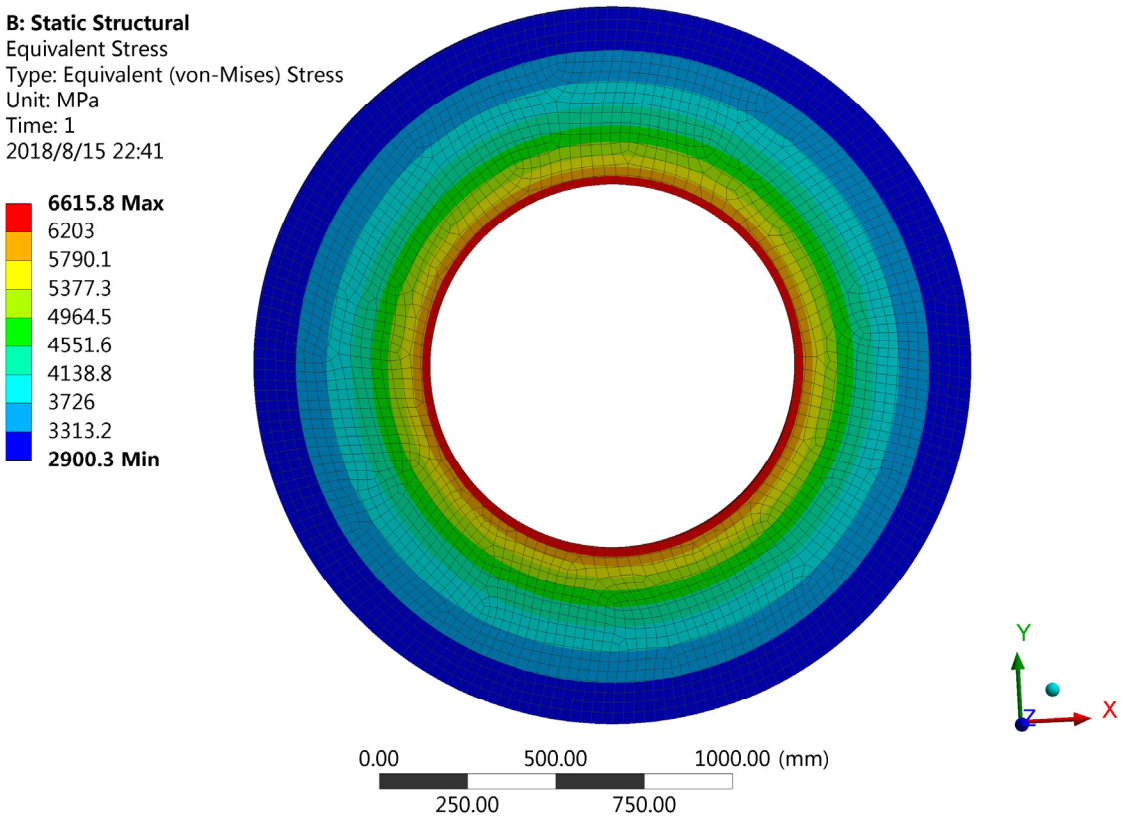


Figure 2.1 Von-Mises stress distribution of the coaxial cylinder at 1000 rad/s.

### *2.2.3 Validation of the Finite Element Model*

To validate the accuracy of the FEM, a comparison of the Von-Mises stress along the radius between the analytical method and FEM is plotted and shown in Figure 2.2. It can be seen that the results match perfectly. Thus, with the FEM, the rough outer dimension and the highest localized stress point of the rotor lamination can be determined.

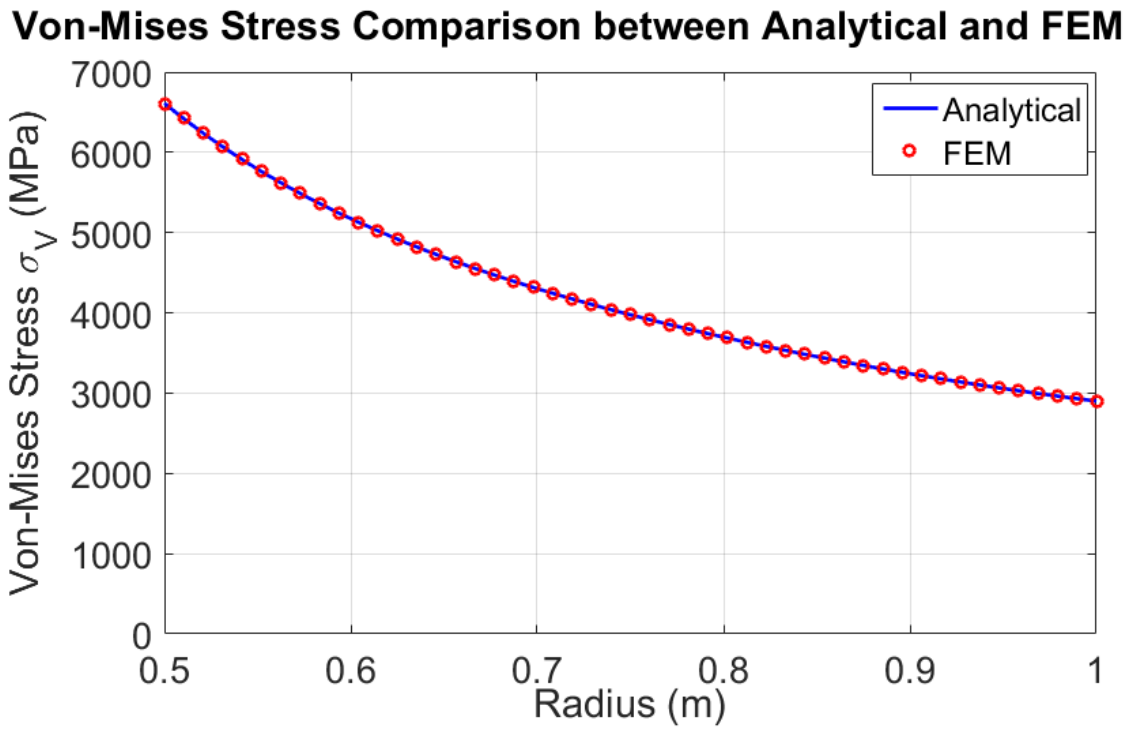


Figure 2.2 Comparison of the Von-Mises Stress between analytical and FEM of the coaxial cylinder.

## 2.3 Problem of Conventional Rotor Designs

At over 1 million rpm, the conventional rotor structures cannot be applied due to the following reasons.

### *2.3.1 Localized Stress Concentration*

Figure 2.3 shows the stress distribution of the regular rotor with an outer diameter of 4 mm at the speed of 1.2 million rpm. As can be seen, the highest stress is about 606 MPa, while most of the rotor steels have a yield strength less than 400 MPa. This localized stress concentration is not a big issue when at low speeds. But it would cause failure when the rotor is rotating at ultra-high speeds.

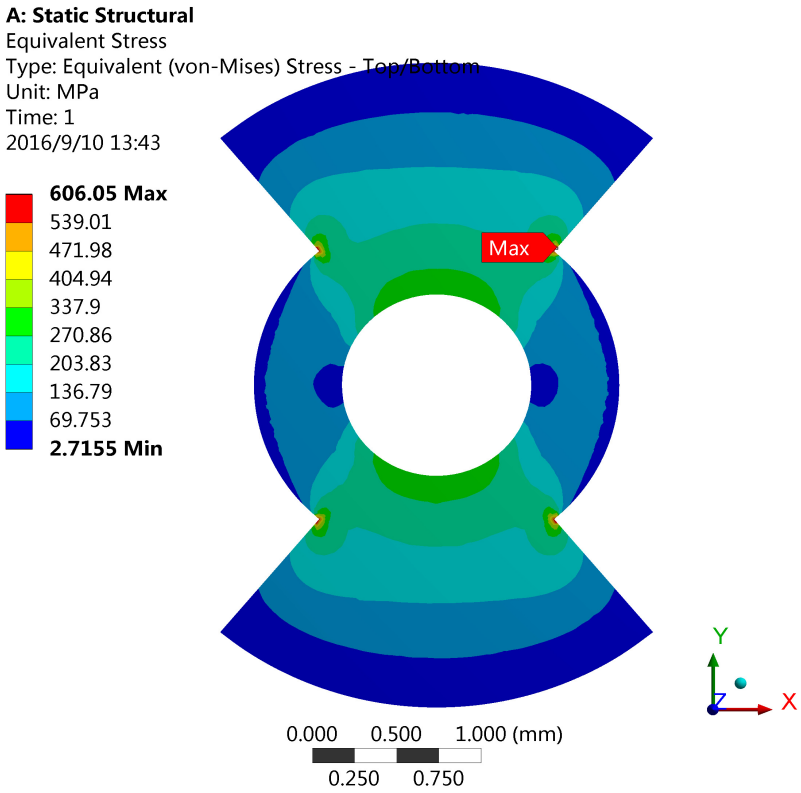


Figure 2.3 Stress distribution of the regular rotor geometry.

### *2.3.2 Too Small Space for the Shaft*

Although the rotor size can be reduced to decrease the highest stress to be less than the yield strength of the lamination material, there is another critical problem that prevents the conventional designs from being used at ultra-high speeds. When at such high speeds, the rotor diameter is usually limited to a maximum length of 3-4 mm, which makes the rotor shaft diameter less than 1 mm (see Figure 2.1). Such thin shafts are very difficult to manufacture and are easy to break at high speed.

### *2.3.3 Too Much Windage Loss*

The high air drag loss is another problem when in ultra-high speed situations since the air drag loss is proportional to the third power of the rotational speed. In addition, the conventional rotor geometry of SRM is actually badly designed in the perspective of aerodynamics because of the rotor saliency. But the rotor saliency, in turn, is the source of the output torque. This implies that the intrinsic properties of the SRM rotors are contrary in terms of aerodynamics and electromagnetics.

## 2.4 Possible Solutions in the Literature

### *2.4.1 Using Bolts Rather Than a Shaft*

To solve the shaft bore problem, a "shaft-less" rotor design (shown in Figure 2.4) has been proposed in [38]. However, this design still needs bolts fed through the rotor laminations, which increases the assembling difficulty and is also not possible in very tiny scales under ultra-high speed cases. On the other hand, the double-salient geometry will still lead to very high windage loss.

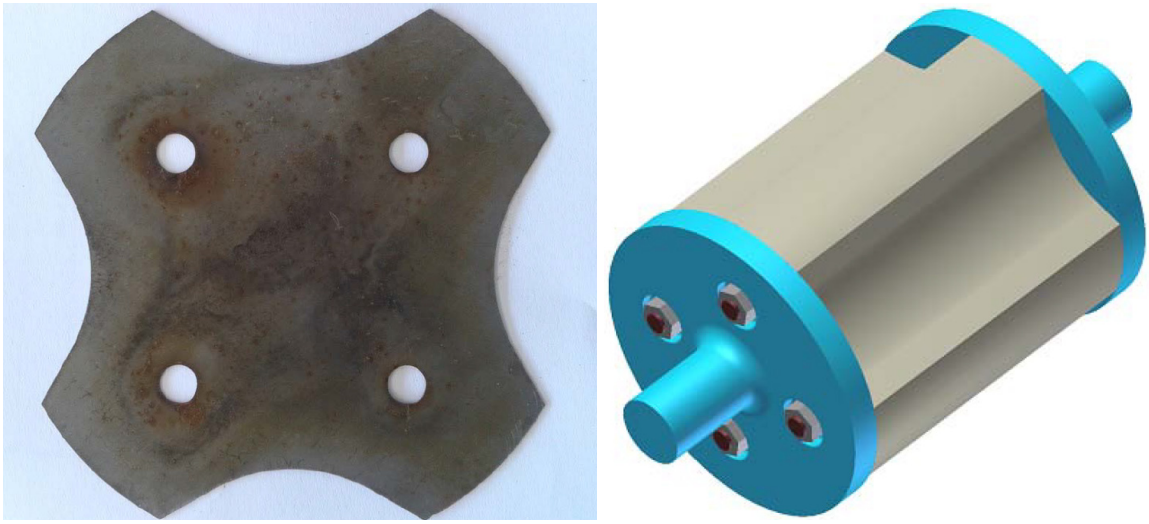

Figure 2.4 High speed rotor lamination with no shaft bore (left) and rotor assembly with end plates (right) [38]

### *2.4.2 Using Rotor Sleeves*

Some efforts has been made to solve the high windage loss problem in the literatures, such as using a rotor sleeve that is made from titanium or carbon fiber, just as in high speed PM machines [34, 39]. Although it is mechanically well designed, it is not a good design in the perspective of electromagnetics. Typically, the air gap of super high speed SRMs is 0.1-0.25 mm in order to reduce the excitation requirement, or in other words, to increase the torque density [33]. Such nonmagnetic sleeves is electromagnetically equivalent to the air gap. This would increase the equivalent air-gap length in the radial direction by twice or more, which leads to a low torque density [39]. As shown in Figure 2.5, the equivalent air gap length is 0.6 mm, which is the summation of the 0.35 mm actual air gap length and the 0.25 mm rotor sleeve thickness. This large air gap results in a low maximum flux density of 0.86 T in the stator teeth.

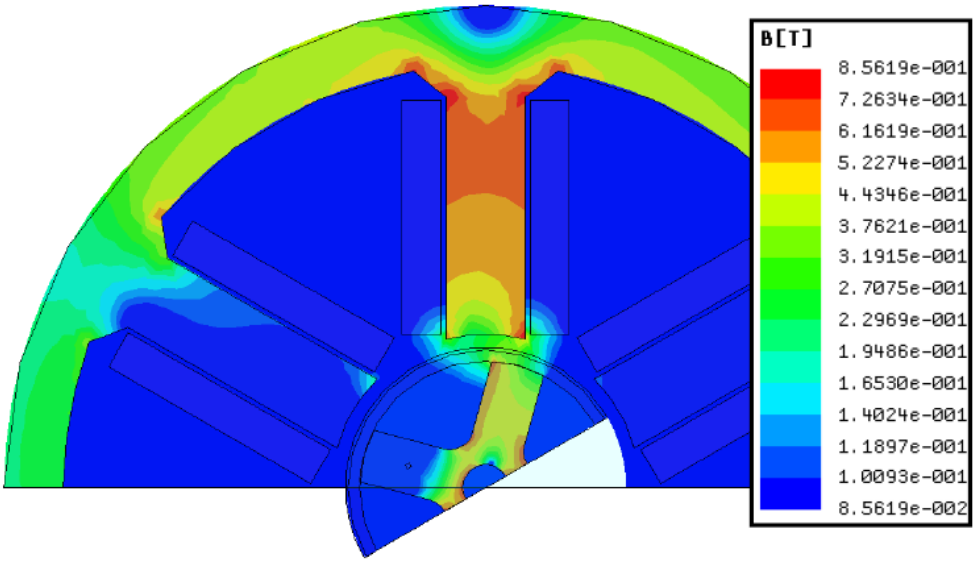


Figure 2.5 High speed SRM with rotor sleeves.

### *2.4.3 Design with "Flux Bridges"*

Another design to solve the high windage loss problem is using "flux bridges" to connect the salient rotor poles [42, 43]. The flux bridge design is a good one from the perspective of aerodynamics. However, it demands the flux bridge to be thin enough to be magnetically saturated. Such thin flux bridge is obviously not mechanically strong enough at ultra-high speeds. Figure 2.6 shows the stress distribution of the rotor with flux bridges with an outer diameter of 4 mm at 1.2 million rpm. As can be seen, the highest stress is 1055 MPa, which is located at the corner of the flux bridge.

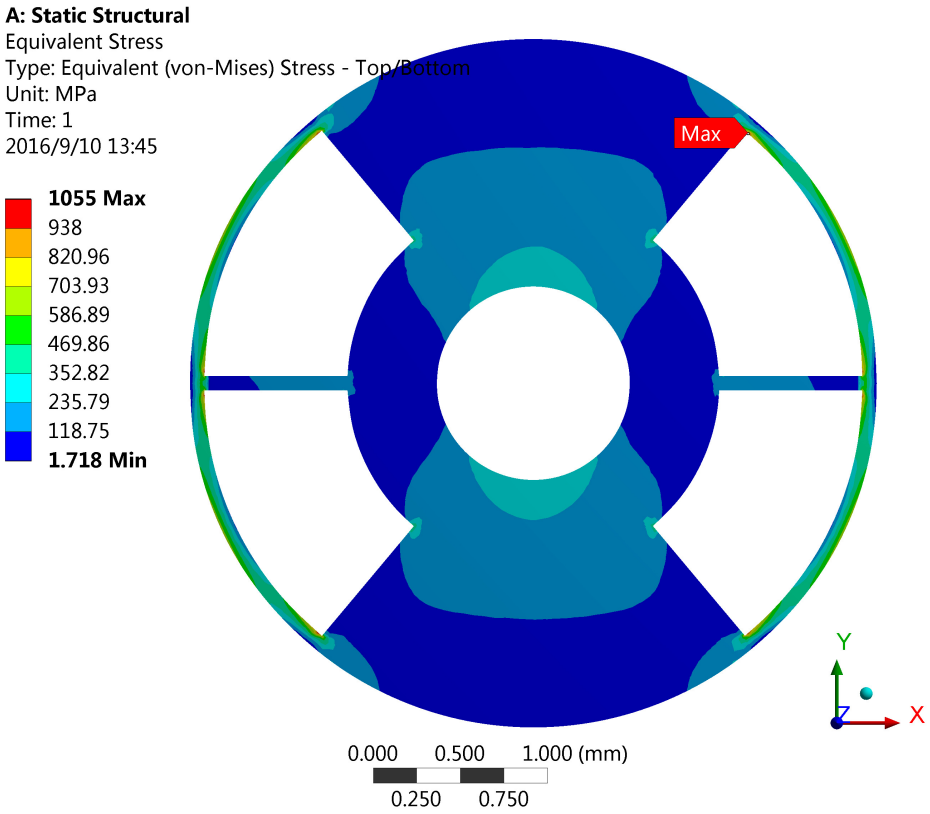


Figure 2.6 Stress distribution of the rotor with "flux bridges".

## 2.5 Design of a Novel Rotor Geometry for Ultra-High Speed Applications

From the analysis above, it can be concluded that a new geometry has to be proposed for UHSSRMs over 1 million rpm. It has to be mechanically strong enough to endure the high centrifugal force at ultra-high speeds. Also it should not have any holes or rotor sleeves. In addition, it should have a good aerodynamic performance. In this sub section a novel rotor geometry that combines all these advantages is proposed in detail.

### *2.5.1 Design Details*

The first step of SRM rotor design is to select a suitable number of poles. Generally speaking, the smaller the pole number is, the less core losses and switching losses it will have due to the less fundamental frequency, which is very important for ultra-high speed applications. The relationship between the fundamental frequency and the rotor pole number is show in (2.4)

$$f = \frac{N_r \cdot N_{rpm}}{60} \tag{2.4}$$

where $N_r$ denotes the number of rotor poles and $N_{rpm}$ denotes the rated speed in rpm [44]. So a rotor pole number of two is chosen in the proposed design.

A novel design of the rotor geometry is shown in Figure 2.2. The rotor is basically made up of two parts: the rotor stack (black) and the clamping shaft (gray). The rotor stack is composed of laminations that are made from magnetic materials such as stainless steel. The clamping shaft is made from nonmagnetic materials such as titanium alloy or carbon fiber. The main idea of this design is to keep the rotor stack as smooth and integrated as possible and transfer the stress that is imposed on the rotor laminations to the clamping shaft, which can be made from those nonmagnetic materials that have much higher tensile

strength. Both sides of the proposed rotor laminations are designed to be smooth curves. In addition, there is no hole in the middle of the rotor laminations, which greatly reduces the highest stress point caused by the large centrifugal force [31]. The mechanical support for the rotor stack is achieved by the contacting curved surfaces between the rotor stack and the two "clamping arms" (yellow shadow in Figure 2.7), which has the equivalent effect of the interference fit between the rotor and the shaft of regular machines or the using of bolts in [38]. Note that if we assume that the rotor is manufactured to be totally symmetrical and balanced, there will be no supporting force produced by the clamping arms when the shaft is rotating (except for the force supporting the gravity of the rotor stack), because there is no trend of relative displacement between the rotor stack and the clamping shaft. The total amount of the radial electromagnetic force put on the rotor stack is also zero because of the symmetrical geometry.

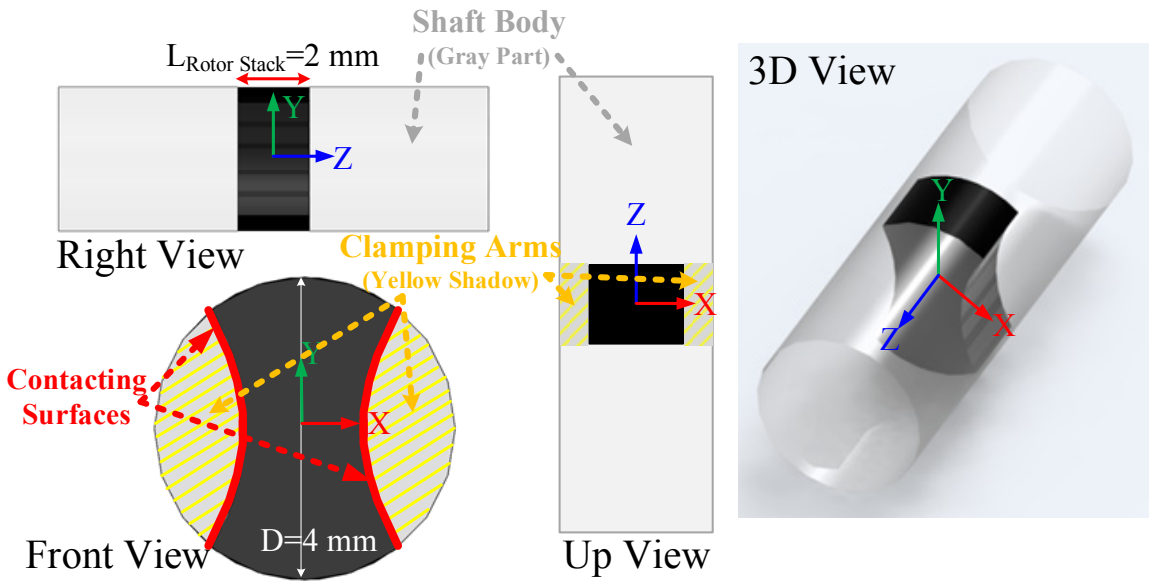


Figure 2.7 Three view drawing and 3D view of the proposed design.

### *2.5.2 Advantages*

The proposed design has many advantages for ultra-high speed applications as follows.

- **High strength**: the surfaces of the rotor stack are all smooth, which means there is no sharp corner as in the regular rotor geometry. Also there is no hole for the shaft in the center of the rotor laminations. These two features can greatly reduce the highest stress in rotor laminations. In addition, the diameter of the shaft is the same as the rotor, which increases a lot the robustness of the shaft.

- **High torque density**: unlike using sleeves, there is no increase of the equivalent air-gap length at both rotor pole ends in the radial direction. To be more specific, when the rotor is in the aligned position, the equivalent air-gap length is just the length of the real distance from the stator pole to the rotor pole, without going through any additional sleeve thickness. This implies that higher power density can be achieved.

- **High efficiency**: due to the cylindrical geometry, the air drag loss is dramatically reduced to a minimum value.

- **High reliability**: there is no need of bolts or other kinds of mechanical connections between the rotor and the shaft, which implies very high simplicity and reliability.

### *2.5.3 Disadvantages*

Although there are many advantages, the proposed design also has the following disadvantages.

- Since both the rotor laminations and the shaft are very small, one needs to be very careful in the procedure of manufacturing. Nevertheless, this is inevitable in ultra-high speed applications.

- The axial length of the rotor lamination stack must be relatively short compared to the total rotor length (see the next sub-section for details). This will reduce the overall torque, but this is rarely a concern in this type of machine.

- The shaft has a larger radius than the regular rotor geometry, which will increase the equivalent moment of inertia of the machine. This can be avoided by using light-weight materials such as carbon fiber.

Table 2.2 shows a comparison of different rotor geometries in the literature regarding ultra-high speed applications.

Table 2.2 Comparison of Different Rotor Geometries

| | Regular | Flux bridge [43] | Rotor sleeve [34, 39] | Through bolts [38] | Proposed |
|---|---|---|---|---|---|
| Practical to construct at ultra-high speeds? | No | No | Yes | No | Yes |
| Rotor lamination strength | Moderate | Low | Moderate | High | High |
| Torque density | High | Moderate | Low | High | High |
| Efficiency | Low | Moderate | High | Low | High |
| Reliability | Low | Low | High | Low | High |
| Axial length | Long | Long | Long | Long | Short |

## 2.6 Stress Analysis of the Proposed Rotor

### *2.6.1 Theoretical Stress Analysis of the Shaft*

Unlike the regular geometry, the proposed rotor geometry needs to be analyzed three-dimensionally. The reason is that the highest stress on the shaft is influenced by the axial length of the rotor stack. The longer the rotor stack is, the higher stress the clamping shaft will have because of the principle of the lever. Figure 2.8 shows this mechanism. Due to the symmetrical geometry, we can analyze the left part of the rotor only.

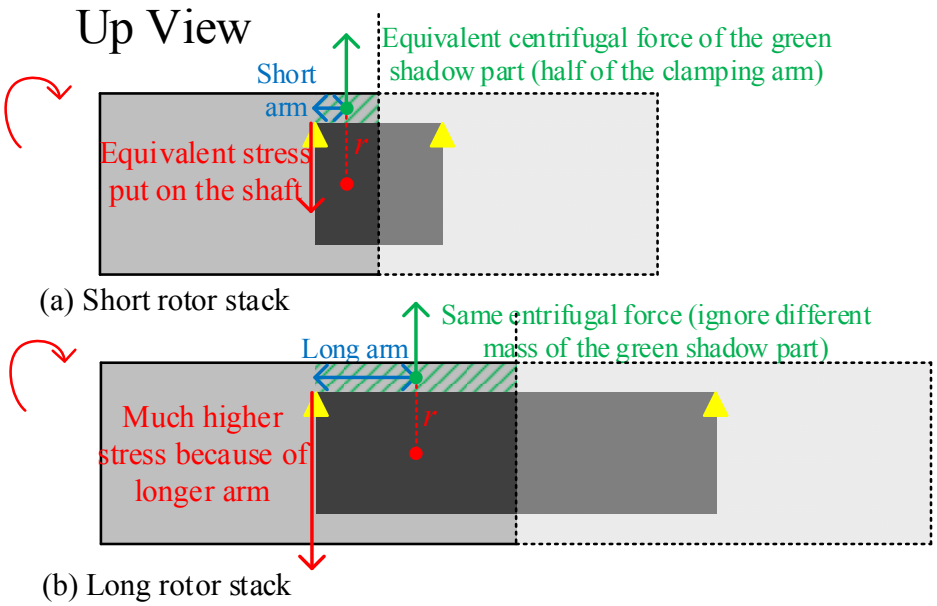


Figure 2.8 Theoretical analysis of the proposed design using principle of the lever.

First let's consider the equivalent centrifugal forces of the clamping arms. When the shaft rotates, the clamping arms (green shadow) are circulating around the center of the shaft (red spot). The centrifugal force $F$ can be determined by (2.5)

$$F = m\omega^2 r \tag{2.5}$$

where $m$ is the mass of the half clamping arm, $\omega$ is the angular velocity, $r$ is the distance between the red spot and the equivalent mass point of the half clamping arm (green spot).

Because of the same rotational speed, the equivalent centrifugal forces of the half clamping arm are almost the same between the short and the long stack (let's ignore the factor of different mass of the clamping arm first). The equivalent forces are indicated by the green arrows.

Now we can apply the principle of the lever. The centrifugal force of the clamping shaft is provided only by the connecting spot between the clamping arm and the rest of the shaft. Thus, this connecting point has to be the fulcrum here (yellow triangle). Due to the linearity of the principle of the lever, the equivalent moment of force of the half clamping arm is equivalent to the moment of force produced by the mass point at the middle point of the half clamping arm (green spot). Thus, the longer the clamping arm is, the greater the moment of force will be since the equivalent forces are the same.

The last step is to take into account the different mass between the short and long arms. According to (2.5), the longer arm actually has greater equivalent centrifugal force due to its greater mass. This makes the moment of the centrifugal force of the longer arm even greater, which means the connecting point of the long shaft (fulcrum) has to endure greater stress.

To better understand this, just imagine a diver is going to dive from a long board. When he jumps at the end of the board, the board would change its form dramatically and thus the connecting point on the other side to the land will endure high stress. If the board

is shorter, say 1 meter instead of 5 meters, the board will endure much less stress at the connecting point.

### *2.6.2 3D Finite Element Analysis of the Shaft*

Figure 2.9 and Figure 2.10 give the stress distribution of two rotor geometries with rotor stacks of 2 mm and 5 mm long at the rotational speed of 1.2 million rpm, respectively. This leaves a safety factor of 1.2 for 1 million rpm applications so as to guarantee that the material can withstand without failure [38]. The rotor stacks are made from stainless steel and the clamping shafts are made from titanium alloy in the simulation.

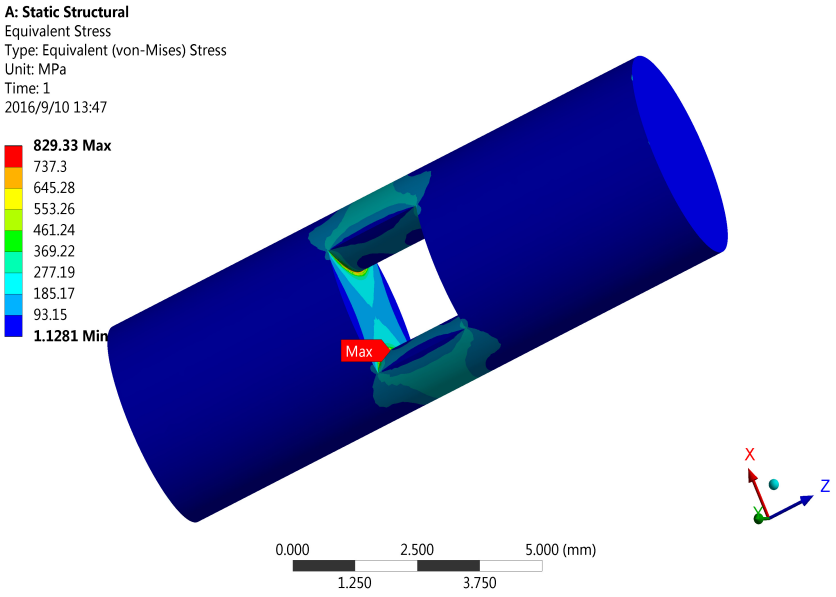


Figure 2.9 Stress distribution of a short rotor with 2 mm rotor stack.

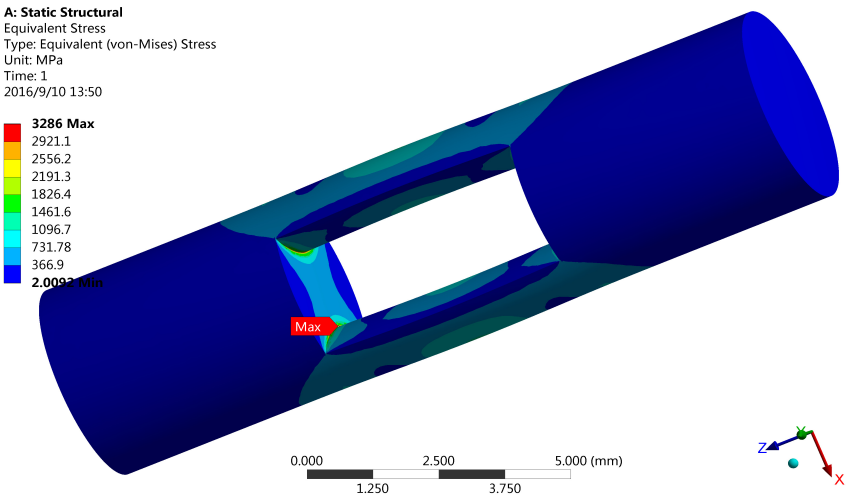


Figure 2.10 Stress distribution of a long rotor with 5 mm rotor stack.

As can be seen, the highest equivalent stress of the short and long rotor is 829 MPa and 3286 MPa, respectively. Titanium alloy and austenitic steel are strong enough to endure the highest stress of the 2 mm shaft [27]. Table 2.3 gives the mechanical properties of different materials. The highest stress is located at the middle point of the inner boundary curve between the clamping arms and the shaft body. Figure 2.11 gives the zoom-in plot of this area.

Table 2.3 Mechanical Properties of Different Materials

| | Titanium grade 5 [27] | Austenitic steel [27] | Carbon fiber [45] | M250-35A [46] | Hiperco 50 [47] |
|---|---|---|---|---|---|
| Alloy | Ti, Al, V | Fe, Cr, Mn, Mo, | T1000G | Fe, Si | Fe, Co, V, Si, Mn,Nb |
| Density | 4.4 g/cm$^3$ | 8 g/cm$^3$ | 1.8 g/cm$^3$ | 7.6 g/cm$^3$ | 8.1 g/cm$^3$ |
| Tensile strength | 895 Mpa | 975 Mpa | 6370 Mpa | 575Mpa | 827-1034 Mpa |
| Yield strength | 826 Mpa | 615 Mpa | N/A | 455Mpa | 386 Mpa |

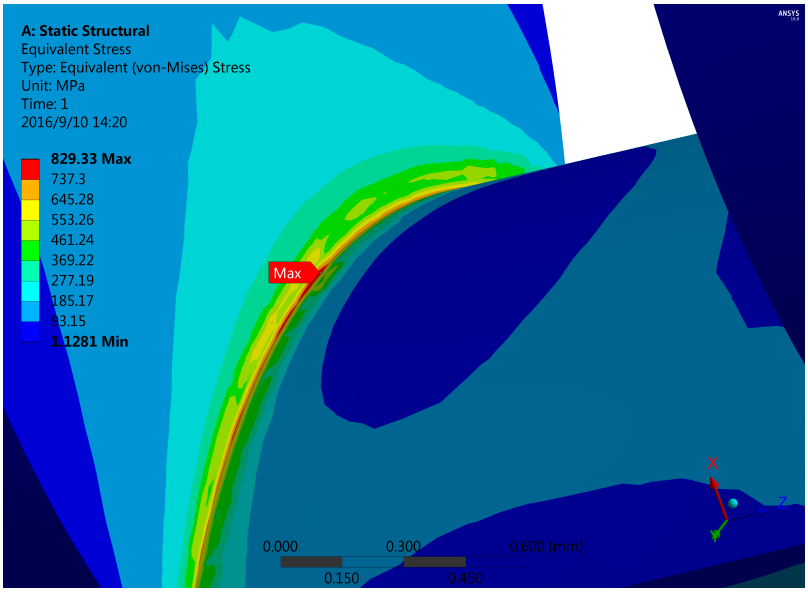


Figure 2.11 Zoom-in plot of the area with maximum stress.

Because of the centrifugal force, the clamping arms will tend to move away in the radial direction from the center of the shaft (just as in the diving board case). Figure 2.12 and Figure 2.13 give the total deformation of the short and long rotors, respectively. As can been seen, the highest deformation is about 0.0066mm and 0.061mm for the short and long rotor, respectively. Assuming the length of the air gap to be 0.1mm, the deformation of the long rotor is not acceptable (61%) considering the ultra-high speed situations, while the deformation of the short rotor (6.6%) is totally acceptable. Note that the ratio of the rotor length to bore diameter is usually ranged from 0.25 to 0.7 [48]. The proposed 2 mm rotor is well suited for this criterion.

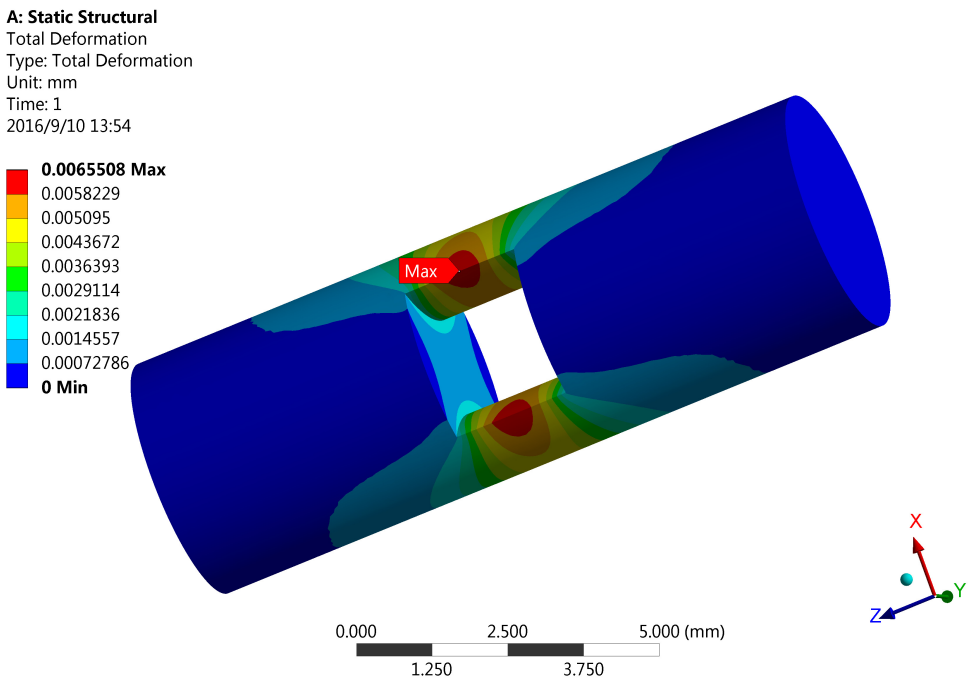


Figure 2.12 Total deformation of the short rotor.

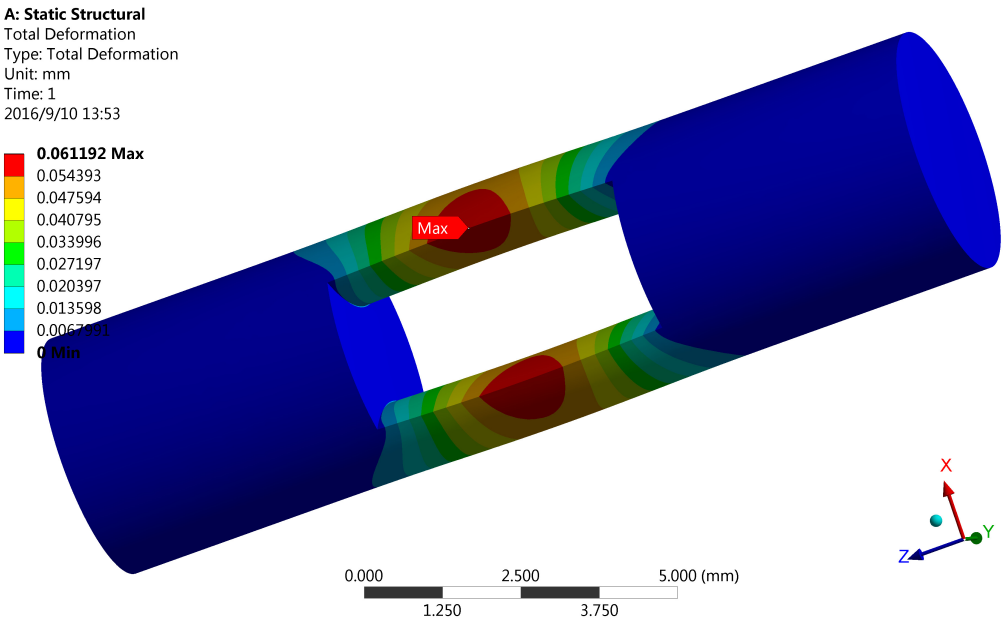


Figure 2.13 Total deformation of the long rotor.

### *2.6.3 3D Finite Element Analysis of the Rotor Stack*

Due to the very smooth side surfaces and the non-shaft-hole design, the stress distribution of the rotor stack is reduced to a minimum value. Figure 2.14 gives the stress distribution of the rotor stack. The highest stress is 324 MPa, which is located in the middle of the side surface. Compared with the highest stress of 606 MPa of the regular rotor, the new design has reduced the highest stress on the rotor stack by 47%. Typical high speed electrical steels such as M250-35A and Hiperco 50 are strong enough to be used as rotor laminations.

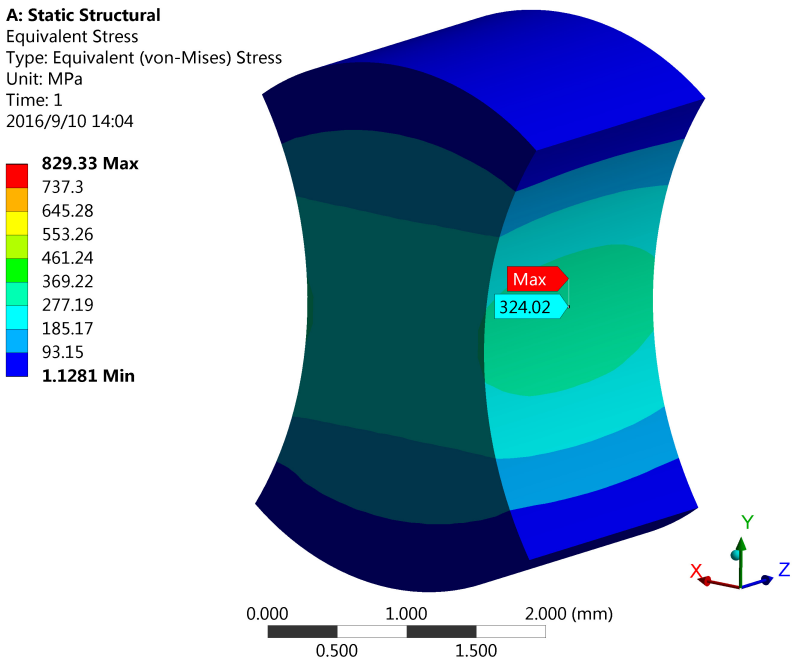


Figure 2.14 Stress distribution of the rotor stack.

## 2.7 Chapter Summary

This chapter mainly focuses on the mechanical design and analysis of a novel rotor for ultra-high speed applications. First, the stress distribution of a coaxial cylinder is

calculated using the finite element method. The results are validated with the analytical solutions. Then, a novel rotor design is proposed for ultra-high speed SRMs over 1 million rpm. The rotor stack has a unique smooth shape without any holes in the middle. A shaft that has the same outer diameter contains the rotor stack in the middle. Compared with the conventional design, the proposed design has many advantages such as high strength, high power density, high efficiency and high reliability. The new geometry is validated with the 3D finite element model. The results show that the highest stress on the rotor stack has been reduced by 47%.

# CHAPTER 3. ROTOR ROBUSTNESS ANALYSIS

## 3.1 Introduction

The proposed design in Chapter 2 is a good one in terms of higher mechanical strength of the rotor stack, higher efficiency due to lower windage losses at ultra-high speeds and higher torque density due to the elimination of rotor sleeves. However, the unique design of using clamping arms instead of rotor sleeves leads to a comparatively short rotor stack, since small gaps will appear between the rotor stack and the shaft due to the high centrifugal force at high speeds. This may cause failures in ultra-high speed situations. The small gaps will also yield localized stress concentration problems on the shaft [49].

In this chapter, an improved design of using adhesives is proposed to increase the bonding between the rotor stack and the clamping arms [50]. In order to evaluate the performance of the adhesives at high speeds, a model in fracture mechanics is introduced, namely the cohesive zone model (CZM). A finite element model with detailed descriptions is built in ANSYS to simulate the debonding process of the clamping arms on the shaft. Then, a parametric study is conducted to study the shaft mechanical robustness for different shaft length under different adhesive strength. The results show that the rotor stack length and the corresponding output torque can be increased by 15% with the improved design. The highest strength on the shaft is also reduced by 60%. The model introduced in this chapter also gives a good reference for estimating the mechanical stress of the rotors in high speed electric machines when adhesives are applied.

## 3.2 Problem of Small Gaps and Stress Concentration

The main idea of the design is to eliminate all holes and sharp corners in the regular rotor and transfer the stress that is imposed on the rotor laminations to the clamping shaft that can be made from those nonmagnetic materials that have much higher tensile strength. However, due to high centrifugal force, the clamping arms will tend to move away in the radial direction from the center of the shaft, exerting high stress on the connecting points and forming small gaps between the rotor stack and the clamping arms. The longer the rotor stack is, the larger the stress and the gaps will be because of principle of the lever. This limits the maximum length of the rotor stack.

Figure 3.1 shows the simulation results of a 4 mm diameter carbon fiber shaft with a 2 mm long rotor stack in the middle, rotating at 1.2 million rpm. The lower left figure shows the zoom-in version of the contacting region between the rotor stack and the clamping arms. Although the gap is only 14 μm, it may still cause failures, considering such high rotational speed.

In addition to the problem of the small gap, another problem is the localized stress concentration. The lower right figure of Figure 3.1 shows the highest stress point of the shaft (with the rotor stack hidden), which is located at the middle point of the inner boundary curve between the clamping arms and the shaft body. The reason for this high stress point is that the two clamping arms are only connected to the shaft body by these high stress boundary regions. All the centripetal force needed for the clamping arms to rotate at high speeds is provided by these small regions, which yields very high local stress.

This high stress limits the maximum length of the rotor stack and the corresponding maximum torque.

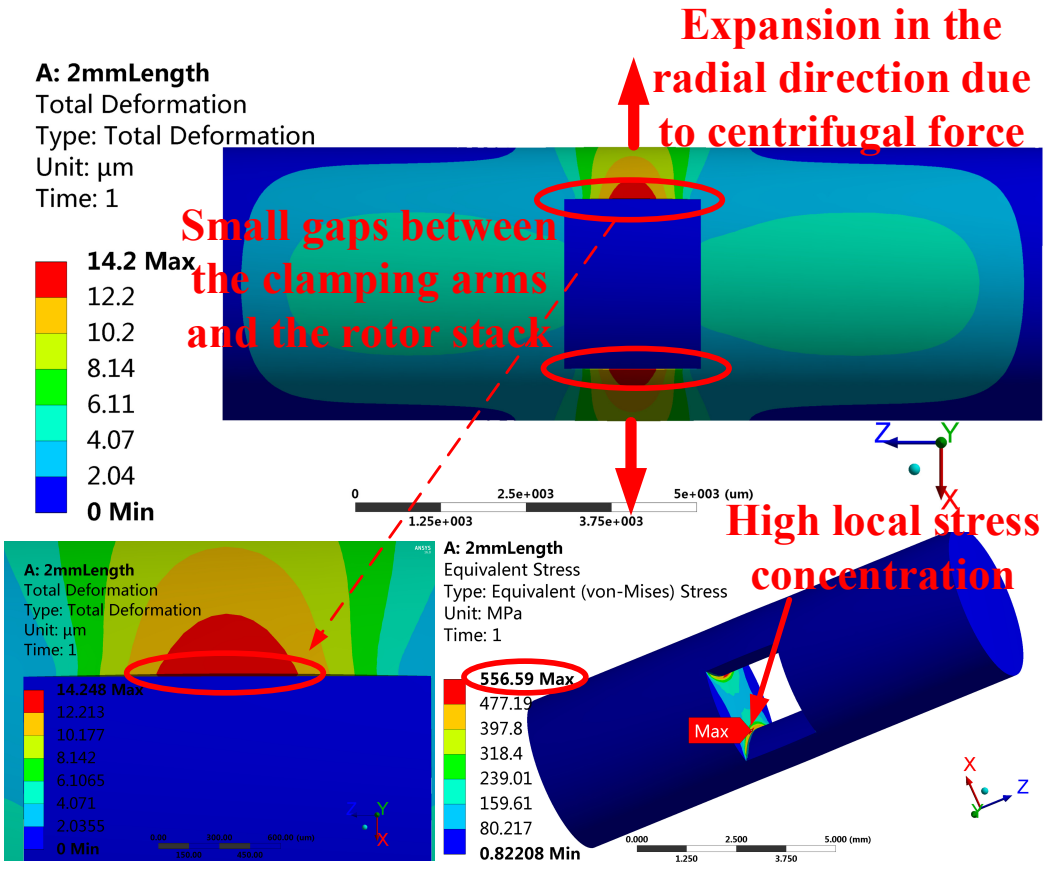


Figure 3.1 Mechanical finite element analysis of the shaft at 1.2 million rpm

## 3.3 Improved Design with Adhesives

An intuitive way to solve these two problems is to add more bonding between the clamping arms and the rotor stack. One simple but effective method is to put some adhesives between the contacting surfaces labeled in Figure 2.7. The use of adhesives in demanding engineering applications is very common and popular in the modern world, especially in the area of fiber reinforced composites or aerospace industries. Adhesives have the ability to join surfaces of nearly any type of material as well as evenly distribute

load throughout the joint. It is reported that approximately 50% of the primary structures of the Boeing 787 rely heavily on reinforced polymer composites and adhesive joints [51]. By adding adhesives between the surfaces, additional force can be provided from the rotor stack to hold the clamping arms against the centrifugal force. If the maximum strength of the adhesive is high enough to hold the two clamping arms from any expansion, the small gap will be eliminated and the rotor is more robust to rotate at ultra-high speeds. In addition, the localized stress concentration problem is also expected to be solved at the same time. However, little, if any, research has been conducted to model such problem of using adhesives in the area of electric machines, to the best of the authors' knowledge. With the emerging of high speed machines, fiber reinforced composites are becoming more and more popular in electric machines [52]. The model described in the next section can also provide a detailed reference for such applications.

## 3.4 Cohesive Zone Model

### *3.4.1 General Description*

The proposed problem is actually in the field of fracture mechanics. In conventional modeling methods, adhesives and adherends are assumed to be perfectly bonded [53]. This means the bonding force of the interface is assumed to be stronger than the adhesive strength, which is not true in real situations. The Virtual Crack Closure Technique (VCCT) is a model that can be used to describe the failure behavior of adhesives [54]. However, it requires some knowledge of a pre-existing crack, which is rarely known *apriori* [55].

The Cohesive Zone Model (CZM) is an emerging technique in fracture mechanics. It models the failure of a single material or the interface delamination and progressive

failure where two materials are joined together under force. The fracture formation is regarded as a gradual phenomenon in which separation of the surfaces involved in the crack takes place across an extended crack tip and is resisted by cohesive tractions in the cohesive zone. The origin of the model can be track back to the early sixties by Barenblatt [56] and Dugdale [57]. Unlike traditional fracture mechanics models, CZM can predict starter crack locations and directions without the need of a pre-existing crack. Actually it is reported that CZM is the most popular and appropriate method for modeling the failure behavior of adhesives [51].

### *3.4.2 Traction-Separation Law and Important Parameters*

The CZM can be visualized by a series of ligaments (elements) spanning the adhesive thickness between two substrates in the adhesive layer. It allows three modes of separation: Mode I debonding for normal separation, Mode II debonding for shearing separation and mixed mode debonding for normal and shearing separation (Figure 3.2). When an external force or loading is applied, the ligaments in the cohesive zone start to deform. Those ligaments near the crack tip start to deform first. The deformation then propagates until all the ligaments in the process zone have begun to deform. This process will continue until a ligament reaches a critical crack opening displacement ($\delta_c$) [51]. Figure 3.3 gives an illustration of this process.

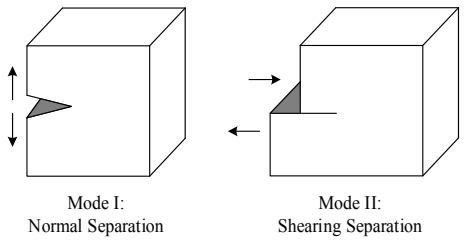


Figure 3.2 Mode I and Mode II separation.

Before loading is applied, the surfaces are said to be undamaged. When the surfaces are completely separated, there will be no force interactions between them, which is defined as fully damaged. Within the cohesive zone region, there is active traction stress between the cohesive surfaces, where the behavior of these ligaments is governed by a traction-separation law (shown in Figure 3.3). The vertical axis denotes the cohesive stress $\sigma$ exerted by the interface while the horizontal axis denotes the interfacial separation displacement $\delta$. It depicts a material's ability to carry load from the onset of loading to failure. To extend a crack, external energy is required to create two new surfaces within the material. The rate of change of this energy with respect to crack area is defined as the fracture energy release rate $G$. Note that for Mode I and Mode II separation, the traction-separation curves should be determined respectively.

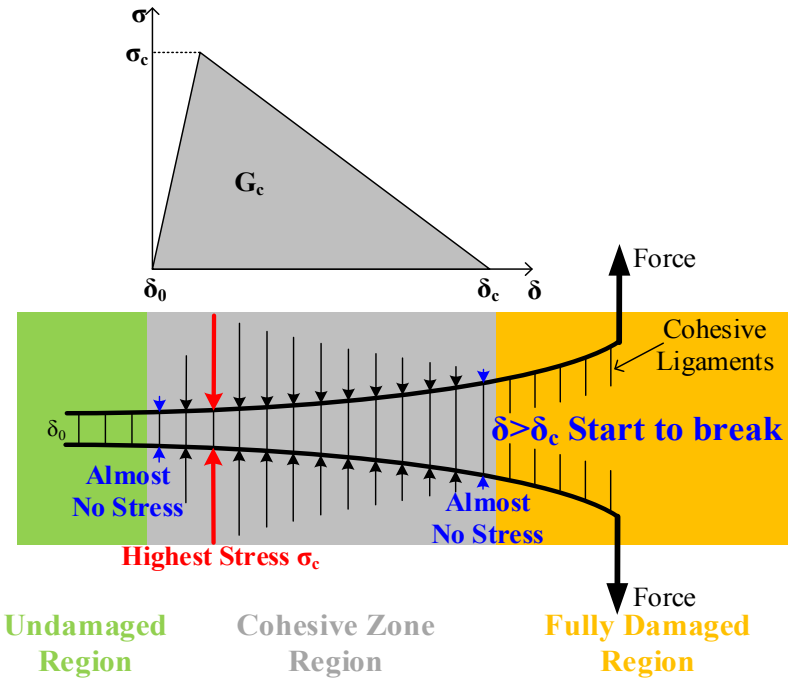


Figure 3.3 Traction-seperation curve and illustration of the adhesive region. The length of the arrows represents the value of the stress.

There are two methods to determine whether a fracture happens. The first is to see whether the interfacial separation $\delta$ reaches the critical crack opening displacement $\delta_c$, which is called displacement-based model. The second is to see whether the amount of mechanical work needed to separate the interface as the elements become damaged exceeds the value of the critical fracture energy release rate $G_c$. This is called energy (potential)-based model. From the definition it can be implied that the area beneath the traction-separation curve is equivalent to $G_c$ (see Figure 3.3). In many linear elastic fracture mechanics cases it is synonymous with interface toughness $\Gamma_c$ [51].

Besides the fracture energy release rate, there is another important parameter in the traction-separation curve called the critical (peak) opening stress $\sigma_c$, which represents the cohesive strength of the interface. From Figure 3.3 it can be seen that the stress of the ligaments start to increase rapidly from the beginning of the cohesive zone region, with displacement increases slowly. As it moves closer to the external force, the stress first reach the maximum value of $\sigma_c$ and then gradually decreases to zero, when the displacement reaches the critical value of $\delta_c$. If the deformation of the system is dominated by linear elasticity, $G_c$ is the only parameter required to characterize fracture. On the other hand, if the condition of linear elastic fracture mechanics do not apply, the critical opening stress $\sigma_c$ provides an additional parameter that is crucial in determining the failure of the joint. In particular, the parameter $G_c$ alone cannot be used to characterize fracture when the adherends deform in a plastic fashion; both $G_c$ and $\sigma_c$ control the fracture process [58, 59].

There are different shapes of the traction-separation curve available in the literature such as bilinear, exponential, trapezoidal and cubic polynomial [60]. The mostly widely used model is the bilinear model shown in Figure 3.3, since it is defined by only three

parameters: $\sigma_c$, $G_c$ and $\delta_c$. However, the precise details of the shape have a minor influence on the fracture behavior, and this effect can generally be ignored [58].

## 3.5 Modeling and Simulation

### *3.5.1 Interface Delamination v.s. Contact Debonding*

To apply CZM, commercial finite element analysis software ANSYS is used. There are two methods of implementation of CZM in ANSYS, namely interface delamination and contact debonding. The first is failure in a laminated material, often a composite, which leads to separation of the layers of reinforcement or plies. It can be fracture within either adhesive or reinforcement. Debonding occurs when an adhesive stops sticking to an adherend, when the physical, chemical or mechanical forces that hold the bond together are broken due to an external force. Therefore, debonding is actually a special form of delamination. But using contact debonding to model interface delamination in ANSYS has the advantage of ease of use. Existing models can be easily modified to include debonding analysis using CZM by changing the definition of the contact regions to "bonded" and adding the "contact debonding" fracture analysis in ANSYS. Figure 3.4 shows the highlighted contact region of the clamping shaft and rotor stack.

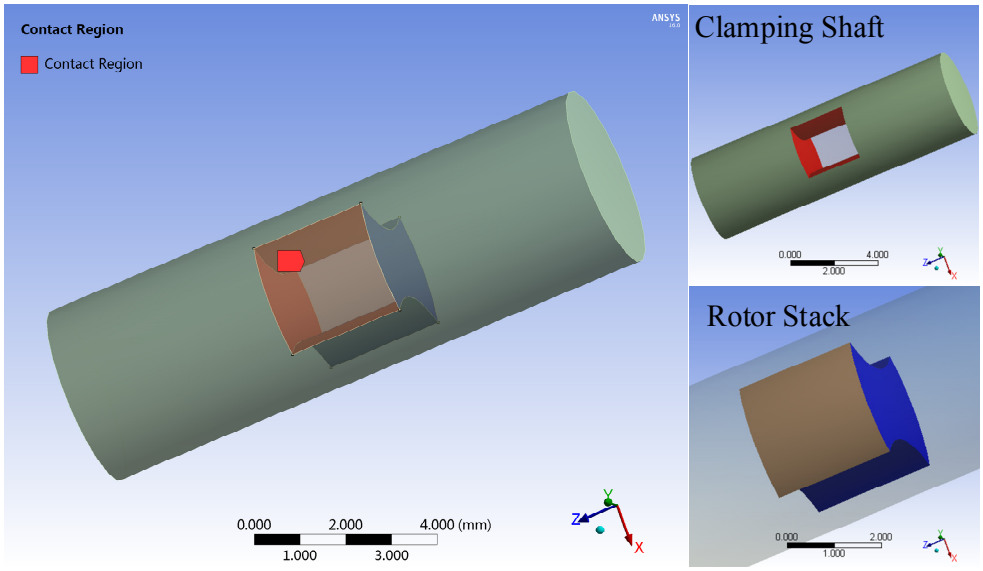


Figure 3.4 Highlighted contact region.

### *3.5.2 Meshing*

Meshing is important in CZM. Additional refinement should be added to the contact region. Figure 3.5 shows the meshing of the rotor. The total node number is about 150,000 in the proposed model.

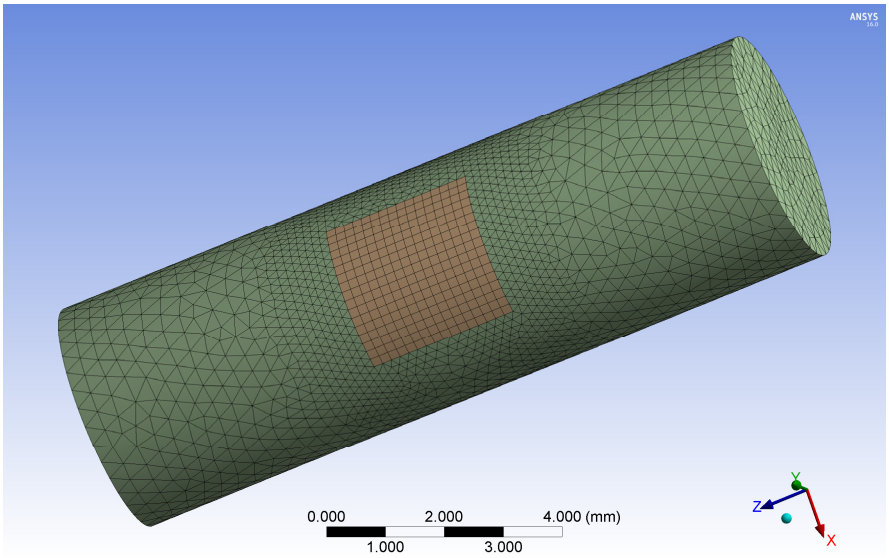


Figure 3.5 Meshing of the proposed model.

### *3.5.3 Separation-Distance Based v.s. Fracture-Energy Based*

For adhesives, there is a special category of cohesive zone material in ANSYS. Once the contact debonding method is used, there are two models of modeling the adhesive material, namely separation-distance based debonding and fracture-energies based debonding. The energy-based method has multiply advantages against the displacement-based model as reported in [60] and is used in the model.

### *3.5.4 Mode I v.s. Mode II Separation*

Under the material properties, the first is to determine the debonding interface mode. For the proposed model, Mode I is used since the clamping arms tend to debond only in the radial direction. One can also set it to mixed mode as long as the maximum equivalent tangential contact stress and critical fracture energy for tangential slip are set be a very small value such as 1E-30 Pa and $J/m^2$. No artificial damping is added and the coefficient is set to be 1E-8 s.

## 3.6 Adhesive Selection

For different adherends, different adhesives have different properties. Figure 3.6 gives a comparison of different adhesives for different adherends by 3M [61]. As can be seen DP420 has almost the highest adhesive strength for both metal and carbon fiber and will be used in the proposed shaft. To increase the bonding strength, it is also suggested in the technical bulletin that “lightly abraded surfaces give a better profiled surface for adhesive bonding than do highly polished surfaces [62]”, which has to be kept in mind when two adherends are being bonded in practice.

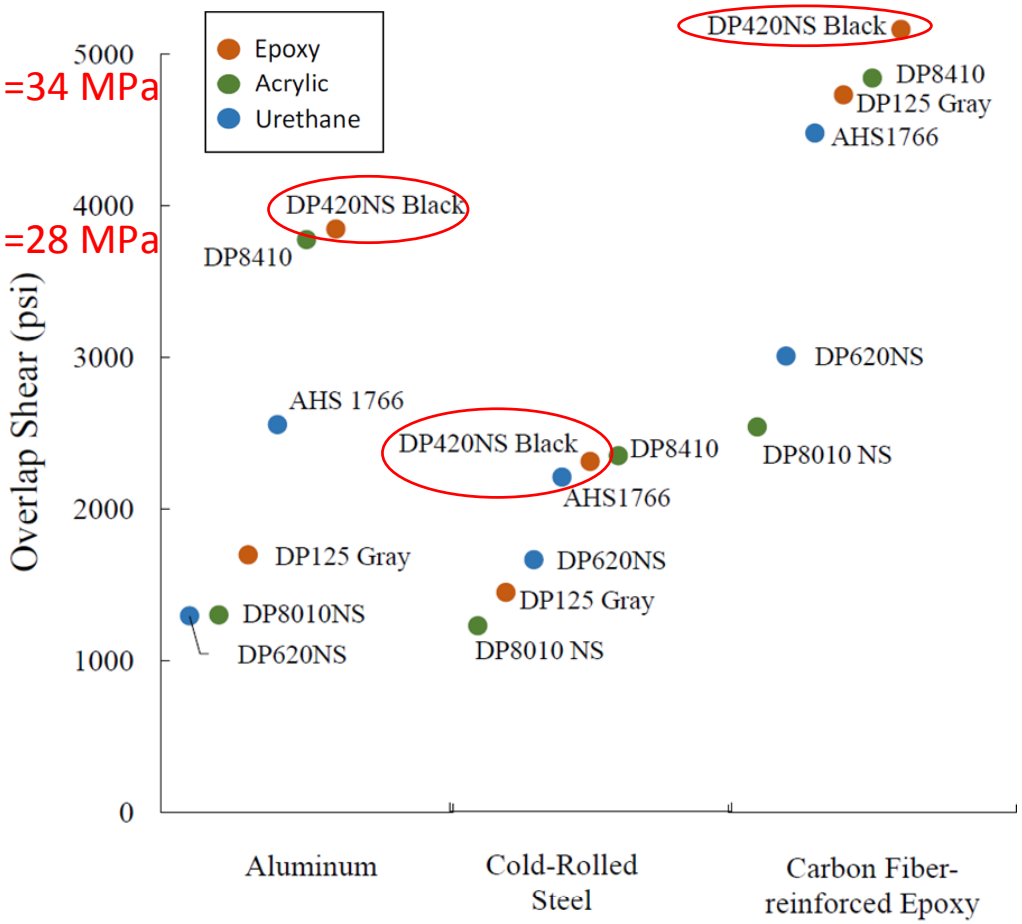


Figure 3.6 Comparison of different adhesives for different adherends [61].

The most important two parameters are the maximum normal contact stress and critical fracture energy for normal separation. Usually these two parameters are very difficult to be measured accurately. Fortunately, five different high strength adhesives were tested for calculating the cohesive parameters in both mode I and II loading respectively in [51], which includes the 3M DP420. However, little agreement was shown using different test methods. In addition, only aluminum bars were tested as adherends. For different adherends, different tested values of adhesive strength are shown in Table 3.1 [63]. For the lamination material used in the rotor stack, which is Hiperco 50, it is reported to be most similar to galvanized steel according to technicians from both 3M and Carpenter

Technology. However, if the laminations were heat treated at lower temperatures for stronger mechanical properties, it would be closer to cold rolled steel than galvanized steel. So the critical opening stress $\sigma_c$ may vary from 15 to 20 MPa and has a higher possibility to be closer to 20 MPa than 15 MPa.

For the critical fracture energy release rate $G_c$, test results show a value between 600 J/m$^2$ to 1900 J/m$^2$ for aluminum substrates using different setups [51]. Considering that the adhesive stress of cold-rolled steel is only about half of aluminum as shown in Figure 3.6, the $G_c$ is set to be 280 J/m$^2$ in the simulation, considering the worst case. This value is also selected based on [64] and [65]. Note that these two parameters of adhesive strength determined in the model are underestimated on purpose to ensure that the real shaft can achieve the simulation performance easily.

Table 3.1 Adhesive Strength of DP 420 Black for Different Materials [63]

| | | DP 420 Black Adhesive Strength Tested at 23 °C (MPa) |
|---|---|---|
| Aluminum- | Etched | 31 |
| | Oakete degrease | 28 |
| | MEK/abrade/MEK | 17 |
| Cold Rolled Steel- | Oakete degrease | — |
| | MEK/abrade/MEK | 15 |
| Copper- | MEK/abrade/MEK | 35 |
| Brass- | MEK/abrade/MEK | 19 |
| Stainless Steel- | MEK/abrade/MEK | 12 |
| Galvanized Steel- | Hot dipped | 20 |
| | Electrodeposited | 21 |

## 3.7 Parametric Study Results

After the model is set up, a parametric study is conducted. The length of the rotor stack is set to be 2 mm, 2.3 mm and 2.6 mm. Due to the uncertainty of adhesive strength for different adherends, different values of 10MPa, 20MPa and 30MPa are studied compared with the original design without adhesives. In addition, from the typical traction-separation curve shown in Figure 3.3, it can be inferred that before the critical opening stress, the separation displacement increase very slowly. Once it passes $\sigma_c$, the displacement will increase rapidly, which means the bonding effect of the adhesive decreases dramatically. Thus the critical fracture energy release rate is fixed and the effect of critical opening stress, which is generally available from datasheets, is parameterized and studied.

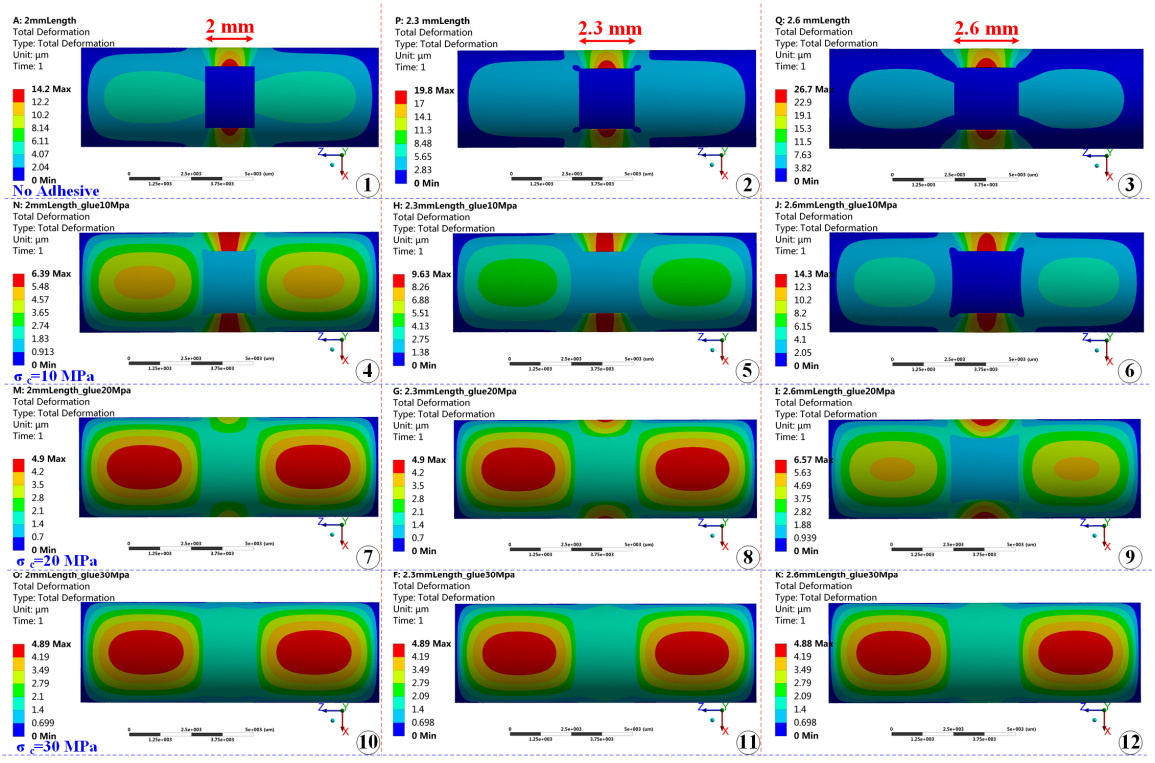


Figure 3.7 Parametric study results of total deformation of the shaft at 1.2 Mrpm.

Figure 3.7 shows the parametric study results of total deformation of all the 12 cases at 1.2 Mrpm. The shafts in the first, second and third columns have rotor stacks of 2, 2.3 and 2.6 mm length, respectively. The first to the fourth rows represent no adhesive, adhesive with critical opening stress of 10, 20 and 30 MPa, respectively. It can be seen that both of the clamping arms and the shaft body experience deformation because of the high speed. Table 3.2 concludes the results of Figure 3.7. From the table it can be observed that the larger the adhesive strength is, or the shorter the rotor stack is, the smaller the gaps between the clamping arms and the rotor stack will be. It also can be inferred from Figure 3.7 that when the deformation of the clamping arms is less than the deformation (expansion) of the shaft body itself (the pure round part on both sides of the rotor stack, whose deformation is 5 μm at 1.2 Mrpm), which means when it is red on the shaft body rather than clamping arms, there will be no gap observed between the clamping arms and the rotor stack, and the rotor is safe to stay in the shaft. Among all the 12 cases only case 7, 8, 10, 11 and 12 satisfy this criteria. Considering that the critical opening strength is mostly close to 20 MPa for Hiperco 50, 2.3 mm rotor stack will be robust enough to rotate at 1.2 Mrpm. This means 15% more torque can be achieved safely by using 3M DP420 adhesives.

Table 3.2 Maximum Gap Length under Different Adhesive Strength

| Rotor Stack Length | | 2 mm | 2.3 mm | 2.6 mm |
|---|---|---|---|---|
| Maximum Gap Length under Different Adhesive Strength | No Adhesive | 14.2 μm | 19.8 μm | 26.7 μm |
| | 10 MPa | 6.4 μm | 9.6 μm | 14.3 μm |
| | 20 MPa | 3.2 μm | 4.5 μm | 6.6 μm |
| | 30 MPa | 1.1 μm | 1.4 μm | 1.6 μm |

The maximum local stress on the shaft is also reduced significantly by about 60% from 557 MPa to 231 MPa as shown in Figure 3.8. The reason is that additional bonding is provided by the adhesives, eliminating the gaps as well as supporting the clamping arms against high centrifugal force.

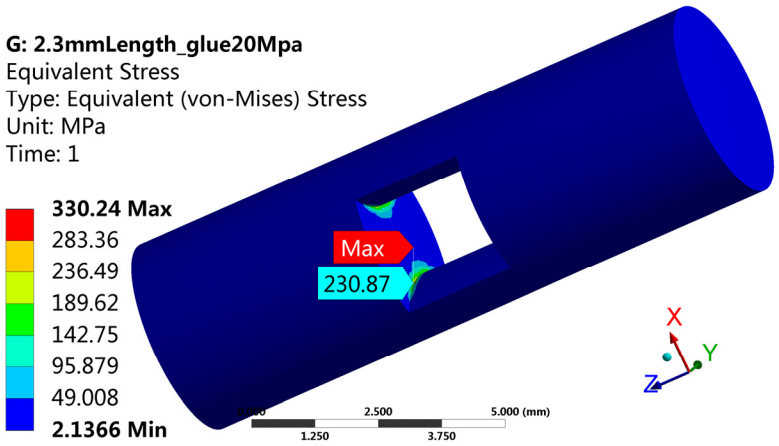


Figure 3.8 Strength analysis of the shaft with 2.3 mm rotor stack using adhesives.

## 3.8 Chapter Summary

In this Chapter, the cohesive zone model (CZM), a model in fracture mechanics, is introduced to analyze the mechanical robustness of an improved designed SRM rotor for ultra-high speed applications over 1 million rpm, where high strength adhesives are used to increase the bonding as well as to reduce the high localized stress. A detailed finite element model is built in ANSYS to simulate the debonding process of the clamping arms. A parametric study is conducted for different rotor length under different adhesive strength. The results show that the maximum output torque can be increased by 15% and the highest strength on the shaft is reduced by 60% with the improved design. The detailed model introduced in this chapter can also provide a good reference for estimating the mechanical stress of high speed rotors where adhesives are used.

# CHAPTER 4. ROTOR DYNAMICS ANALYSIS AND PROTOTYPING

## 4.1 Introduction

For ultra-high speed machines, rotor dynamics are a major issue and must be considered in the design stage. In this Chapter, a rotor dynamics study of the 1 million rpm SRM is proposed [66]. First, rotor shafts made of both isotropic and orthotropic materials are studied through both analytical and numerical methods. Then, shafts of both laminated and solid rotor stacks are studied and compared. Next, three different geometries of single, tandem and bilateral rotor stacks are proposed and compared in order to increase torque as well as avoid critical speeds near the rated speed. Finally, the issues in manufacturing of the rotor stack and shaft are described with the demonstration of several prototypes.

## 4.2 Bearing Selection

### *4.2.1 Category*

In order to reach ultra-high speeds beyond 1 million rpm, bearing selection is the key to the final success. Generally speaking, there are three kinds of bearings: ball bearings, air bearings and magnetic bearings. Table 4.1 gives a comparison of different bearing technologies [67].

Table 4.1 Comparison of Different Bearing Technologies [67]

| | Ball Bearing | Air Bearing | Magnetic Bearing |
|---|---|---|---|
| Maximum Speed (m/s) | 50 to 160 | 150 to 225 | 180 to 200 |
| Load Capacity | Moderate to high | Low to moderate | Low to moderate |
| Oil free | No | Yes | Yes |
| Complexity | Low | Moderate | High |
| Weight | Moderate | Light | High |
| Stiffness | High | Low | Depend on tuning |
| Shock tolerance | Moderate | Good | Can |
| Cost | Low | Moderate | high |

The absolute rotational speed depends on the size of the bearing. The DN number, which is the product of the bearing diameter (*D*) in mm and the top speed (*N*) in rpm, is used as the measure of the highest possible speed performance of a bearing. Table 4.2 gives a comparison of the DN number among different bearings [68].

Table 4.2 Comparison of DN Number of Different Bearing Technologies [68]

| Bearings | DN number (mm·rpm) |
|---|---|
| Steel ball bearings | 1,000,000 |
| Ceramic ball bearings | 2,000,000 |
| Air bearings | 4,400,000 |
| Magnetic bearings | 4,500,000 |

### *4.2.2 Ball Bearing*

High speed ball bearings are a traditional choice for high speed electric motors. The advantages of ball bearings are the simplicity and high stiffness. Rather than steel ball bearings, ceramic ball bearings are the main type of ball bearings for ultra-high speed applications due to the harder and smoother surface of ceramic. However, because of the physical contact between the balls and the outer/inner races, the life time and the maximum speed is limited. The 1 million rpm electric motor proposed in [20] used ceramic high speed ball bearings and had to stop before the "disintegration of the ball bearings". To achieve even higher speeds, ball bearings are not a good choice.

### *4.2.3 Magnetic Bearing*

Magnetic bearings use magnetic force to actively levitate the rotor and shaft with advanced feedback control [41]. The benefit of using magnetic bearings is that the rotor and shaft do not touch the stator of the bearing. This implies that longer life and higher speed can be achieved. However, magnetic bearings require very complex auxiliary control system, which includes sensors, actuators and control circuitry [67]. Because of this, there is a very limited number of commercially available magnetic bearings on the market. For the simplicity of the system, magnetic bearings are not chosen, either.

### *4.2.4 Air Bearing*

Air bearings support the rotor and shaft using air pressure. There are two ways of generating the air pressure: if the air pressure is generated by the relative movement of the rotor with respected to the stator and the bearing is sealed, it is called an aerodynamic bearing; if the air pressure is generated by an external supply, it is called an aerostatic bearing. The benefit of the air bearings is also the non-contact characteristic as magnetic

bearings. In addition, they do not need complex feedback control systems to work. The drawback is the poor dynamic stability [67]. This can be avoided by having a light weight rotor and increasing the air pressure.

In conclusion, ball bearings have relatively short life and lower maximum speed and magnetic bearings are too complex to control and implement. Thus, high speed air bearings will be selected in this thesis. Fortunately, an aerostatic bearing of 4 mm inner diameter from OAV air bearing company has just been recently available and will be used in this thesis [69].

## 4.3 Analytical Analysis of Rotor Dynamics

The length of the shaft is dependent on the length of the bearings. Unlike the regular ball bearings, air bearings technically have an infinite life time and will only have air friction between the rotor and the bearings, resulting in extremely low air friction losses. But at such a small size, the air bearings must have a minimum length in order to support the shaft. A pair of customized thrust air bearings made by the OAV air bearing company will be used here as shown in Figure 4.1 [69]. They have an inner diameter of 4 mm and an outer diameter of 16.1 mm. The length is customized to be a minimum value of 7.5 mm.


Figure 4.1 A pair of air bearings from OAV air bearing company.

Besides the air bearings, suitable position sensors have to be applied in order to control the machine. A length of 7.5 mm is reserved for the setup of optical sensors. Thus, a total shaft length of 40 mm is assumed for a preliminary case study. Figure 4.2 shows the side view of the machine.

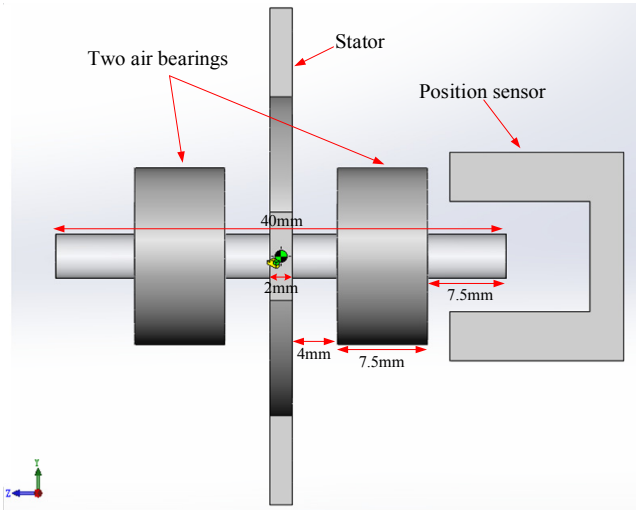


Figure 4.2 Side view of the ultra-high speed SRM.

For a high-speed machine design, natural frequencies should be avoided before the machine reaches the rated speed. However, for ultra-high speed applications over 500,000 rpm, it is generally impossible to do so. Nevertheless, the rated speed should fall between the two critical speeds in order to avoid resonance [27].

Before the proposed rotor system is studied, a regular pure cylindrical shaft made from a single material is studied and the results are compared with an analytical and numerical (finite element) method. The natural frequency of a beam without damping can be calculated from (4.1) [70].

$$\omega_n = a_n \sqrt{\frac{EI}{\mu_1 l^4}} \tag{4.1}$$

where $\omega_n$ is the $n^{th}$ natural frequency, $E$ is the Young's modulus in the direction of the rotational axis, and $l$ is the length of the shaft. In addition, $\mu_l$ is the mass per unit length, $a_n$ is a series constant which depends on boundary conditions, and $I$ is the moment of inertia of the cross section. For a cylinder, $I$ can be calculated from (4.2)

$$I = \frac{\pi d^4}{64} \tag{4.2}$$

where $d$ is the diameter of the cross section. Substitute (4.2) into (4.1), we have (4.3)

$$\omega_n = a_n \sqrt{\frac{Ed^2}{16\rho l^4}} \tag{4.3}$$

Because of the special design of the rotor geometry, high-strength and light-weight materials should be used to make the shaft. Titanium alloy and carbon fiber are two good candidates. Table 4.3 gives the analytical and numerical calculation of the first three natural frequencies of the two materials without the support of bearings. The mechanical properties of the two materials can be found in Table 4.4. Unlike titanium alloy, which is isotropic, carbon fiber is an orthotropic material that is stronger in one direction than in the other two directions. Two different carbon fiber shafts which have a higher Young's modulus in either the X or Z direction are listed in Table 4.3. As shown in the table, the analytical solution is much closer to the numerical solution in lower speeds than in higher speeds. One of the reasons is that the rotation of the rotor would affect the natural frequencies when the machine is at a standstill. This is known as the gyroscopic effect [71]. Note that these results are for cylindrical shafts that are made from a single material without the rotor stack in the middle. The purpose of this is to get a general idea of the natural frequencies of the proposed shaft as well as to check the validity of the basic numerical model.

Table 4.3 Analytical and Numerical Calculation of the First Three Natural Frequencies of Titanium Alloy and Carbon Fiber

| Material | Mode | 1st (Hz) | 2nd (Hz) | 3rd (Hz) |
|---|---|---|---|---|
| **Titanium Alloy** | *Analytical* | 9975 | 27975 | 54863 |
| | *Numerical* | 9888 | 26101 | 48396 |
| **Carbon fiber (strengthened in X)** | *Analytical* | 5257 | 14743 | 28914 |
| | *Numerical* | 5228 | 13906 | 26033 |
| **Carbon fiber (strengthened in Z)** | *Analytical* | 19720 | 55307 | 108463 |
| | *Numerical* | 17903 | 40049 | 63911 |

Table 4.4 Mechanical Properties of Different Materials

| **Mechanical Properties** | **Shaft Material** | | **Mechanical Properties** | **Rotor Stack Material** | |
|---|---|---|---|---|---|
| | *Titanium Alloy* | *Carbon Fiber (strengthened in X)* | | *Solid Hiperco 50* | *Laminated Hiperco 50* |
| **Density (ρ)** | 4620 kg/m$^3$ | 1490 kg/m$^3$ | **Density (ρ)** | 8110 kg/m$^3$ | 7740 kg/m$^3$ |
| **Young's Modulus ($E_x$)** | 96 GPa | 121 GPa | **Young's Modulus ($E_x$, $E_y$)** | 210 GPa | 210 GPa |
| **Young's Modulus ($E_y$, $E_z$)** | 96 GPa | 8.6 GPa | **Young's Modulus ($E_z$)** | 210 GPa | 7.8 GPa |
| **Shear Modulus ($G_{yz}$)** | 35.3 Gpa | 3.1 GPa | **Shear Modulus ($G_{xy}$)** | 79 GPa | 52.5 GPa |
| **Shear Modulus ($G_{xy}$, $G_{xz}$)** | 35.3 Gpa | 4.7 GPa | **Shear Modulus ($G_{xz}$, $G_{yz}$)** | 79 GPa | 7.6 GPa |
| **Poisson's Ratio ($\nu_{yz}$)** | 0.36 | 0.4 | **Poisson's Ratio ($\nu_{xy}$)** | 0.33 | 0.33 |
| **Poisson's Ratio ($\nu_{xy}$, $\nu_{xz}$)** | 0.36 | 0.27 | **Poisson's Ratio ($\nu_{xz}$, $\nu_{yz}$)** | 0.33 | 0.11 |

Figure 4.3 shows the stress analysis of the shaft made from carbon fiber at 1.2 million rpm. As can be seen, the highest stress calculated is only 556 MPa, as opposed to the titanium shaft, which is under 829 MPa of stress. The reason for the lower stress is the lower centrifugal force due to the lighter weight of the carbon fiber. The stress direction is shown to be from the center towards the clamping arm (X direction), shown in both the force analysis and Figure 4.3. So the carbon fiber strengthened in the X direction will be analyzed here.

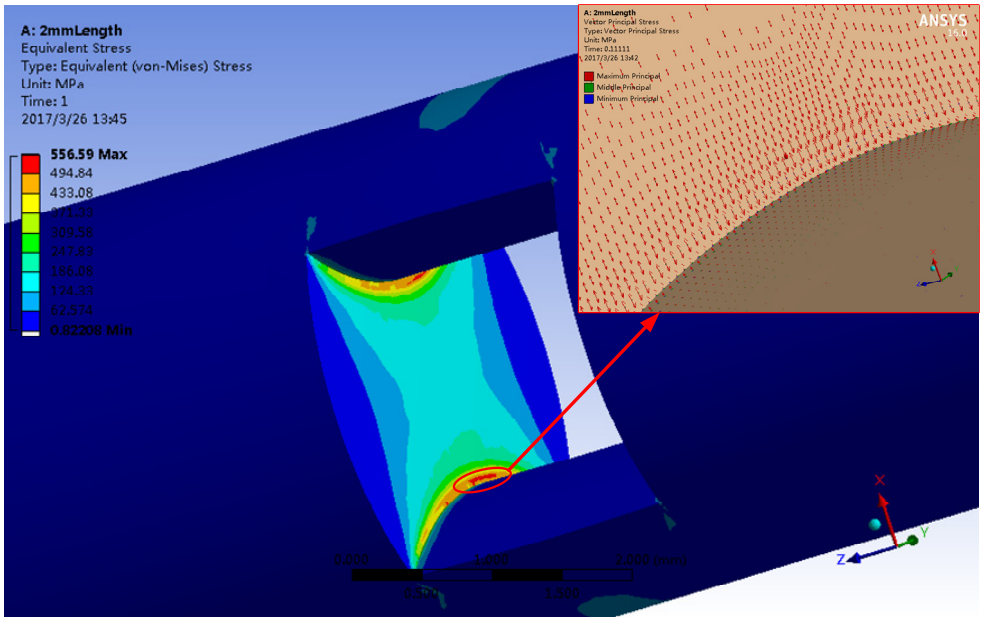


Figure 4.3 Strees analysis of the carbon fiber shaft at 1.2 million rpm.

## 4.4 Finite Element Analysis of Rotor Dynamics

### *4.4.1 Modal Analysis of the Basic Geometry*

To analyze the natural frequencies of the proposed rotor-bearing system, a finite element model was built in ANSYS. The dynamic behavior of the system is modeled using the discrete differential equation in the stationary reference frame shown in (4.4)

$$[M]\{\ddot{u}\} + ([C] + [C_{gyr}])\{\dot{u}\} + [K]\{u\} = \{F\} \tag{4.4}$$

where [$M$] is mass matrix, $u$ is spinning velocity, [$K$] is stiffness matrix, [$C$] is damping matrix, and [$C_{gyr}$] is gyroscopic matrix. ANSYS derives the gyroscopic matrix [$C_{gyr}$] from the kinetic energy expression as is shown in (4.5) [72, 73]:

$$E_{mass}^{Ki} = \frac{1}{2}\begin{Bmatrix}\dot{u}_y \\ \dot{u}_z\end{Bmatrix}^T \begin{bmatrix} m & 0 \\ 0 & m \end{bmatrix} \begin{Bmatrix}\dot{u}_y \\ \dot{u}_z\end{Bmatrix} + \frac{1}{2}\begin{Bmatrix}\dot{\theta}_y \\ \dot{\theta}_z\end{Bmatrix}^T \begin{bmatrix} I_d & 0 \\ 0 & I_d \end{bmatrix} \begin{Bmatrix}\dot{\theta}_y \\ \dot{\theta}_z\end{Bmatrix} - w_x I_p \dot{\theta}_z \dot{\theta}_y \tag{4.5}$$

where m is mass, $I_p$ is polar moment of inertia, $I_d$ is diametral moment of inertia, $\theta$ is angular displacement.

The system is built as shown in Figure 4.4. Two air bearings of 7.5 mm in length were included in the model. The bearing stiffness was set to 5 N/μm according to [69]. The rotor is assumed to be a solid stack, which is made from Hiperco 50. Figure 4.5 (a) to (e) show the first five vibration modes at 6505, 10314, 15816, 27712 and 30263 Hz, respectively.

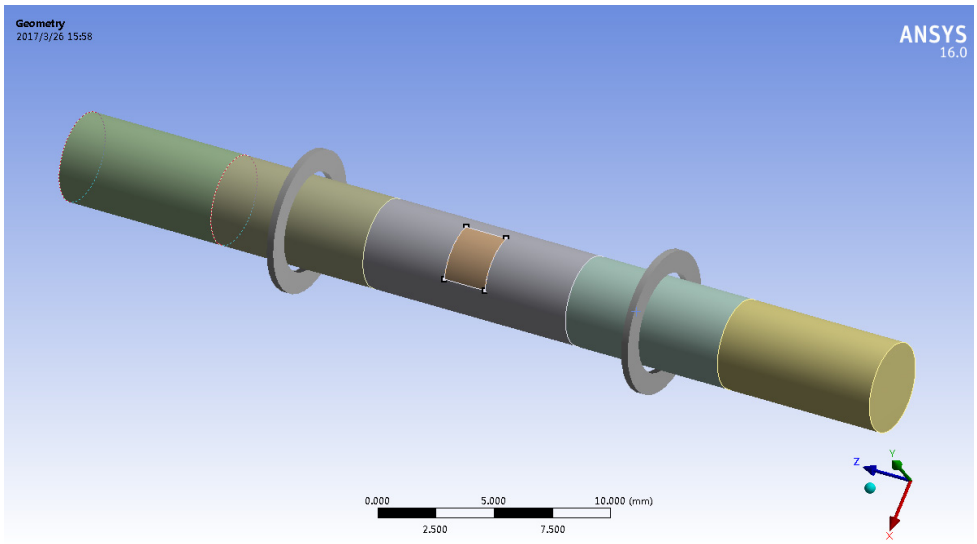


Figure 4.4 Shaft model with two bearings.

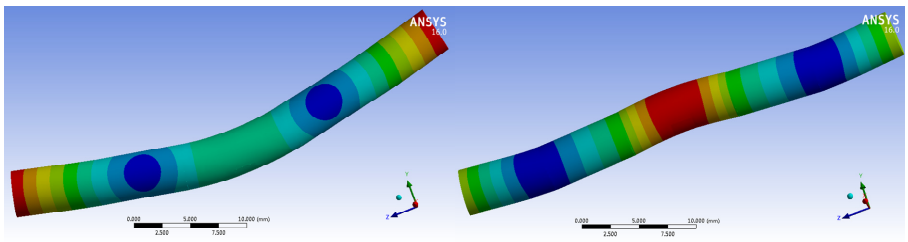

(a) $f_1$=6505 Hz (b) $f_2$=10314 Hz

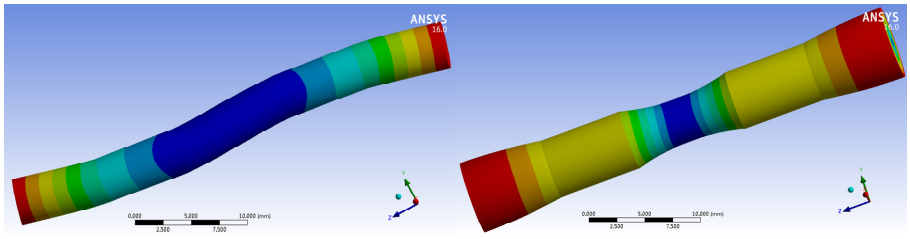

(c) $f_3$=15816 Hz (d) $f_4$=27712 Hz

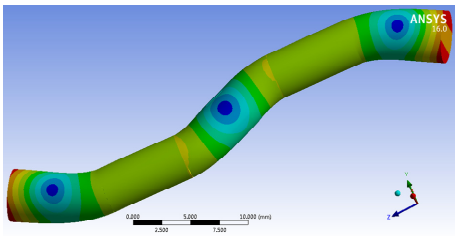

(e) $f_5$=30263 Hz

Figure 4.5 First five vibration modes.

### *4.4.2 Solid and Laminated Stack*

In the real design, the rotor stack is made from 0.006'' Hiperco 50 laminations. The effect of the laminations of a stack on the natural frequencies against its solid counterpart was studied in [74]. It has been shown that the axial component of Young's modulus of the laminated stack in large electric machines can be as low as 0.25% of a solid stack, depending on clamping pressure [75]. However, it is unclear whether the effect of the rotor stack's lower Young's modulus will have a great impact on the natural frequencies of the whole shaft, considering the small and simple geometry of the proposed high-speed rotor. Thus, both laminated rotor and solid rotor are studied in this chapter.

Figure 4.6 shows a comparison of the Campbell diagram of the shaft with solid and laminated rotor stacks in the middle of the shaft with a similar assumption in the modification of the mechanical properties of the laminated stack against the solid stack made in [75]. Figure 4.2 shows the mechanical properties of different materials in the simulation. This assumption may not necessarily be exactly accurate to the case in discussion, but it can still give us a good estimation of the impact of the laminated rotor on the proposed shaft.

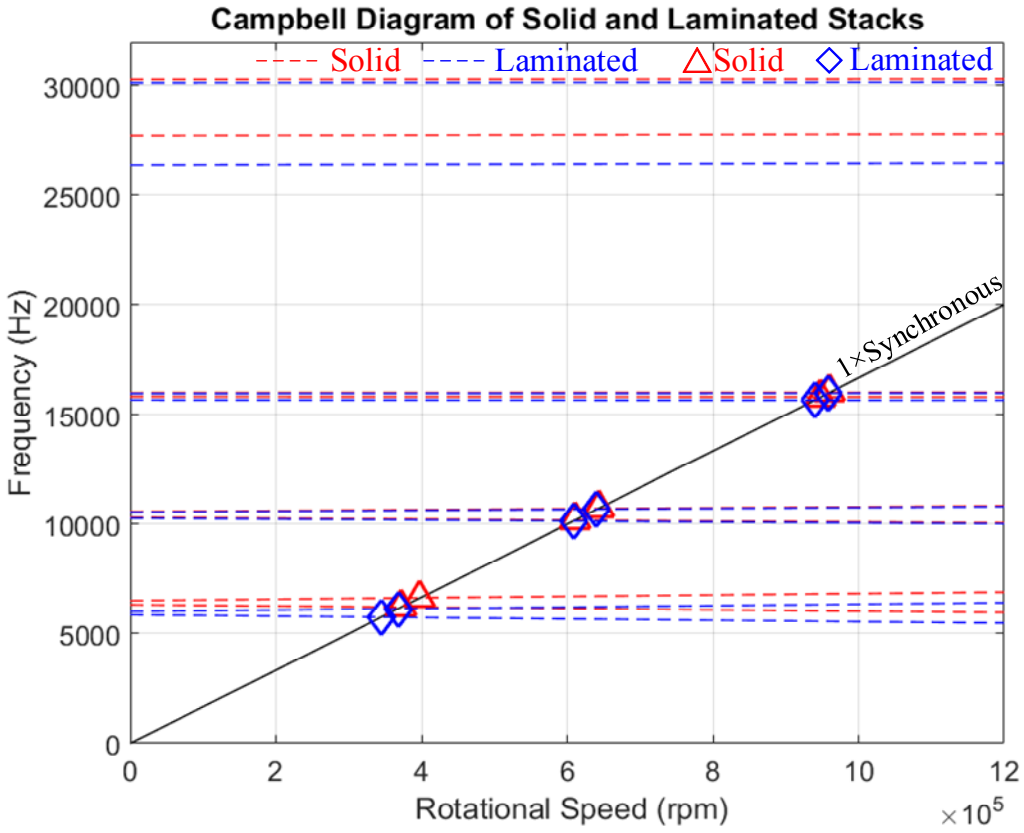


Figure 4.6 Comparison of the Campbell diagram of the shaft with solid and laminated rotor stack. The third critical speeds are near the rated speed of 1 million rpm

From Figure 4.6 it can be seen that there are three critical speeds from 0 to 1.2 million rpm for the proposed single rotor shaft. Except for the first bending modes, which have

only minor differences between them, the second and third critical speeds between the laminated and solid rotor stacks are almost the same. Thus, the solid stack assumption is reasonable and will be continued to be used in the following discussion.

### *4.4.3 Two Alternative Geometries*

As analyzed in Chapter 2 and 3, the rotor stack can not be as long as desired because of the high centrifugal force exerted on the shaft. In addition, from Figure 4.6 we can see that the third vibration mode exists near the rated speed of 1 million rpm, which means it is quite possible for the rotor to break in the rated condition. To solve these two problems, two alternative geometries are proposed and studied.

Figure 4.7 shows the first design of a shaft with tandem rotors in the middle. This geometry would increase the output torque by a factor of two while retaining the robustness of the original design. Figure 4.8 shows the 3D stress analysis of the design. Compared with Figure 4.3, the new design actually has more desirable mechanical characteristics since it reduces the highest stress exerted from 556 MPa to 499 MPa. The reason is that the clamping arms of the additional rotor also tend to move away from the center, which is in the same direction as the original clamping arms. This same tendency of movement releases the highest stress to some extent.

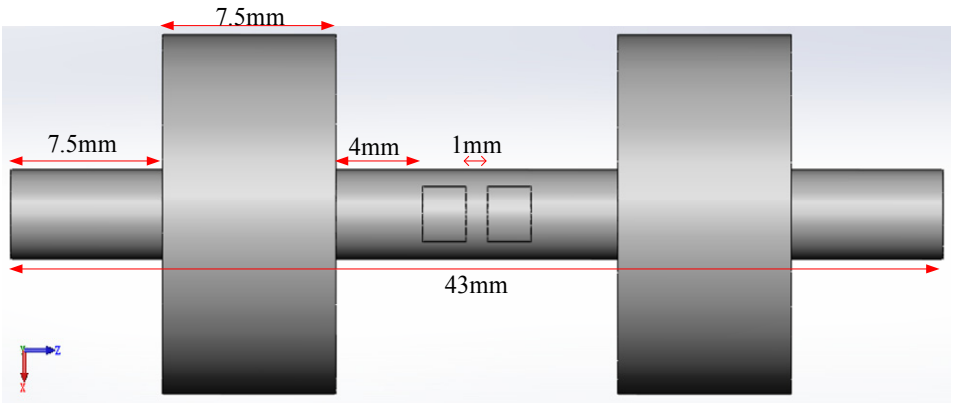


Figure 4.7 Shaft with tandem rotors in the middle.

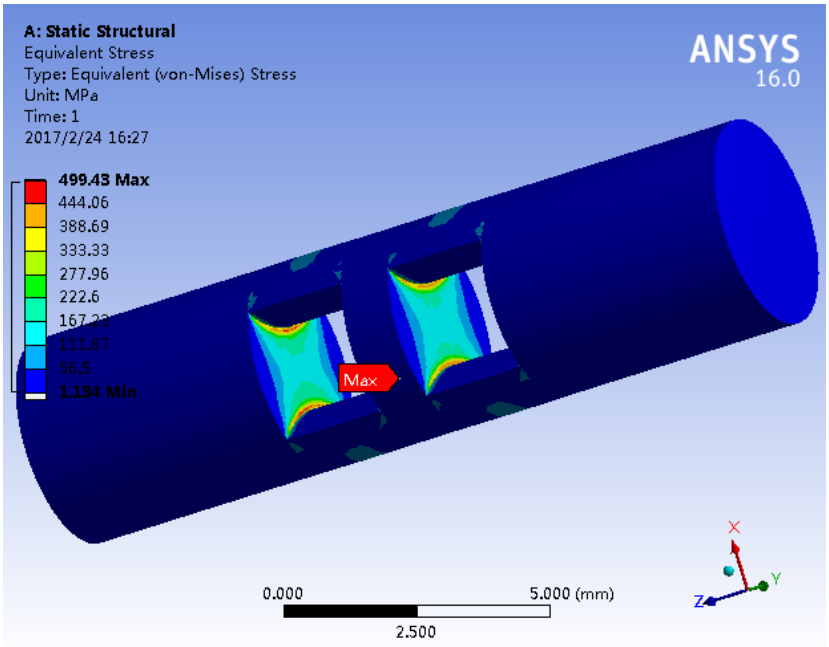


Figure 4.8 Stress analysis of the shaft with tandem rotors.

The other design is shown in Figure 4.9. It is a single bearing shaft with two rotor stacks at both ends of the shaft. The purpose of this design is to reduce the total length of the shaft by using only one bearing. This increases the critical speed since the critical speed is inversely proportional to the square of the length. Two rotor stacks are put at both ends, so as to increase the torque, as well as keep the balance of the shaft.

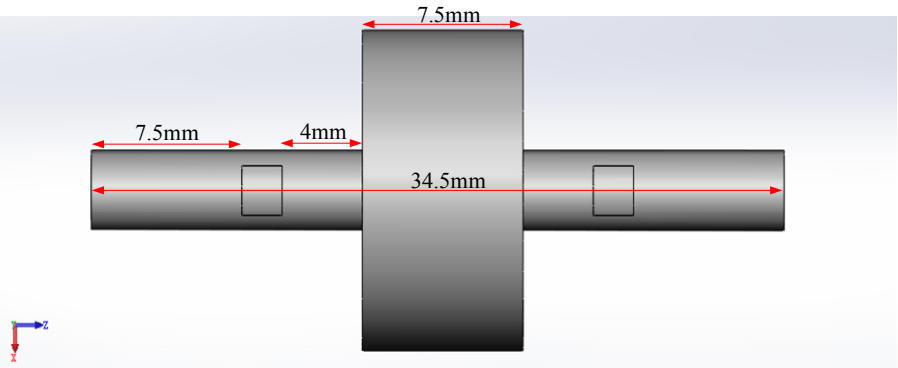


Figure 4.9 Shaft with bilateral rotors at both ends.

Figure 4.10 shows the Campbell diagram of the three different shaft geometries: single (red), tandem (blue) and bilateral (green) rotor. Compared with the single rotor design, the first three vibration modes of the tandem rotor design are shifted to lower speeds due to the heavier equivalent rotor stack in the middle as well as the longer length of the shaft. However, in this case, this may be a good thing because it moves the third vibration mode away from the rated speed of 1 million rpm.

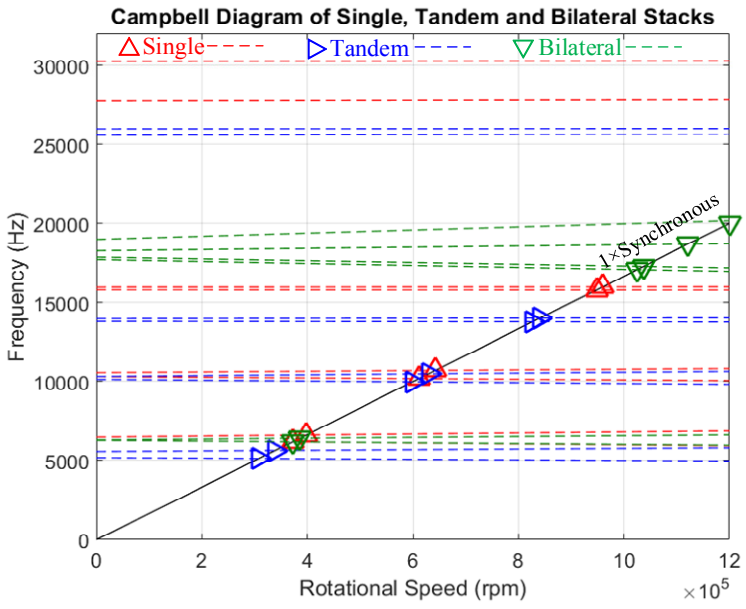


Figure 4.10 Campbell diagram of the three different shaft geometries: single (red), tandem (blue) and bilateral (green).

For the bilateral rotor design, because of the reduction in rotor length, the critical speeds increase. The second vibration mode increases beyond the third vibration modes of both the single and tandem rotor designs, relocated near the rated speed of 1 million rpm, which attenuates the stability at the rated speed. The third vibration mode (between 1.1 to 1.2 million rpm) is very close to the second one. In addition, the gyroscopic effect is more prominent in the third vibration mode. It can been seen that the forward and backward whirl line of the third vibration mode gradually separates into two critical speeds at about 1.1 and 1.2 million rpm, which are close enough to be treated as one critical speed in the other two cases. This instability phenomenon can be intuitively acknowledged by using a single bearing instead of two, which is similar to a cantilever fixed in the middle point. Longer and heavier parts of the shaft protrude from the bearing on both sides without any support, making the gyroscopic phenomenon more significant. Thus, instead of three, four critical speeds are observed from 0 to 1.2 million rpm. Moreover, there are three critical speeds between 1 to 1.2 million rpm (one speed of the second mode and two of the third mode). This makes the rotor very unstable and more fragile to break near the rated condition.

To conclude, the two alternative designs have their own advantages and disadvantages. Both of the designs can increase the output torque twice because of the double rotor stack applications. The tandem rotor design has a better mechanical robustness as well as better rotor dynamics. However, it may be more difficult to manufacture, depending on the gap between the two rotors. Note that the tandem design can also be generalized into multiple rotors in the middle, which will eliminate the limitation of the maximum length of the equivalent rotor stack in the original single rotor design.

The bilateral rotor design has more economic benefits due to only having one air bearing, and only has one vibration mode below 1 million rpm. However, this geometry is not stable, and will have three critical speeds between 1 and 1.2 million rpm. So, this design is more applicable to machines with a lower rated speed. Table 4.5 gives a comparison between the single, tandem and bilateral design.

Table 4.5 Comparison between the Three Different Designs

| | Single | Tandem | Bilateral |
|---|---|---|---|
| Cost | Moderate | High | Low |
| Torque Density | Low | High | High |
| Manufacturing Complexity | Low | High | Moderate |
| Stability near 1 million rpm | Moderate | Good | Bad |

## 4.5 Rotor Stack Prototype

### *4.5.1 Lamination Selection*

To verify the manufacture feasibility of the proposed rotor geometry, several prototypes have been built. 0.006'' Hiperco 50 laminations were chosen as the rotor lamination material because of its high magnetic saturation, comparatively low loss and high mechanical strength [31]. The laminations were laser cut before going through proper heat treatment to gain the best magnetic properties. Figure 4.11 shows the 0.006'' Hiperco 50 lamination in comparison with a pen nib.

Figure 4.11 0.006’’ Hiperco 50 lamination in comparison with a pen nib

### *4.5.2 Stacking*

The laminations have to be stacked together to be a useful rotor. There are several methods of stacking such as welding, riveting/bolting and adhesive bonding. For such small size only adhesive bonding is possible here. The adhesive used is the Magna-Tac E-645 [76]. Figure 4.12 shows a picture of the rotor prototype. There are 13 laminations in each rotor stack. The final rotor length is within the range of 2.00±0.02 mm. So the final stacking factor is calculated to be over 97.5%.

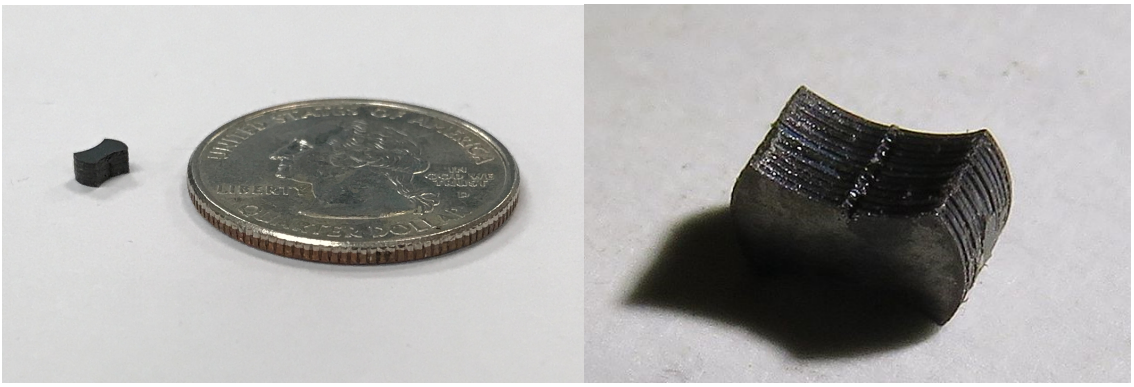

Figure 4.12 Left: prototype of the rotor stack in comparison with a US quarter
Right: zoom-in look of the rotor stack

## 4.6 Shaft Prototype

Due to the special design of using clamping arms rather than the traditional rotor sleeves, there are unique challenges in manufacturing the shaft. Two high-strength materials are considered with different possible construction methods.

### *4.6.1 Titanium Alloy Shaft*

The first approach is to use a titanium alloy for the shaft as in [23] and [77]. One of the difficulties in using titanium alloy or other metals is the integration of the lamination stack into the shaft. Due to the curved contact surface, the rotor stack will remain firmly inside the shaft when rotating at ultra-high speeds. However, with this material the rotor stack cannot be inserted into position after the entire shaft is made.

One possible method of manufacturing the shaft is shown in Figure 4.13. The shaft is separated into two halves. The first half is integrated as one piece with clamping arms that slotted. The other half has two protruded keys that can be inserted into the slots. Proper interference fit methods such as shrink-fitting need to be used to secure a safe and very tight fit at ultra-high speeds.

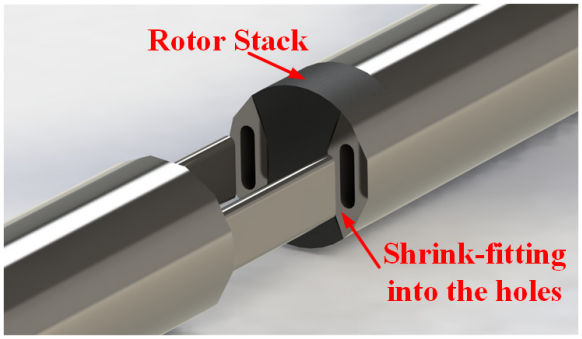


Figure 4.13 Construction of the shaft using interference fit.

Another possibility is to use a 3D printed shaft, as in [78]. Figure 4.14 shows the necessary construction procedure. The shaft is printed from the bottom along the axial direction and stopped after finishing the clamping arms. Then, the rotor stack is inserted into the proper position. Appropriate adhesives must be applied to increase the bonding during insertion. After that, the printing continues to the clamping arms, and completing the shaft. This technique allows for an accurate and convenient way to construct the shaft, and allows for rapid prototyping.

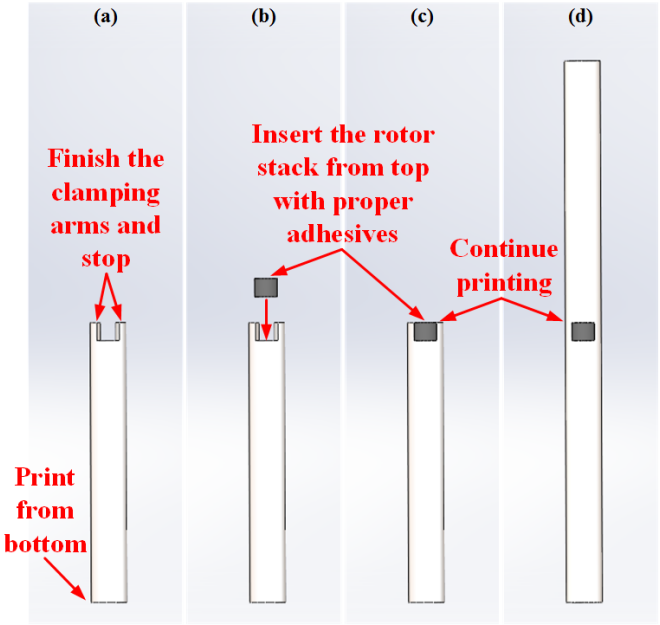


Figure 4.14 Procedure of the 3D printed shaft.

### *4.6.2 Carbon Fiber Shaft*

Another candidate shaft material is carbon fiber. Carbon fibers have very good mechanical properties including high tensile strength, light weight and low (or even negative) thermal expansion. High tensile strength can ensure safe operation at ultra-high

speeds, while the light weight and low thermal expansion are very critical for the stable operation of air bearings which are required at extreme speeds.

Another benefit of using carbon fiber is its versatility in forming arbitrary shapes. Carbon fibers are intrinsically thin filaments. This implies that arbitrary shapes can be formed using proper manufacturing. Figure 4.15 shows how a high strength carbon fiber shaft is made. The red and blue filaments indicate the left and right halves of the carbon fibers, respectively. The highest strength boundaries, indicated by the green arrow in Figure 4.15, are located at the connecting boundaries between the clamping arms and the shaft [50]. Therefore, the fibers have to be wrapped around the rotor stack in order to keep these high stress boundaries very strong.

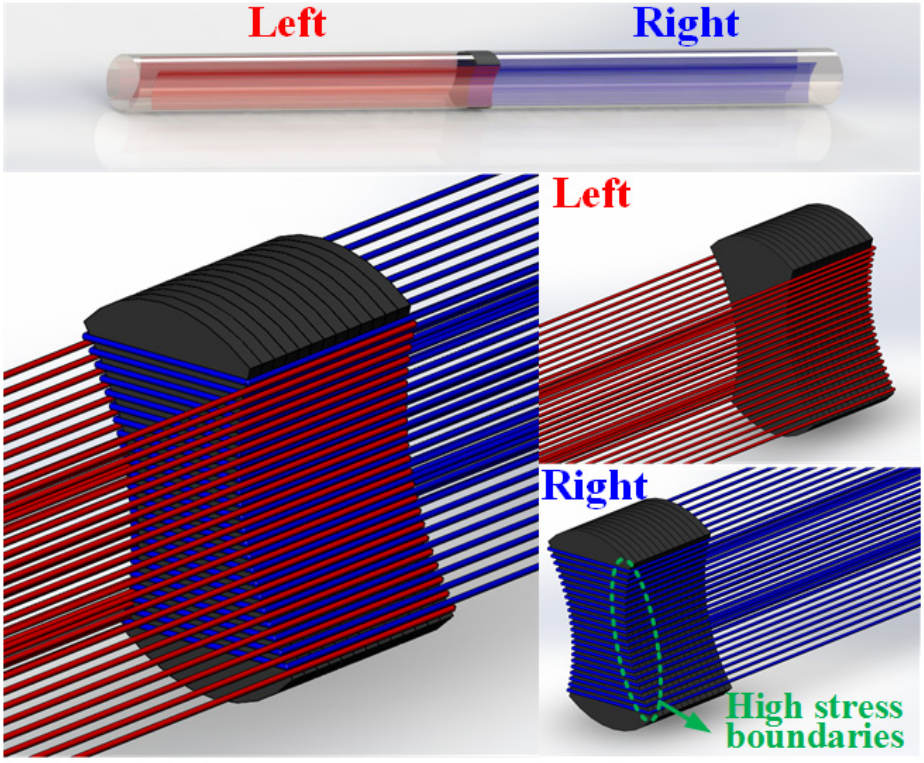


Figure 4.15 Illustration of the process of manufacturing a carbon fiber shaft

## 4.7 Manufacturing Tolerance

For ultra-high speed applications over 1 million rpm, manufacturing tolerances must be addressed to achieve stable and long-term operation. Several of carbon fiber prototype shafts were constructed. Several practical issues are listed below for manufacturing these prototypes.

### *4.7.1 Surface Joint Issues*

For safe operation, the contact joint between the rotor stack and the shaft is very important. Figure 4.16 shows a comparison of three prototypes. As can be seen, prototype number 2 has cracks in the surface joint between the rotor stack and the shaft. This leads to a skewed position of the rotor stack in the shaft. After applying the method described in Figure 4.15, much better joints are achieved for prototype number 1 and 3.

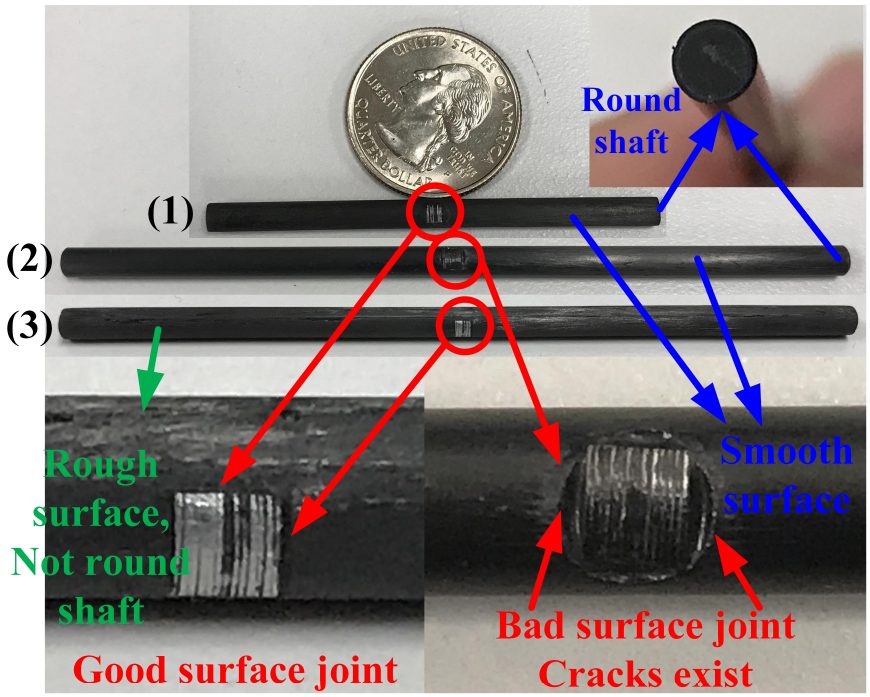


Figure 4.16 Comparison of three prototypes of carbon fiber shafts.

### *4.7.2 Roundness and Straightness*

Because of the air bearings being used in the machine, and considering the ultra-high speed conditions, the surface finish of the shaft is of great importance. This includes the smoothness, roundness and straightness of the shaft. In manufacture, they are generally related. Prototype number 3 shows a rough surface finish as well as a not round shaft (not shown in the picture), although it provides better joints between the rotor stack and the shaft. On the other hand, although prototype number 2 has a bad joint, the final finish of the surface is very smooth and the shape of the shaft is more close to a pure round cylinder (shown in the picture). Prototype number 1 combines the advantages of the other two and will be used in the final machine.

### *4.7.3 Temperature*

The final step in shaft construction is to mix and bake the fibers with the right type of epoxy in order to harden the fibers. Special attention should be taken regarding the baking temperature. It cannot be too high so as to deactivate the epoxy and adhesives used for the bonding and stacking, but must be high enough to achieve the excellent mechanical properties of carbon fiber.

## 4.8 Chapter Summary

This chapter presents a rotor dynamics study and prototyping of the shaft for an ultra-high speed SRM with a rated speed of 1 million rpm. Different rotors composed of isotropic and orthotropic materials of titanium alloy and carbon fiber are studied and compared through both analytical and numerical methods. Based on the stress analysis, it is proposed

that the carbon fiber strengthened in the X direction should be used. Then, the impact of a laminated stack against a solid stack is studied. The results show that there is very few differences observed between the two, because of the rotor's small size. After that, two alternative geometries of tandem and bilateral rotor designs are proposed, analyzed and compared with the original single rotor shaft based on cost, torque density, manufacturing complexity and stability. The tandem rotor design has a better mechanical robustness, as well as better rotor dynamics performance near the rated speed. However, manufacturing may be more difficult. The bilateral design offers more economic benefits, but it has the worst rotor dynamic performance near the rated speed. Tradeoffs need to be considered in the design stage in its different applications. Finally, the manufacturing issues of the rotor and shaft are described and several prototypes of the single rotor shaft are demonstrated.

# CHAPTER 5. ELECTROMAGNETIC DESIGN

## 5.1 Introduction

After the rotor is designed, the stator and windings should also be designed properly to meet the power and torque requirement. At such high speed, the stator copper loss and core loss will be significant. The former is due to the skin effect of the stator windings while the latter is because of the high switching frequency. In addition, a proper value of the air gap length should also be determined. It should be as small as possible in order to reduce the electric loading but it can not be too small to be manufactured. In this chapter a complete design of an ultra-high speed SRM for applications beyond 1 million rpm is proposed. Pole pair number, dimension calculation, air-gap calculation, material selection, winding selection and windage torque calculation are included in details. The proposed designed will be validated in the next chapter with finite element analysis.

## 5.2 Pole Pair Selection

The first thing to consider is to select a suitable value for the stator pole pair number. Generally speaking, for such high speed, the stator pole pair number should be as small as possible. For example, the two 100,000 rpm SRMs in [32] and [33] have a stator/rotor combination of 4/2 and 6/4, respectively. Obviously the 4/2 combination is a better choice at ultra-high speed in terms of lower switching and core losses and is also selected in [44, 79]. The fundamental frequency of a 4/2 SRM operating at 1 million rpm is 33.3 kHz according to (2.4).

## 5.3 Air Gap Design

Air gap is very critical in the design of ultra-high speed electric machines. Different types of machines have different needs for air gap. SRMs need smaller air gaps than PM machines due to the lack of PMs in the rotor. For example, the high speed PM machine in [80] has an air gap of 0.5 mm. The equivalent air gap is larger due to the use of the retaining sleeve. The typical value of the air gap of high speed SRMs is in the range of 0.1-0.25 mm according to [33]. For example the SRM in [33] has an air gap of 0.2 mm. The air gap of the SRM in [1] is designed to be 0.3 mm and was changed to 0.5 mm due to manufacturing limitations. The air gap of the SRM in [39] is 0.35 mm with an additional 0.25 mm of the sleeve thickness. This large air gap leads to a low flux density in the stator and rotor core. Considering the extremely small size as well as the manufacturing limitations, the final air gap length is determined to be 0.3 mm. This value is comparatively large for such a small machine. But it can give better mechanical robustness when the machine is passing through the natural frequencies before reaching the rated speed of 1 million rpm, which is very important. The trade-off is that the electric loading will be higher to achieve the same torque density.

## 5.4 Stator Winding Design

### *5.4.1 Winding Type Selection*

Since the fundamental frequency of the machine is 33.3 kHz, the skin effect of the stator windings will be significant at such high frequency. Thus Litz-wire is recommended to be used in the stator windings [27]. For different operational frequencies different types of Litz-wires are recommended. Choosing the most suitable type of Litz-wire requires a balanced consideration among different aspects such as the operational frequency, the

cross-section area, the maximum allowed amperes and so on. For the fundamental frequency of 33.3 kHz, we can assume that the switching frequency of the power electronics is about ten times this frequency. So the Litz-wire of strand gauge of 42 is chosen to be used here [81]. Among all different types of Litz-wires that have the strand gauge of 42, those who have a strand number of 66, 105 and 165 are of particular interest because of the maximum amperes allowed for chassis wiring [27, 28, 39, 82]. The characteristic of these three Litz-wires are listed in Table 5.1. The maximum current is finally chosen to be 3.5A based on [27, 28, 39], which is a compromise between high maximum current value and low cross-section area. This choice of maximum current will be verified in the next chapter.

Table 5.1 The Characteristic of Different Types of Litz-wires

| Strand gauge | Equivalent gauge | Cross-section area ($mm^2$) | Number of strands | Maximum amps for chassis wiring (A) |
|---|---|---|---|---|
| 42 | 24 | 0.2093 | 66 | 3.5 |
| 42 | 22 | 0.3324 | 105 | 7 |
| 42 | 20 | 0.5224 | 165 | 11 |

### *5.4.2 Winding Area Calculation*

After choosing the Litz-wire, the winding area can be determined. Due to the large air gap, the winding turn number has to be greater than usual. In order to generate enough flux and torque, the turn number is chosen to be 50 by an iterative design procedure, which is also a compromise between high torque and small winding area. Assuming a filling factor of 0.25, the winding area is calculated to be 40 $mm^2$.

## 5.5 Stator Design

### *5.5.1 Material*

Due to ultra-high speeds, high frequency stator core material has to be applied. Iron-based amorphous metal Metglas 2605SA1 is reported to have less than tenth of the losses of the thinnest standard iron laminations in high frequency applications [77]. However, amorphous alloys such as Metglas are extremely difficulty to work with, not only because of their necessary thickness but also because of their inherent (and extreme) brittleness. It only has limited available shapes because it's nearly impossible to be stamped and laser cutting is problematic as well [83]. So 0.006'' Hiperco 50 laminations, which is used in the rotor stack, will also be used to make the stator stack in order to increase the torque density as well as to reduce the cost.

### *5.5.2 Dimension*

The basic stator dimension is determined according to the method in [44], particularly the stator and rotor pole arcs. The out diameter is calculated to be 30 mm so as to provide a winding area of 42 $mm^2$. A CAD model is shown in Figure 5.1 to verify that the proposed design has enough area to put 50 turns of Litz-wire inside.

The yoke thickness is reported to have a significant effect on the vibration behavior of the stator. Thicker yokes have higher natural frequencies [84]. Thus the yoke thickness is set to be 2 mm despite that 1 mm is thick enough to keep away from yoke saturation. The teeth are modeled as cantilevers that are attached to the stator core in [85]. So a wedge-

shaped teeth that is thicker in the junction and thinner in the tip is designed to increase the stability of the stator. Figure 5.1 shows the cross-section of the stator.

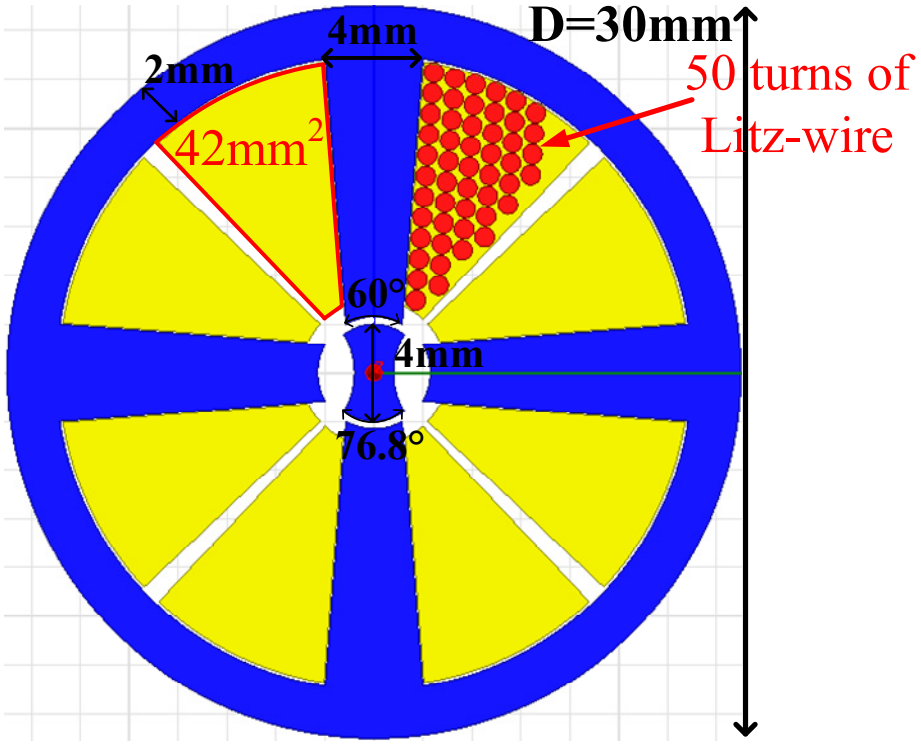


Figure 5.1 CAD model of the machine with 50 turns of Litz-wire.

## 5.6 Windage Torque Estimation

In ultra-high speed applications, air friction losses can be very significant since they are proportional to the third power of the rotational speed. This phenomenon is particularly prominent for SRMs because of the salient geometry of the rotor. However, due to the cylindrical design of the rotor geometry, the air friction losses are greatly reduced and so is the corresponding windage torque. In this thesis, the ultimate goal is to drive the rotor to as high speed as possible to reach beyond 1 million rpm. So no external load will be applied at the first stage and thus the windage torque will be the only load torque.

The general equation for air friction losses of a cylinder is:

$$P_{f,air} = c_f \pi \rho_{air} \omega^3 r^4 l \tag{5.1}$$

where $\rho_{air}$ is the density of the air, $\omega$ is the angular frequency, $r$ and $l$ are the radius and the length of the cylinder, respectively. The model of a cylinder encased in another cylinder is applied here for simplification despite that the four inner surfaces of the stator tooth tips are not actually connected with each other. This two-cylinder model itself is a very complex topic in aerodynamics and many different methods can be applied to calculate the loss. According to the method in [77], the air flow can be divided into three different situations: laminar Couette flow, laminar flow with Taylor vortices and turbulent flow, depending on the rotational speed and the corresponding Taylor number $Ta$ ($Ta$ <41.3, 41.3 < $Ta$ < 400 and $Ta$ > 400 for the three situations, respectively), which is defined as follows:

$$Ta = \frac{r\omega\delta}{\nu}\sqrt{\frac{\delta}{r}} \tag{5.2}$$

where $\nu$ is the kinematic viscosity of the air and $\delta$ is the air gap length.

For laminar Couette flow the friction coefficient $c_f$ can be calculated as follows:

$$c_f = \frac{1.8}{Re}\left(\frac{\delta}{r}\right)^{-0.25}\frac{(r+\delta)^2}{(r+\delta)^2 - r^2} \tag{5.3}$$

where $Re$ is the Reynolds number and can be determined as follows:

$$Re = \frac{r^2\omega}{\nu} \tag{5.4}$$

According to a different model in [39], the $c_f$ can be calculated as follows:

$$c_f = \begin{cases} 0.515\dfrac{(\dfrac{\delta}{r})^{0.3}}{Re^{0.5}}, & 500<Re<10^4 \\ 0.0325\dfrac{(\dfrac{\delta}{r})^{0.3}}{Re^{0.2}}, & Re>10^4 \end{cases} \tag{5.5}$$

From the above equations, at 1 million rpm, the corresponding *Ta* is calculated to be 1315. This means that the machine is already in the turbulent flow area, where the windage loss increases dramatically. Usually it is very difficult to calculate the windage loss in the turbulent flow area from analytical equations. This problem itself is a hot research topic in mechanical engineering. In order to make sure that the machine has the capability of generating enough torque to overcome the air drag when over 1 million rpm, the windage loss is estimated assuming the same relationship of the friction coefficient as in [77]. The final friction loss is estimated to be 38w at 1 million rpm and 64w at 1.2 million rpm. The corresponding friction torques are calculated to be 0.36 and 0.51 mN·m. Assuming a safety factor of two, the machine should be able to produce a maximum torque of 0.7 mN·m and 1 mN·m at 1 million and 1.2 million rpm, respectively. Although this assumption may not necessarily be true, it still gives us a good estimation of the windage losses of the proposed machine in turbulent flow area especially in the design stage.

## 5.7 Complete Design

The complete design parameters are shown in Table 5.2.

Table 5.2 Complete Design Parameters

| Stator | | Rotor | | Windings | | Electrical | |
|---|---|---|---|---|---|---|---|
| Outer diameter | 30 mm | Outer diameter | 4mm | Wire type | Litz | Rated power | 100~200 w |
| Stack length | 2 mm | Stack length | 2mm | Strand gauge | 42 | Rated speed | 1,000,000 rpm |
| Pole number | 4 | Pole number | 2 | Equivalent gauge | 24 | Rated torque | 0.7 mN·m |
| Stator pole arc angle | 60° | Rotor pole arc angle | 76.8° | Turns per pole | 50 | Max speed | 1,200,000 rpm |
| Material | Hiperco 50 | Material | Hiperco 50 | Filling factor | 0.25 | Max torque | 1 mN·m |
| Back iron thickness | 2 mm | Air gap | 0.3 mm | Max current | 3.5A | Supply voltage | 0~150V |

## 5.8 Chapter Summary

In this chapter a complete design of an ultra-high speed SRM for applications beyond 1 million rpm is proposed. Pole pair number, air gap selection, dimension calculation, material selection, winding selection and windage torque calculation are included in details. The proposed 4/2 SRM has an outer diameter of 30 mm. It has 50 turns of gauge 42/24 Litz-wire in each stator pole. The air gap is 0.3 mm. Both of the stator and rotor are made from 0.006'' Hiperco 50 laminations. The machine should be able to produce a maximum torque of 0.7 mN·m and 1 mN·m at 1 million and 1.2 million rpm, respectively in order to overcome the high windage torque. The proposed designed will be validated in the next chapter with finite element analysis.

# CHAPTER 6. ELECTRICAL MODELLING AND SIMULATION

## 6.1 Introduction

To estimate the electromagnetic performance of the proposed design. Different models are built. First, a finite element model (FEM) is built using the ANSYS/Maxwell software to estimate the output torque under single-pulse control. Then, a Maxwell/Simplorer co-simulation model is built to realize the hysteresis current control model. Finally, in order to get a faster simulation model of the proposed design, a Simulink equivalent model is built based on a lookup table extracted from the flux/torque curve generated by the FEM.

## 6.2 2D Finite Element Modelling

### *6.2.1 Model Description*

In order to verify the electromagnetic performance of the proposed design, especially the output torque, a 2D FEM is built as shown in Figure 5.1. Two cases of 1 million and 1.2 million rpm steady state simulations were performed. The supply DC voltage is set to be 90 and 120 volts, respectively. The one-pulse control is used to drive the motor at ultra-high speeds. The external drive circuit is shown in Figure 6.1. The turn-on and turn-off angles are set to be 0° and 60° for both cases.

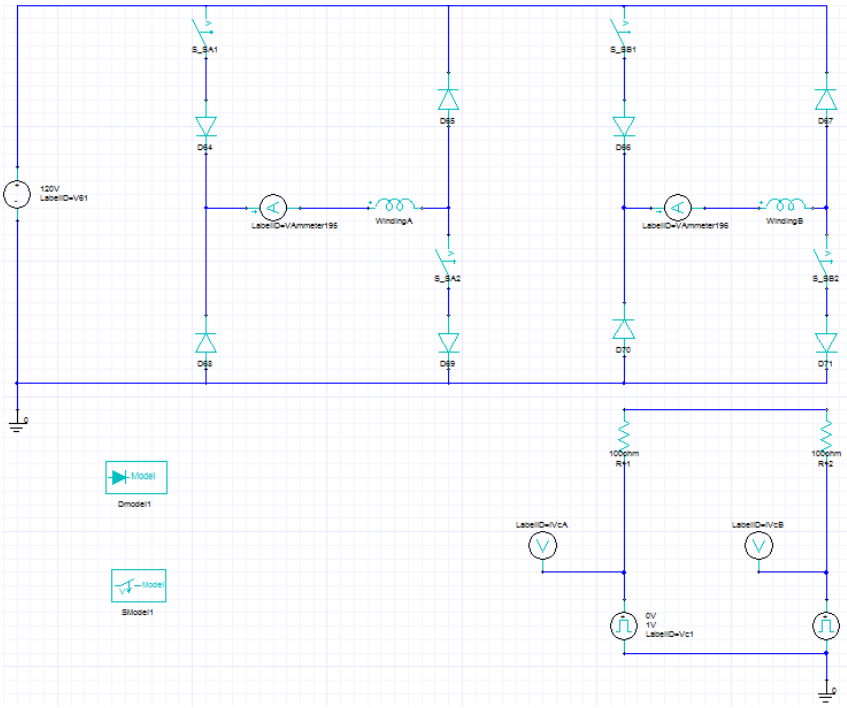


Figure 6.1 External drive circuit.

### *6.2.2 Simulation Results*

Figure 6.2 shows the flux density at the peak current position of 60°. The average flux density in the active stator teeth is about 1.4 T, while the average flux density in the rotor is about 2 T. The highest value is located at the corner of the stator, which is around 2.4 T.

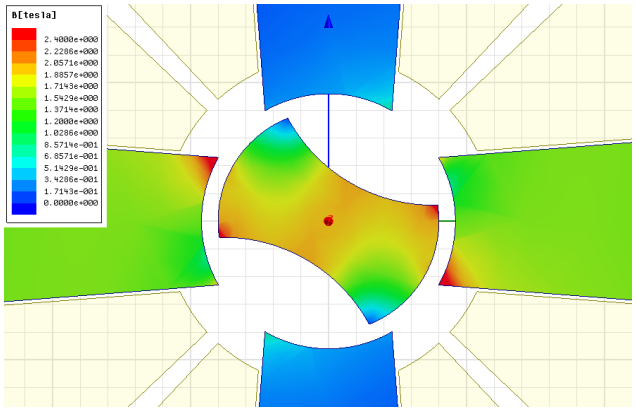


Figure 6.2 Flux density at the position of the maximum value.

Figure 6.3 to Figure 6.6 show the torque and current profile of the simulation results under the two different speeds. The average torque is about 0.7 mN·m and 1 mN·m respectively, which satisfies the design requirement. The RMS current is 3.5 A and 4 A and at 1 million rpm and 1.2 million rpm respectively, which is a little higher than the maximum value at 1.2 million rpm. So additional cooling may need to be added.

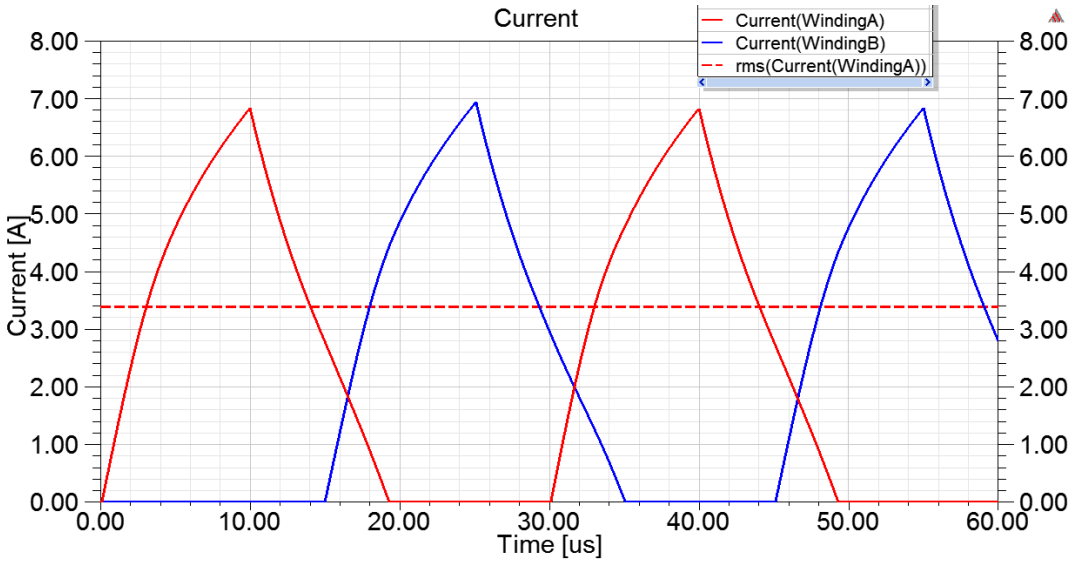


Figure 6.3 Current profile at 1 million rpm.

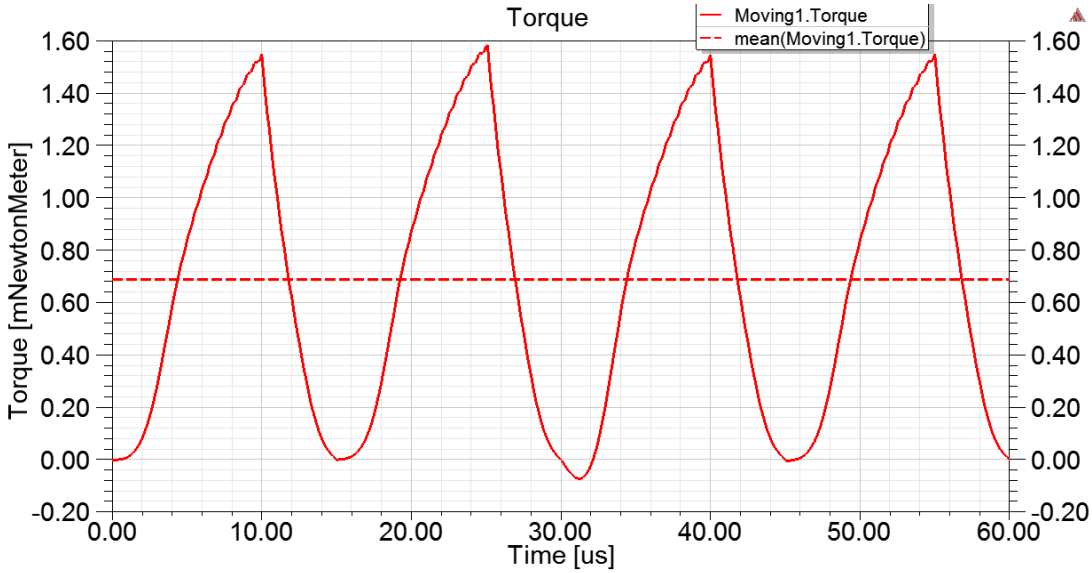


Figure 6.4 Torque profile at 1 million rpm.

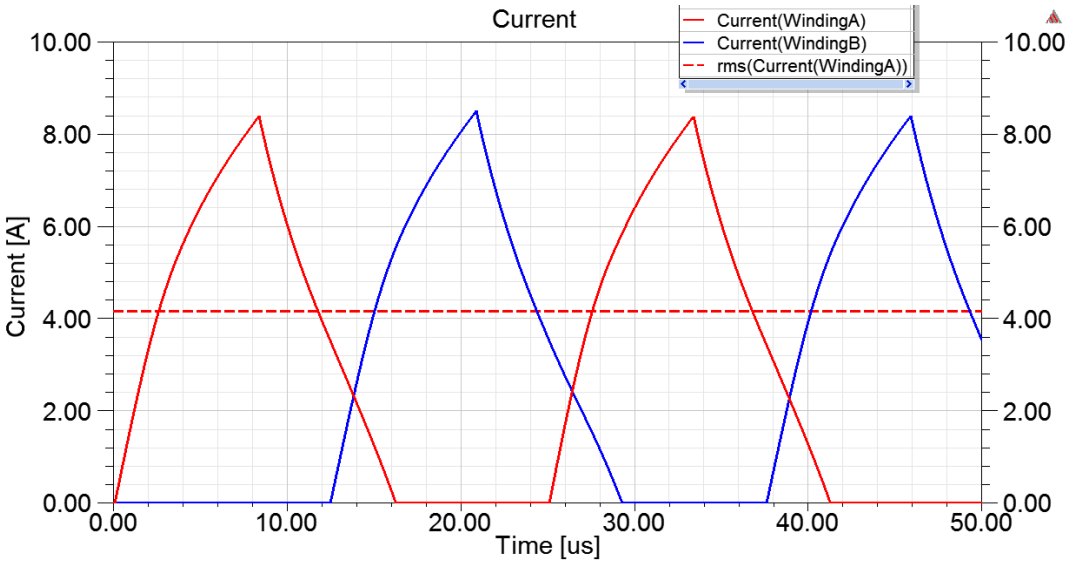


Figure 6.5 Current profile at 1.2 million rpm.

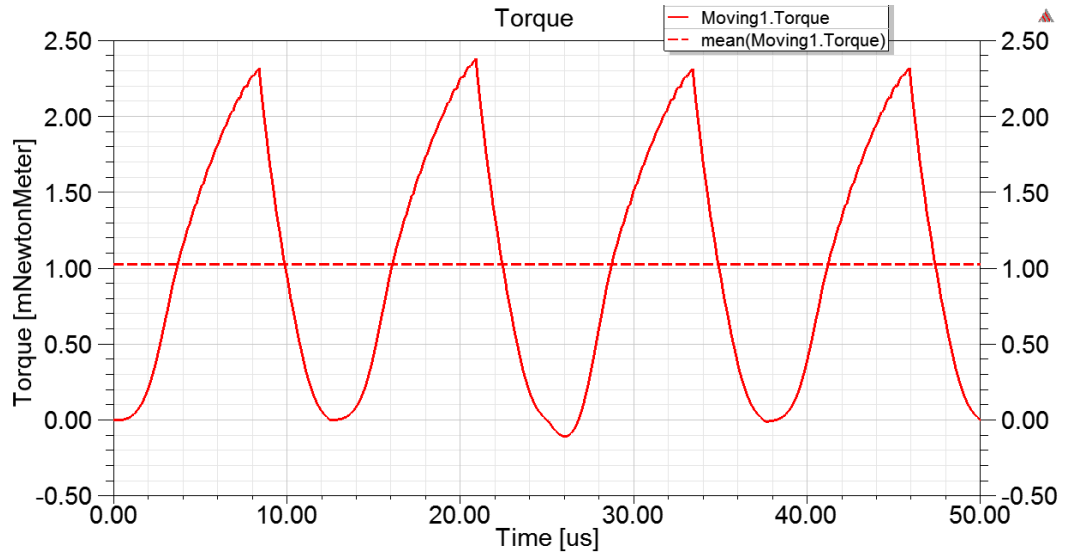


Figure 6.6 Torque profile at 1.2 million rpm.

## 6.3 Maxwell/Simplorer Co-Simulation Model

In order to achieve the hysteresis current control, a Maxwell/Simplorer co-simulation model is built. The FEM is embedded in a Simplorer circuit model. Figure 6.7 shows the simulation diagram. For each time step, the 2D FEM in Maxwell will run first according to the external excitation in order to get the equivalent model of the machine. Then the

drive circuit will run with the equivalent circuit of the machine in Simplorer. The results are compared with the Simulink model in Section 6.4.

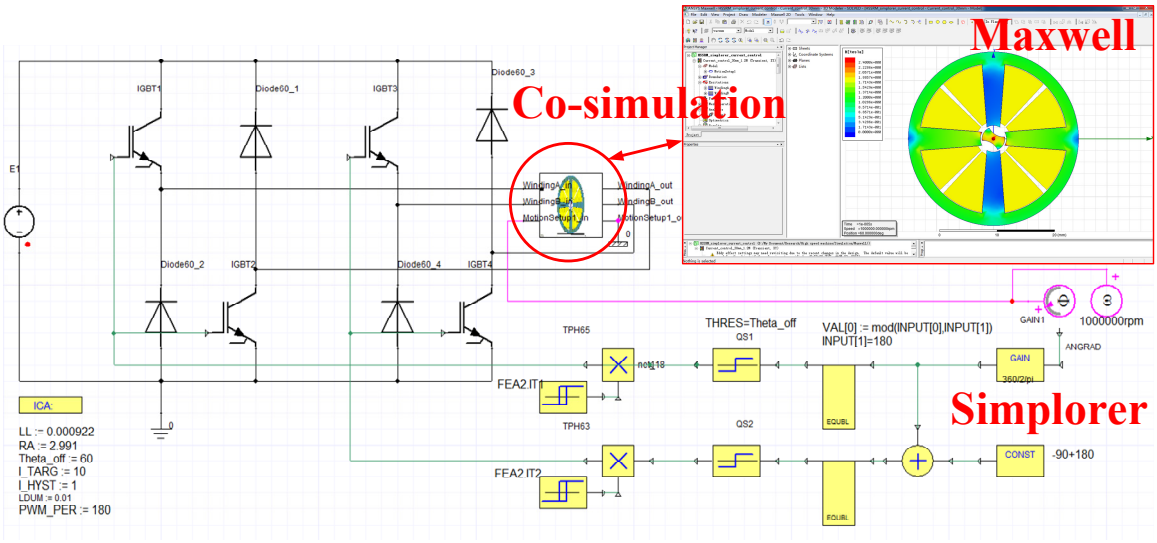


Figure 6.7 Simulation diagram.

## 6.4 Fast Equivalent Model in Simulink

### *6.4.1 Equivalent model using lookup tables*

The above two FEMs are good in terms of accuracy. However, they are too slow for optimization or closed loop control simulation. So, an equivalent model with a much higher speed was built in Simulink based on the magnetization and torque curves extracted from the FEA model [86]. The main idea is to get a search table by sweeping the excitation current and get the flux/torque against the rotor position from 0° to half of the cycle. A linear interpolation is used when an intermediate point is needed [48]. Figure 6.8 and Figure 6.9 show the flux curves and torque curves against the rotor positions from 0 to 90° with the sweep of current from 0 to 10A, with a step of 0.2A.

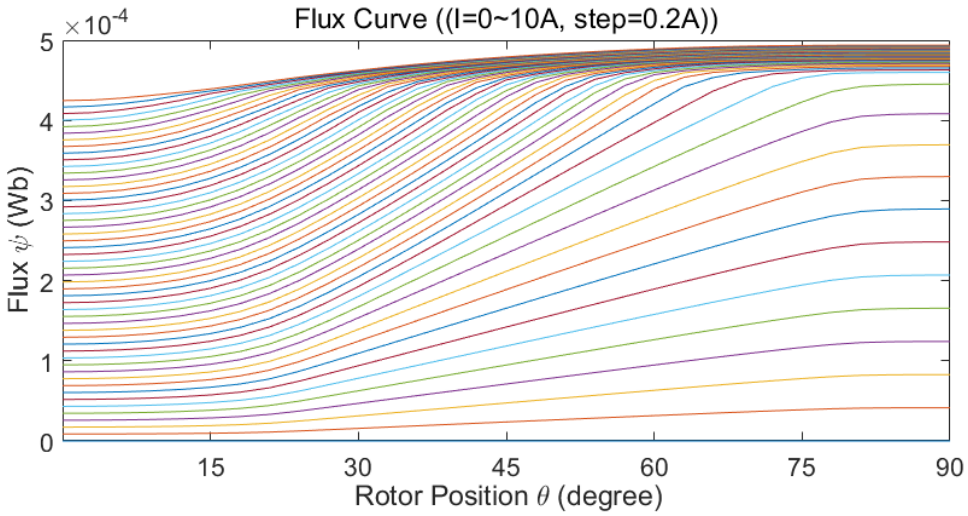


Figure 6.8 Flux against rotor position

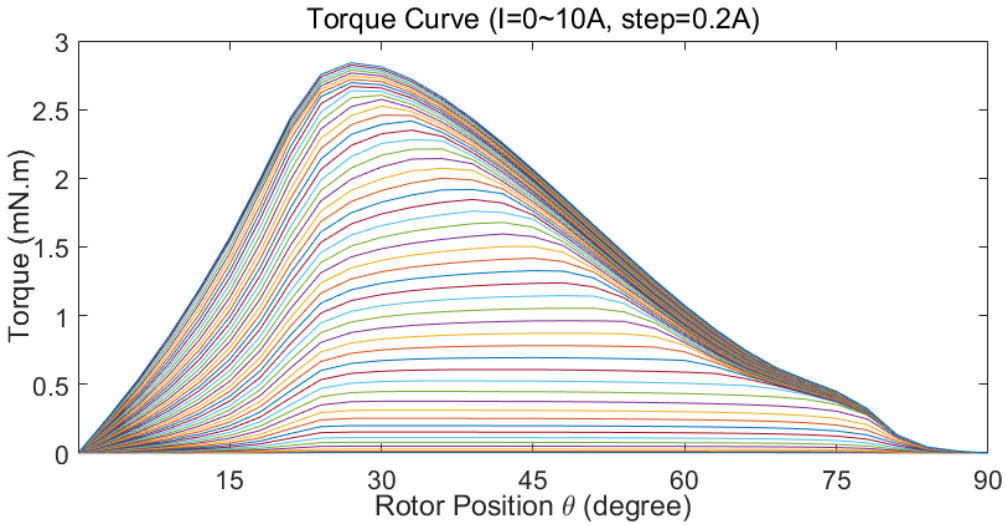


Figure 6.9 Torque against rotor position

### *6.4.2 Hysteresis Current Control for Steady State Simulation*

Then, a closed loop hysteresis current control model is built using Simulink. Figure 6.10 shows the model. There are two closed loops: a speed control outer loop and a current control inner loop.

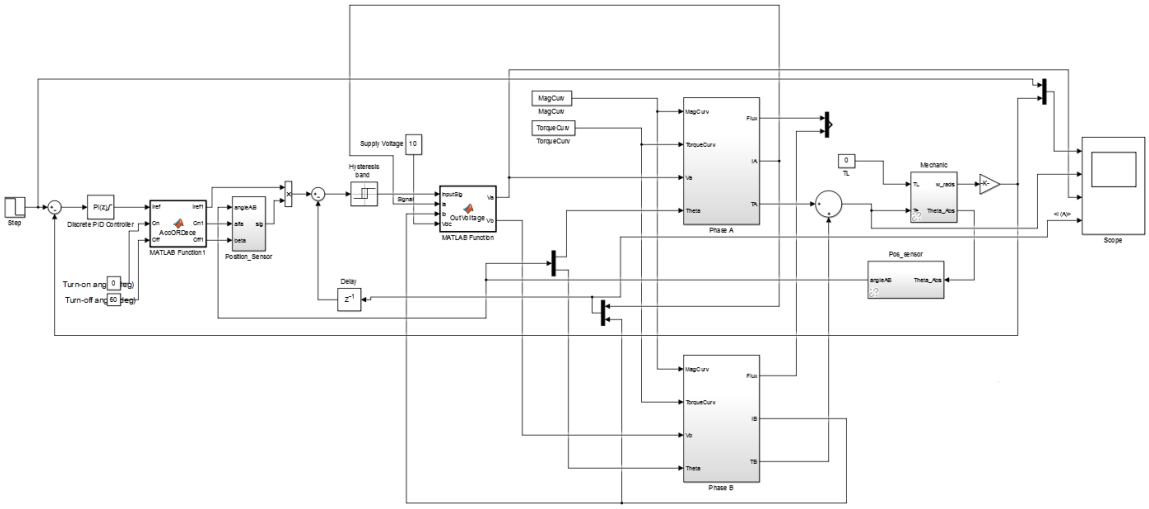


Figure 6.10 Closed loop hysteresis current control model in Simulink

The inner loop is a current hysteresis control. The stator currents are measured and compared with the reference current. If the measured current is larger than the reference current, the corresponding switches are turned off and the current will decrease. When the current is lower than the reference value, the switches will be turned on and the current increases again. This implies that the currents are controlled within a certain band of the reference value. The comparisons of the current and torque curves between the Maxwell model and the equivalent Simulink model of the proposed machine are shown in Figure 6.11 and Figure 6.12, respectively. The current is maintained at 4.5 A with a $\Delta i$ of 1 A. As can be seen, the Simulink model matches the FEM well. It should be noted that the Maxwell model takes 20 minutes to solve while the Simulink model only takes less than 1 second.

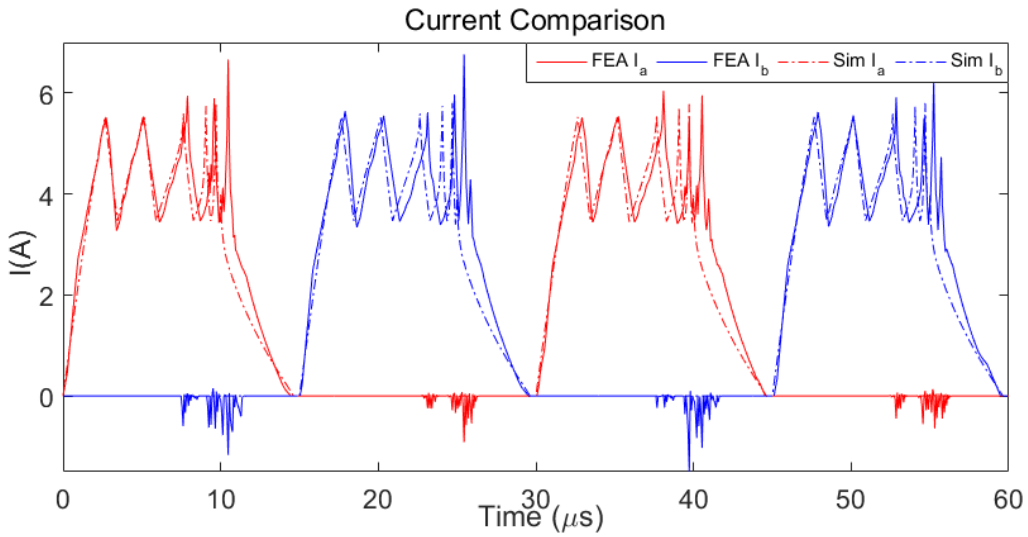


Figure 6.11 Comparison of current curves between Simplorer and Simulink model.

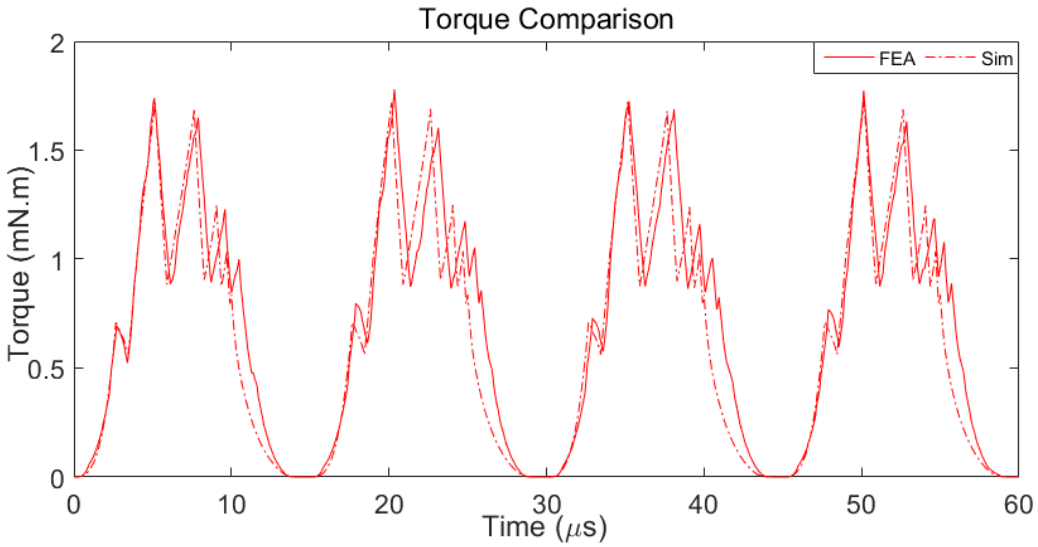


Figure 6.12 Comparison of torque curves between Simplorer and Simulink model.

### *6.4.3 Speed Feedback Control for Dynamic Simulation*

The outer loop is a speed control. The measured speed is compared with the reference speed and the difference goes through a PI controller and a limiter. The output is the reference current that controls the current value. With the speed control loop, the dynamic performance of the machine can be simulated. Figure 6.13 to Figure 6.16 shows the

simulation results of the speed, torque, DC voltage and phase currents. At time zero, the SRM starts from standstill and gradually speeds up to the reference speed of 10,000 rpm. At 0.05s the SRM follows the reference speed and slows down to 5,000 rpm. The speed up process corresponds to a positive torque and the slow down process corresponds to a negative torque. The DC supply voltage changes rapidly between ±10 V in order to maintain the phase current within the ±1 A range of the reference current of 2 A.

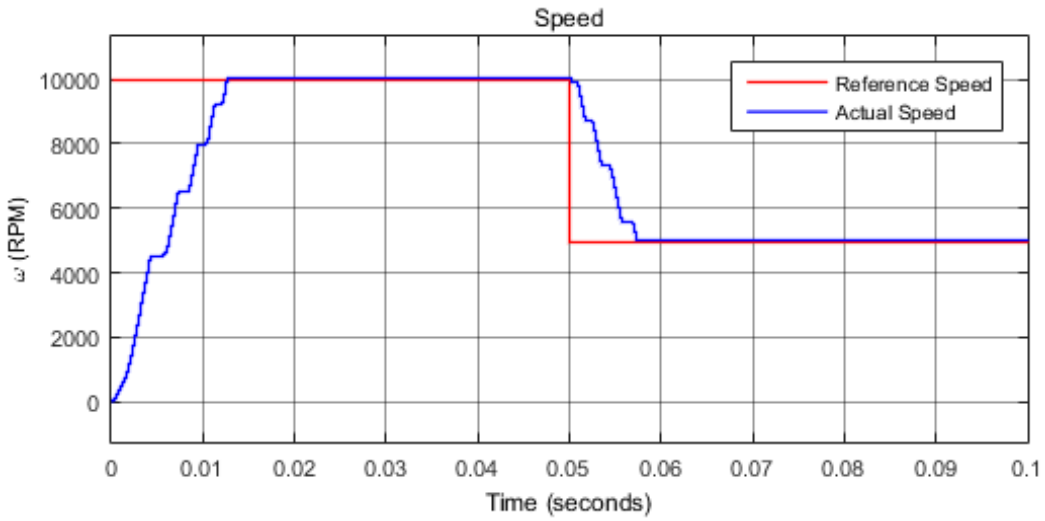


Figure 6.13 Reference speed and real speed profile.

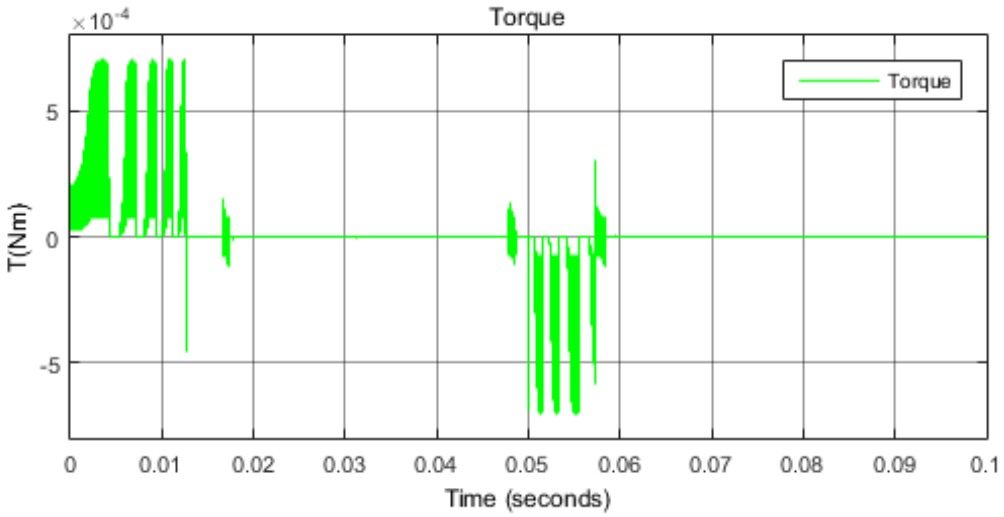


Figure 6.14 Output torque profile.

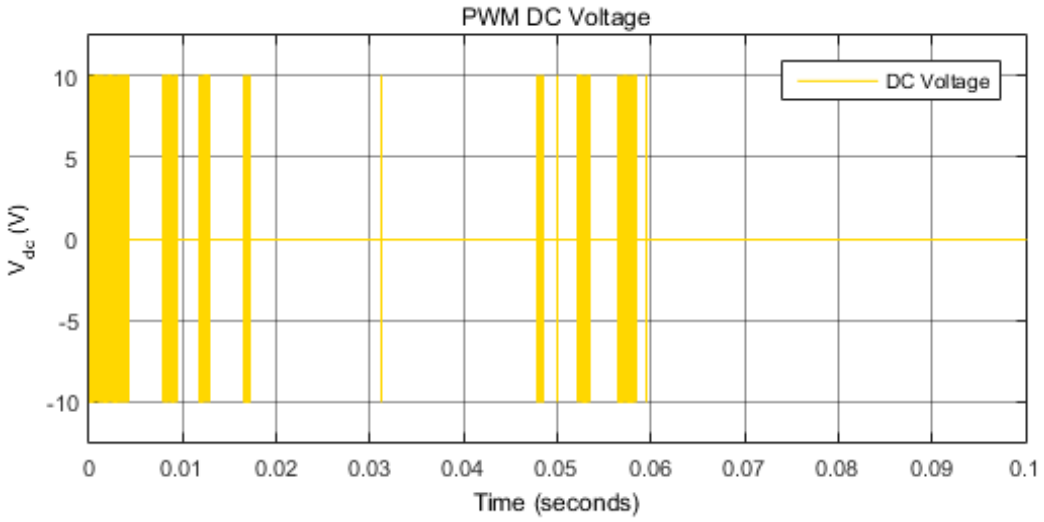


Figure 6.15 DC supply voltage profile.

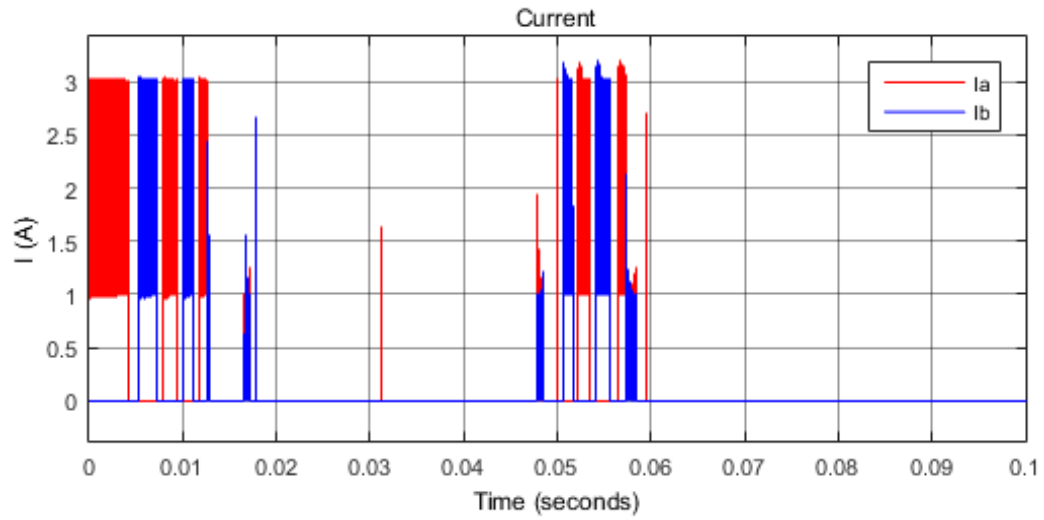


Figure 6.16 Phase current profile.

## 6.5 Chapter Summary

In this chapter, different models of the proposed UHSSRM are built. First, a FEM is built using the ANSYS/Maxwell software to estimate the output torque under single-pulse control. Then, a Maxwell/Simplorer co-simulation model is built to realize the hysteresis current control model. Finally, in order to get a faster simulation model of the proposed design, a Simulink equivalent model with the speed and current feedback control is built

based on lookup table extracted from the flux/torque curve generated by the FEM. The Simulink model can achieve much faster simulation while remains a high accuracy.

# CHAPTER 7. CONSTANT V/F CONTROL FOR UHSSRM

## 7.1 Introduction

For UHSSRMs, the traditional hysteresis control strategy is not suitable due to the following reasons. First, for ultra-high speeds over 500,000 rpm, the fundamental frequency is in the order of 10 kHz. If the hysteresis current control is applied, the switching frequency will be at least an order of magnitude higher than the fundamental frequency, which is about 100 kHz [87]. Such a high frequency requires a very high current control loop bandwidth, which makes the system difficult to be realized. Second, at such high switching frequencies with hysteresis current control, the iron and copper losses will be significant, which will result in thermal problems considering the small volume of typical ultra-high speed electric machines. Third, it is difficult to determine the value of the supply voltage. If the voltage is too low, the current will not have enough time to increase to a desired value because of the very high speeds. If the voltage is too high, the current will increase rapidly into the saturation region, in which case hysteresis control must be applied. Even if a suitable value of the supply voltage at a high speed is chosen, it is obviously not suitable for other speeds in the lower speed region because of the higher switching frequency.

In this chapter, a constant volts per hertz ($V/f$) control over the entire speed range for ultra-high speed SRMs is proposed [88]. The main idea is to reduce the switching frequency to a minimum value over the entire speed range by controlling the supply voltage over the rotational speed to be a constant value and fixing the switching on and off angles before the machine goes into saturation. The current shape during one cycle is discussed in

detail below. To validate the proposed control, an equivalent Simulink model based on a finite element analysis (FEA) model has been built. The results show that the proposed control can reach a one pulse curve per stroke over the entire speed range.

## 7.2 Analysis of the Current Profile

Before the control is proposed, we need to do a detailed analysis of the current profile of one phase with a constant supply voltage.

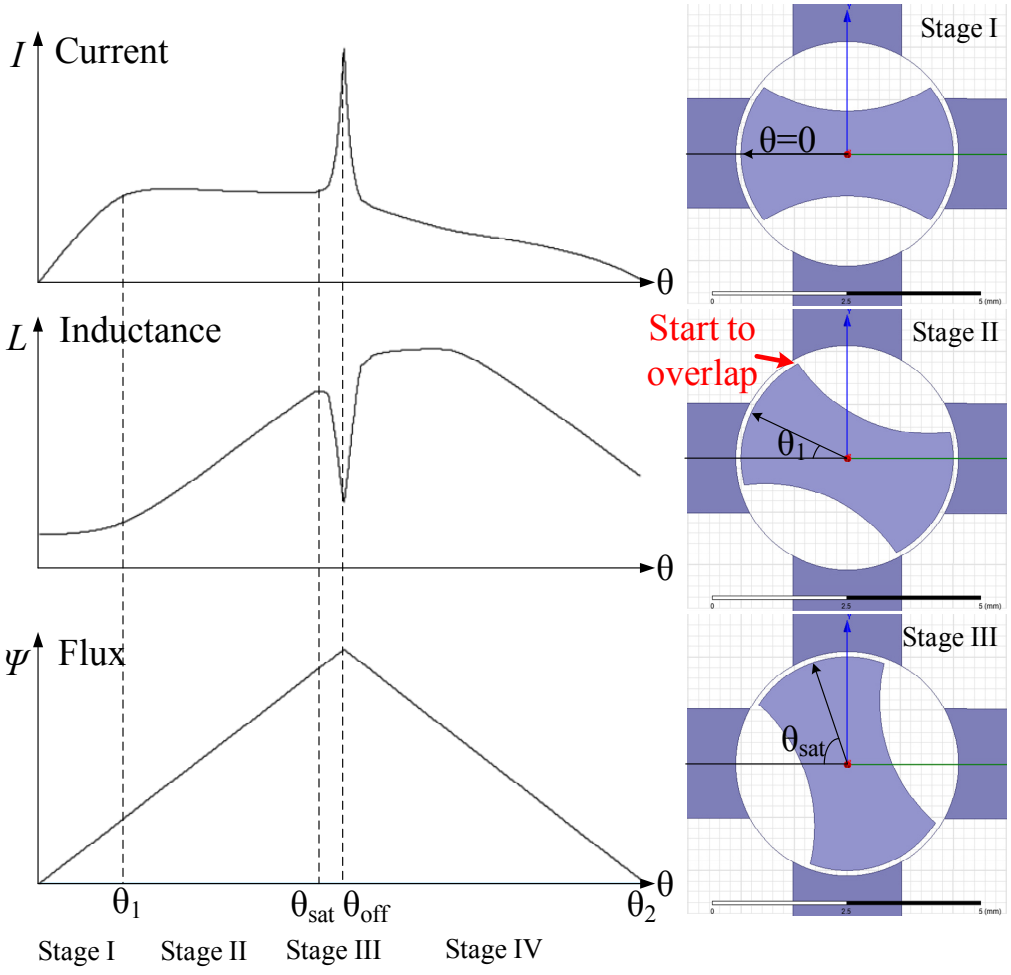


Figure 7.1 Typical profile of current, inductance and flux considering saturation.

Figure 7.1 shows a typical profile of the current, inductance and flux of one phase of a 4/2 SRM, considering saturation. The 4/2 machine has been chosen here because it is the typical choice for ultra-high speed SRMs [44]. The equivalent equation of an SRM is as follows:

$$V = iR + \frac{\partial \psi(\theta, i)}{\partial t} \tag{7.1}$$

If we ignore $iR$, we have

$$V = \frac{\partial \psi(\theta, i)}{\partial i} \cdot \frac{di}{dt} + \frac{\partial \psi(\theta, i)}{\partial \theta} \cdot \frac{d\theta}{dt} \tag{7.2}$$

$$V = L \cdot \frac{di}{d\theta} \cdot \omega + i \frac{\partial L}{\partial \theta} \cdot \omega \tag{7.3}$$

where the first term on the right-hand side of the equations is the inductance term and the second term is the back electromotive force (EMF). The steady state current profile can be divided into four stages according to the status of the inductance:

### *7.2.1 Stage I: Low inductance stage (0, $\theta_1$).*

The current profile starts from the unaligned position ($\theta$=0). From (0,$\theta_1$), $L$ is very small and almost does not change since it is near the unaligned position. So, we have d$L$/d$\theta$≈0. Thus, the back EMF term can be ignored and we have

$$V \approx L \cdot \frac{di}{d\theta} \cdot \omega \tag{7.4}$$

Because of the small $L$, for a constant voltage the rate of d$i$/d$\theta$ is large and the current increases rapidly.

### *7.2.2 Stage II: Inductance increasing stage ($\theta_1$, $\theta_{sat}$).*

From the position where the rotor edge starts to overlap with the stator edge (shown red in Figure 7.1), the inductance starts to increase, which means d$L$/d$\theta$ becomes positive and gradually increases to a certain value. This makes the back EMF term increase and it gradually becomes a major element. As a result, the inductance term (the first term on the right-hand side in (7.3)) has to decrease according to (7.3). Since $L$ is increasing, the d$i$/d$\theta$ has to decrease [89]. There will be three different shapes of current, depending on whether the value of the back EMF is equal, less or greater than the supply voltage according to (7.5).

$$L \cdot \frac{di}{d\theta} \cdot \omega = V - i\frac{\partial L}{\partial \theta} \cdot \omega \tag{7.5}$$

7.2.2.1 $i\frac{\partial L}{\partial \theta} \cdot \omega = V$

The back EMF is almost the same as the supply voltage. So, d$i$/d$\theta$ is equal to 0 and the current flattens out. Figure 7.1 is just this case.

7.2.2.2 $i\frac{\partial L}{\partial \theta} \cdot \omega < V$

The back EMF is less than the supply voltage. So d$i$/d$\theta$ is still positive, but with a smaller value than in Stage I. This means the current is still increasing, but at a slower rate. As the current increases, the back EMF also increases (because d$L$/d$\theta$ and $\omega$ remain the same), resulting in the right-hand side of (7.5) decreasing. Since $L$ is increasing and $\omega$ does not change, the d$i$/d$\theta$ has to decrease further. This will gradually reach a balancing point that is similar to case a (d$i$/d$\theta$=0). In fact, case a does not happen exactly as considered, because the back EMF cannot be exactly the same as the supply voltage. Actually, case a is a special case of case b, but with an "instant transient time". Figure 7.2 (a) shows the typical shape of this case with longer "transient time".

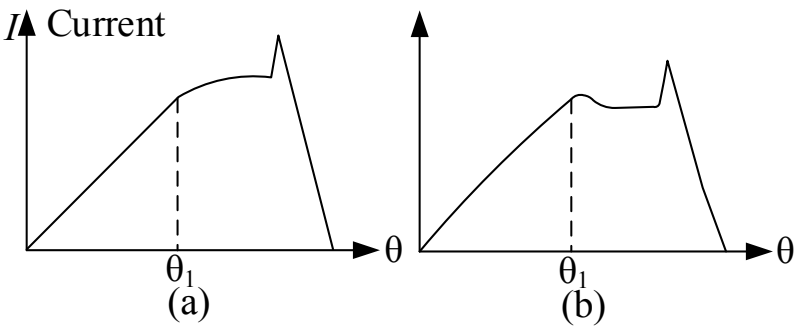


Figure 7.2 Typical current profiles of case b and c.

7.2.2.3 $i\frac{\partial L}{\partial \theta}\cdot\omega > V$

The back EMF is greater than the supply voltage. So d$i$/d$\theta$ changes from positive to negative according to (7.5), which forms a peak in the current profile [90]. As the current decreases, the back EMF becomes smaller, resulting in the right-hand side of (7.5) becoming larger. Note that the right-hand side of (7.5) is a negative number, which means it becomes "less negative". Let's take a look at the left-hand side of (7.5). The inductance $L$ is always positive and increasing in stage II. The d$i$/d$\theta$ is a negative number. So, as the right-hand side of the equation becomes larger (less negative), with the increasing positive $L$, the d$i$/d$\theta$ also has to be less negative, which means the current will also gradually flatten. This can be better understood if we take the absolute value of both sides of (7.5).

$$L\cdot\left|\frac{di}{d\theta}\right|\cdot\omega=\left|V-i\frac{\partial L}{\partial\theta}\cdot\omega\right| \tag{7.6}$$

As the right hand side of (7.5) becomes larger, the right hand side of (7.6) becomes smaller. With increasing $L$ and constant ω, the absolute value of d$i$/d$\theta$ must decrease, which means the changing rate (slope) of the current becomes closer to zero. Fig 2 (b) shows the typical shape of this case.

### *7.2.3 Stage III: Saturation stage ($\theta_{sat}$, $\theta_{off}$)*

As the positive voltage is being applied, the flux increases. At $\theta_{sat}$ the machine goes into the saturation region. From (7.1), we know that the increasing rate of the flux is almost the same as the supply voltage. In order to maintain the same increasing rate of flux (assuming the supply voltage is a constant during a stroke), the magnetic field intensity, $H$, or, in other words, the current, has to increase dramatically because of the saturation of the material. Since the flux is equal to the inductance times the current, the inductance has to decrease dramatically.

### *7.2.4 Stage IV: Freewheel stage ($\theta_{off}$ to $\theta_2$)*

When the switch is turned off, the current will go to zero. The decreasing rate of the current profile dependents on the drive configuration.

## 7.3 Constant Volts per Herts Control

Based on the aforementioned analysis, let's see what would happen if we keep the supply voltage divided by the rotational speed at a constant value. Current profiles can be divided into different stages as before depending on the state of the current.

### *7.3.1 Stage I: Current increasing stage (0, $\theta_1$)*

The inductance $L$ is very small because we are now near the unaligned position. Since all currents start from 0 for all different speeds, the inductance can be assumed to be almost the same for different speeds. So from (7.4), we have

$$\frac{di}{d\theta} \approx \frac{V}{\omega} \cdot \frac{1}{L} \tag{7.7}$$

If we keep $V/\omega$ constant, current will increase linearly. Because $\theta_1$ is determined only by the relative position of the rotor and stator poles, which is a constant for each individual machine, the end current $I(\theta_1)$ is also a constant for different speeds.

### *7.3.2 Stage II: Current constant stage (θ1, θsat)*

Since the three cases of current profiles in Stage II will eventually become flat, we can assume a short "transient time." The current in this stage is a constant directly from $\theta_1$ (case a). So, the flux is only a function of the inductance.

Let's consider the saturation position of $\theta_{sat}$. For a certain magnetic material, the saturation value of the flux density $B$ does not change. From (7.1), the flux can be written as

$$B \cdot S = \psi = \int V dt = \int V d(\theta / \omega) = \int \frac{V}{\omega} d\theta \tag{7.8}$$

So, if we remain at a constant $V/\omega$, the saturation position $\theta_{sat}$ will be a constant value over the entire speed range, which depends on the material and the geometry of the machine.

Although the voltage changes with speed, we can assume in one stroke the speed does not change, and thus the voltage remains at a constant value. So, the flux increases linearly with the rotor position and we have (7.9) from (7.1) (ignoring $iR$ term).

$$V = \frac{\partial \psi(\theta)}{\partial \theta} \cdot \omega = \frac{\psi(\theta_{off}) - \psi(\theta_1)}{\theta_{off} - \theta_1} \cdot \omega \tag{7.9}$$

Solve for $\psi(\theta_{off})$, we have (7.10)

$$\psi(\theta_{off}) = \frac{V}{\omega} \cdot (\theta_{off} - \theta_1) + L(\theta_1) \cdot i(\theta_1) \tag{7.10}$$

With $V/\omega$ being constant, and $L(\theta_1)\&i(\theta_1)$ not changing over the entire speed range as previously explained, we can control the final switching off flux to be the same value at different speeds by fixing the turn off angle with a certain value that is a little smaller than $\theta_{sat}$, so that we are close but not crossing into the saturation region ($\psi(\theta_{off})<\psi(\theta_{sat})$) so as to fully use the material and avoid the current becoming too high.

### *7.3.3 Stage III: Skipped*

With the same $\theta_{off}<\theta_{sat}$, the machine will not go into the saturation region. So, this *stage is skipped and we directly go into the freewheel stage.*

### *7.3.4 Stage IV: Freewheel stage ($\theta_{off}$ to $\theta_2$)*

With the same switching off angle and the assumption that the current flattens quickly in Stage II, $I(\theta_{off})$ is also about the same value at different speeds. So, the decreasing curve will also be similar among different speeds.

In conclusion, with constant volts per hertz, we will get a very similar shape of the current profile over the entire speed range if the switching off angle is fixed to be a constant value that is a little smaller than the saturation position $\theta_{sat}$. To be more specific, the current curve will have the same increasing rate and the end current $I(\theta_1)$ as in Stage I, a similar curve that flattens gradually in stage II, and a similar decreasing curve in stage IV. The benefit of this is that we can reach one switch per stroke over the entire speed range. This will reduce the switching frequency and consequent switching losses to a minimum value at both low and high speeds.

When the machine is starting, the speed is near zero, and thus the supply voltage is very small. In such cases the *iR* term can no longer be ignored. So, in the very low speed region near starting, the traditional hysteresis control will be applied as a backup solution. Figure 7.3 gives the control block diagram of the proposed constant volts per hertz control.

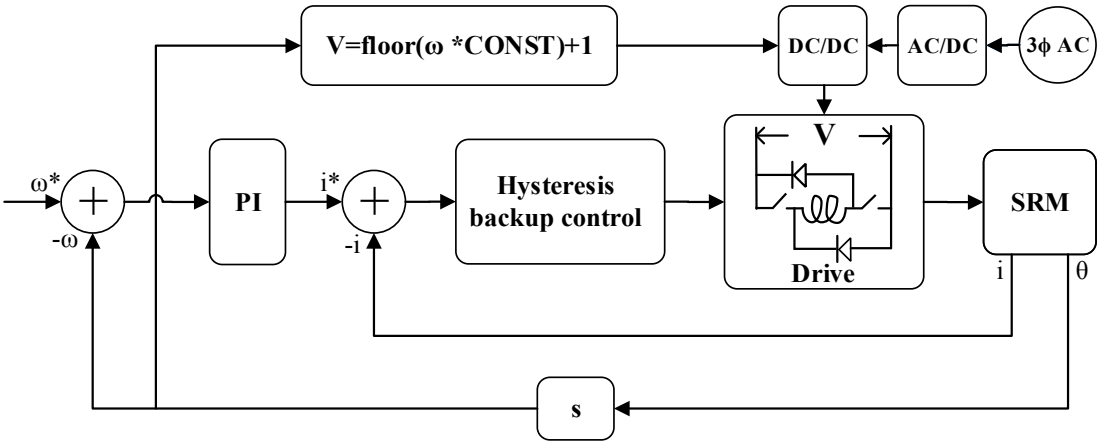


Figure 7.3 Block diagram of the proposed constant volts per hertz control.

From the block diagram, we can see that the DC supply voltage is generated from a DC/DC converter, which is connected to an AC/DC converter with a three phase source. To avoid changing the DC supply voltage too rapidly in each cycle, the voltage command is set to change by 1 volt per step as in (7.11).

$$V = floor(\omega \cdot CONST) + 1 \tag{7.11}$$

where CONST is the constant value of the supply DC voltage over rotational speed.

Note that the value of $\theta_{off}$ is dependent on this constant value of voltage over speed. Figure 7.4 shows the typical profiles of three different situations. For example, if this value is too high, the machine will go into saturation very quickly and the corresponding $\theta_{off}$ will

be very small (red curve). If this value is too low, the machine will never go into saturation, and $\theta_{off}$ should be the largest value that will not produce negative torque (blue curve).

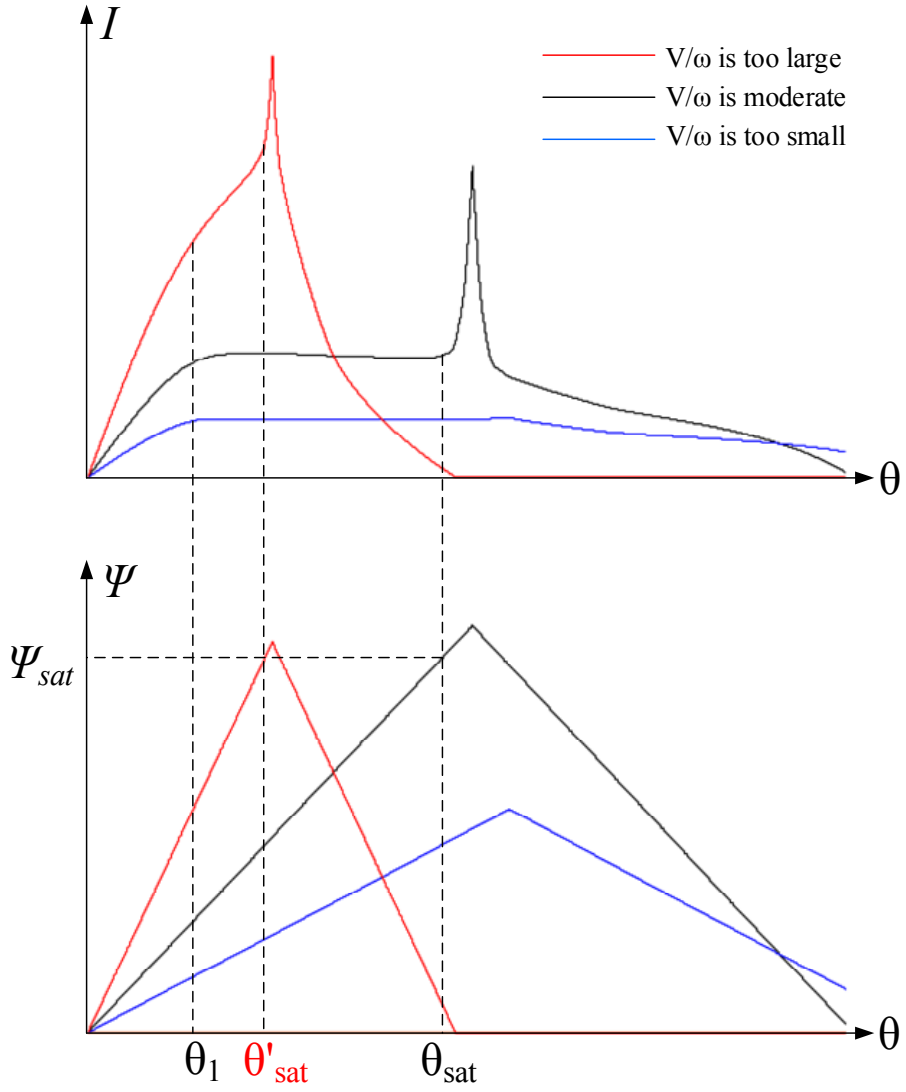


Figure 7.4 Typical profiles of the three situations.

## 7.4 Simulation Results

### *7.4.1 Validation of the Constant Volts/Hertz Control*

The fundamental and key point of the proposed constant volts per hertz control is that the current profile maintains a similar shape over the entire speed range. To validate this, a voltage over speed value of 40V over 1 million rpm was chosen and tested in the Simulink model. Figure 7.5 shows four current profiles at the speed of 1M, 500k, 250k and 100k rpm. The switching off angle was selected to be 60°. As shown by the figure, the four current profiles share a very similar shape.

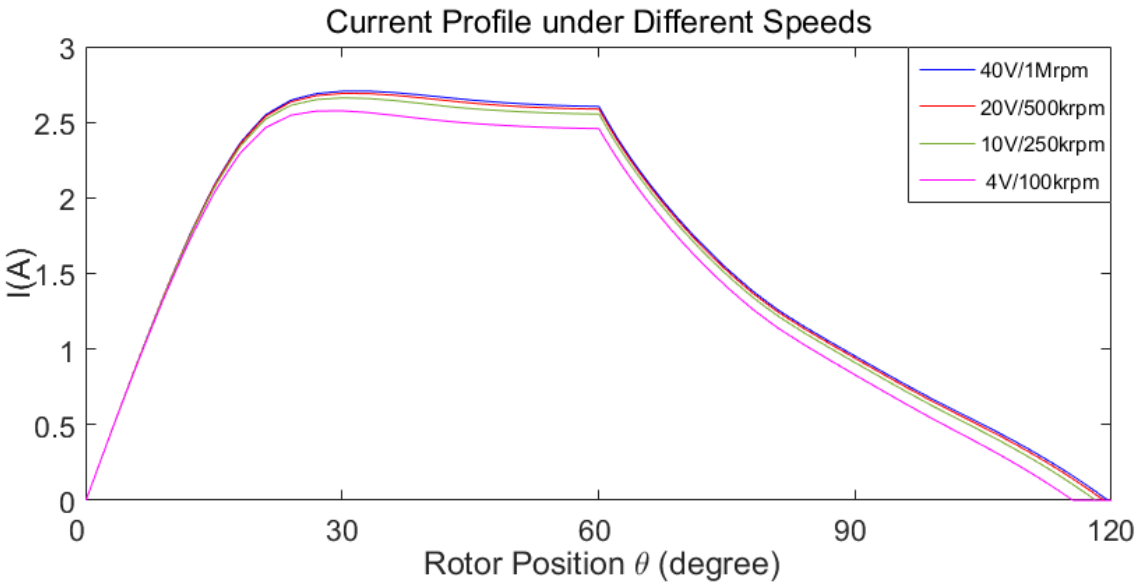


Figure 7.5 Current profile under different speeds.

The machine is run from standstill to 1 million rpm. Figure 7.6(a) shows the simulation results of the current, switching signal, torque, flux, applied voltage and speed. Figure 7.6(b) to (e) show the zoom-in plot of the current, switching signal and torque around t=0, 0.22, 0.4 and 0.6s respectively. As demonstrated by the figure, near standstill the hysteresis backup control was applied because at standstill only a voltage of 1V can be applied, instead of 0V (for $\omega$=0, $V$ is supposed to be 0). In a very low speed region, some of the assumptions do not hold (e.g. the $iR$ term can no longer be ignored). Figure 7.6(b)

shows the hysteresis backup control at very low speeds. After starting up, the current is controlled to only one pulse per stroke over the entire speed range. The current shapes are controlled to be almost the same over the entire speed range as analyzed in Chapter 7.3. Figure 7.6(c) to (e) show one switching per stroke shape after starting up.

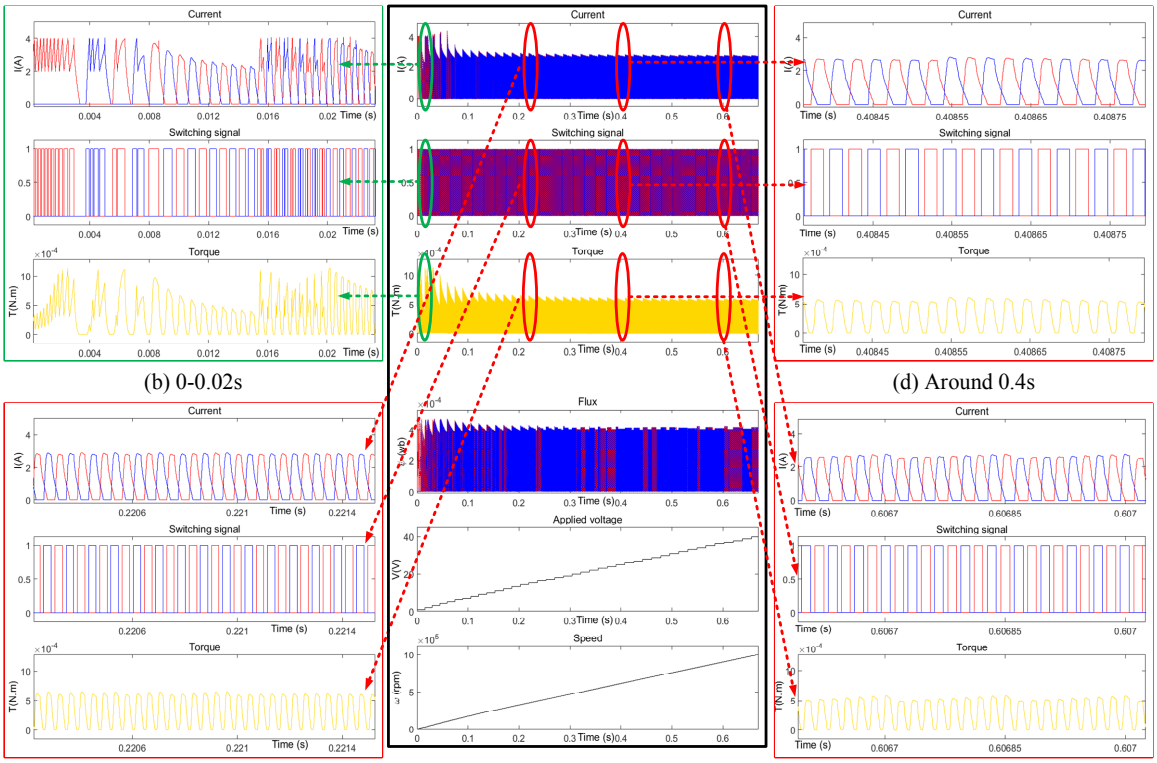


(b) 0-0.02s (d) Around 0.4s

(c) Around 0.22s (a) From 0 to 0.67s (e) Around 0.6s

Figure 7.6 Simulation results from 0 to 1 million rpm.

### *7.4.2 Find the Suitable Value of V/ω*

As is mentioned in Figure 7.4, different values of voltage over speed corresponds to different saturation positions. To find a suitable combination of $V/\omega$ and $\theta_{off}$, the following method can be applied.

From (7.1) we know that

$$V \approx \frac{d\psi(\theta,i)}{dt} = \frac{d\psi(\theta,i)}{d\theta}\omega \tag{7.12}$$

At a certain speed, if we implement the current sweep and calculate the value of d$\psi$/d$t$, we will find several voltage curves against the rotor position. Figure 7.7 shows the d$\psi$/d$t$ curves at 1 million rpm, with a current sweep from 0 to 10A with a step of 0.2A. In the middle part of the curve, we can see that it also has a flat shape because the change in current is flat in stage II if we apply a constant voltage. For example, the voltage of the constant current excitation of 2.6A drops at about 62° because the machine goes into saturation, and not enough current is supplied (highlighted in Figure 7.7). The curve flattens at about 40 V as is shown in the plot. With this information, we can infer that if a constant $V/\omega$ value of 40V/1 million rpm and a switching off angle of 60° is used to control the machine, the current will flatten around 2.6A, which corresponds to Figure 7.5. Note that this is not the only suitable combination for a control. Other combinations of constant $V/\omega$ and $\theta_{off}$ can also be applied according to Figure 7.7.

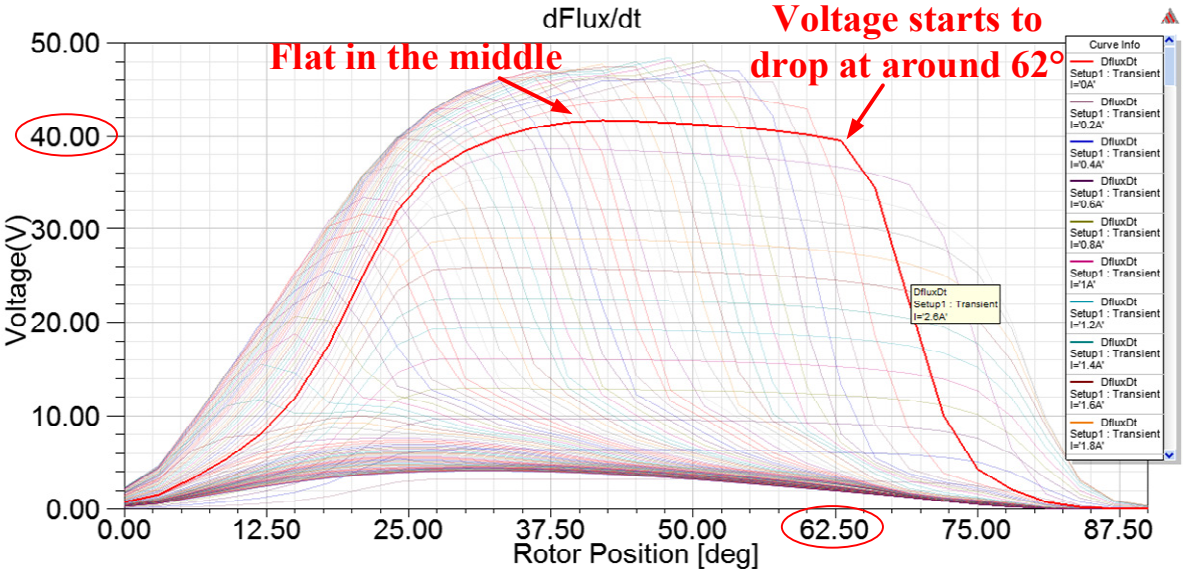


Figure 7.7 Curve of d$\psi$/d$t$ at 1 million rpm.

## 7.5 Chapter Summary

In this chapter, a constant volts per hertz control for ultra-high speed SRMs over an entire range of speeds from 0 to 1 million rpm is proposed, in order to reduce the switching losses. The main idea is to control the supply voltage over rotational speed to a constant value, and fix the switching on and off angles close but before the machine goes into saturation to reach one pulse per stroke over the entire speed range. A Simulink closed loop control model was built based on the FEA model to validate the proposed control. The results show that the switching frequency is decreased to a minimum value.

# CHAPTER 8. DIRECT POSITION CONTROL FOR UHSSRM

## 8.1 Introduction

Switched reluctance machines (SRMs) are famous for their low cost and robustness due to the lack of permanent magnets. They are very good candidates for working in high-temperature environments such as high speed turbine applications. High speed SRMs up to 60,000 rpm have been studied extensively in the literature [31, 44, 91-103]. One reason that SRMs cannot reach even higher speeds is the speed/position sensor [43]. Commercial rotary encoders are limited in speeds up to around 60,000 rpm due to their own internal mechanical considerations [104]. Other types of shaft-connected encoders, such as resolvers, suffer from the same problem, and custom designs are far too expensive. In order to break this mechanical limitation, either sensorless control or non-intrusive sensor-based control using Hall-effect, optical or inductive sensors have to be applied.

Table 8.1 gives a review of the sensor types used for different designs of high-speed SRMs reported in the literature. Most of the high-speed SRMs are below the maximum speed limit of commercial encoders. Only four ultra-high speed SRMs beyond 60,000 rpm were reported. Reference [32] uses the current gradient sensorless (CGS) method to control a 4/2 SRM up to 80,000 rpm. The reason for using CGS rather than other sensorless methods is that it is not computationally intensive and thus is suitable for high speed applications. However, the CGS scheme failed when the machine peak flux linkage became too large due to saturation effects, which prevented it from reaching the original target of 100,000 rpm. Reference [33] was aware of the sensor problem at the design stage and used a Hall sensor to control the motor by detecting the rotor pole saliency. However, the Hall

sensor has to be located as close as 1.5 mm to the rotor laminations, which means it cannot be applied to off-the-shelf machines. In addition, an asymmetry in detection was observed because of the asymmetrical removal of material from the rotor lamination stack for the purpose of rotor balancing, resulting in the need for some calibration in the control algorithm. Reference [34] used a different sensorless method proposed in [105] and achieved 110,000 rpm although the targeted speed was 200,000 rpm. Their method uses the resonant characteristic of the RLC circuit to detect the rotor position. To implement this method, a complicated external circuitry has to be built and the resonant frequency has to be selected carefully. Reference [106] reports a 6/4 SRM with experimental results at 150,000 rpm, which is the highest rotational speed of SRM that can be found in the literature. They uses a special rotational sensor (unclear type) that generates square waveform pulses with 4 times the frequency (50% duty cycle) of the shaft rotational speed, and the sensor output waveform is processed through a complicated hardware circuit and compared with the clock frequency of the FPGA to provide the exact rotational position for the control purpose. However, this method is far too complicated and computationally intensive for practical use. For even higher speeds, a simpler and faster method needs to be developed.

In this Chapter, a very simple and fast direct position sensing and control system for ultra-high speed SRMs based on low-cost non-intrusive reflective sensors is proposed [107]. The system uses reflective optical sensors to detect the relative rotor and stator positions. An analog trigger signal is generated directly from the optical sensors to control the switching-on and -off angles without any speed/position manipulations. The proposed method has many advantages such as versatility, virtually no speed limit, high simplicity

and low cost. In order to generate the maximum torque, a two-step switching angle optimization is conducted using the equivalent Simulink model based on the flux and torque lookup table extracted from the FEM of a 4/2 high speed SRM. Experiments succeed in driving the motor up to 100,000 rpm.

Table 8.1 Different Sensor Types for High-speed SRMs

| Max Speed (rpm) | Pole No. | Sensor Type | Ref | Max Speed (rpm) | Pole No. | Sensor Type | Ref |
|---|---|---|---|---|---|---|---|
| 20,000 | 6/4 | Sensorless | [91] | 50,000 | 6/4 | Resolver | [100] |
| 20,000 | 8/6 | Optical | [92] | 50,000 | 6/4 | Optical | [101] |
| 25,000 | 6/4 | Resolver | [93] | 50,000 | 4/2 | Optical | [44] |
| 30,000 | 8/6 | Sensorless | [94] | 52,000 | 6/4 | Resolver | [102] |
| 30,000 | 4/2 | Hall Effect | [95] | 60,000 | 4/2 | Unclear | [103] |
| 40,000 | 6/6 | Unclear | [96] | 80,000 | 4/2 | Sensorless | [32] |
| 48,000 | 4/2 | Unclear | [97] | 100,000 | 6/4 | Hall Effect | [33] |
| 50,000 | 6/4 | Resolver | [98] | 110,000 | 6/2 | Sensorless | [34] |
| 50,000 | 6/4 | Hall Effect | [99] | 150,000 | 6/4 | Unclear | [106] |

## 8.2 Limitation of Conventional Sensing Methods for UHSSRMs

### *8.2.1 Optical Encoder*

The working mechanism of the conventional optical rotary encoder is show in Figure 8.1. There are two or more optical detectors used in a rotary encoder. The light source is detected through a code disc, which is mounted on the shaft. The code disc is a transparent plastic disc with hundreds of nontransparent increments on it. When the shaft rotates, the

code disc also rotates, resulting in a series of square waves on each output signal. The speed and position of the rotor is calculated indirectly from the output wave in the digital signal processor (DSP). There is one trigger signal Z for each full rotation as a reference point on the disk.

The CPR (cycles per revolution) is defined as the number of increments on the disc. It determines the resolution and accuracy of the rotary encoder. The maximum speed is also related to this number. The lower the CPR is, the higher the maximum speed is. A typical combination is listed as follows [104]: a. CPR=1250, max rpm=14400, b. CPR=100, max rpm=60000. The absolute maximum speed is limited to a certain value due to the mechanical instability of the code disc [104]. Reference [108] proposes an interesting way of using gray gradation to control the applied voltage in order to reduce the cost of the machine, but it cannot be applied to ultra-high speed SRMs due to the mechanical limitations.

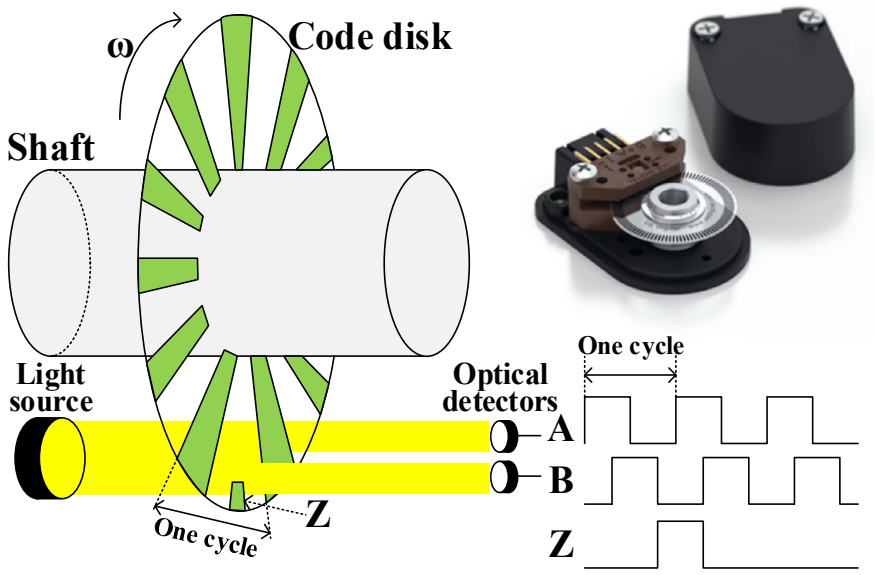


Figure 8.1 Working mechanism and typical appearance of conventional rotary encoders.

### *8.2.2 Hall-Effect Sensor*

Hall-effect sensors are also used in some high speed SRMs [33, 95, 99]. Due to the lack of permanent magnets in the rotor, either the Hall sensor has to be located very close to the rotor [33], or an encoder with magnets has to be attached to the shaft [95, 99]. The problem with the first solution is that the sensor (or sensing coil) has to be taken into consideration at the design stage and is placed too close to the rotor inside the machine. Thus, it is not possible to apply the method to off-the-shelf machines without opening them. The second solution of using an encoder with magnets suffers from the same mechanical limitations as the optical encoders.

### *8.2.3 Resolver*

A resolver is a rotary transformer used for measuring the degrees of rotation [109]. It acts like a small electric motor. The rotor of the resolver is attached on the shaft to be sensed with windings and a stator surrounding it. The resolver generates the position signals to the resolver-to-digital converter (RDC) circuit. Resolvers have been successfully applied to high speed SRMs in the literature [93, 98, 100, 102]. There are different kinds of induction methods used in resolvers. Each method requires a different kind of rotor to be attached on the shaft, such as externally-excited rotors, PM rotors, and variable reluctance rotors, all of which are similar to synchronous, PM and reluctance motors. The advantage of using resolvers is that they are better suited for harsh applications such as high temperature and high vibration. The disadvantage of using resolvers is that the conversion rate of the resolver-to-digital converter limits a resolver's maximum speed because the output signal is analog [110]. In addition, a much heavier rotor than the code

disc, which is made from iron, has to be attached to shaft. This results in the same mechanical limitations as the optical encoders.

### *8.2.4 Sensorless Control*

Sensorless control of SRMs has always been a hot topic. Reference [111] gives a good review of the sensorless control methods of SRMs in the literature. They can be broadly classified into: 1) hardware-intensive methods, 2) data-intensive methods, and 3) model-based methods that require a very fast microprocessor. Although sensorless control is very promising, directly applying sensorless control to SRMs in ultra-high speed applications is fraught with its own set of problems, such as expensive current and voltage signal processing or complicated use of external injection circuits. An easy-to-implement and computationally-efficient sensing method needs to be developed for even higher speed SRMs.

From the previous discussion, it can be seen that all the existing commercial speed/position sensing methods have limitations in the mechanical maximum speed they can reach due to the need to physically attach detectable objects to the shaft, and sensorless control is either too difficult to be implemented or computationally-intensive, which is not suitable for ultra-high speed applications over 100,000 rpm. In the following section, a direct position control for ultra-high speed SRMs based on low-cost non-intrusive reflective position sensors is proposed. A combination of LED and photodiode is used to detect the reflective markers painted on the shaft and to generate the analog trigger signal so that it controls the switching angles directly without any speed/position manipulations, which allows the control to be as simple and fast as possible.

## 8.3 Non-intrusive Direct Position Control for UHSSRMs

### *8.3.1 Non-intrusive Reflective Position Sensor*

In order to exceed the maximum speed limit of the conventional commercial sensors, the code disc has to be eliminated. A contactless sensor system has to be applied using either optics or Hall-effect. Unlike PM machines, applying Hall-effect to detect the magnetic field of SRMs requires the Hall sensor to be located very close to the rotor and windings, which needs to be taken into consideration at the design stage and is not suitable for off-the-shelf SRMs. Therefore, the optics-based method is chosen for both simplicity and its non-intrusive property.

Unlike the photo interrupting method used in the conventional rotary encoders, a contactless reflective photon-detecting method is selected. The benefit of using the reflective method instead of the interrupting method is its versatility. A simple black mark can be made directly on any kind of shaft for the detecting purpose without changing the highly critical balance of the shaft, which happens in the interrupting case.

Figure 8.2 shows the setup of the proposed sensing system. Photons are emitted from the LED, shot to the shaft, then reflected by the surface of the shaft and finally received by the photodiode when they are facing to a white mark. A small current signal is thus generated by the photodiode and it goes through an amplifier, a Schmitt trigger and an output transistor to output a trigger signal for the control purpose. When the photons are emitted to a black mark, all of them are absorbed and thus no current signal will be generated. As the shaft rotates, a series of square wave is then generated.

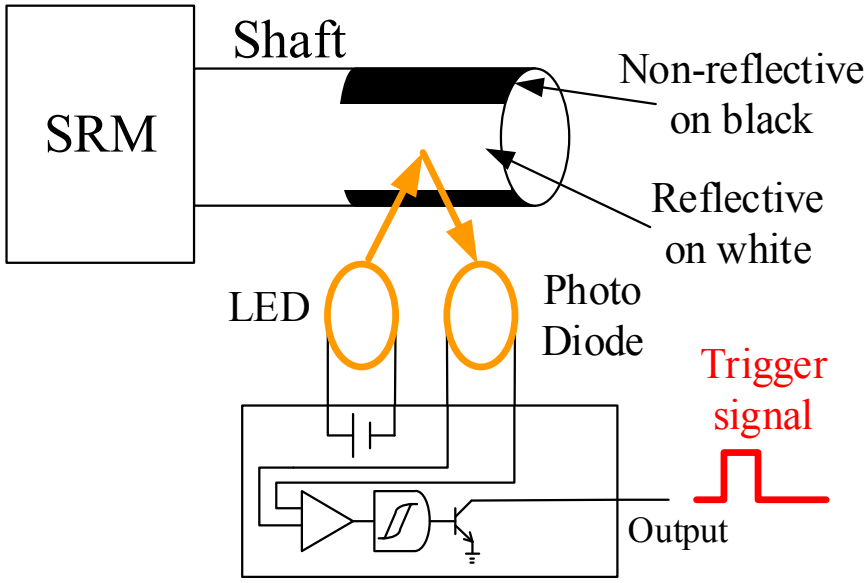


Figure 8.2 Setup of the proposed sensor.

### *8.3.2 Direct Positoin Control for Ultra-high speed SRMs*

The conventional way of measuring the speed and position of the rotor with an incremental rotary encoder is by manipulating with the incremental signals and the clock time in the DSP or FPGA. There are some disadvantages of this method that prevents it from being applied to the ultra-high speed case. For example, the accuracy is dependent on the CPR. But for ultra-high speed SRMs over 1,000,000 rpm, the rotor diameter is usually as small as 3 to 4 mm [49], which results in a small surface area for making a series of reflective indicating marks. In addition, the black mark has a minimum width required to be properly detected and processed. These two facts imply that only a low value of CPR can be achieved, which means low accuracy with the conventional method.

A simple and fast direct position control for ultra-high speed SRMs is proposed in Figure 8.3. A 4/2 SRM is used for discussion because it is the typical choice for ultra-high speed SRMs [43]. Nevertheless, other types of SRMs are similar. The idea is to reduce the

CPR to the minimum value of the number of the rotor poles and then apply single pulse control for each phase. The switching-on and -off angles (denoted as $\theta_1$ and $\theta_2$, respectively) are indicated by the black and white marks on the shaft. Note that from this point the photodiodes are assumed to be light on mode, which means the trigger signal is LOW when a white surface is detected and is HIGH when a dark surface is detected [112]. As shown in Figure 8.3 (a), when the rotor is $\theta_1$ degrees away from the unaligned position ($\theta$=0°, which is also the aligned position for the other phase in the 4/2 case), the optical sensor detects the black mark, resulting in a rising edge of the output trigger signal. As the rotor rotates (clockwise in this case, as shown in Figure 8.3 (b)), the black mark continues and the trigger signal of the optical sensor continues to output a high voltage. When the rotor pole is $\theta_2$ degrees away from the unaligned position, the black mark ends and the trigger signal returns to a low voltage. The switching-on and -off angles can be easily modified by changing the start position and the cover angle of the black mark. The trigger signal is then fed to the DSP or FPGA to determine the switching angles. Then a logic AND is performed between the trigger signal and the PWM signal for the gate signals to control the current of the corresponding phase. Figure 8.4 shows a typical waveform of the trigger signals and phase currents in one revolution of the rotor.

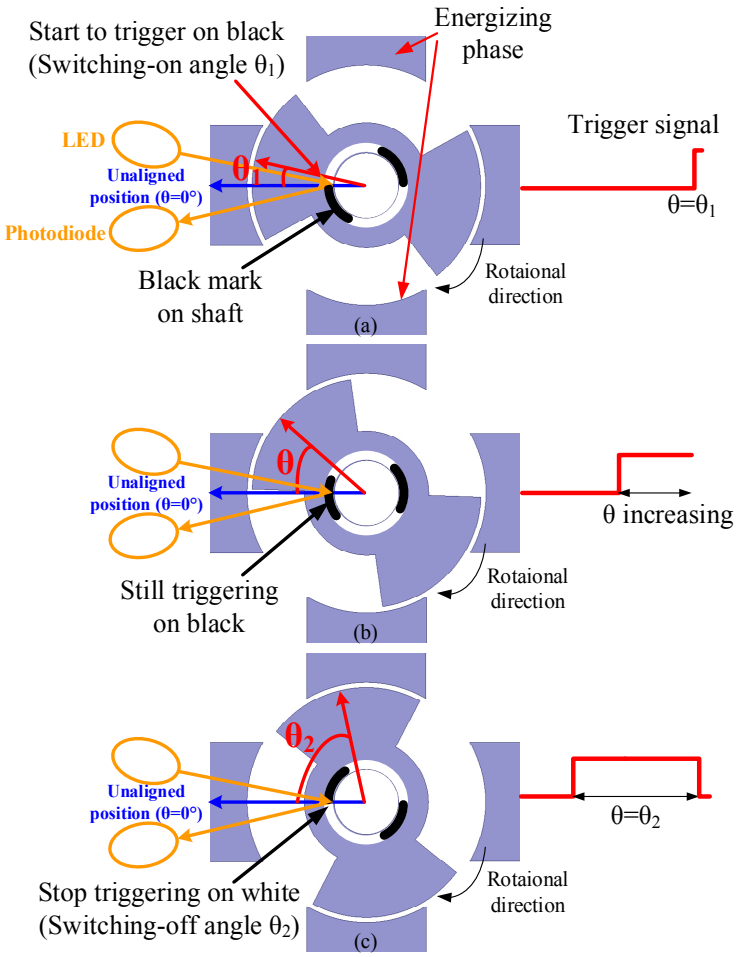


Figure 8.3 Proposed direct position control.

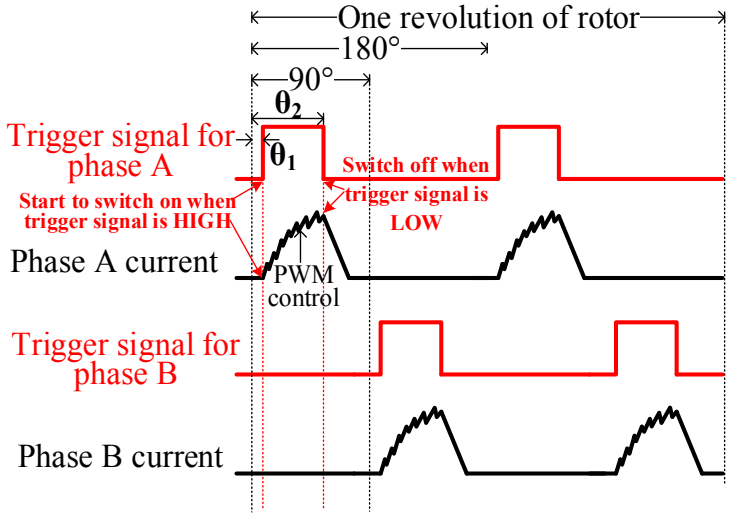


Figure 8.4 PWM current control with the optical sensors.

### *8.3.3 Advantages*

The advantages of the proposed control are as follows:

• **Versatility.** Since it uses the reflective optical sensors, it is suitable for any kind of off-the-shelf SRM without changing the shaft geometry or opening the machine. A simple painting of the marks is just enough.

• **Virtually no speed limit.** Due to the contactless setup, there is no mechanical speed limit. Actually the speed limit is determined only by the signal delay of the optical processing circuit, which can be designed to be a very small number.

• **High simplicity.** There is no need to worry about the calculation of the speed/position, or the sampling frequency of the DSP. The trigger signal is an analog type and is generated directly from the optical sensor without any speed position manipulations.

• **Low cost.** The conventional rotary encoders are expensive. A typical high speed US digital® E5 rotary encoder is in the order of a few hundred dollars. But the proposed method only costs several dollars for cheap components such as LEDs and operational amplifiers.

### *8.3.4 Disadvantages*

However, there are also some disadvantages:

• The optical sensors have to be setup and aligned with the stator carefully to get accurate switching-on and -off angles. But it is not a big issue if there is a slight inaccuracy

of the position, because the output torque will maintain almost constant within a certain range of $\theta_2$. This will be discussed in details in the next section

• The switching-on and -off angles cannot be modified in the software. It can only be changed by redrawing the marks on the shaft. However, considering the ultra-high speed condition, the switching-on and -off angles are always predetermined offline to generate the maximum torque, which does not need modification. An optimization of the switching angles to generate the maximum torque will be conducted in the next section

• The number of the optical sensors is equal to the number of pole pairs of the stator, which may cost more if there are more stator pole pairs. Nevertheless, high speed machines should have the minimum number of pole pairs.

• The proposed method can only be used unidirectionally.

Table 8.2 gives a comparison of different sensing methods from various aspects. It can be seen that the method proposed in this chapter has the best performance for every aspect except for a comparatively low accuracy, which can be easily solved by a careful setup as discussed before. All these advantages imply that the proposed control is especially suitable for ultra-high speed SRMs. For even higher speeds up to 1,000,000 rpm, the economic benefit will become more significant, because the raw material cost for the machine is very low due to the tiny size of the machine [113].

Table 8.2 Comparison of Different Sensing Methods

| | Optical encoder | Hall sensor | Resolver | Sensorless | Proposed |
|---|---|---|---|---|---|
| Maximum speed limit | Low | Low | Low | Medium | High |
| Simplicity of implementation | Medium | Medium | Medium | Low | High |
| Non-intrusive? | No | No | No | Yes | Yes |
| Direct control without signal processing? | No | No | No | No | Yes |
| Accuracy | High | High | High | Medium | Low |
| Typical cost | $200 | $300 | $300 | $0 | $5 |

## 8.4 Modeling and Optimization

For ultra-high speed applications such as turbo chargers, the load torque is usually only the air/bearing friction, which does not change at a constant speed. From the previous discussion, for a certain voltage supply, various combinations of $\theta_1$ and $\theta_2$ will result in different values of the output torque. An early switching-off angle will result in not fully use of the machine, while a late switching-off angle will cause a negative torque, which results in a decrease of the average torque [48].

In this section, a systematic way of finding the optimal combination of the switching-on and -off angles to generate the maximum output torque is described. A 4/2 high-speed SRM [44] is used as an example. First, a finite element model (FEM) is built to simulate the performance of the motor. Then an equivalent model with much faster computation speed is built in Simulink based on the flux/position and torque/position lookup table

extracted from the FEM. Finally a two-step sweep optimization of the switching-on and -off angles is conducted to determine the optimal value of $\theta_1$ and $\theta_2$.

### *8.4.1 Finite Element Model*

A 4/2 high speed SRM is used for an example in this section. First, the machine is modeled using the commercial finite element analysis software ANSYS. Figure 8.5 shows a screenshot of the model. Table III gives a list of the machine parameters.

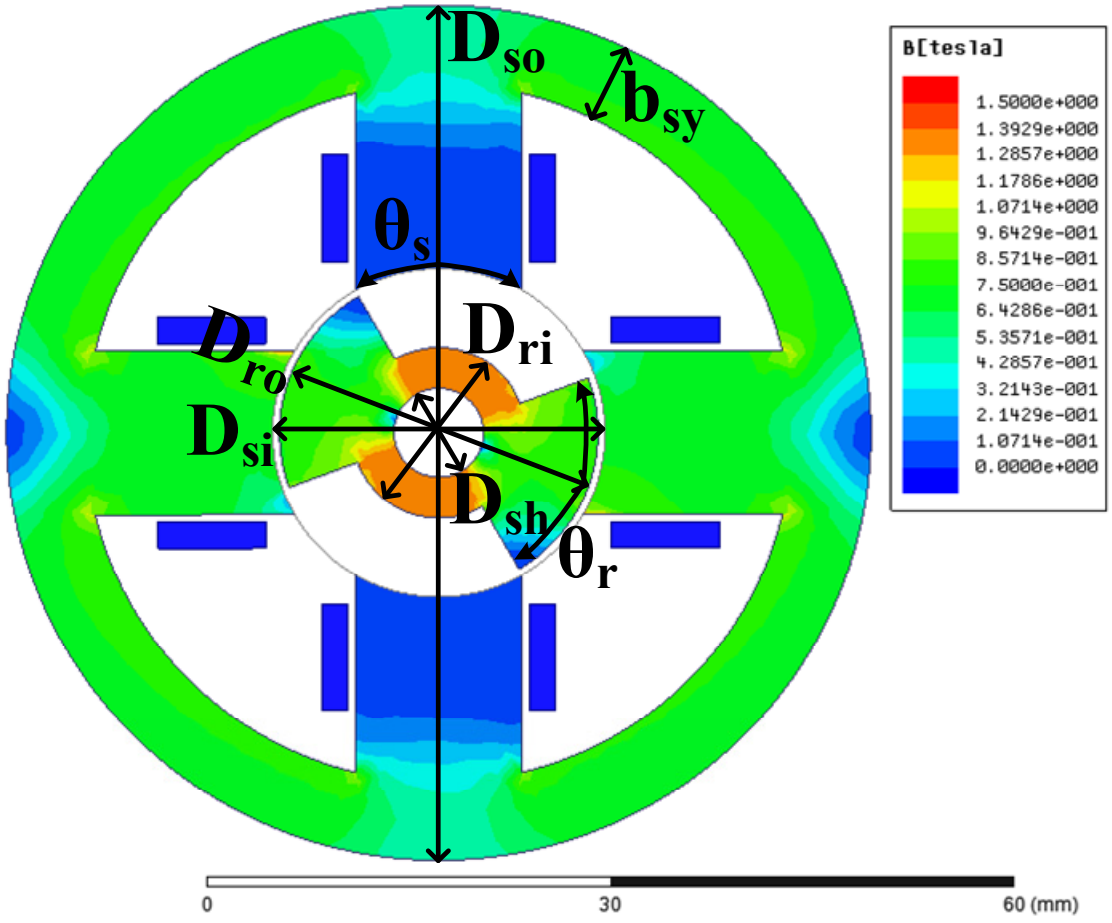


Figure 8.5 FEM of the SRM.

Table 8.3 List of the Machine Parameters

| Stator outer diameter ($D_{so}$) | Stator Inner diameter ($D_{si}$) | Yoke thickness ($b_{sy}$) | Stator pole arc ($\theta_s$) |
|---|---|---|---|
| 65 mm | 25 mm | 6 mm | 60° |
| Rotor outer diameter ($D_{ro}$) | Rotor inner diameter ($D_{ri}$) | Shaft diameter ($D_{sh}$) | Rotor pole arc ($\theta_r$) |
| 24 mm | 13 mm | 6.7 mm | 80° |
| Stack length ($l$) | Air gap length | No. of turns per pole | Pole pair No. ($P_s/P_r$) |
| 20 mm | 0.5 mm | 90 | 4/2 |

### *8.4.2 Simulink Equivalent Model*

The FEM is very accurate in terms of evaluating the machine performance. However, it is not time-efficient to be used as an optimization tool. An equivalent model in Simulink is built to simulate the performance of the machine with much faster calculation speed based on the flux and torque curves extracted from the FEM as described in Chapter 6. Figure 8.6 and Figure 8.7 show the flux linkage and torque curves from 0 to 90° under different current excitations from 0 to 10 A with a step of 0.2 A, respectively.

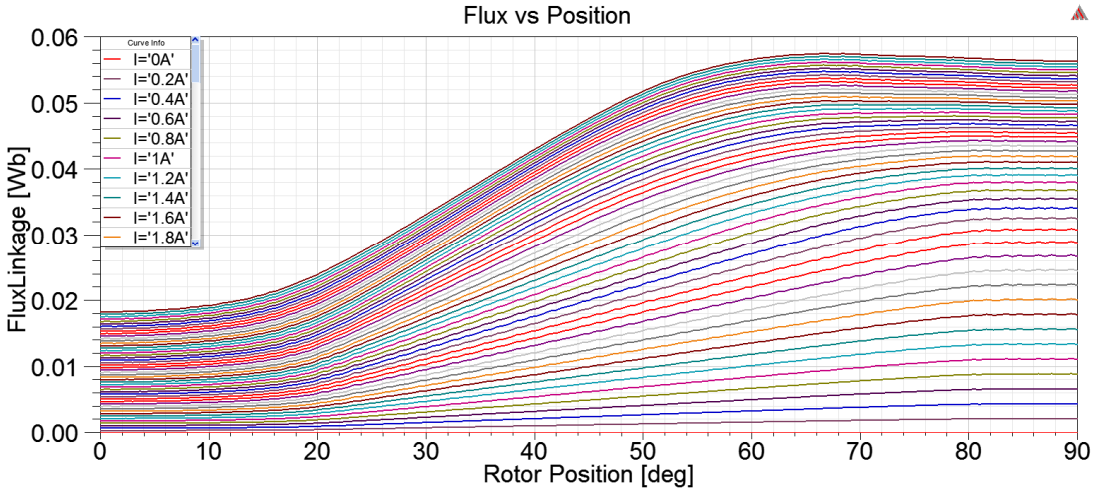


Figure 8.6 Flux linkage against rotor position under various excitation currents.

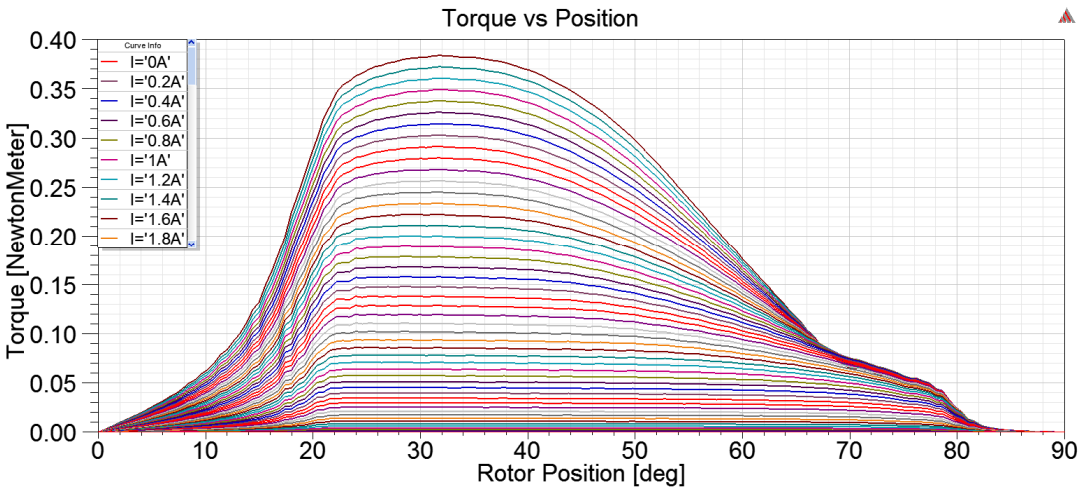


Figure 8.7 Torque against rotor position under various excitation currents.

### *8.4.3 Output Torque Optimization*

With the equivalent Simulink model, the output torque can be optimized easily. A two-step optimization is conducted. First, the switching-on and -off angles are swept from 0° (unaligned position) to 90° (aligned position) with a step of 5° to get a general pattern of the torque-switching angle relationship. Figure 8.8 shows the optimization result of the SRM under 140 V DC voltage supply at 100,000 rpm. It can be seen that when the switching-on angle is 0° and the switching-off angle is between 60° to 70°, the machine will generate the maximum torque. In addition, it can also be observed that the when the switching-on angle is 0°, the output torque is maximized, which is true because of the longer excitation of the current. Thus, a second step optimization of fixing the switching-on angle at 0° and varying the switching-off angle from 0 to 90° with a finer step of 1° is conducted. Figure 8.9 shows the optimization result of the second step. An optimal switching-off angle of 65° can be clearly observed, which generates the maximum torque of 7.6 mN·m. This implies that a shorter duration of excitation will lead to an insufficient use of the machine while a longer duration of excitation will produce a negative torque.

Note that a negative switching on angle must lead to a negative instantaneous attraction/torque in the opposite direction, which may risk rotating reversely. Thus, for a safe operation, only positive switching angles are considered for the optimization.

From Figure 8.9 it can be also seen that near the optimal point, the output torque changes gradually, which means that a little variation from the optimal point will not change the output torque too much. Actually for any $\theta_2$ between 60° to 73° the output torque is between 7.3 to 7.6 mN·m, resulting in a variation of only 4% of the maximum output torque.

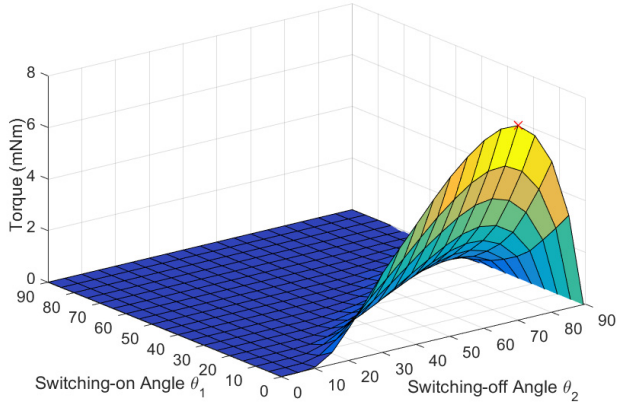


Figure 8.8 Torque optimization under 140 $V_{dc}$ at 100,000 rpm.

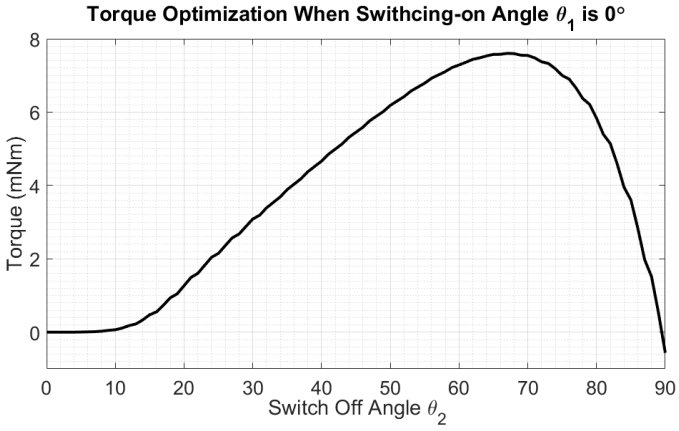


Figure 8.9 Torque optimization when switching-on angle is 0°.

## 8.5 Experimental Results

In order to verify the proposed models and control system, experiments are done on the 4/2 high speed SRM. A good matching among the experimental results, the proposed FEM , and the equivalent Simulink model is observed. Then the proposed sensing system is built and tested on the motor. The motor was successfully driven to 100,000 rpm with the proposed sensing and control system.

### *8.5.1 Experimental Setup*

Figure 8.10 shows a picture of the 4/2 high speed SRM and the proposed sensing system. Two optical sensors were built for sensing the rotor position for each phase. The circuits use a 5 V power supply, which is provided from the FPGA board used to generate the PWM signal. The optical sensors are the light on mode, which means that the output voltage is 5 V for black and 0 V for white. The output signal goes through a line driver to be changed from 5 V to 3.3 V in order to be fed into the FPGA.

The two optical sensors are fixed at both ends of the SRM (one of them is shown in Figure 8.10). Both of them are setup horizontally instead of one vertically and one horizontally because of the ease of use. Two white paper strips with different black mark patterns are attached to both ends of the shaft with proper adhesives. The black marks are drawn using a regular marker pen. A permanent paint on the shaft can also be used instead. Note that there is no need to open the SRM for the setup. The rotor is locked at the aligned position of a phase when a DC current is fed into its windings. The mark patterns are drawn in such a way that the two optical sensors detect the two different phases, as is shown by the black and white marks in Fig. 3. A ruler and a protractor are used to keep the marks

straight and accurate in angle. The switching-on angle is fixed at 0° and the switching-off angle is drawn at around 70°.

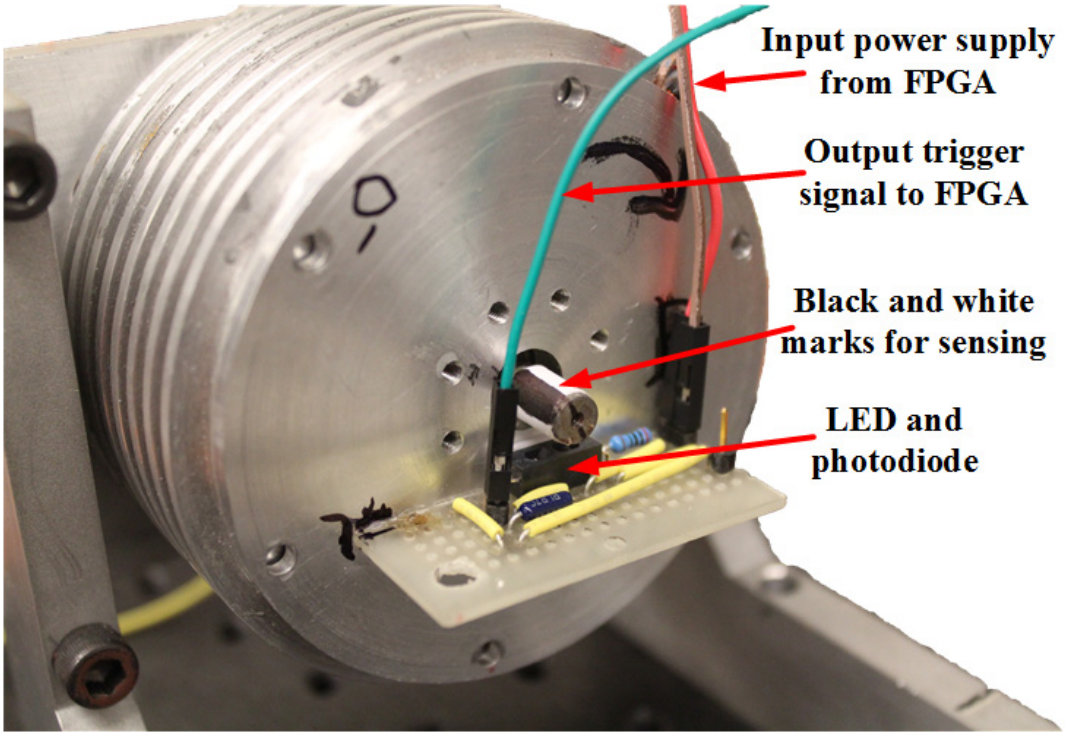


Figure 8.10 Picture of the 4/2 SRM and the optical sensor setup.

Figure 8.11 shows the drive circuit. It is composed of an AC/DC rectifier, a current sensor board, a DSP+FPGA board and two drive boards for each phase. The FPGA has a PWM module programmed in it, as well as a filter to clean the rotor position signals from the optical sensors. The gate signals for the switches are generated by performing a logic AND between the optical trigger signals in Figure 8.2 and the PWM signals in the FPGA. Then, a close loop control is implemented in the DSP to drive the motor. Figure 8.12 shows the block diagram of the close loop control system. The outer loop is the speed feedback loop. The speed information is obtained by the time difference between two consecutive trigger signals. Then, the speed difference goes through a PI controller and generates a reference current. The duty cycle demand to the PWM is defined in the DSP in order to

follow this reference current. The PWM carrier's frequency is 10 kHz. Note that the reference current is set to be around 5A intentionally, which is larger than the actual phase current, in order to maintain a one pulse control. This implies that the duty cycle of the PWM signal is 100% and the actually switching frequency varies with speed. Thus, the current feedback loop is mainly used to prevent the current from being too large instead of maintaining a constant value as in the hysteresis control. The single pulse control is used because it is a typical choice in the control of high speed SRMs [97, 100]. Two classical MOSFET-based asymmetric inverter drive boards are used for each phase [48].

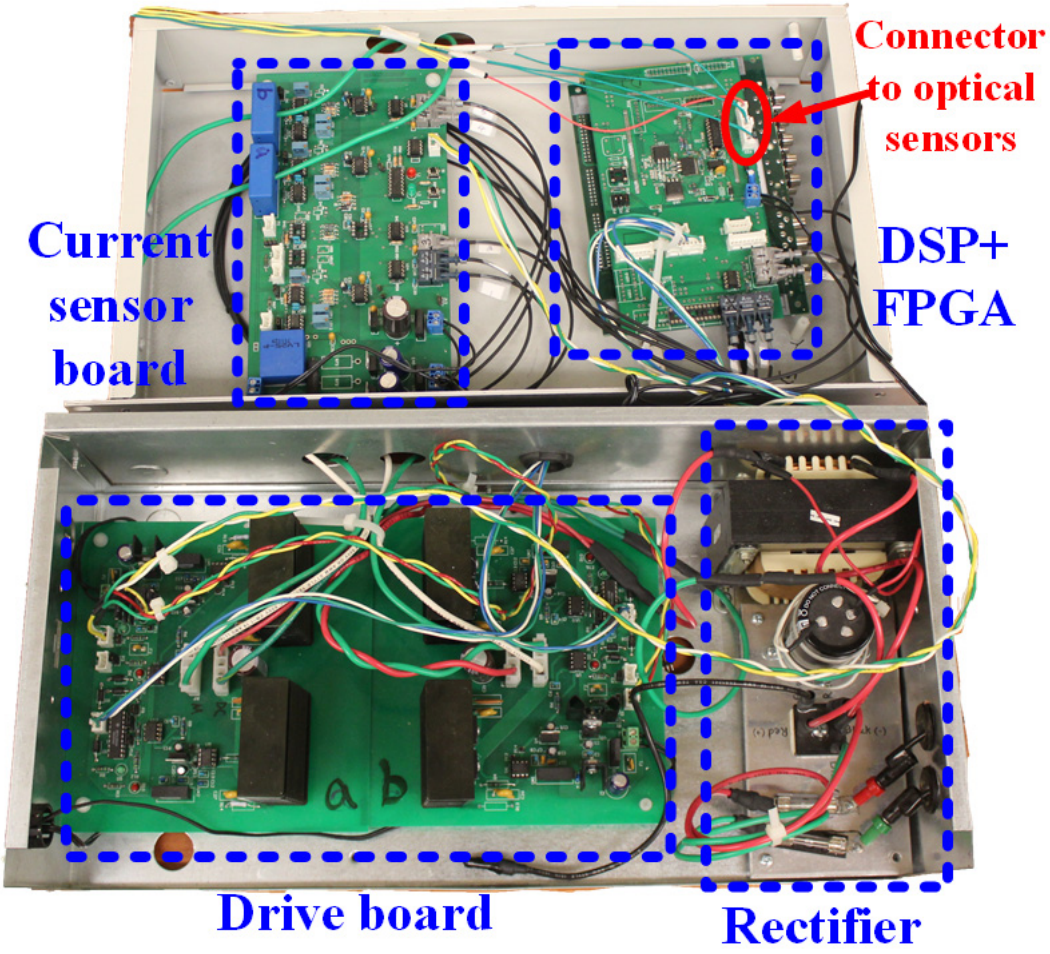


Figure 8.11 Picture of the drive circuit

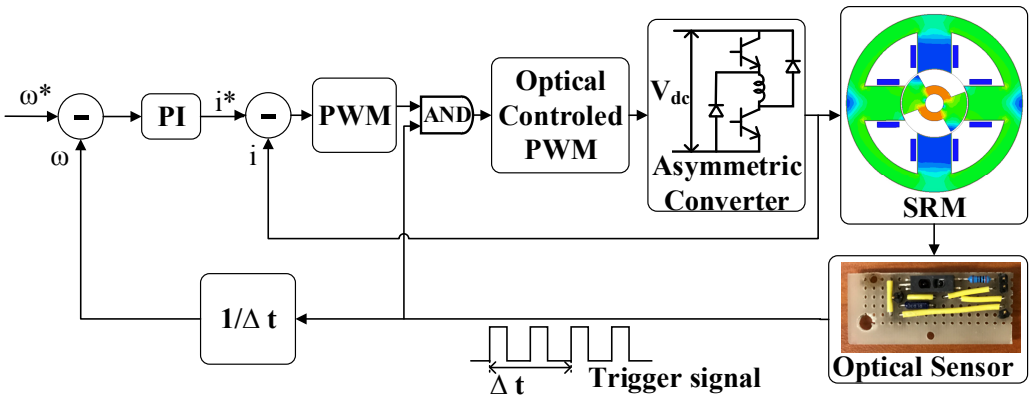


Figure 8.12 Block diagram of the closed loop control

### *8.5.2 Model Validation*

To validate the FEM and the equivalent Simulink model, the motor is first driven at 50,000 rpm with a DC voltage supply of 40 V. Figure 8.13 shows the comparison of the current profiles among the experimental results, the FEM and the Simulink model. It can be seen that the models match the experimental results well. The very little discrepancy between the FEA and the Simulink model is due to the linear interpolation and the one numerical time step lagging in the Simulink. Note that the PWM duty cycle is set to be 1 in order to fully apply the DC voltage to each phase.

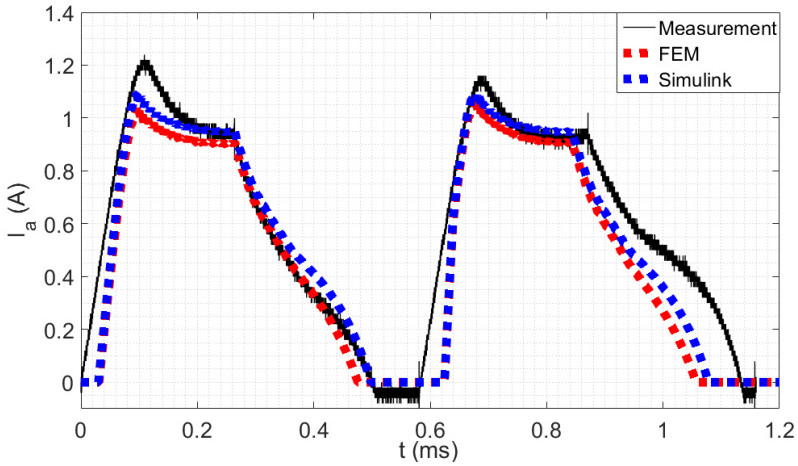


Figure 8.13 Comparison of the current profiles at 50,000 rpm.

### *8.5.3 Experimental Results at 100,000 rpm*

After the models are verified, the motor is driven to 100,000 rpm at no load except for the air/bearing friction. A video reference can be found in [114]. Figure 8.14 shows a screenshot of the oscilloscope at 100,000 rpm. Channel 1 (yellow) is the voltage waveform of phase A with a DC link voltage of 140 V. This value is selected by changing manually the AC power supply with an initial estimation by FEA. Chanel 2 (blue) is the optical trigger signal of phase A. Channel 3 and 4 (magenta and green) are the current profiles of phase A and phase B, respectively. It can be seen that the optical sensor controls the current very well. The current sensor conversion rate is 1A/100mV. From the oscilloscope it can be read that the frequency of the current of phase A (magenta curve) is 3.353 kHz. So the speed is 3353/2·60≈100,000 rpm. Higher speeds could have been achieved, but for the safety concerns of the bearings the final speed was stopped at 100,000 rpm.

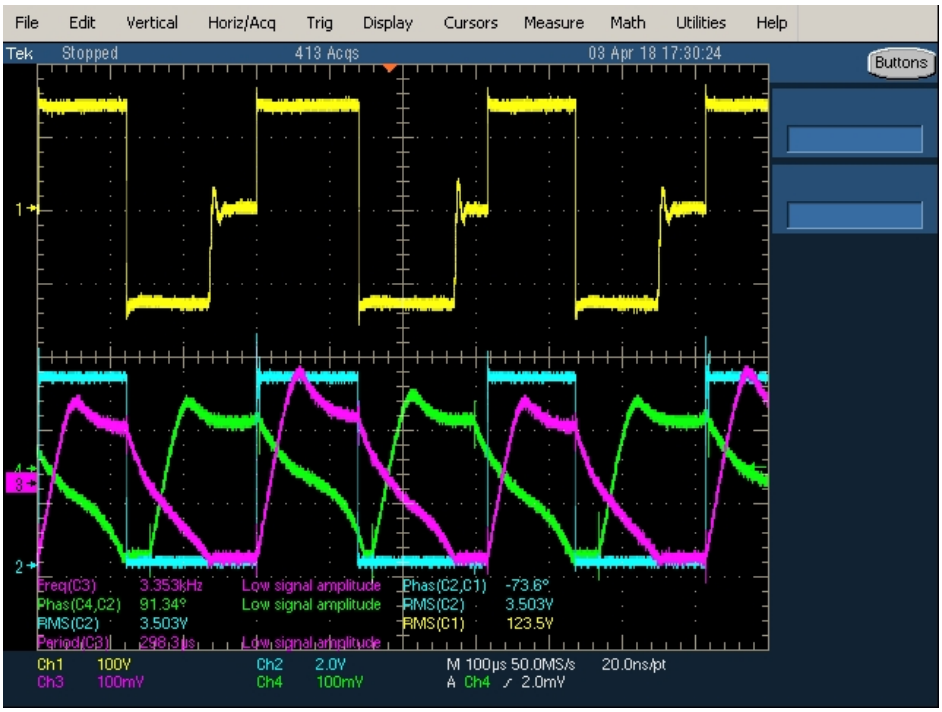


Figure 8.14 Experimental result at 100,000 rpm.

## 8.6 Chapter Summary

The maximum speed of ultra-high speed SRMs is limited by commercial rotary encoders due to mechanical considerations. In this Chapter, a novel direct position control for ultra-high speed SRMs based on non-intrusive reflective sensors is proposed. We use reflective optical sensors to detect the relative position between the rotor and the stator so as to control the on and off states of the switches directly through the analog output trigger signals generated from the optical sensors. In order to generate the maximum output torque under a certain DC supply voltage at a certain speed, the switching-on and -off angles are optimized. A fast computation model of a 4/2 high speed SRM is built in Simulink, using the method proposed in Chapter 6, for the optimization based on the flux-position and torque-position lookup table extracted from the FEM. Finally, experiments are done to validate the feasibility of the proposed sensing and control system up to 100,000 rpm. The proposed control has many advantages such as versatility, virtually no speed limit, high simplicity and low cost. This will lead to new applications of ultra-high speed SRMs in the field of micro drilling and turbo chargers.

# CHAPTER 9. MULTI-PHYSICS ACOUSTIC ANALYSIS OF UHSSRM

## 9.1 Introduction

With the novel control proposed in Chapter 8, the 4/2 SRM has successfully achieved 100,000 rpm. However, the noise generated at ultra-high speed is so significant that may prevent it from some possible applications [114]. The accurate analysis and prediction of the noise level of ultra-high speed SRMs is very important for the future study of noise reduction measures.

Research has been conducted during the past two decades in the noise and vibration analysis of SRMs. Reference [115] is one of the seminal papers in this area which dealt with the basic origin of acoustic noise in SRMs. A series of experiments are conducted to show that the dominant noise source is the radial deformation of the stator due to its radial magnetic attraction to the rotor. Subsequently, reference [116] analyzed the vibration modes and acoustic noise in a four-phase SRM. Reference [117] presents an analytical calculation of the radial force and acoustic noise in SRMs.

In recent years, with the fast development of modern computer techniques, finite element analysis (FEA) has become more and more popular among researchers due to its accuracy and universality. Reference [118] proposes a method to calculate the acoustic noise spectrum of SRMs using finite element modal analysis and superposition. The prediction of radial vibration [119] and acoustic noise [120] in SRMs using FEA has also been done. A multi-physics NVH (noise, vibration and harshness) finite element modeling

and simulation of a SRM for electric vehicle applications is proposed in [121]. However, all the previous FEA-based analyses are focused on the vibration and noise prediction of low speed SRMs or PM motors. Modeling and predicting the noise level of SRMs accurately at ultra-high speeds has not been previously presented.

In this Chapter, multi-physics acoustic modeling and prediction of ultra-high speed SRMs is presented based on FEA [122]. First, a 3D electromagnetic FEA is conducted to calculate the radial force on the stator teeth. Then, a finite element modal analysis and a harmonic response analysis are conducted in the frequency domain to estimate the natural frequencies and the vibration of the whole motor with the case and support included, using the calculated radial force as the input excitation. After that, an acoustic response analysis is conducted to estimate the sound pressure level (SPL) using the superposition of the surface vibration information from the harmonic response analysis. Finally, to verify the proposed model, experiments are done to measure and compare the natural frequencies and the SPL of a 4/2 ultra-high speed SRM at 100,000 rpm.

## 9.2 Electromagnetic Modeling and Analysis

### *9.2.1 Electromagnetic Finite Element Analysis*

For ultra-high speed SRMs, a small number of magnetic poles corresponds to lower switching losses. The 4/2 ultra-high speed SRM with a rated speed of 100,000 rpm described in Chapter 8 is analyzed in this chapter [123]. ANSYS/Maxwell FEA software is used for electromagnetic simulation of the motor, whose parameters are given in Table 8.3. A 3D transient solver is used to simulate the steady state operation. The stator and the rotor are both made from M19 laminations. The excitation currents are controlled by an

external circuit in which the supply DC voltage and the switching angles can be modified. Figure 9.1 shows the FEA analysis of the motor flux density.

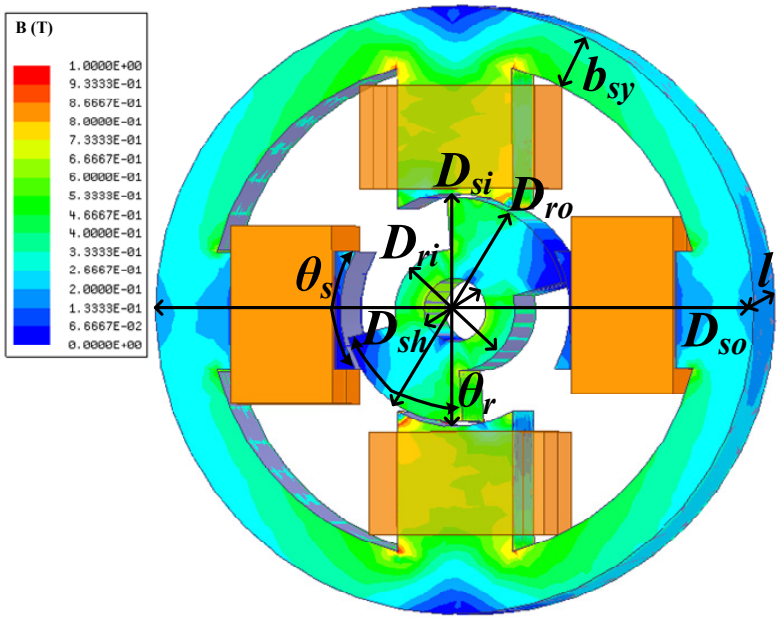


Figure 9.1 3D FEA of the 4/2 SRM.

## 9.3 Radial Force Calculation

The origin of acoustic noise in electromagnetic systems has been studied extensively in the literature. It has been shown experimentally that the dominant noise source of SRMs is the radial deformation of the stator due to its radial magnetic attraction (i.e. radial force) to the rotor, especially when the frequency of deformation coincides with that of a natural mechanical resonance of the stator [115]. According to [124], the surface force density of the stator poles can be calculated using the well-know Maxwell tensor method as,

$$\frac{d\mathbf{f}}{dA} = \frac{1}{\mu_0}\left[(\mathbf{n}\cdot\mathbf{B})\mathbf{B} - \frac{1}{2}B^2\cdot\mathbf{n}\right] \tag{9.1}$$

where **f** is the magnetic force vector, $A$ is the surface area, n is the normal unit vector of the pole surface, and $\boldsymbol{B}$ is the flux density vector calculated by FEA.

The flux density can be separated into the radial and tangential components, and integrates over the surface of the stator teeth to find the radial and tangential components of the total force acting on the stator teeth, given by,

$$f_r = \frac{1}{2\mu_0}\oint (B_r^2 - B_t^2)dA \tag{9.2}$$

$$f_t = \frac{1}{\mu_0}\oint (B_t \cdot B_n)dA \tag{9.3}$$

Figure 9.2 shows the value of the flux density and its radial and tangential components along the air gap at 300 μs (one half cycle) at 100,000 rpm. Figure 9.3 shows the radial force acting on one tooth of phase A and phase B, and the current of each phase winding in one revolution at 100,000 rpm.

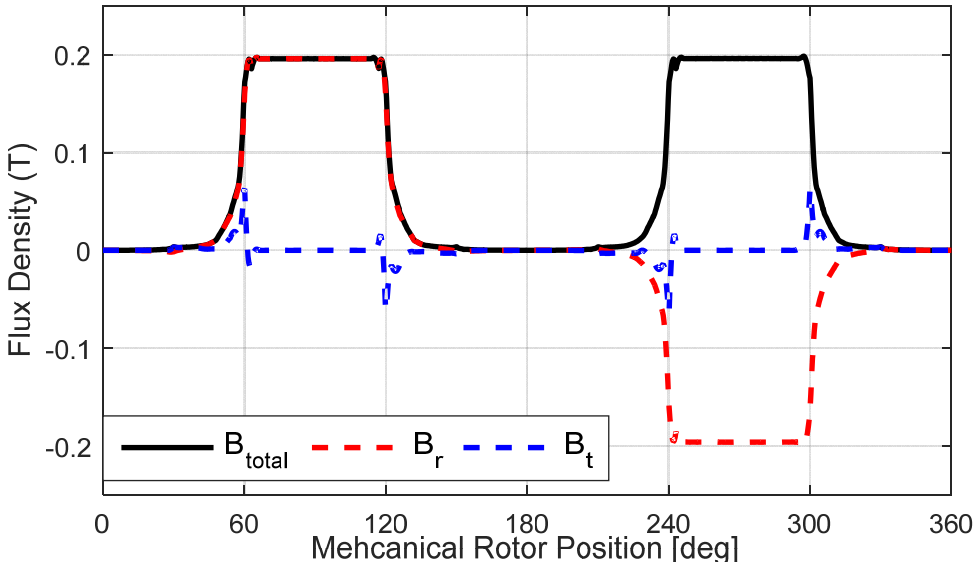


Figure 9.2 Air gap flux density distribution at 300 μs (one half cycle) at 100,000 rpm.

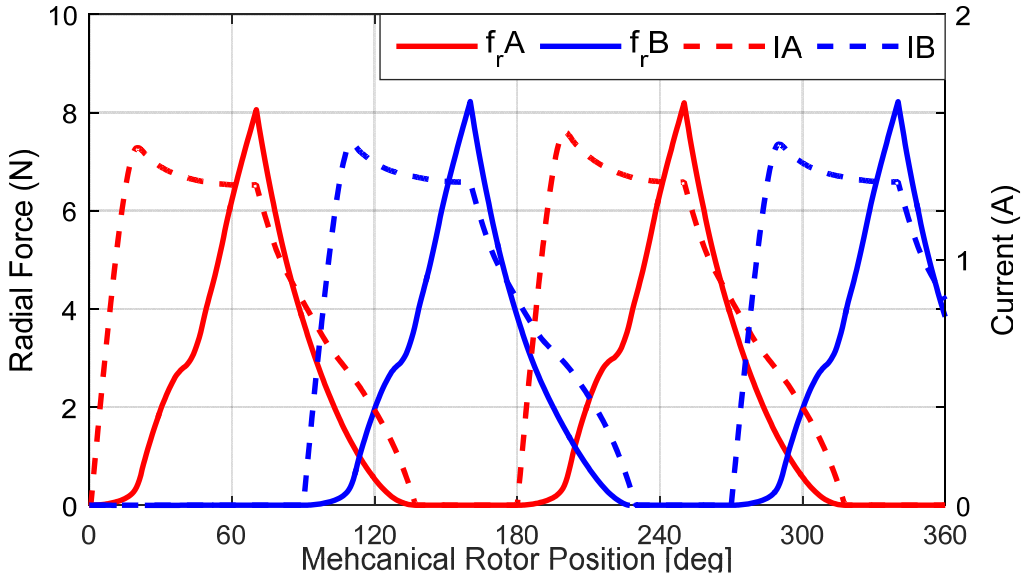


Figure 9.3 Radial force and winding current of each phase at 100,000 rpm.

As can be seen in the figure, as the phase windings move from 0° (unaligned position) to 70° (20° from the aligned position), the radial force increases. When the phase current is switched off at 70°, the radial force starts to decrease, which results a force peak at the time the phase is switched off. The total radial force on the stator can be calculated by adding the radial force of both phases, as is shown in Figure 9.4.

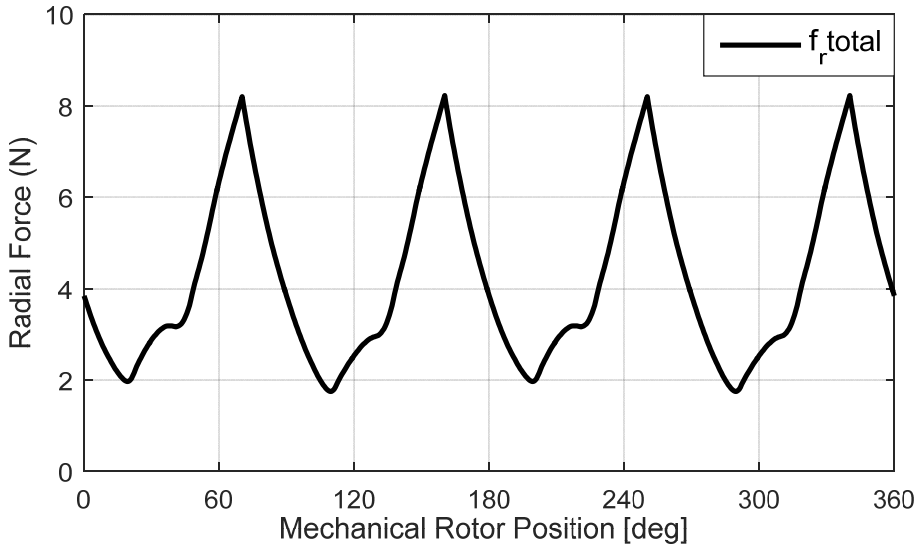


Figure 9.4 Total radial force on the stator at 100,000 rpm.

The FFT (Fast Fourier Transform) of the total radial force on the stator is shown in Figure 9.5. The fundamental frequency, f0, is 6.66 kHz at 100,000 rpm, given by,

$$f_0 = \frac{n \cdot p_r \cdot (p_s / 2)}{60} \tag{9.4}$$

where $n$ is the speed in rpm, and $p_r$ and $p_s$ are the number of rotor and stator poles, respectively.

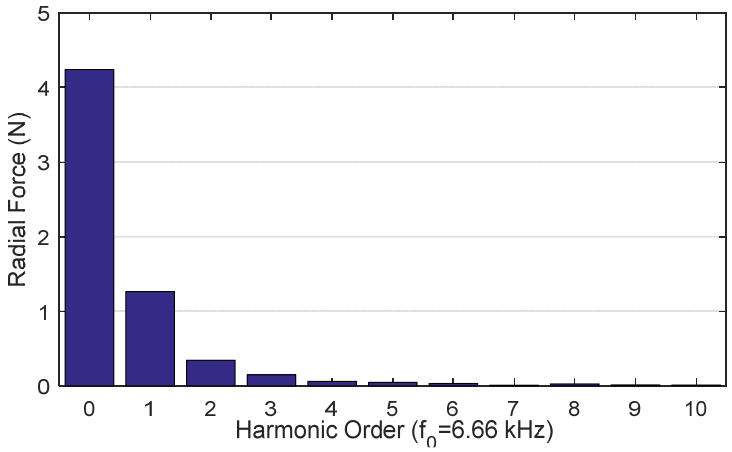


Figure 9.5 FFT of the total radial force on the stator at 100,000 rpm.

## 9.4 Modal and Vibration Analysis

After the radial force is calculated, the vibration of the SRM can be estimated. The radial force of the stator is imported as the input excitation of a 3D harmonic response analysis of the whole machine with the case and support included. Meanwhile, a 3D modal analysis is conducted as a support and validation of the harmonic response to calculate the natural frequencies of the motor. When the harmonic response is finished, the surface vibration of the motor is imported as the input of a 3D acoustic response analysis. Figure 9.6 shows the workflow of the multi-physics acoustic prediction process. In this section, the modal and harmonic analysis will be described in detail.

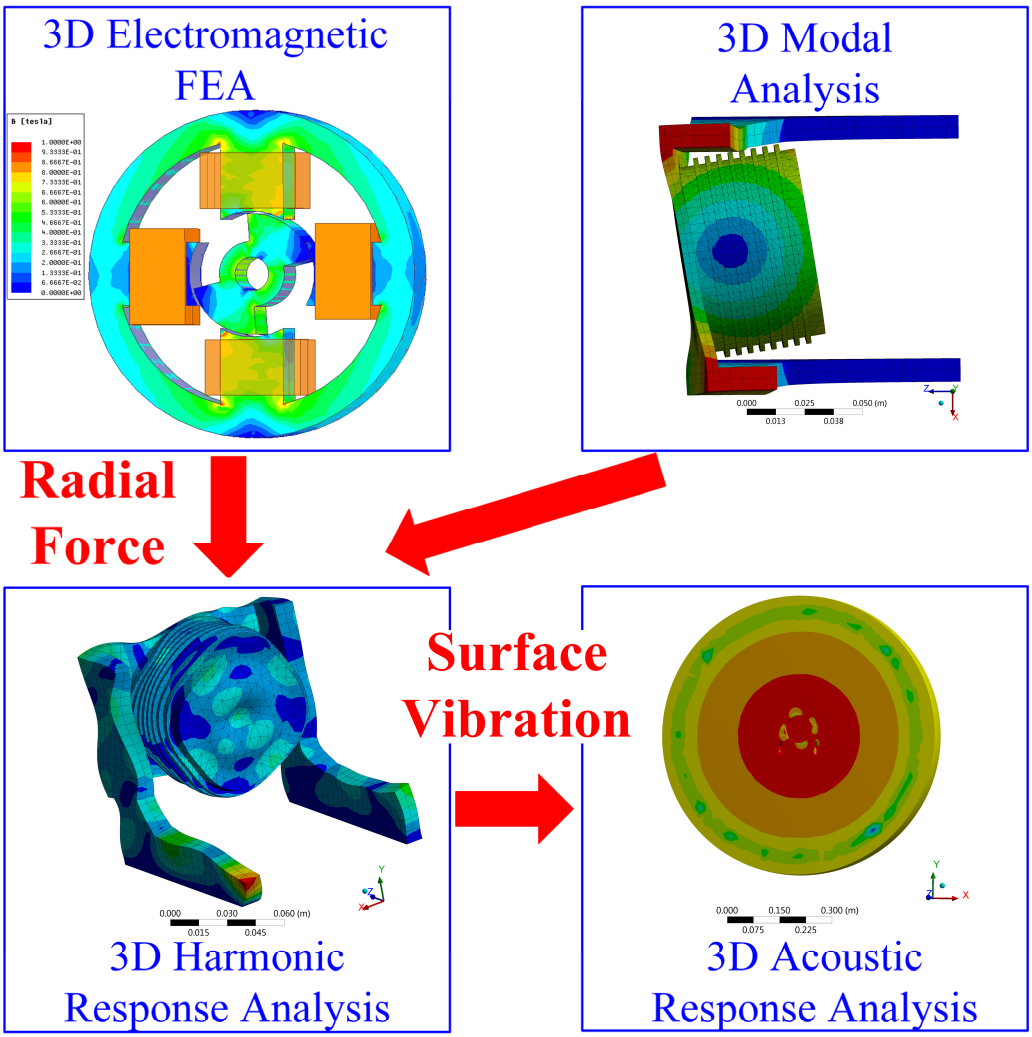


Figure 9.6 Workflow of the proposed acoustic prediction process.

### *9.4.1 Modal Analysis*

#### 9.4.1.1 Governing Equations

The motion equation of a vibration system can be solved based on the Hamilton's principle [121],

$$[M]\{\ddot{x}(t)\}+[C]\{\dot{x}(t)\}+[K]\{x(t)\}=\{F(t)\} \tag{9.5}$$

where $M$, $C$ and $K$ are the mass, damping and stiffness matrices, $x$ is the displacement and $F$ is the excitation force. Generally, the damping of electric machines is very low and therefore can be neglected. In addition, since the modal analysis is used to estimate the intrinsic natural frequencies of a structure, the excitation force can also be set to zero. Therefore the solution of (9.5) with zero damping ($C$=0) can be obtained by solving [121],

$$([K] - \omega^2 [M])\{X(\omega)\} = 0 \tag{9.6}$$

where $\omega$ is the natural frequency, and $X(\omega)$ is the superposition of the corresponding eigenvectors.

#### 9.4.1.2 Contact, Boundary Conditions and Meshing

In order to get a realistic solution, the aluminum case and support of the motor are also included in the finite element model. The windings are modeled as solid copper coils that are bonded with the stator teeth. The outer surface of the stator is also bonded with the aluminum case, which is connected to the rest of the support. Finally the bottom surfaces of the two legs of the support are fixed to the immovable ground, which provides the boundary condition of the system.

To get a sufficiently detailed mesh, adaptive meshing is used. This means that finer meshing will be generated in certain, more complex areas of the geometry. The total number of elements in the model is 27,057. Figure 9.7 shows the model of the whole machine in the modal and harmonic analysis. Figure 9.8 gives the results of the first six mode shapes and the corresponding natural frequencies of the ultra-high speed SRM.

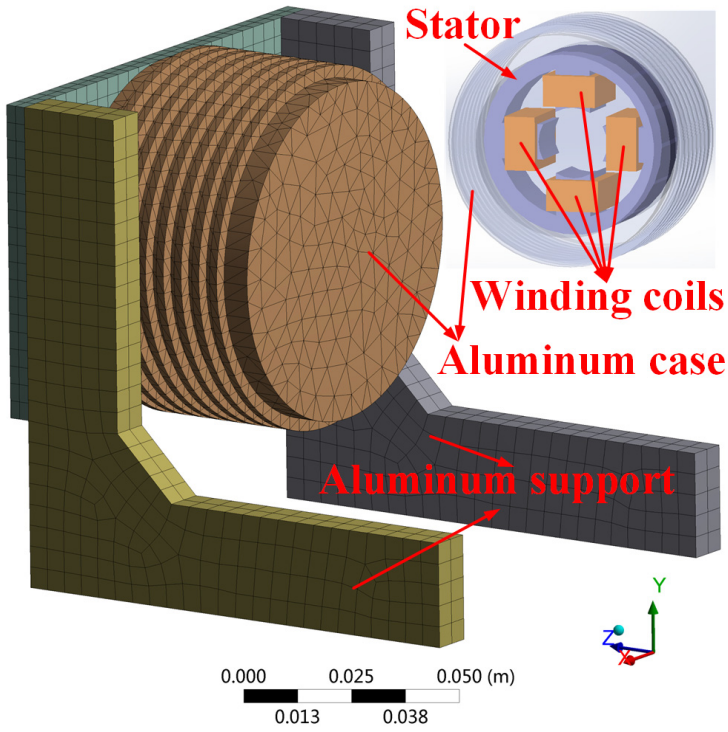


Figure 9.7 Model with meshing of the modal and harmonic analysis.

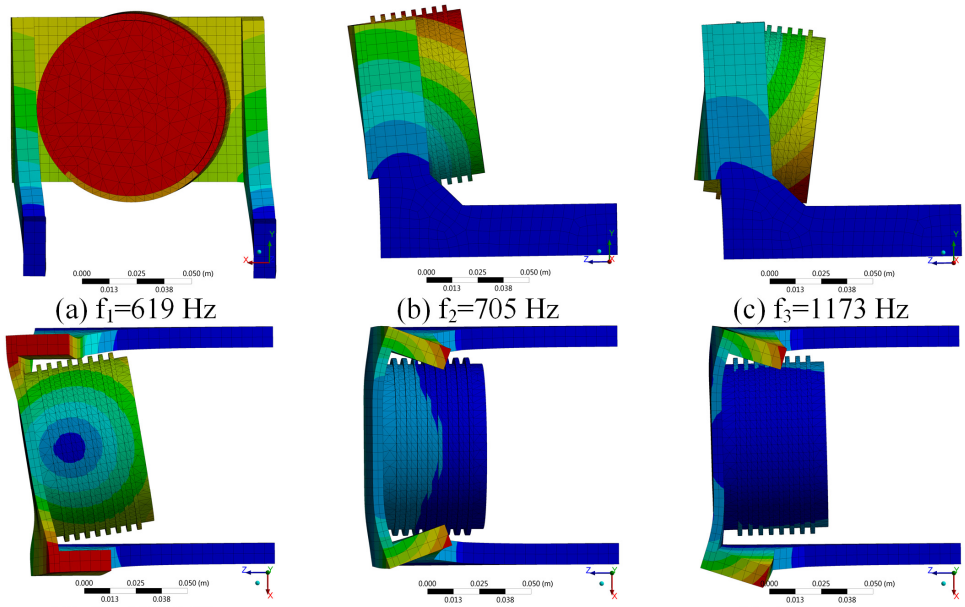


Figure 9.8 First 6 modes and natural frequencies.

### *9.4.2 Harmonic Response Analysis*

The governing equation of harmonic response analysis is also given by (9.5). The difference is that the harmonic response is analyzed at separate harmonic components of the excitation force, and then estimates the vibration of the objective (displacement, velocity and acceleration) using superposition.

#### 9.4.2.1 Radial Force Mappping

The first step of harmonic response analysis is to determine the excitation force. The radial force of the stator calculated from the electromagnetic FEA is imported and mapped to the stator teeth at different frequency components. The maximum effective frequency component $f_{\max}$ can be calculated as,

$$f_{\max} = \frac{1}{2T_s} \tag{9.7}$$

where $T_s$ is the simulation time step. In the electromagnetic simulation, the time step is set to 1 μs. Therefore, the maximum effective frequency is 500 kHz. Considering that the fundamental frequency of the radial force is 6.6 kHz, the maximum frequency imported from the electromagnetic simulation is limited to 50 kHz. This allows for a time-efficient simulation, which is up to roughly 8th harmonic. The frequency response is calculated with a step of 50 Hz so as to get an accurate result. As shown in the results of Figure 9.5, the magnitude of the higher order harmonics is very low. Figure 9.9 shows the mapping of the radial force in the harmonic response analysis at 50 kHz imported from the electromagnetic FEA.

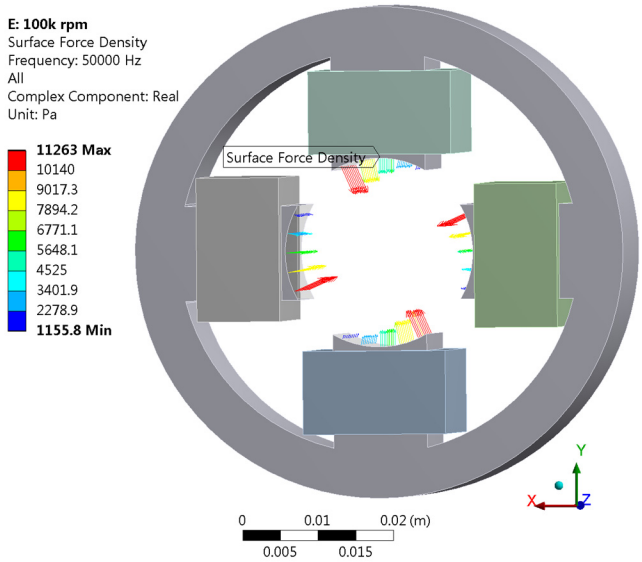


Figure 9.9 Mapping of the radial force imported from electromagnetic FEA.

### 9.4.2.2 Vibration Frequency Response

The setup of the harmonic response analysis is almost the same as in the modal analysis, regarding the contact, boundary condition and meshing. The output is the displacement, velocity and acceleration of all the bodies. The frequency response of the velocity at the outer surface of the aluminum case is show in Figure 9.10.

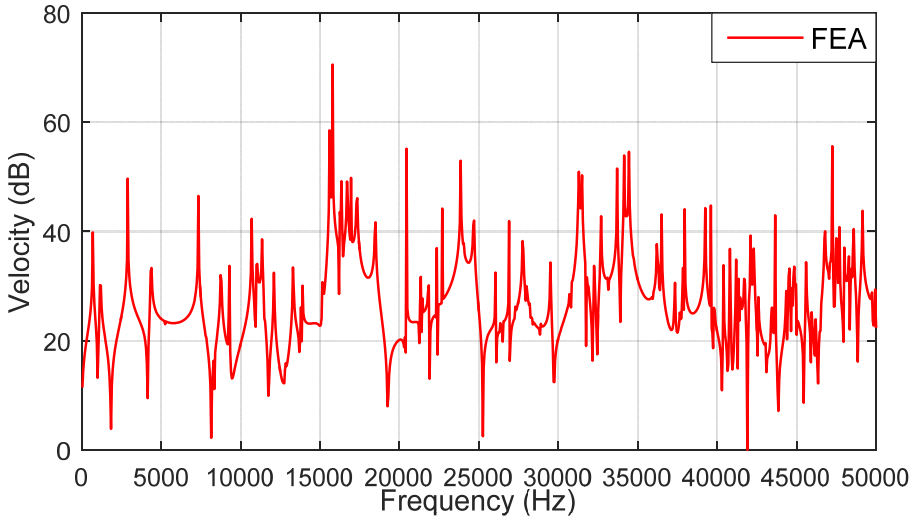


Figure 9.10 Frequency response of velocity of the surface of aluminum case.

## 9.5 Acoustic Analysis and Prediction

The ultimate goal of this chapter is to predict the acoustic noise of ultra-high speed SRMs. After the modal and harmonic response analysis, an acoustic FEA is used to predict the sound pressure level (SPL).

### *9.5.1 Modeling*

The vibration of the surfaces of electric machines emit energy to the contacting air molecules. Then this energy will diffuse to the nearby molecules and a series of sound waves is generated. This type of propagation is generally spherical with a speed of 340 m/s in the air. As the sound wave propagates, the energy from the vibration of the motor surfaces will be dissipated and attenuated in the air.

In the FEA, a sphere enclosure with a radius of 0.3 m is modeled as the surrounding air of the SRM. By enclosure it means the body of the motor is excavated from the model, leaving only the outside of the surrounding air. The sphere is then cut into two halves in order to observe the SPL distribution of the surroundings, as shown in Figure 9.11. The gray illustrates the surrounding air. The green piece is hollow, in the shape of the complete machine including the case and support.

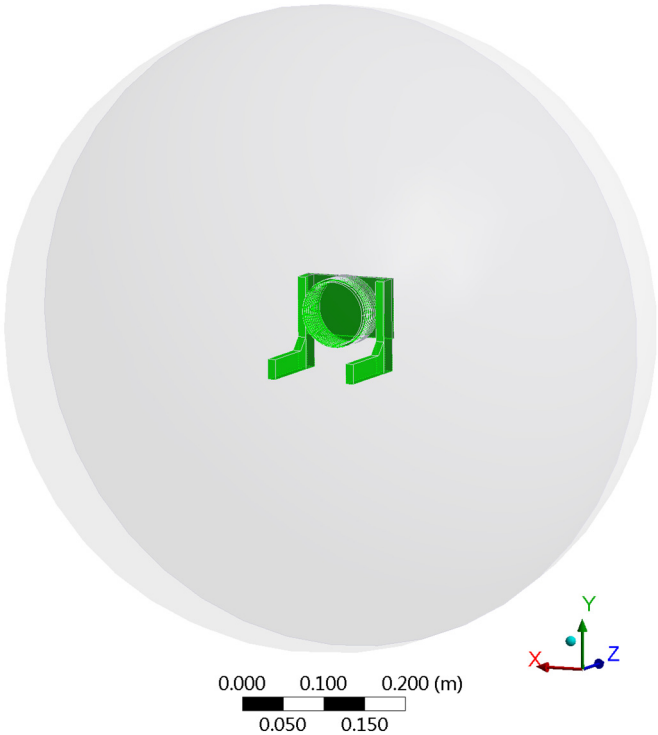


Figure 9.11 Modeling of the acoustic analysis.

### *9.5.2 Model Setup*

The next step is to determine the excitation of the vibration. The vibration velocity at the surface of the motor is mapped from the harmonic response analysis into the corresponding boundary surfaces of the enclosure (i.e., the surfaces that contact the motor). All the 85 surfaces of the motor are mapped. By importing the velocity from the harmonic response analysis, the displacement and acceleration can be also be determined. The velocity is known at frequencies up to 50,000 Hz with a step of 50 Hz.

### *9.5.3 A-weighted Sound Pressure Level*

In practical applications, the background noise can fluctuate. Usually, the sound pressure level is used to evaluate the intensity of the sound. The SPL is a logarithmic

measure of the effective pressure of the sound relative to a reference value. This reference is commonly chosen to be the threshold of human hearing, which is roughly the sound of a mosquito flying 3 meters away (that is $p_0$=20 μPa). Sound pressure is given by,

$$\mathrm{SPL} = 20\log_{10}\left(\frac{p}{p_0}\right)\ \mathrm{dB} \tag{9.8}$$

where $p$ is the rms value of the sound pressure, $p_0$ is the reference sound pressure.

The so-called A-weighted SPL is the most commonly used measurement of noise level defined in the IEC 61672:2003 standard. This is because it takes into account the relative volume perceived by the human ear, which is less sensitive to low audio frequencies [125]. It can be calculated as,

$$A(f) = 20\log_{10}(R_A(f)) + 2.00 \tag{9.9}$$

where the weighting function $R_A(f)$ is,

$$R_A(f) = \frac{12194^2 \cdot f^4}{(f^2 + 20.6^2)\ \sqrt{(f^2 + 107.7^2)(f^2 + 737.9^2)}\ (f^2 + 12194^2)} \tag{9.10}$$

The SPL at two different distances r1 and r2 is,

$$\mathrm{SPL}_{p_2} = \mathrm{SPL}_{p_1} + 20\log_{10}\left(\frac{r_1}{r_2}\right)\ \mathrm{dB} \tag{9.11}$$

Figure 9.12 shows the noise level prediction in the surroundings of the motor at 100,000 rpm. At the location where the sound pressure meter is placed (around 10 mm from top of the motor case), the estimated result is 113 dB. This is extremely loud, and is equivalent to a jet engine or an non-electric chainsaw [125]. It should be noted however, that this intensity is very close to the machine.

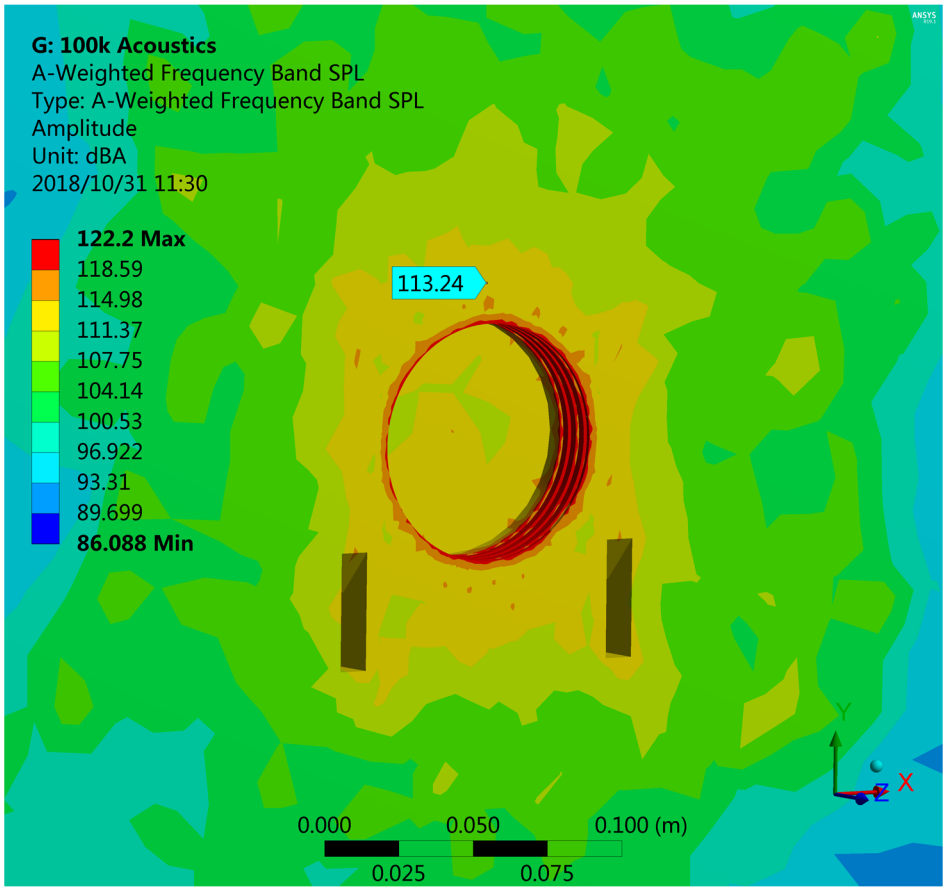


Figure 9.12 A-weighted SPL of the acoustic FEA at 100,000 rpm.

## 9.6 Experimental Verification

In order to verify the proposed multi-physics acoustic modelling of ultra-high speed SRMs, experiments were conducted on the 4/2 SRM.

### *9.6.1 Experimental Setup*

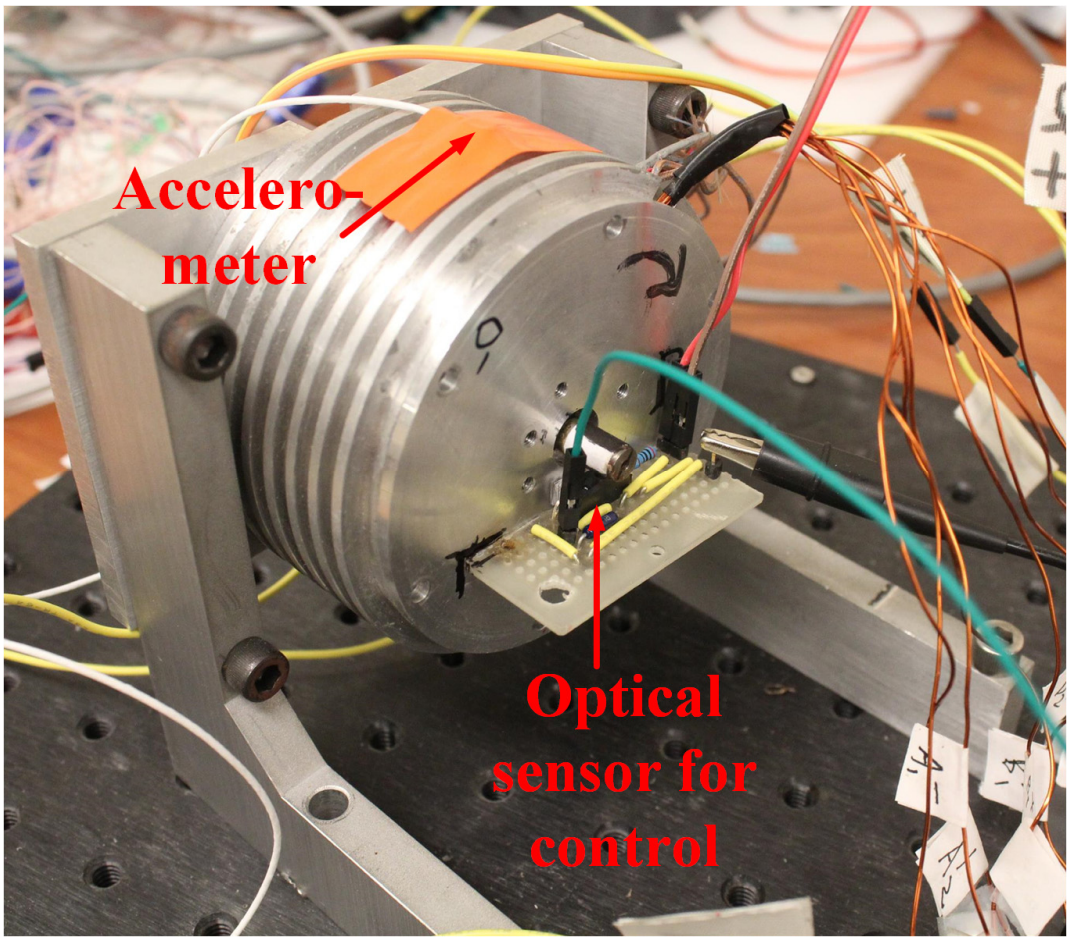


Figure 9.13 Experimental setup of the 4/2 ultra-high speed SRM.

Figure 9.13 shows a picture of the 4/2 ultra-high speed SRM setup. An accelerometer positioned on the top of the aluminum case is used to measure the vibration. The motor is controlled using a DSP and FPGA, along with two customized optical sensors [123] as described in Chapter 8. Figure 8.12 shows the block diagram of the close loop control system. Two conventional MOSFET-based asymmetric inverter drive boards are used for each phase.

### *9.6.2 Verification of Natural Frequencies*

The acceleration of the surface of the motor at 100,000 rpm is measured and recorded from the accelerometer with a sampling frequency of 2 Ms/s. The frequency response of the vibration is shown in Figure 9.14. The natural frequencies are clearly seen and labeled in the figure. Table 9.1 shows a comparison of the natural frequencies from the FEA and the experimental results for the first 16 modes. As can be seen, at the lower frequencies the prediction show a small discrepancy from the measurement. This is due to fact that the FEA results remain accurate as the mode number increases (the error less than 5%). Note that there are two additional vibration modes between the 8th and 9th natural frequencies observed in the experiment, which are not predicted by the FEA. This is likely a result of the simplification of the model, which does not include modalities associated with the windings, fasteners and assembly non-idealities.

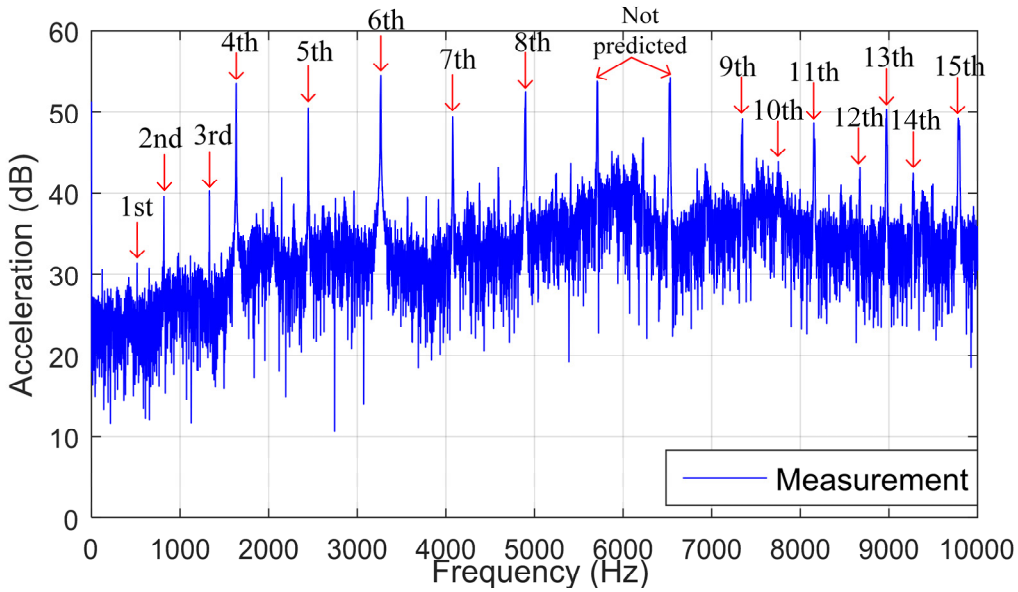


Figure 9.14 Measured frequency response at 100,000 rpm.

Table 9.1 Comparison of natural frequencies between FEA and experiment

| Mode No. | 1 | 2 | 3 | 4 | 5 | 6 |
|---|---|---|---|---|---|---|
| FEA (Hz) | 619 | 705 | 1173 | 1886 | 2898 | 3072 |
| Exp (Hz) | 515 | 818 | 1331 | 1634 | 2448 | 3265 |
| Error (%) | 20.2 | 13.8 | 11.9 | 15.4 | 18.4 | 5.9 |
| Mode No. | 7 | 8 | Not Predicted | | 9 | 10 |
| FEA (Hz) | 4374 | 5252 | | | 7353 | 7837 |
| Exp (Hz) | 4077 | 4901 | 5712 | 6533 | 7348 | 7752 |
| Error (%) | 7.3 | 7.2 | NA | NA | 0.1 | 1.1 |
| Mode No. | 11 | 12 | 13 | 14 | 15 | 16 |
| FEA (Hz) | 8345 | 8745 | 8771 | 9247 | 9302 | 10628 |
| Exp (Hz) | 8153 | 8672 | 8975 | 9276 | 9783 | 10600 |
| Error (%) | 2.4 | 0.8 | 2.3 | 0.3 | 4.9 | 0.3 |

### *9.6.3 Verification of Acoustic Prediction*

#### 9.6.3.1 Measured A-weighted SPL at 100,000 rpm

An A-weighted SPL meter is placed 10 mm on top of the motor case to measure the acoustic noise. Figure 9.15 shows the measurement results. The motor speed is gradually increased up to 100,000 rpm at 18s. At 25s the supply voltage is turned off. It can be seen from the figure that the steady state SPL is between 108 and 115 dB. The reason for this variation is that when the motor reaches the reference value, the speed PI controller sets the reference current to zero, turning off the MOSFETs. This means that at 100,000 rpm, with the excitation voltage, the SPL is 115 dB, which is very close to the 113 dB predicted value shown in Figure 9.12.

It is interesting to note that at the instant when the power is turned off, the SPL had an instantaneous increase to 120 dB. This finding is consistent with reference [116], which states that "the greatest stator vibration was excited by turn-off of the current."

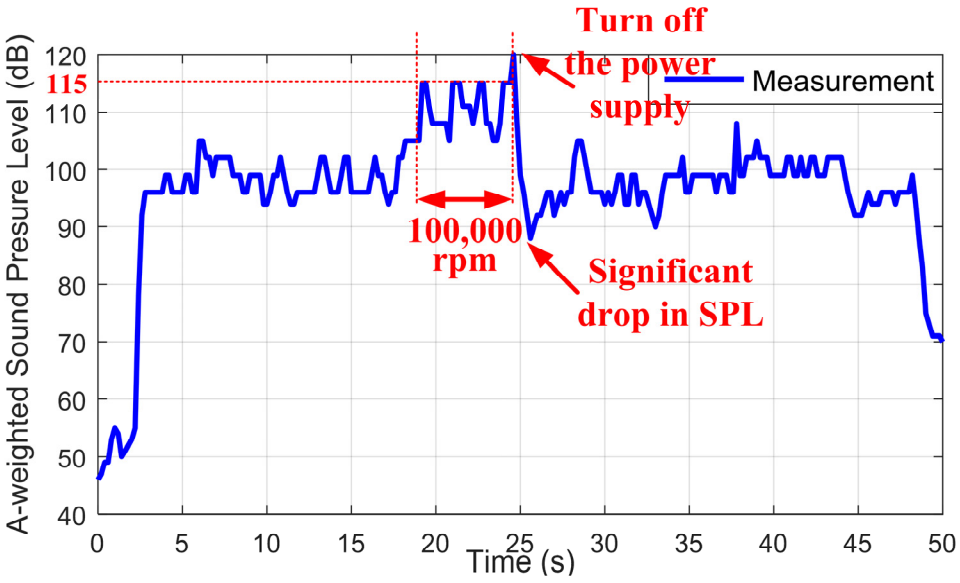


Figure 9.15 Measured A-weighted SPL at 100,000 rpm.

9.6.3.2 Impact of Bearings

At ultra-high speeds, the bearing noise is often thought to be in the same range as the noise due to the radial force. From Figure 9.15, it can be seen that there is a significant drop in the SPL down to 90 dB at 25s, when the power is turned off. That means the SPL due to the bearings is only 90 dB. From 25s to 50s when the motor is fully stopped, the average SPL is around 100 dB. This is more than 10 dB lower than 115 dB with the motor on. As shown in (9.12), the noise generated purely by the radial force is still 114.86 dB. This shows that for ultra-high speed SRMs at 100,000 rpm, bearing noise is rather insignificant.

$$SPL = 10\log_{10}(10^{115/10} - 10^{100/10}) = 114.86 \text{ dB} \qquad (9.12)$$

## 9.7 Conclusion

Switched reluctance machines (SRMs) are very competitive candidates for ultra-high speed applications due to their intrinsically simple and robust geometry. However, at speeds over 100,000 rpm, the acoustic noise can be a significant hindrance. In this Chapter, a multi-physics acoustic modeling and prediction of ultra-high speed SRMs was presented based on finite element analysis. First, a 3D electro-magnetic FEA is conducted to calculate the radial force on the stator teeth, which is the origin of the noise. A modal analysis and a harmonic response analysis were then conducted to estimate the natural frequencies and the vibration of the whole motor with the case and support included, using the calculated radial force as the input excitation. Next, an acoustic response analysis was conducted to estimate the A-weighted sound pressure level. Finally, in order to verify the proposed model, experiments were done to measure and compare the natural frequencies and the SPL of a 4/2 ultra-high speed SRM at 100,000 rpm. The results show that the A-weighted SPL of the motor is as high as 115 dB, which matches the simulation results 113 dB well. The impact of the bearing is proved to be negligible compared with the noise generated by the radial force. The proposed study gives a good method of estimating the noise level for ultra-high speed SRMs and provides a good foundation for the future noise reduction study of ultra-high speed SRMs over 1,000,000 rpm.

# CHAPTER 10. SYSTEM INTEGRATION AND TEST RESULTS

## 10.1 Introduction

Due to the use of aerostatic bearings, special attention needs to be taken in the mounting and assembling of the motor. This chapter presents the detailed system integration and prototyping of the whole motor. Proper housings and air compression systems are designed and integrated together. The motor was then tested and a detailed experimental analysis is shown.

## 10.2 Stator Prototype

According to the electromagnetic design in Chapter 5, a prototype of the stator is made. To fix the stator and reduce the deformation due to resonance, four outer tabs with a hole of 4 mm in diameter each are added at the position of the four teeth. Figure 10.1 shows one piece of stator lamination and the prototype of the stator. 50 turns of Litz-wire are then wound manually layer by layer around each stator tooth, as shown in Figure 10.2.

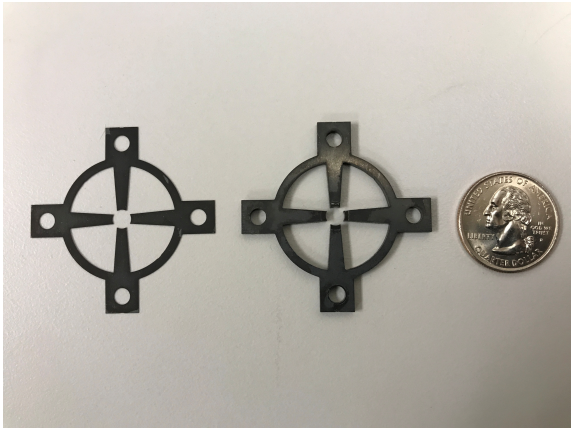

Figure 10.1 Stator lamination and prototype.

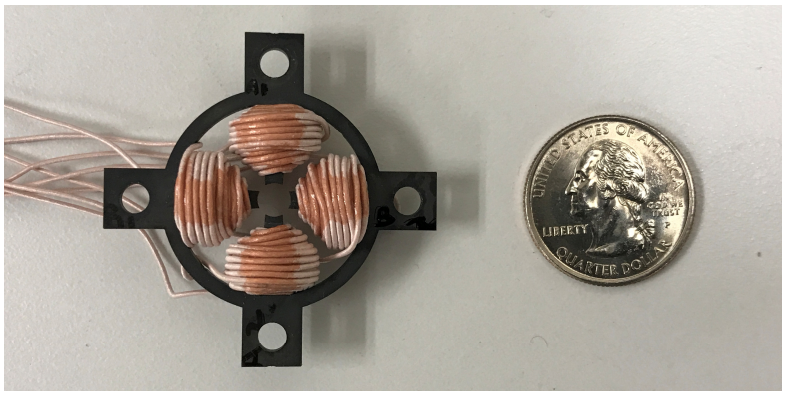


Figure 10.2 Stator prototype with windings.

## 10.3 Machine Assembly

### *10.3.1 Bearing Housing and Face Collars*

Since the machine is designed to run over 1 million rpm, ball bearings are not feasible. A pair of hydrostatic air bearings are used as described in Chapter 4. To integrate the bearings with the rest of the machine, a pair of bearing housings have been designed. Special epoxy is used to provide additional damping for the bearings.

The air bearings provide support in both radial and tangential directions. In order to prevent the shaft from moving in the axial direction, two face collars have been designed. In the first attempt, two small screws are used to fix two aluminum face collars with the shaft. Note that the length of the air bearings and face collars are designed to be a minimum length of 7.5 mm and 3 mm, respectively, in order to reduce the overall length of the shaft and push the critical speeds as high as possible. Figure 10.3 shows an air bearing in a bearing housing and two aluminum face collars.

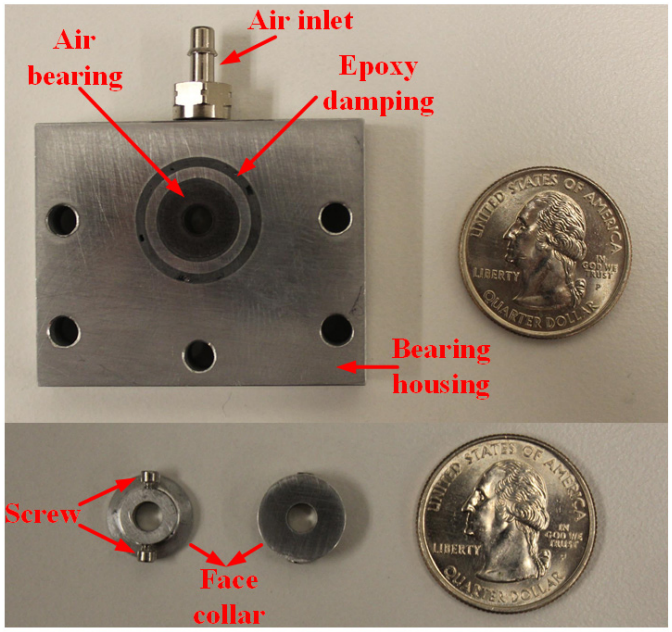


Figure 10.3 Air bearing, bearing housing and face collars.

*10.3.2 Sensor Tables*

Motor control at 1 million rpm is very challenging. No commercial encoders are available on the market for such high speed. Sensorless control is undoubtedly even more challenging. A pair of customized optical sensors are used to control the motor at 1 million rpm using very simple one pulse control at ultra-high speeds. To mount the sensors a pair of tables are designed to integrate the optical sensors. The sensor tables are designed so that the height can be adjusted in order to optimize the sensor reflection and concomitant signal integrity. The adjustable sensor tables are shown in Figure 10.4.

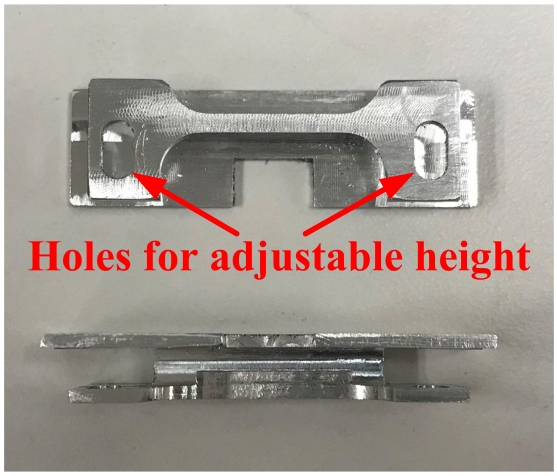


Figure 10.4 Adjustable sensor tables.

*10.3.3 Final Assembly*

In order to integrate the stator with the rest of the motor, two aluminum cases have been designed. The cases also act as spacers to prevent the windings from contacting the air bearings. The final assembly of the complete motor is shown in Figure 10.5 [126]. Finally, the completed prototype of the motor is shown in Figure 10.6.

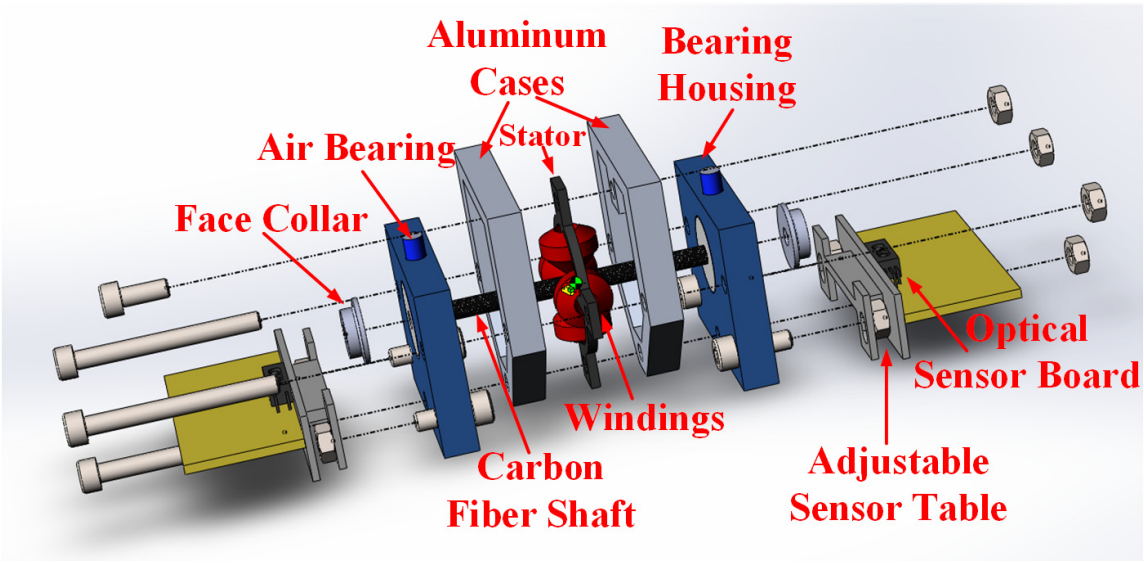


Figure 10.5 Final assembly of the proposed ultra-high speed SRM.

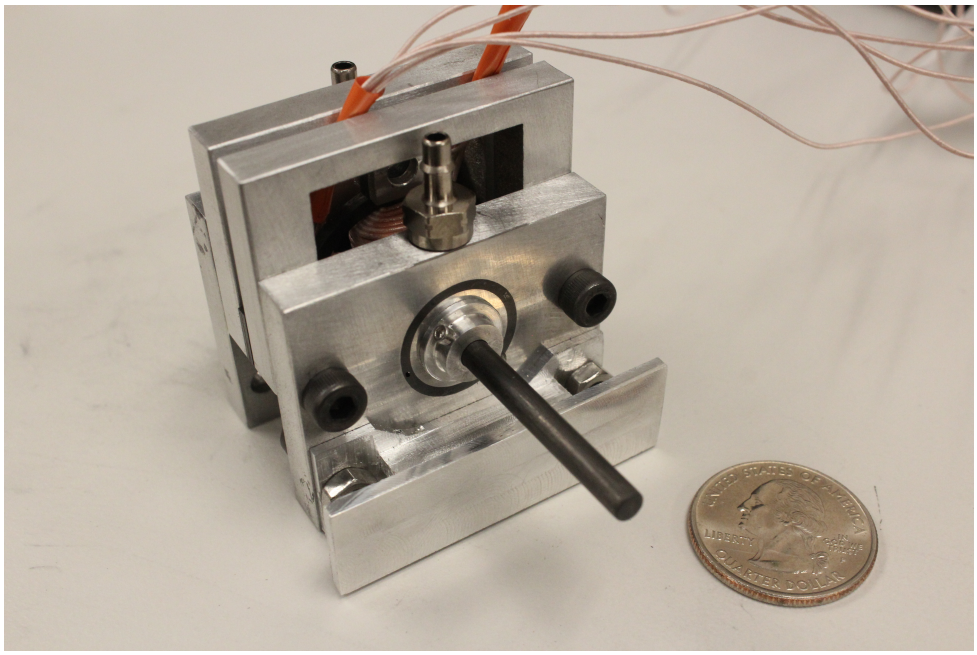

Figure 10.6 Prototype of the 1 million rpm SRM.

*10.3.4 Alignment Issues*

The last but not least step is to align and balance the entire drive system. Due to the small size of the motor, the air gap is designed to be very small (0.3 mm). Even this air gap length is relatively quite large when considering the tiny size of the motor. The typical value is around 0.1 to 0.25 mm [113]. Nevertheless, a "larger" air gap allows for higher mechanical tolerances.

The alignment is the most important step of the overall success of the motor design. Owing to the separate half-case design, the rotor can be aligned and measured in the middle of the stator teeth half by half. One half of the case can be aligned with the left bearing and shaft first, and then aligned with the other half. Figure 10.7 shows an illustration of this process.

Another way to align the rotor in the right axial position is to apply low voltage DC current to one phase windings. The electromagnetic force will align the rotor stack automatically in the right position.

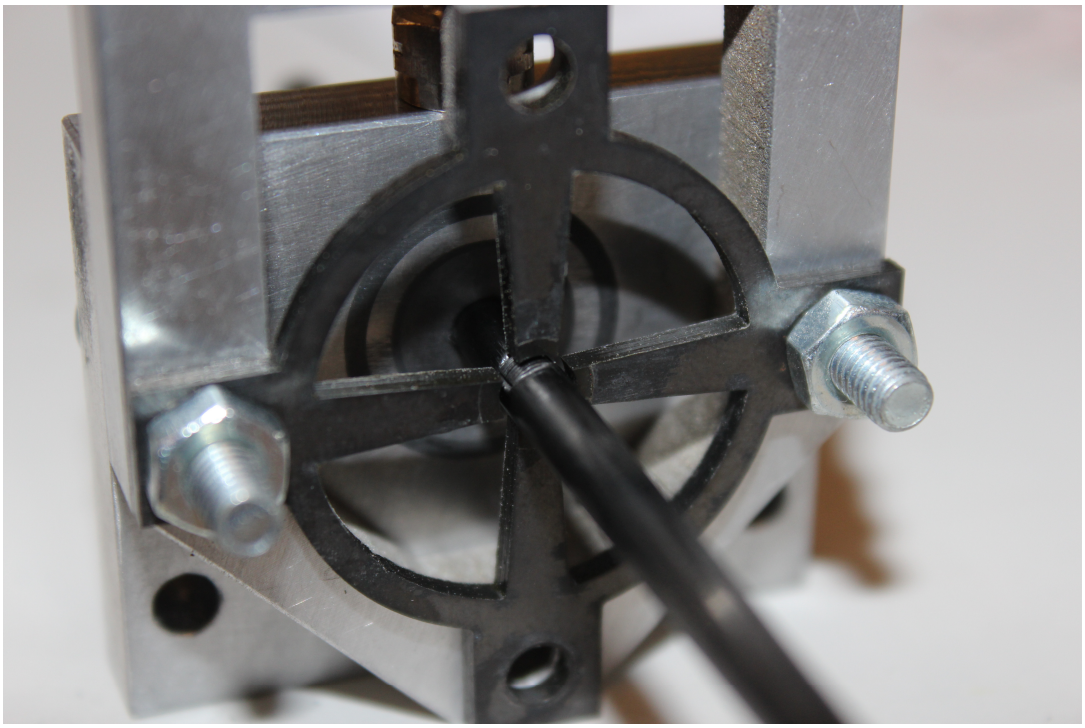

Figure 10.7 Alignment of the shaft with the stator half by half.

When doing the alignment, it was found that the two aluminum face collars with screws are not balanced enough to rotate at ultra-high speeds. Thus, two carbon fiber face collars with proper interference fit are made. Figure 10.8 shows the motor with two carbon fiber face collars.

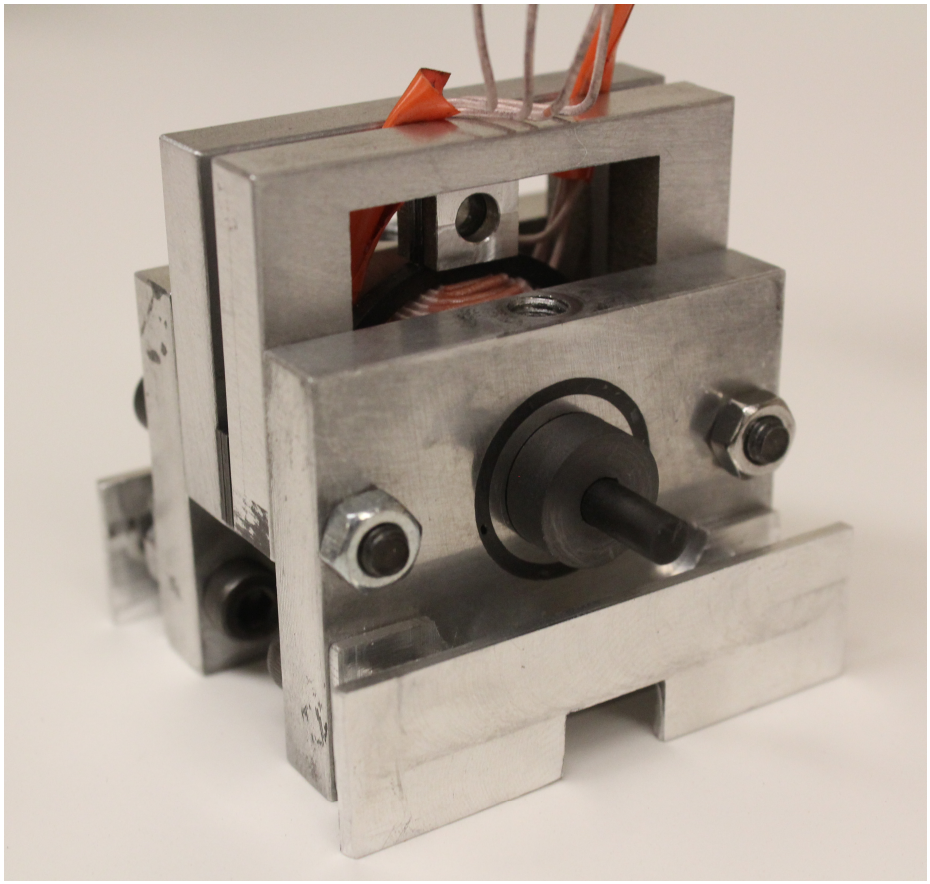

Figure 10.8 Motor with carbon fiber face collars.

## 10.4 Fitting and Tubing

The fittings and tubing are very tricky. The rated working pressure of the air bearings is between 60 psi to 90 psi. At such high pressure, a solid connection between the fittings and tubing is very important. Various fittings with different sizes and styles are tried. It is found that using 3/16" barbed brass fittings with 6mm OD, 4mm ID nylon tubing provides the best bonding. Figure 10.9 shows various fittings and union tees have been tried. Figure 10.10 shows the polyurethane tubing and nylon tubing.

Figure 10.9 Various fittings and union tees.

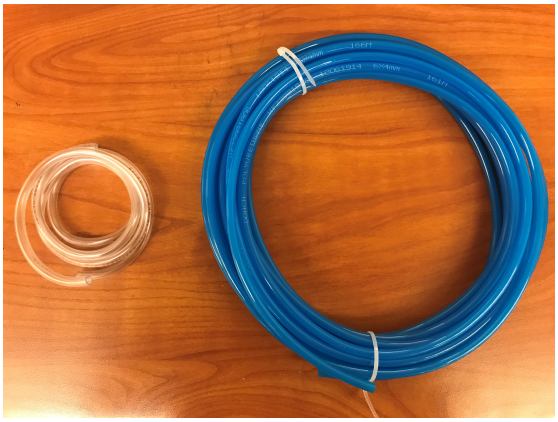

Figure 10.10 Polyurethane tubing (left) and nylon tubing (right).

## 10.5 Air Compression System Setup

After the whole motor is completed, proper air compression system is installed. In order to get pure air into the bearings, two air filters from RTI are installed. An air regulator with a pressure gauge is also installed to control the air flow at certain air pressure. Figure 10.11 shows the air filters. Figure 10.12 and Figure 10.13 show the air regulator and the pressure gauge, respectively.


Figure 10.11 Air filters from RTI.

Figure 10.12 Air regulator.

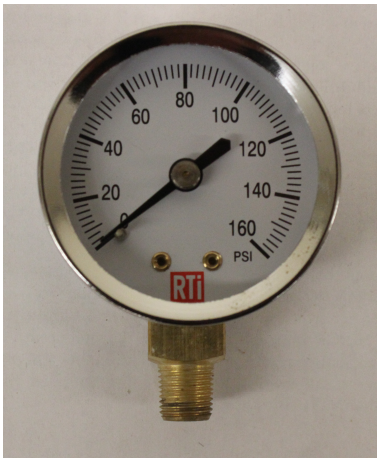


Figure 10.13 Air pressure gauge.

After going through the air filters, the clean and dry air then separates into two paths using a 3/16" barbed union tee. Three segments of 0.25" OD, 0.17" ID polyurethane tubing are used to connect the 3/16" barbed fittings of the air bearings. Note that all the connections must be sealed properly and there should be no air leak throughout the air path. Figure 10.14 shows the setup of the complete air compression system.

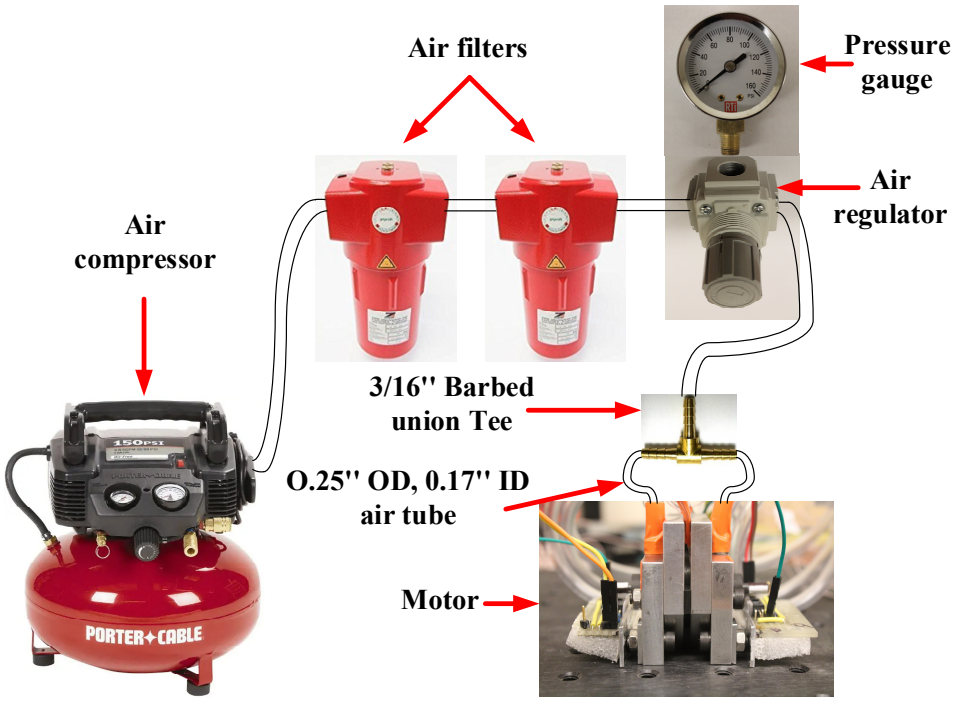


Figure 10.14 Setup of the air compression system.

## 10.6 Experimental Results

### *10.6.1 Inductance Measurement*

In order to verify the FEA models, $L_d$ and $L_q$ are measured using Keysight E4990A impedance analyzer. Considering the working frequency, low voltage and high frequency excitation signals are applied to each phase from 20 Hz to 100 kHz. The magnitude and

phase angle of the winding impedance of each phase are measured at different frequencies. Figure 10.15 shows a screenshot of the measurement of phase A inductance at the aligned position, which is defined as $L_d$. As can be seen, the magnitude of the impedance is linear with the change of frequency. The inductance can be read directly from the screen.

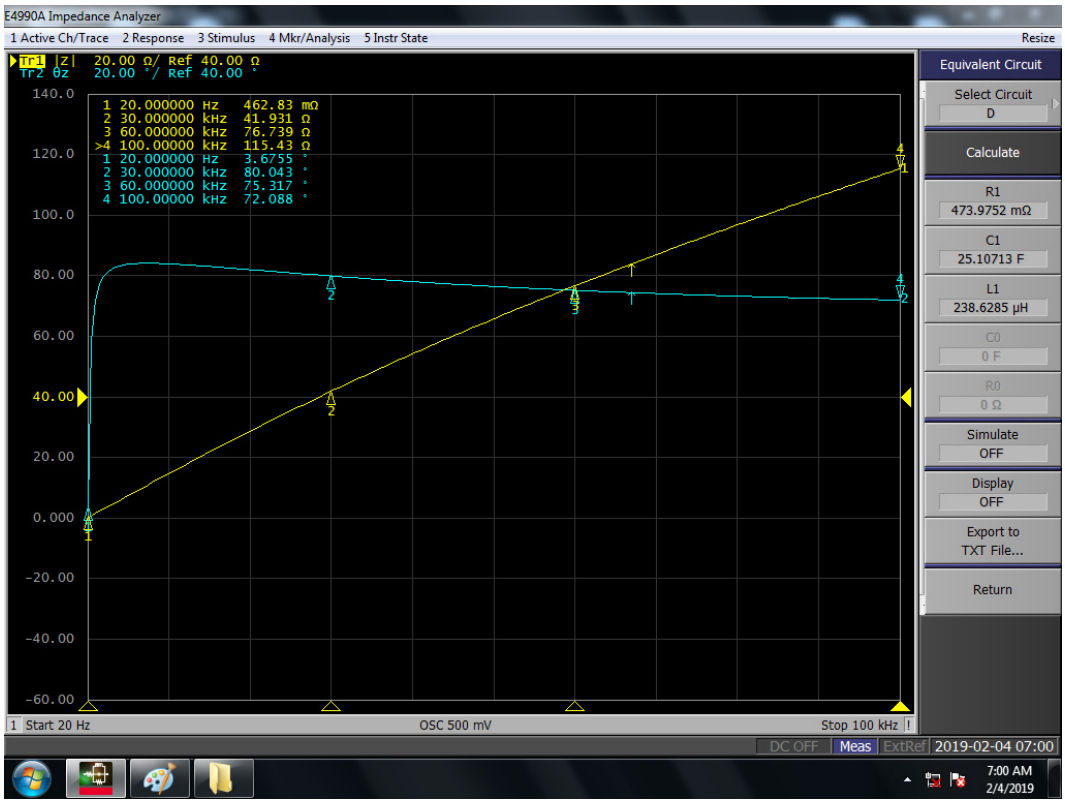


Figure 10.15 Inductance measurement of phase A at the aligned position.

Because of the unusually large number of turns of the phase windings, the 3D end effect needs to be taken into account. A 3D FEA model is built and shown in Figure 10.16.

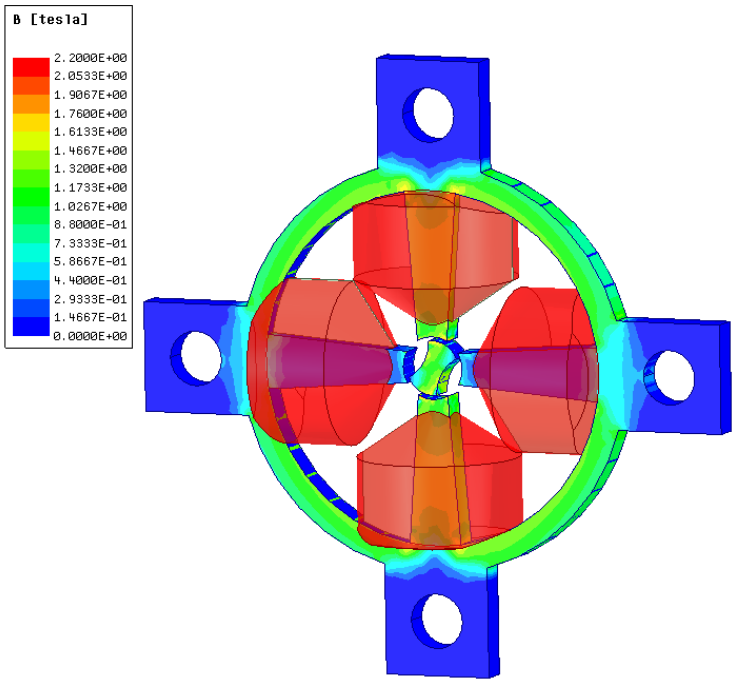


Figure 10.16 3D FEA of the motor.

Both phase A and B inductance are measured at 0° (unaligned), 30°, 60° and 90° (alinged). Figure 10.17 shows the comparison of the inductance of 2D FEA, 3D FEA and experiment. It can be seen that, due to the fringing flux from the 3D end effect, the estimated inductance of 3D FEA is larger than 2D FEA. The measured inductance is between the 2D and 3D FEA estimation. Nevertheless, the slopes of the inductance profile from unaligned position to aligned position, which determine the output torque, are similar among the three.

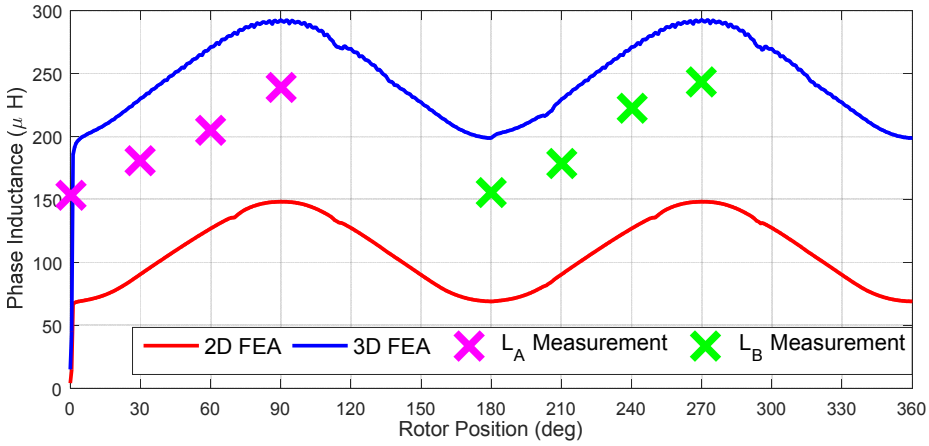


Figure 10.17 Comparison of inductance of 2D FEA, 3D FEA and experiment.

### *10.6.2 Current Comparison*

The motor was first run at 78,000 rpm. Figure 10.18 shows the comparison between 2D FEA and experiment under the DC voltage supply of 18V. Each phase is switched on from 0° to 45°. As can be seen the results match well. Note that the rms value of the phase current is 9A, which is larger than the rated value. Considering that the motor only ran for a very short period, this high current value is acceptable.

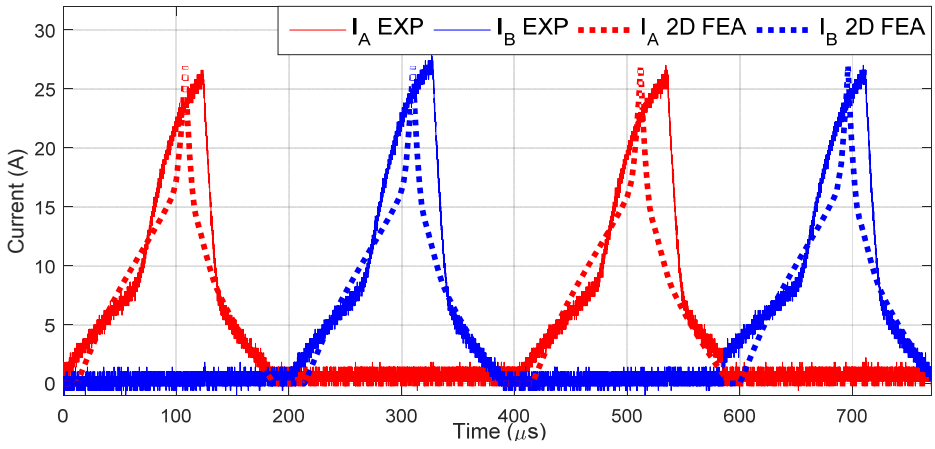


Figure 10.18 Current comparison between 2D FEA and experiment at 78,000 rpm under 18 Vdc.

### *10.6.3 Torque Estimation*

Because of the ultra-high speed and critical balance, no torque sensor can be used to estimate the output torque. Nevertheless, FEA can be used to estimate the output torque, considering the good agreements of the current profiles as shown in Figure 10.18. As can be seen from Figure 10.19, the average output torque is 2.5 mNm.

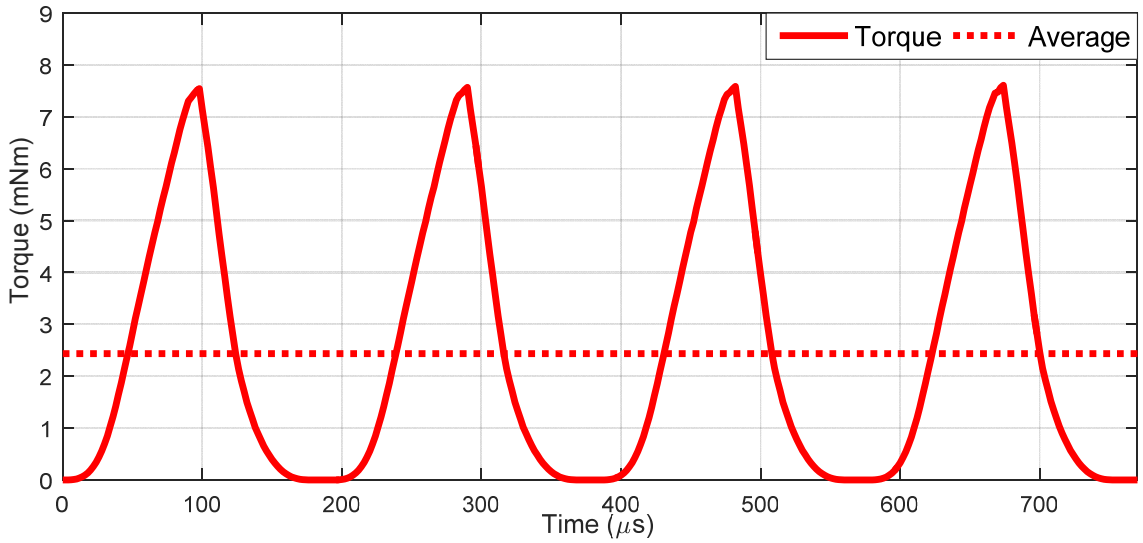


Figure 10.19 Torque estimation from 2D FEA at 78,000 rpm.

To increase the maximum speed, the maximum instantaneous current limited by the sensor board for protection purpose is changed to 40 A. This is the highest protectable current that can be achieved by the sensor board, and can be changed by adjusting the resistor values. For each phase, there are two variable resistors that set the current limits (one for positive limit and another for negative limit), as shown in Figure 10.20. In order to set an accurate value of current limit, one can wrap several turns of wires around the current sensors and inject DC current into the wires. The current limit would be the current going through the wire multiply by the number of turns.

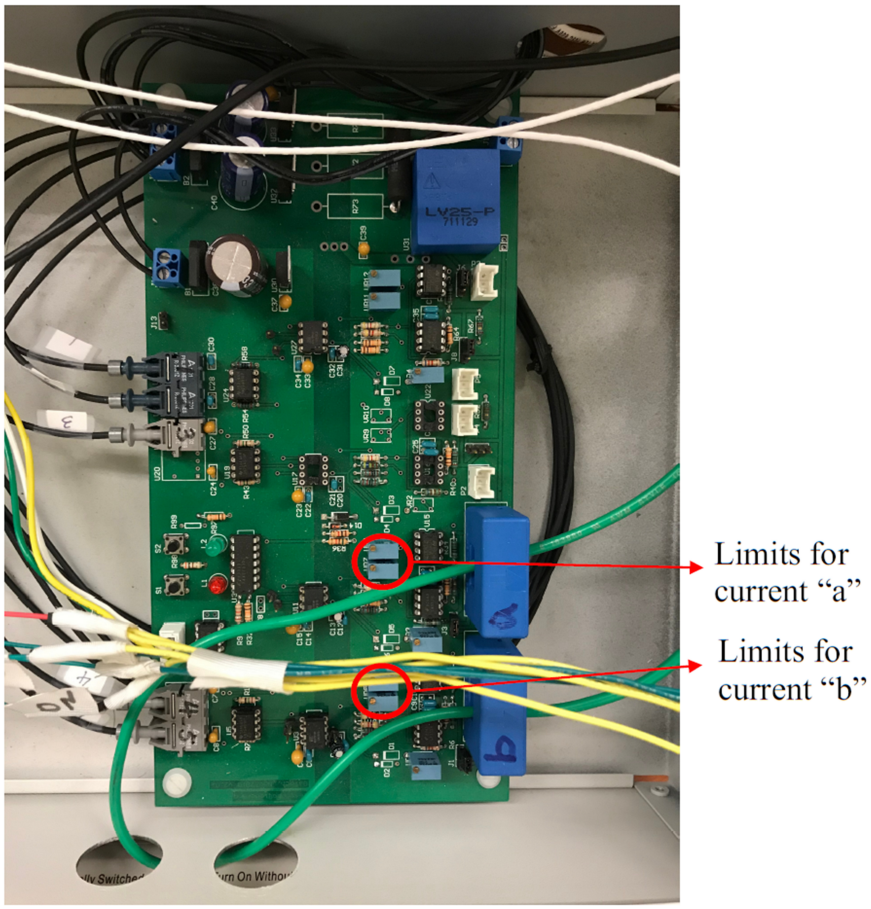


Figure 10.20 Variable resistors for changing the current limit.

After the current limit is set to the maximum value of 40 A, the motor was run up to 90,000 rpm. Figure 10.21 shows the test results of the voltage (yellow), optical (blue), current A (green) and current B (magenta). It can be seen that the rotational speed is 2.98 kHz/2*60≈90,000rpm.

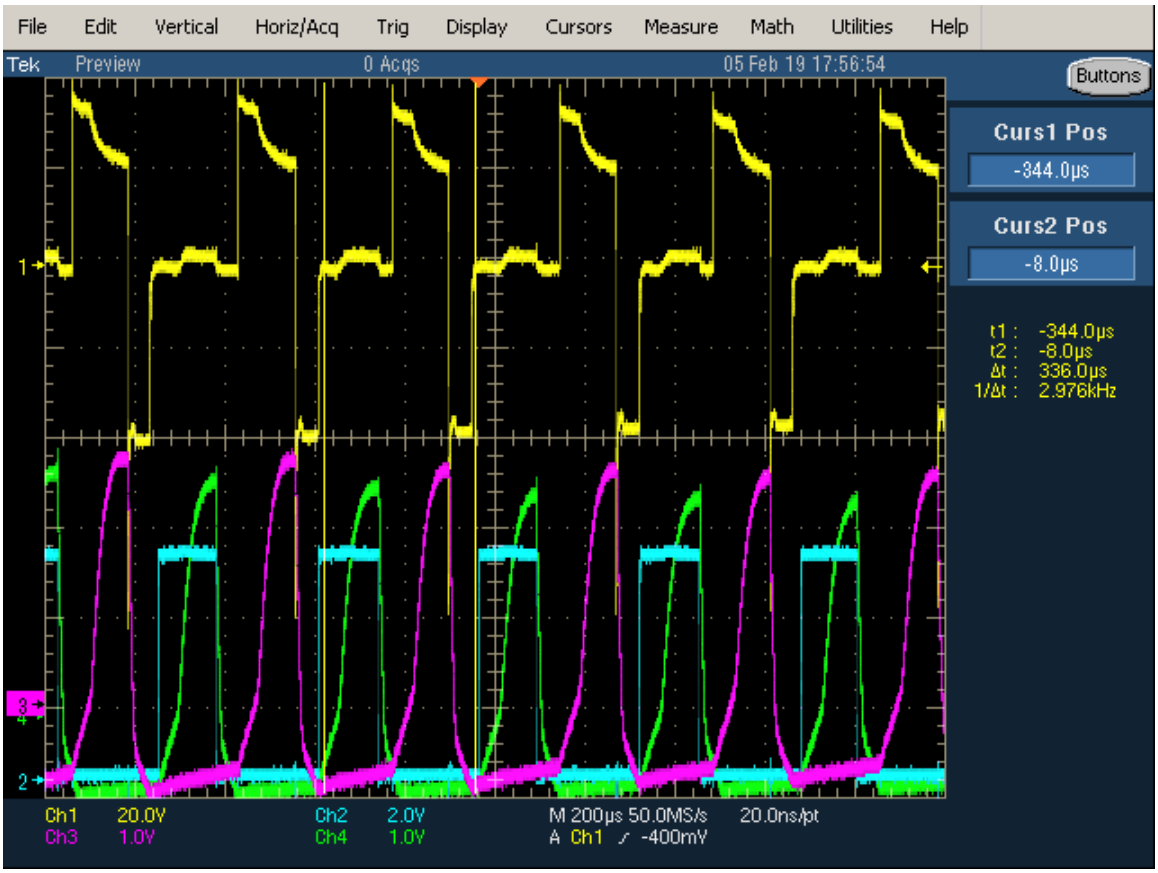


Figure 10.21 Test results at 90,000 rpm.

## 10.7 Freewheeling Test

The unexpectedly large air friction torque of 2.5 mNm at 78,000 rpm is the main obstacle that prevents the motor from reaching even higher speeds. Several freewheeling tests were conducted to analyze the air friction torque under no excitation. The rotor and shaft was accelerated to a certain speed for a while, then the power supply is cut off and the motor is slowed down by bearing friction.

To measure the speed, the signal from the optical sensors is recorded at a sampling rate of 40,000 samples/s ($\Delta t$=25 µs) for 10 seconds. The time difference of the adjacent zero crossing points is calculated and converted to the actual speed in Matlab. Not that the

frequency of the optical signal is twice of the rotational speed due to the two rotor poles. It was found that at speeds blow 40,000 rpm, the air friction torque is very low as expected. However, it creases dramatically from 40,000 rpm.

### *10.7.1 Speed below 40,000 rpm*

The motor was first run at 30,000 rpm and then freewheeled down to 10,000 rpm in 10 seconds. A cubic function was then used to fit the curve. Figure 10.22 shows the experimental data and the fitted curve.

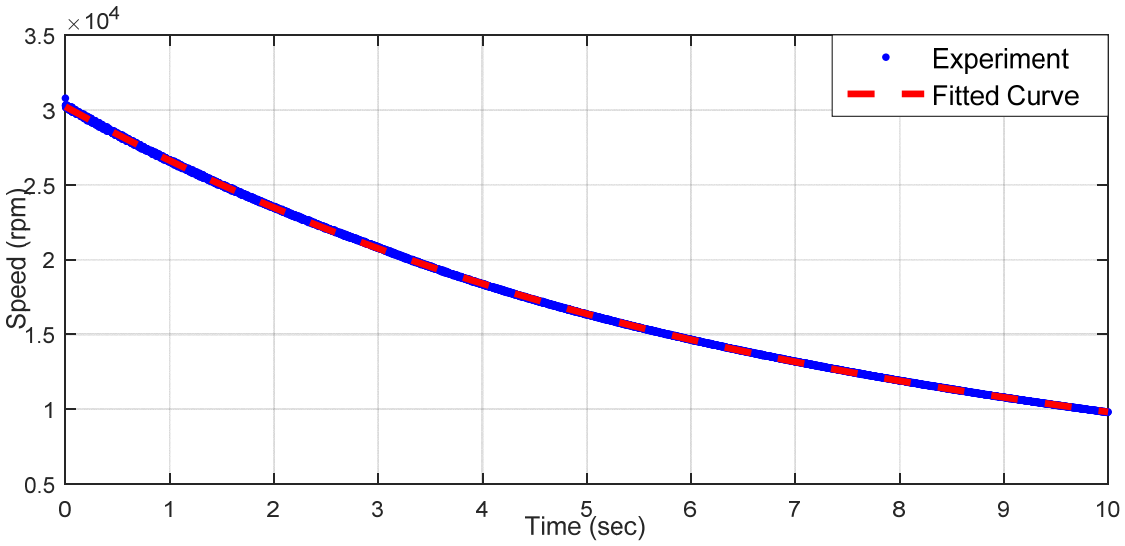


Figure 10.22 Freewheeling test at 30,000 rpm.

The fitted relationship of the speed $n$ in rpm versus time $t$ is shown in (10.1).

$$n = -6.95t^3 + 250.1t^2 - 3844t + 30210 \tag{10.1}$$

So the deceleration at t=0s is

$$\left.\frac{d\omega}{dt}\right|_{t=0} = -3844/60 \times 2\pi = 402.54 \, rad/s^2 \tag{10.2}$$

The inertia of the pure shaft is estimated to be 3e-9 kg.m$^2$ using Solidworks. It can also be modeled roughly as a pure cylinder made of carbon fiber. So the inertia of the pure shaft is:

$$J = \frac{1}{2}mr^2 = \frac{1}{2}\rho(\pi r^2 l)r^2 = \frac{1}{2}\times 1.8\times 1000\times \pi \times 0.06\times 0.002^4 = 2.7\times 10^{-9}\,\mathrm{kg\cdot m^2} \quad (10.3)$$

which is about the same value.

The inertia of the shaft with the two carbon fiber face collars is estimated to be 2e-8 kg.m$^2$ using Solidworks. So the load torque, which is the bearing friction torque, can be calculated as

$$T_f = J\frac{d\omega}{dt} = 2\times 10^{-8}\times 402.54 = 8.1\times 10^{-6} = 8.1\ \mu\mathrm{N\cdot m} \quad (10.4)$$

The corresponding FEA predicted value at the same operation condition is 10 μNm at $Vdc$= 2V, $I_{max}$=1A, which validates this estimated torque from measurement. This value is within the range of a reasonable expected windage torque. However, it is about 300 time lower than the friction torque at 78,000 rpm! This phenomena of low friction torque at 30,000 rpm and extremely high friction torque at 78,000 rpm is very abnormal and needs to be analyzed in detail.

*10.7.2 Speed beyond 40,000 rpm*

In order to find the reason for the low friction torque at 30,000 rpm and tremendously large friction torque at 78,000 rpm, more freewheeling tests at 35,000 rpm, 45,000 rpm, 62,000 rpm and 80,000 rpm were conducted. Figure 10.23 shows the freewheeling test results at different speeds. As can be seen, there is a knee point at round 40,000 rpm. Below

this speed, the air friction is very low. Once the speed increases beyond this value, the slope of the speed time curve, which is proportional to the deceleration, increases dramatically. This reveals the reason for unreasonably large torque needed at ultra-high speeds. This finding suggests that the aerostatic bearings are good for "frictionless" applications below 40,000 rpm. For ultra-high speed applications beyond 40,000 rpm, they are not good choices.

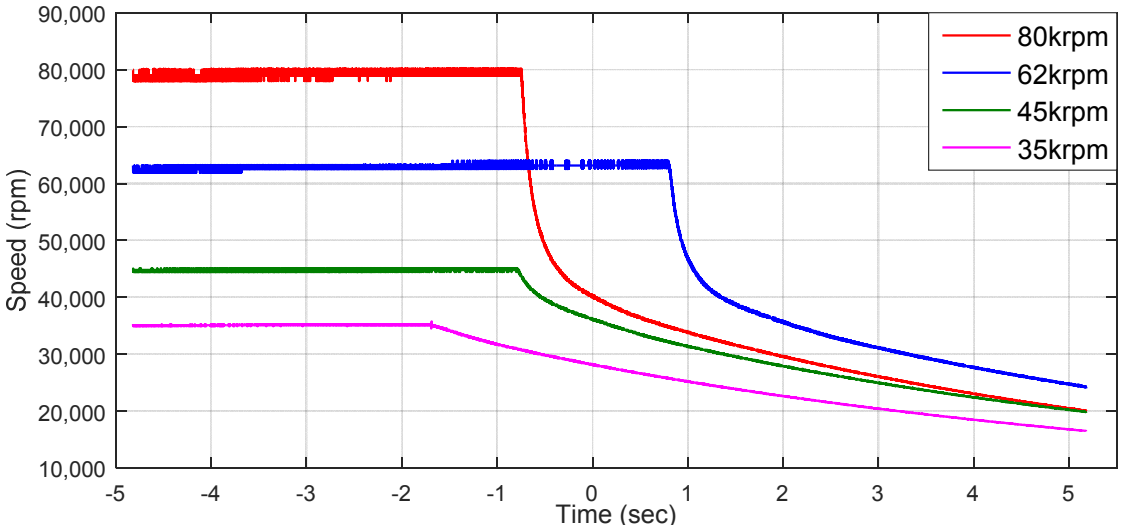


Figure 10.23 Freewheeling test results at different speeds.

## 10.8 Possible Reasons for Too Much Windage Torque

As analyzed before, the output torque, which is mainly due to the bearing friction, is way more than what was expected. Some possible reasons are listed as follows.

### *10.8.1 Unsmooth Surface Finish*

As is discussed in Chapter 4, the surface finish of the carbon fiber shaft is neither smooth nor round enough. For air bearings, especially aerostatic bearings, very accurate

shaft diameter and surface finish are critical to high speed operation. Usually the tolerance is the scale of micrometers [127]. For the specific bearings used in this project, the required roundness is 2.5 μm max and the surface finish needs to be 6 rms or better, according to the supplier. This is consider to be the major reason for the dramatical friction increase from 40,000 rpm.

### *10.8.2 Radial Force*

Another possible reason for the unexpectedly large air friction torque may be due to the periodically fluctuating radial force. Figure 10.24 shows the estimated radial force of phase A and B at 78,000 rpm. As can be seen, the radial force fluctuates at high frequency between 0 to 5 N. This value is very large, considering the small size of the motor. According to the bearing supplier, aerostatic bearings are supposed to work under extremely balanced and constant load conditions. This fluctuating radial force causes rotor wobbling, breaks the highly balanced rotor, and consequently increases the bearing friction torque.

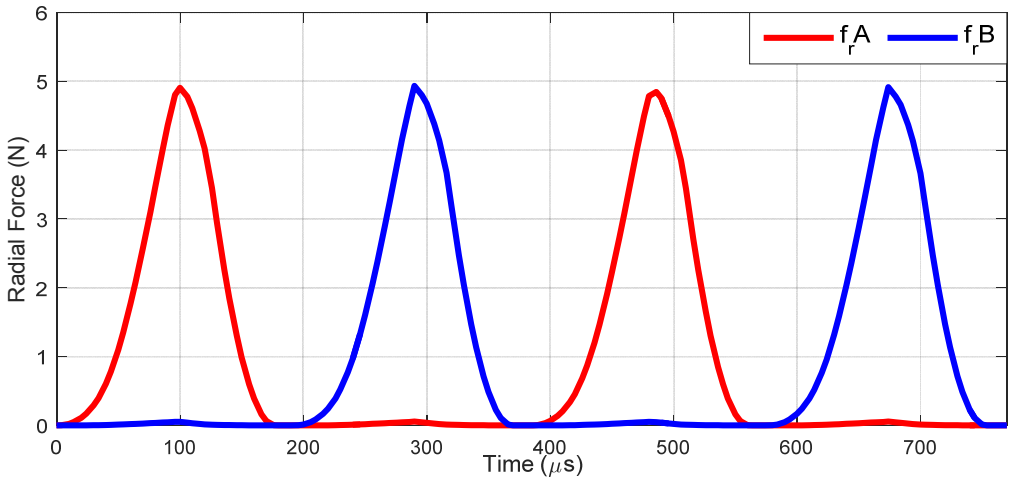


Figure 10.24 Estimated radial force at 78,000 rpm.

## 10.9 Conclusion

In this chapter, the system integration and assembly of the complete SRM system with the air compression system for the air bearings is presented. The motor consists of a stator, four windings, a shaft with rotor embedded, two aluminum cases, two air bearings and housings, two face collars and two optical sensors with adjustable sensor tables. The air compression system consists of an air compressor, two air filters, an air regulator with gauge, a barbed union tee and nylon tubing.

After the system is setup, the motor is tested. Detailed experimental results at ultra-high speeds are presented up to 90,000 rpm. The test measurements show that the motor inductance and current profile match the estimation from the FEA well. However, the unsmooth finish of the shaft surface and the fluctuating radial force increase the friction torque dramatically from 40,000 rpm, which prevents the motor from reaching even higher speeds.

# CHAPTER 11. CONCLUSION AND FUTURE WORKS

## 11.1 Conclusion

This dissertation has proposed a comprehensive design, analysis and control of ultra-high speed switched reluctance machines (UHSSRMs) for applications over 1,000,000 rpm. For the design, both mechanical and electromagnetic design have been conducted under ultra-high speed conditions. For the analysis, the rotor robustness, rotor dynamics and acoustic analysis have been shown in detail. For the control, the constant volts per hertz control and direct position control have been proposed for ultra-high speed applications. A 100,000 rpm and a 1,000,000 rpm SRM have been prototyped to validate the proposed ideas.

Chapter 1 has introduced the background and given a literature review for ultra-high speed electric machines. The expected challenges are also listed.

Chapter 2 has proposed a novel high-strength, high torque-density and high-efficiency rotor structure for UHSSRMs over 1,000,000 rpm. First, a benchmark "von-Mises" stress analysis is conducted to validate the boundary conditions and setups of the FEA. Then, the problems of the traditional rotor structures as well as the existing rotor structures are analyzed. Next, a novel rotor structure is proposed for UHSSRMs over 1,000,000 rpm. Finally, a comprehensive 3D FEA is conducted to validate the design.

Chapter 3 has conducted a rotor robustness analysis on the proposed new rotor geometry to improve the mechanical strength and bonding between the rotor stack and the clamping shaft, using proper high-strength adhesives. The cohesive zone model (CZM), a

model in fracture mechanics, is applied and a parametric study is conducted to find the optimal length of the rotor stack.

Chapter 4 conducted a rotor dynamics analysis of the proposed shaft. Both analytical and FEA have been used to find the natural frequencies of the shaft, which should be passed through quickly when operating the machine. Two alternative geometries have been proposed to increase the overall torque and their rotor dynamics characteristics have been compared with the original design. Three prototypes of the new rotor structure have been made to validate the manufacturing feasibility of the proposed design.

After the comprehensive mechanical design and analysis of the new rotor structure proposed in Chapter 2, 3 and 4, Chapter 5 focuses on the electromagnetic design of the 1,000,000 rpms SRM. New winding type and lamination materials have been used to generate enough torque at the rated speed based on the estimated windage torque.

Chapter 6 focuses on the electrical modeling and simulation of the SRM designed in Chapter 5. Both the Maxwell/Simplorer co-simulation and the fast equivalent model in Simulink have been proposed to validate the electromagnetic design.

Chapter 7 proposes a new constant volts per hertz (V/f) control for ultra-high speed SRMs. A detailed analysis of the current profile has been conducted. The simulation results show that the switching frequency over the entire speed range from 0 to 1,000,000 rpm is reduced to the minimum value.

Chapter 8 proposed a novel direct position control for UHSSRMs based on non-intrusive, low-cost optical sensors. The idea is to use non-contact optical sensors to detect

the rotor position and switch on/off the phase windings in the optimal position that generates the maximum output torque. A switching angle optimization has been conducted to generate the maximum torque based on the fast equivalent Simulink model. Experiments have been done to validate the control at 100,000 rpm.

Chapter 9 proposed a multi-physics acoustic analysis of UHSSRMs. First, the radial force is calculated using Maxwell. Then a modal analysis and a harmonic response analysis have been conducted to find the surface vibration of the motor, using the radial force calculated in the frequency domain. Next, an acoustic analysis has been conducted to predict the sound pressure level of the SRM at 100,000 rpm. The model predicts a 113 dB(A) sound, which matches the 115 dB(A) measurement well. The bearing noise is proven to be negligible compared with the sound generated by the radial force.

Chapter 10 gives the system integration of the 1,000,000 rpm SRM with two aerostatic bearings. The test results are compared with the FEA and good agreement is observed. However, the unsmooth surface finish of the carbon fiber shaft dramatically increases the air friction torque from 40,000 rpm, which stops the motor at 90,000 rpm and prevents the motor from reaching the target 1,000,000 rpm.

## 11.2 Recommendations for Future Work

Although the work presented in this dissertation has made contributions to the design, analysis and control of UHSSRMs, there are future improvements which may pave the way for further in-depth research in the related area.

### *11.2.1 Exploring More New Applications with the New Rotor Design*

Although the design proposed in this thesis is based on 1.2 million rpm. The new rotor geometry can be easily scaled down to "lower" speeds between 100,000 rpm to 1 million rpm. This will inspire many new applications for UHSSRMs where low cost or harsh working conditions are required, such as high speed turbo-chargers for automotive industry, high speed PCB spindles with an infinitely long lifetime and high-energy flywheels. There will be many possibilities and chances in these new applications.

### *11.2.2 Fatigue Analysis*

For these potential new applications in the real-world industry, a correct fatigue analysis of the shaft and bearings has to be conducted correctly. For example, with the high speed ceramic ball bearings, the 1 million rpm in [20] only runs for a very short time before the "disintegration of the ball bearings". Such a motor obviously will not pass the fatigue test and can not be used in real-world applications. However, with air bearings, a long-time stable and continuous running at ultra-high speeds might be possible, if the problem of high friction can be solved.

### *11.2.3 Investigation of the Influence of Temperature on Shaft*

Temperature is another important factor that will affect a reliable long-term operation at ultra-high speeds. The difference of the thermal expansion between the rotor and the shaft may cause some mechanical failures, if the motor runs for a long-time under large loads. A deep investigation of the influence of temperature on the shaft has to be conducted.

### *11.2.4 New Shaft with High-Accuracy Surface Finish*

Based on the test results and feedback from the bearing supplier, it seems that the surface finish of the shaft is extremely important for the air bearings to work properly at ultra-high speeds. A new shaft with much better roundness and surface finish should be manufactured accurately. Various new materials such as titanium alloy should be tried and compared experimentally.

### *11.2.5 Using Thin Sleeves outside the Existing Shaft*

Another way to make a smooth surface is to insert a thin sleeve with extremely accurate surface finish outside the existing shaft, as shown in Figure 11.1. The outer diameter of the existing shaft is measured to be 3.92 mm. A very thin smooth sleeve can be manufactured around or inserted onto the shaft between the shaft surface and the air bearings to "create" a smooth surface. The shaft can also be reduced a little in the outer diameter in order to fit the sleeves.

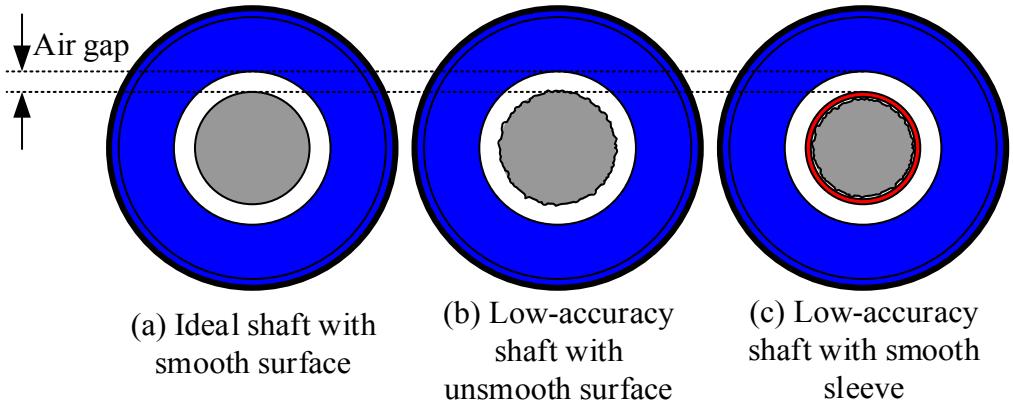


Figure 11.1 Air bearing (blue) and shaft (gray) with high-accuracy thin sleeves (red)

### *11.2.6 Hysteresis Control at Low Speed*

Because the proposed SRM is designed to work in high saturation, the current will increase dramatically if the supply voltage is too high. So for comparatively "low speed" regions, proper current hysteresis control can be used in order not to trigger the current protection as well as remain a full use of the machine.

### *11.2.7 Loss Estimation*

Proper methods have to be applied to measure the efficiency of the machine. Considering the small size and ultra-high speed rotation, it is very challenging to calculate and measure the loss/torque of the motor.

#### 11.2.7.1 Electromagnetic Loss Estimation

The estimation of the losses of the proposed ultra-high speed SRM is a little challenging. For copper losses, since Litz-wires are used, the AC winding loss is reduced significantly. Nevertheless, an accurate model to estimate the copper losses needs to be developed. However, for iron losses, measured loss data for Hiperco 50 laminations at such a high excitation frequency (33.3 kHz at 1 million rpm) is not available. Estimating the iron losses at that frequency is very difficult, if not impossible.

On the other hand, other materials that have low losses at high frequencies such as amorphous laminations can be tried, although they are not easily available in arbitrary shapes. Some special cutting techniques like wire EDM (electrical discharge machining) might help with the shaping of this kind of brittle material

#### 11.2.7.2 Windage Loss Estimation

At 1 million rpm, turbulence in the air flow must be evaluated [113]. A sufficiently accurate estimation method for the turbulence effect is not available without experimental data to determine parameters. The calculation and estimation of the windage loss in turbulent flow itself is a hot research topic in mechanical engineering. Analytical equations can be employed in the design phase, however, in order to ensure a success. Another method is to use the CFD (Computational Fluid Dynamics) FEA to estimate the windage loss.

#### 11.2.7.3 Bearing loss estimation

Estimation of the air bearing losses depends on the load, air pressure, temperature, the contact between the shaft and the bearing, and the smoothness of the shaft. It is very difficult to give a reasonable estimation of the bearing friction loss especially in the design stage. Measurements must be conducted in order to obtain a reliable estimation of the bearing losses. An accurate mathematical model might be proposed based on the fitted curve from the observations and measurements.

### *11.2.8 Loss and Torque Measurement*

The estimation of the losses over 1 million rpm is very challenging without experimental measurements. Even with experimental data, the losses and torque are still difficult to be determined.

For the torque measurement, no commercial torque sensors are available to measure such low torque at such high speeds. Nevertheless, the torque can be determined using with

high-accuracy piezoresistive force sensors as described in [77]. A motor-generator test setup with two carefully aligned machines is required, however.

### *11.2.9 Thermal Analysis*

With the loss calculated and measured, a proper thermal analysis can be conducted to estimate the temperature of the motor. Proper cooling methods can also be applied to the motor in order to increase the power density.

### *11.2.10Noise Reduction*

The model proposed in Chapter 9 can be modified to analyze the acoustic performance of the motor. Proper noise reduction methods can be used to reduce the SPL of the motor.

## 11.3 Contributions

The main contributions of this research are summarized as follows:

1. A novel high-strength, high-torque-density and high-efficiency rotor geometry for UHSSRMs over 1,000,000 rpm has been proposed. The design is then enhanced with adhesives to ensure a robust operation at ultra-high speeds. Proper rotor dynamics analysis has also been conducted.
2. A complete electromagnetic design of the 1,000,000 rpm SRM has been conducted using Ansys/Maxwell. Litz-wire and Hiperco 50 laminations have been used to generate the estimated windage torque at ultra-high speeds.

3. A constant volts per hertz control and optical-based direct position control have been proposed for UHSSRMs. Experiments have been done to validate the idea at 100,000 rpm.
4. A multi-physics acoustic analysis has been conducted to predict the sound pressure level of UHSSRMs. Experiments have verified the model at 100,000 rpm.
5. For the first time in the literature, aerostatic bearings have been used for ultra-high speed electric motors. The comprehensive test results and challenges for ultra-high speed applications have been discussed in detail.

The research work presented in this dissertation has resulted in several publications, which are listed as follows:

Journal papers:

**[J1] C. Gong**, S. Li, T. Habetler and J. Restrepo, B. Soderholm, "Direct position control for ultra-high speed switched reluctance machines based on low-cost non-intrusive reflective sensors," *IEEE Transactions on Industrial Applications*, vol. 55, no. 1, pp. 480-489, Jan.-Feb. 2019. doi: https://doi.org/10.1109/TIA.2018.2868037

**[J2] C. Gong**, S. Li, T. Habetler and P. Zhou, "Acoustic Modeling and Prediction of Ultra-High Speed Switched Reluctance Machines Based on Multi-Physics Finite Element Analysis," *IEEE Transactions on Energy Conversion*, under review

**[J3] C. Gong**, S. Li, and T. Habetler, "High-Strength Rotor Design for Ultra-High Speed Switched Reluctance Machines over 1 Million rpm," *IEEE Transactions on Industrial Applications*, under review

**[J4]** **C. Gong**, S. Li, and T. Habetler, "Electromagnetic Design and Experimental Analysis of An Ultra-high Speed Switched Reluctance Machine with Aerostatic Bearings for Applications over 1,000,000 rpm," *IEEE Transactions on Industrial Electronics*, to be submitted soon

**[J5]** **C. Gong**, S. Li, and T. Habetler, "Rotor Dynamics Analysis of Ultra-high Speed Switched Reluctance Machines over 1,000,000 rpm," *IEEE Transactions on Industrial Applications*, to be submitted soon

Conference papers

**[C1]** **C. Gong** and T. Habetler, "A novel rotor design for ultra-high speed switched reluctance machines over 1 million rpm," *2017 IEEE International Electric Machines and Drives Conference (IEMDC)*, Miami, FL, 2017, pp. 1-6. doi: https://doi.org/10.1109/IEMDC.2017.8002290

**[C2]** **C. Gong**, T. Habetler, J. Restrepo and B. Soderholm, "Direct position control for ultra-high speed switched reluctance machines based on non-contact optical sensors," *2017 IEEE International Electric Machines and Drives Conference (IEMDC)*, Miami, FL, 2017, pp. 1-6. doi: https://doi.org/10.1109/IEMDC.2017.8002289

**[C3]** **C. Gong** and T. Habetler, "Electromagnetic design of an ultra-high speed switched reluctance machine over 1 million rpm," *2017 IEEE Energy Conversion Congress and Exposition (ECCE)*, Cincinnati, OH, 2017, pp. 2368-2373. doi: https://doi.org/10.1109/ECCE.2017.8096459

**[C4] C. Gong** and T. Habetler, "Constant volts per hertz control of ultra-high speed switched reluctance machines," *IECON 2017 - 43rd Annual Conference of the IEEE Industrial Electronics Society (IECON)*, Beijing, China, 2017, pp. 1868-1873. doi: https://doi.org/10.1109/IECON.2017.8216316

**[C5] C. Gong**, S. Li and T. G. Habetler, "Rotor Dynamic Analysis of Ultra-high Speed Switched Reluctance Machines over 1 Million rpm," *2018 IEEE Energy Conversion Congress and Exposition (ECCE)*, Portland, OR, 2018, pp. 1704-1709. doi: https://doi.org/10.1109/ECCE.2018.8557776

**[C6] C. Gong**, S. Li and T. G. Habetler, "Analysis of Rotor Robustness of Ultra-high Speed Switched Reluctance Machines over 1 Million rpm Using Cohesive Zone Model," *2018 IEEE Energy Conversion Congress and Exposition (ECCE)*, Portland, OR, 2018, pp. 2401-2406. doi: https://doi.org/10.1109/ECCE.2018.8558106

**[C7] C. Gong**, S. Li, T. Habetler and P. Zhou, "Acoustic Modeling and Prediction of Ultra-high Speed Switched Reluctance Machines Based on Finite Element Analysis," *2019 IEEE International Electric Machines and Drives Conference (IEMDC)*, San Diego, CA, 2019, Accepted

**[C8] C. Gong**, S. Li, and T. Habetler, "Practical Considerations in the Design and Manufacture of Ultrahigh-Speed Switched Reluctance Machines over 1 Million rpm," *2019 IEEE International Electric Machines and Drives Conference (IEMDC)*, San Diego, CA, 2019, Accepted

Additional papers (no included in this dissertation):

**[J6]** **C. Gong**, A. Tüysüz, T. Stolz, M. Flankl, J. W. Kolar and T. Habetler, "Experimental analysis and optimization of a contactless eddy-current-based speed sensor for smooth conductive surfaces," *IEEE Transactions on Industrial Electronics*, under review

**[J7]** S. Li, S. Zhang, **C. Gong**, T. Habetler, and R. Harley, "An enhanced analytical calculation of the phase inductance profile of switched reluctance machines," *IEEE Transactions on Industry Applications*, vol. 55, no. 2, pp. 1392-1407, March-April 2019. doi: 10.1109/TIA.2018.2879303

**[J8]** M. Flankl, A. Tüysüz, **C. Gong**, T. Stolz, and J. W. Kolar, "Analysis and modeling of eddy-current couplings for auxiliary power generation on a freight train wagon," *IEEE Power and Energy Technology Systems Journal,* vol. 5, no. 4, pp. 139-147, Dec. 2018. doi: https://doi.org/10.1109/JPETS.2018.2871629

**[C9]** S. Li, **C. Gong**, L. Du, J. Rhett Mayor, R. G. Harley and T. G. Habetler, "Parametric Study for the Design of the End Region of Large Synchronous Generators Based on Three-Dimensional Transient Finite Element Analysis," *2018 IEEE Energy Conversion Congress and Exposition (ECCE)*, Portland, OR, 2018, pp. 7356-7362. doi: https://doi.org/10.1109/ECCE.2018.8558162

**[C10]** S. Li, **C. Gong**, J. R. Mayor, R. G. Harley and T. G. Habetler, "Efficient Calculation of the Strand Eddy Current Loss Distributions in the End Stepped-Stator Region of Large Synchronous Generators," *2018 IEEE Energy Conversion Congress and Exposition (ECCE)*, Portland, OR, 2018, pp. 1783-1789. doi: https://doi.org/10.1109/ECCE.2018.8558239

**[C11]** S. Li, **C. Gong**, L. Du, J. R. Mayor, R. G. Harley and T. G. Habetler, "Fast Calculation of the Magnetic Field and Loss Distributions in the Stator Core End Packets and Finger Plates of Large Synchronous Generators," *2018 IEEE Energy Conversion Congress and Exposition (ECCE)*, Portland, OR, 2018, pp. 822-828. doi: https://doi.org/10.1109/ECCE.2018.8557473

**[C12]** S. Li, **C. Gong**, N. A. Gallandat, J. R. Mayor and R. G. Harley, "Analyzing the impact of press plate structure on the flux and loss distributions in the end region of large generators by transient 3-dimensional finite-element method with an improved core loss model," *2017 IEEE International Electric Machines and Drives Conference (IEMDC)*, Miami, FL, 2017, pp. 1-8. doi: https://doi.org/10.1109/IEMDC.2017.8002363

**[C13]** S. Li, **C. Gong**, N. A. Gallandat, J. R. Mayor and R. G. Harley, "Implementation of surface impedance boundary conditions in the quasi three-dimensional finite-difference simulations of generator end regions," *2017 IEEE International Electric Machines and Drives Conference (IEMDC)*, Miami, FL, 2017, pp. 1-7. doi: https://doi.org/10.1109/IEMDC.2017.8002366

In addition, several more journal and conference papers are being prepared.

# APPENDIX A. DRAWINGS OF MOTOR PARTS

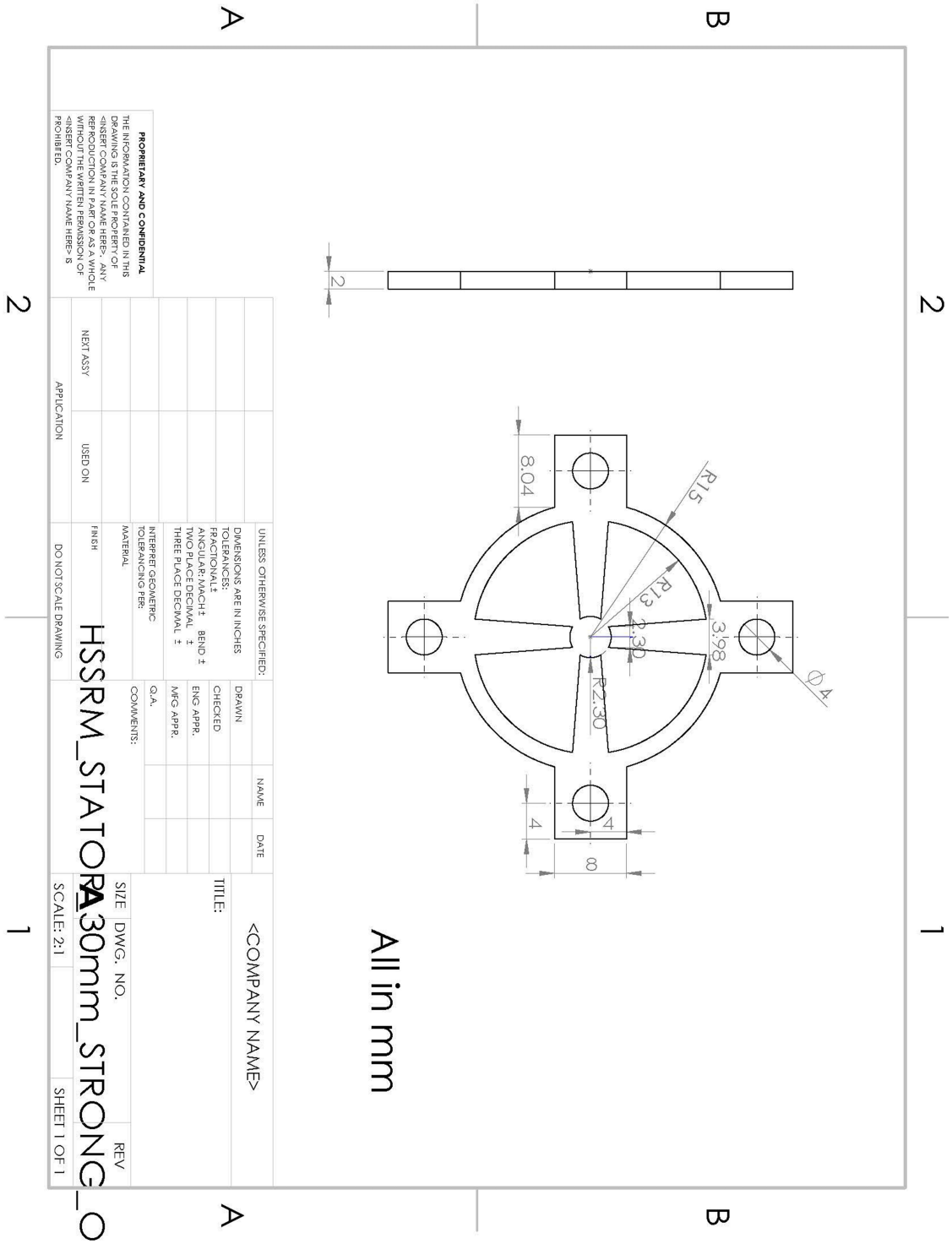

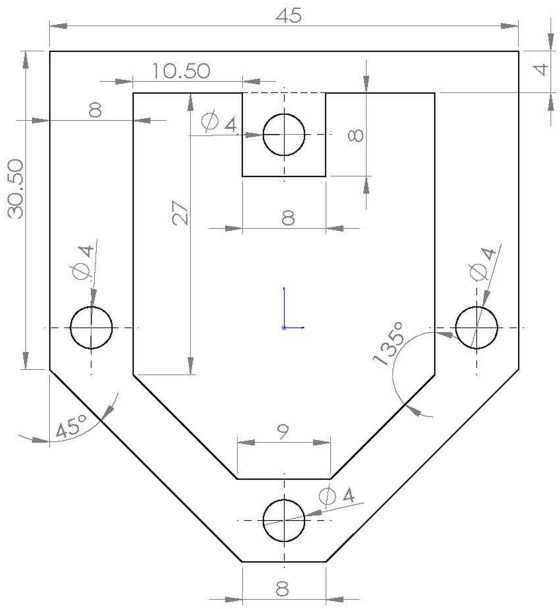


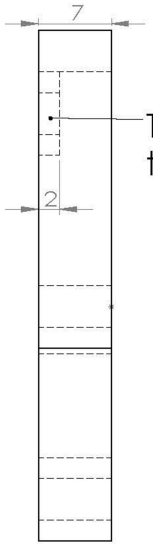


The thickness of the square tab on the top is 2 mm

All the numbers are in mm.

| | | | | | |
|---|---|---|---|---|---|
| | | UNLESS OTHERWISE SPECIFIED: | | NAME | DATE |
| | | DIMENSIONS ARE IN INCHES<br>TOLERANCES:<br>FRACTIONAL ±<br>ANGULAR: MACH ± BEND ±<br>TWO PLACE DECIMAL ±<br>THREE PLACE DECIMAL ± | DRAWN | | |
| | | | CHECKED | | |
| | | | ENG APPR. | | |
| | | | MFG APPR. | | |
| | | INTERPRET GEOMETRIC TOLERANCING PER: | Q.A. | | |
| | | MATERIAL | COMMENTS: | | |
| NEXT ASSY | USED ON | FINISH | | | |
| APPLICATION | | DO NOT SCALE DRAWING | | | |



<COMPANY NAME>

TITLE:

| SIZE | DWG. NO. | REV |
|---|---|---|
| A | HALF CASE | |
| SCALE: 2:1 | | SHEET 1 OF 1 |

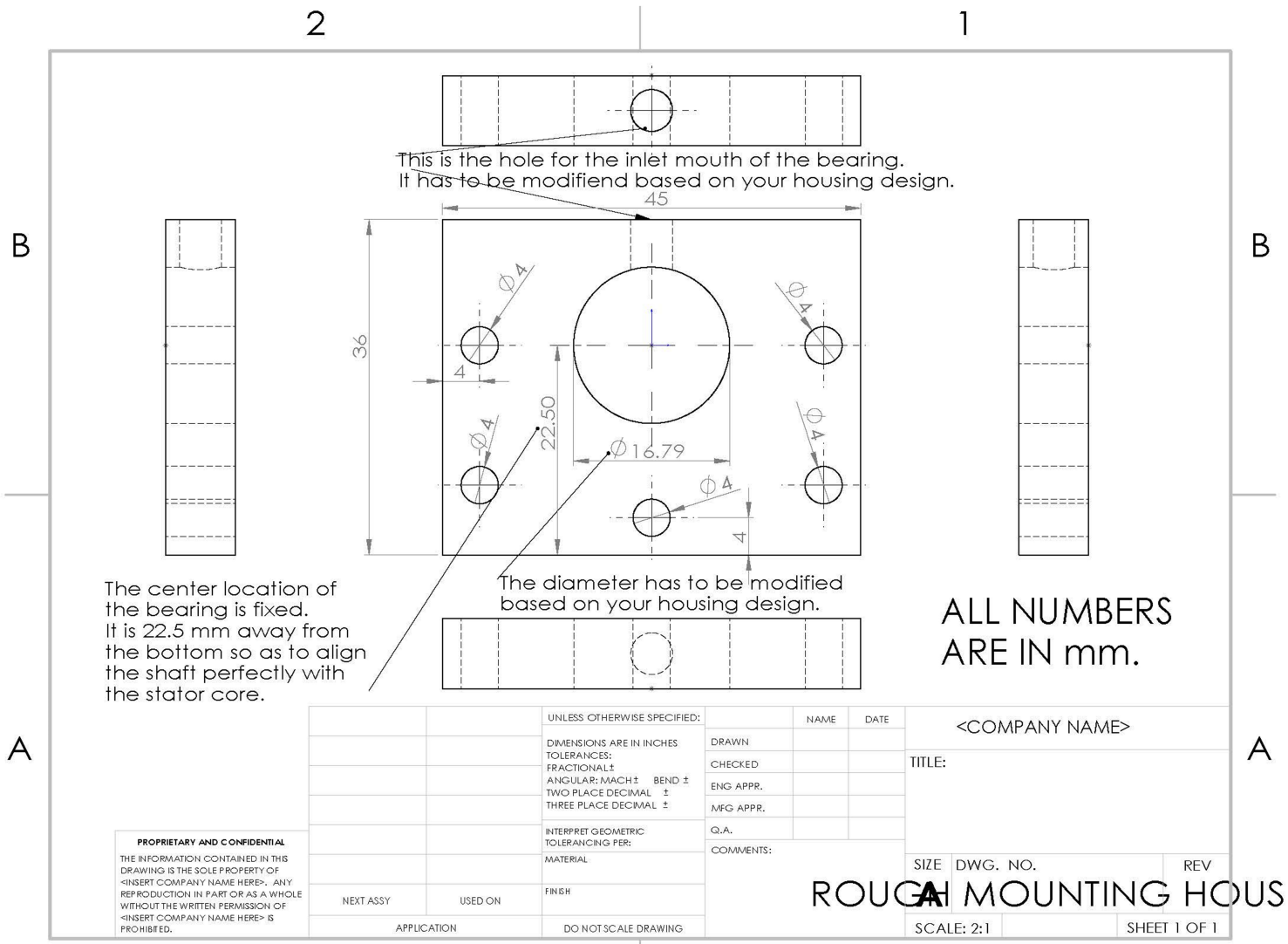


| | | | | | |
|---|---|---|---|---|---|
| | | UNLESS OTHERWISE SPECIFIED: | | NAME | DATE |
| | | DIMENSIONS ARE IN INCHES<br>TOLERANCES:<br>FRACTIONAL ±<br>ANGULAR: MACH ± BEND ±<br>TWO PLACE DECIMAL ±<br>THREE PLACE DECIMAL ± | DRAWN | | |
| | | | CHECKED | | |
| | | | ENG APPR. | | |
| | | | MFG APPR. | | |
| | | INTERPRET GEOMETRIC TOLERANCING PER: | Q.A. | | |
| | | MATERIAL | COMMENTS: | | |
| NEXT ASSY | USED ON | FINISH | | | |
| APPLICATION | | DO NOT SCALE DRAWING | | | |



<COMPANY NAME>

TITLE:

ROUGH MOUNTING HOUS

| SIZE | DWG. NO. | REV |
|---|---|---|
| A | | |
| SCALE: 2:1 | | SHEET 1 OF 1 |

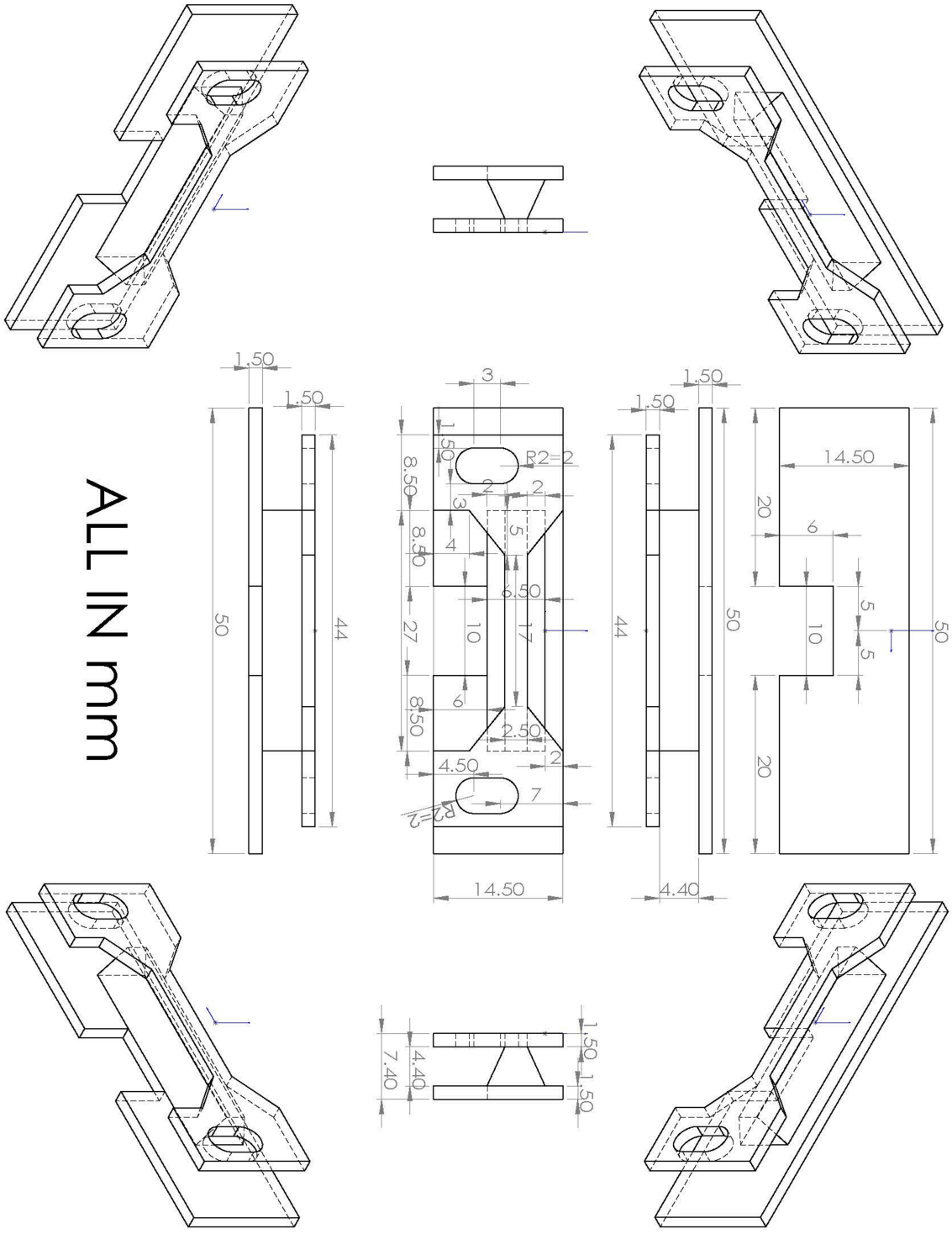
ALL IN mm
1.50
1.50
50
44
3
1.50
1.50
8.50
8.50
R2=2
2
2
3
5
4
6.50
27
10
17
6
8.50
2.50
2
4.50
7
R2=2
14.50
1.50
1.50
44
50
4.40
14.50
20
6
5
10
5
50
20
7.40
4.40
1.50
1.50

# REFERENCES


[1] J. Dang, "Switched reluctance machine electromagnetic design and optimization," Georgia Institute of Technology, 2015.

[2] C. Gong, S. Zhang, F. Zhang, J. Jiang, and X. Wang, "An integrated energy-efficient operation methodology for metro systems based on a real case of Shanghai metro line one," *Energies,* vol. 7, pp. 7305-7329, 2014.

[3] S. Li, C. Gong, N. A. Gallandat, J. R. Mayor, and R. G. Harley, "Implementation of surface impedance boundary conditions in the quasi three-dimensional finite-difference simulations of generator end regions," in *Electric Machines and Drives Conference (IEMDC), 2017 IEEE International*, 2017, pp. 1-7.

[4] S. Li, C. Gong, N. A. Gallandat, J. R. Mayor, and R. G. Harley, "Analyzing the impact of press plate structure on the flux and loss distributions in the end region of large generators by transient 3-dimensional finite-element method with an improved core loss model," in *Electric Machines and Drives Conference (IEMDC), 2017 IEEE International*, 2017, pp. 1-8.

[5] S. Li, C. Gong, L. Du, J. R. Mayor, R. G. Harley, and T. G. Habetler, "Fast calculation of the magnetic field and loss distributions in the stator core end packets and finger plates of large synchronous generators," in *2018 IEEE Energy Conversion Congress and Exposition (ECCE)*, 2018, pp. 822-828.

[6] M. Flankl, A. Tüysüz, C. Gong, T. Stolz, and J. W. Kolar, "Analysis and Modeling of Eddy-Current Couplings for Auxiliary Power Generation on a Freight Train Wagon," *IEEE Power and Energy Technology Systems Journal,* vol. 5, pp. 139-147, 2018.

[7] S. Li, C. Gong, L. Du, J. R. Mayor, R. G. Harley, and T. G. Habetler, "Parametric Study for the Design of the End Region of Large Synchronous Generators Based on Three-Dimensional Transient Finite Element Analysis," in *2018 IEEE Energy Conversion Congress and Exposition (ECCE)*, 2018, pp. 7356-7362.

[8] S. Li, C. Gong, J. R. Mayor, R. G. Harley, and T. G. Habetler, "Efficient Calculation of the Strand Eddy Current Loss Distributions in the End Stepped-Stator Region of Large Synchronous Generators," in *2018 IEEE Energy Conversion Congress and Exposition (ECCE)*, 2018, pp. 1783-1789.

[9] S. Li, S. Zhang, C. Gong, T. Habetler, and R. Harley, "An Enhanced Analytical Calculation of the Phase Inductance of Switched Reluctance Machines," *IEEE Trans. Ind. Appl.,* vol. 55, pp. 1392-1407, 2019.

[10] C. Zwyssig, "An ultra-high-speed electrical drive system," ETH Zurich, 2008.

[11] "PCB Overview," *http://www.westwind-airbearings.com/pcb/overview.html*.

[12] A. Tuysuz, C. Zwyssig, and J. W. Kolar, "A novel motor topology for high-speed micro-machining applications," *IEEE Transactions on Industrial Electronics,* vol. 61, pp. 2960-2968, 2014.

[13] "How A Turbo Works - Garrett By Honeywell," *https://garrett.honeywell.com/products/how-a-turbo-works/*.

[14] "CT-15-150 Data sheet," *http://www.celeroton.com/fileadmin/user_upload/produkte/kompressor/datasheets/Datasheet-CT-15-150.pdf*.

[15] S. Kang, S.-J. J. Lee, and F. B. Prinz, "Size does matter: The pros and cons of miniaturization," *ABB Review,* vol. 2, pp. 54-62, Jan 2002.

[16] R. H. Jansen and K. L. McLallin, "G2 Flywheel Module Operated at 41,000 rpm," 2005.

[17] P. Tsao, M. Senesky, and S. R. Sanders, "An integrated flywheel energy storage system with homopolar inductor motor/generator and high-frequency drive," *IEEE Transactions on Industry Applications,* vol. 39, pp. 1710-1725, 2003.

[18] W. Wang, "Design of high speed flywheel motor/generator for aerospace applications," 2004.

[19] D. Gerada, A. Mebarki, N. L. Brown, C. Gerada, A. Cavagnino, and A. Boglietti, "High-speed electrical machines: Technologies, trends, and developments," *IEEE Transactions on Industrial Electronics,* vol. 61, pp. 2946-2959, 2014.

[20] C. Zwyssig, J. W. Kolar, and S. D. Round, "Megaspeed drive systems: Pushing beyond 1 million r/min," *IEEE/ASME Trans. Mechatron.,* vol. 14, pp. 564-574, 2009.

[21] I. Takahashi, T. Koganezawa, G. Su, and K. Ohyama, "A super high speed PM motor drive system by a quasi-current source inverter," *IEEE Trans. Ind. Appl.,* vol. 30, pp. 683-690, 1994.

[22] J. Oyama, T. Higuchi, T. Abe, K. Shigematsu, and R. Moriguchi, "The development of small size ultra-high speed drive system," in *Power Conversion Conference-Nagoya, 2007. PCC'07*, 2007, pp. 1571-1576.

[23] L. Zhao, C. Ham, L. Zheng, T. Wu, K. Sundaram, J. Kapat*, et al.*, "A highly efficient 200 000 RPM permanent magnet motor system," *IEEE Trans. Magn.,* vol. 43, pp. 2528-2530, 2007.

[24] P.-D. Pfister and Y. Perriard, "Very-high-speed slotless permanent-magnet motors: Analytical modeling, optimization, design, and torque measurement methods," *IEEE Trans. Ind. Electron.,* vol. 57, pp. 296-303, 2010.

[25] "ATE System," *http://www.ate-system.de/*.

[26] "Calnetix Technologies," *https://www.calnetix.com/electric-magnet-motor-generators*.

[27] C. Zwyssig, J. Kolar, W. Thaler, and M. Vohrer, "Design of a 100 W, 500000 rpm permanent-magnet generator for mesoscale gas turbines," in *Fourtieth IAS Annual Meeting. Conference Record of the 2005 Industry Applications Conference, 2005.*, 2005, pp. 253-260.

[28] C. Zwyssig, M. Duerr, D. Hassler, and J. Kolar, "An ultra-high-speed, 500000 rpm, 1 kW electrical drive system," in *Power Conversion Conference-Nagoya, 2007. PCC'07*, 2007, pp. 1577-1583.

[29] "Turbocharger for an exhaust temperature of 1050°C," *http://www.turbos.bwauto.com/en/products/turbochargerExhaustTemperature.aspx*.

[30] "Valeo's electric supercharger," *http://articles.sae.org/11244/*.

[31] E. W. Fairall, B. Bilgin, and A. Emadi, "State-of-the-art high-speed switched reluctance machines," in *2015 IEEE International Electric Machines & Drives Conference (IEMDC)*, 2015, pp. 1621-1627.

[32] C. J. Bateman, B. C. Mecrow, A. C. Clothier, P. P. Acarnley, and N. D. Tuftnell, "Sensorless operation of an ultra-high-speed switched reluctance machine," *IEEE Trans. Ind. Appl.,* vol. 46, pp. 2329-2337, 2010.

[33] S. D. Calverley, "Design of a high-speed switched reluctance machine for automotive turbo-generator applications," Ph.D. dissertation, Department of Electronic and Electrical Engineering, University of Sheffield, 2002.

[34] L. Morel, H. Fayard, H. V. Fos, A. Galindo, and G. Abba, "Study of ultra high speed switched reluctance motor drive," in *2000 IEEE Industry Applications Conference*, 2000, pp. 87-92.

[35] Steinmetz's equation [Online]. Available: https://en.wikipedia.org/wiki/Steinmetz%27s_equation

[36] Skin effect [Online]. Available: https://en.wikipedia.org/wiki/Skin_effect

[37] Proximity effect (electromagnetism) [Online]. Available: https://en.wikipedia.org/wiki/Proximity_effect_(electromagnetism)

[38] M. Besharati, J. Widmer, G. Atkinson, V. Pickert, and J. Washington, "Super-high-speed switched reluctance motor for automotive traction," in *2015 IEEE Energy Conversion Congress and Exposition (ECCE)*, 2015, pp. 5241-5248.

[39] J. Kunz, S. Cheng, Y. Duan, J. R. Mayor, R. Harley, and T. Habetler, "Design of a 750,000 rpm switched reluctance motor for micro machining," in *2010 IEEE Energy Conversion Congress and Exposition*, 2010, pp. 3986-3992.

[40] P. Imoberdorf, C. Zwyssig, S. Round, and J. W. Kolar, "Combined radial-axial magnetic bearing for a 1 kW, 500,000 rpm permanent magnet machine," in *Applied Power Electronics Conference, APEC 2007-Twenty Second Annual IEEE*, 2007, pp. 1434-1440.

[41] A. Looser and J. W. Kolar, "An active magnetic damper concept for stabilization of gas bearings in high-speed permanent-magnet machines," *IEEE Transactions on Industrial Electronics,* vol. 61, pp. 3089-3098, 2014.

[42] S. H. Won, J. Choi, and J. Lee, "Windage loss reduction of high-speed SRM using rotor magnetic saturation," *IEEE Transactions on Magnetics,* vol. 44, pp. 4147-4150, 2008.

[43] J. Dang, J. R. Mayor, S. A. Semidey, R. Harley, T. Habetler, and J. Restrepo, "Practical Considerations for the Design and Construction of a High-Speed SRM With a Flux-Bridge Rotor," *IEEE Trans. Ind. Appl.,* vol. 51, pp. 4515-4520, 2015.

[44] J. Dang, S. Haghbin, Y. Du, C. Bednar, H. Liles, J. Restrepo*, et al.*, "Electromagnetic design considerations for a 50,000 rpm 1kW Switched Reluctance Machine using a flux bridge," in *2013 IEEE International Electric Machines & Drives Conference (IEMDC)*, 2013, pp. 325-331.

[45] "T1000G Data Sheet," *http://www.toraycfa.com/pdfs/T1000GDataSheet.pdf*.

[46] "M250-35A Data Sheet," *http://cogent-power.com/cms-data/downloads/m250-35a.pdf*

[47] "CarTech Hiperco 50 Alloy Data Sheet," *http://cartech.ides.com/datasheet.aspx?i=103&e=200&c=TechArt*

[48] R. Krishnan, *Switched reluctance motor drives: modeling, simulation, analysis, design, and applications*: CRC press, 2001.

[49] C. Gong and T. Habetler, "A novel rotor design for ultra-high speed switched reluctance machines over 1 million rpm," in *2017 IEEE International Electric Machines and Drives Conference (IEMDC)*, 2017, pp. 1-6.

[50] C. Gong, S. Li, and T. G. Habetler, "Analysis of Rotor Robustness of Ultra-high Speed Switched Reluctance Machines over 1 Million rpm Using Cohesive Zone

Model," in *2018 IEEE Energy Conversion Congress and Exposition (ECCE)*, 2018, pp. 2401-2406.

[51] J. G. Hortnagl, "Determination of cohesive parameters for aerospace adhesives," 2013.

[52] K. Grace, S. Galioto, K. Bodla, and A. El-Refaie, "Carbon-fiber-wrapped synchronous reluctance traction motor," in *Energy Conversion Congress and Exposition (ECCE), 2017 IEEE*, 2017, pp. 3913-3920.

[53] A. Sheppard, D. Kelly, and L. Tong, "A damage zone model for the failure analysis of adhesively bonded joints," *International journal of adhesion and adhesives,* vol. 18, pp. 385-400, 1998.

[54] D. Xie and S. B. Biggers, "Progressive crack growth analysis using interface element based on the virtual crack closure technique," *Finite Elements in Analysis and Design,* vol. 42, pp. 977-984, 2006.

[55] W. E. Krieger, "Cohesive zone modeling for predicting interfacial delamination in microelectronic packaging," Georgia Institute of Technology, 2014.

[56] G. I. Barenblatt, "The mathematical theory of equilibrium cracks in brittle fracture," *Advances in applied mechanics,* vol. 7, pp. 55-129, 1962.

[57] D. S. Dugdale, "Yielding of steel sheets containing slits," *Journal of the Mechanics and Physics of Solids,* vol. 8, pp. 100-104, 1960.

[58] V. Tvergaard and J. W. Hutchinson, "The relation between crack growth resistance and fracture process parameters in elastic-plastic solids," *Journal of the Mechanics and Physics of Solids,* vol. 40, pp. 1377-1397, 1992.

[59] M. Kafkalidis, M. D. Thouless, Q. Yang, and S. Ward, "Deformation and fracture of adhesive layers constrained by plastically-deforming adherends," *Journal of Adhesion Science and Technology,* vol. 14, pp. 1593-1607, 2000.

[60] K. Park and G. H. Paulino, "Cohesive zone models: a critical review of traction-separation relationships across fracture surfaces," *Applied Mechanics Reviews,* vol. 64, p. 060802, 2011.

[61] "Joining & Bonding of Composite Parts -- The Structural Adhesive Advantage," *https://multimedia.3m.com/mws/media/1198329O/joining-bonding-of-composite-parts-white-paper.pdf*.

[62] "Surface Preparation and Pretreatment for Structural Adhesives," *http://multimedia.3m.com/mws/media/933332O/surface-prep-pretreatment-for-structural-adhesive-techbulletin.pdf*.

[63] "3M DP420 Black Data Sheet," *http://multimedia.3m.com/mws/media/66998O/scotch-weldtm-epoxy-adhesive-dp420-blck-ns-blck-offwhit-lh.pdf*.

[64] M. J. Lee, T. M. Cho, W. S. Kim, B. C. Lee, and J. J. Lee, "Determination of cohesive parameters for a mixed-mode cohesive zone model," *International Journal of Adhesion and Adhesives,* vol. 30, pp. 322-328, 2010.

[65] M. Wasseem and K. Kumar, "Finite Element Modelling for Delamination Analysis of Double Cantilever Beam Specimen," *SSRG-IJME. India,* 2014.

[66] C. Gong, S. Li, and T. G. Habetler, "Rotor Dynamic Analysis of Ultra-high Speed Switched Reluctance Machines over 1 Million rpm," in *2018 IEEE Energy Conversion Congress and Exposition (ECCE)*, 2018, pp. 1704-1709.

[67] S. Li, Y. Li, W. Choi, and B. Sarlioglu, "High-speed electric machines: Challenges and design considerations," *IEEE Transactions on Transportation Electrification,* vol. 2, pp. 2-13, 2016.

[68] X. Xie, "Comparison of Bearings: For the Bearing Choosing of High-speed Spindle Design," *Dept. of Mechanical Engineering, U. of Utah,* 2003.

[69] 16x04 mm 3 way Frictionless ID Thrust Air Bushings [Online]. Available: http://www.oavco.com/oavtb16i04.html

[70] J. D. Hartog, "Mechanical vibrations," *New York: McGraw-Hall Book Company,* 1947.

[71] E. Swanson, C. D. Powell, and S. Weissman, "A practical review of rotating machinery critical speeds and modes," *Sound and vibration,* vol. 39, pp. 16-17, 2005.

[72] M. S. Kumar, "Rotor dynamic analysis using ANSYS," in *IUTAM Symposium on Emerging Trends in Rotor Dynamics*, 2011, pp. 153-162.

[73] H. Nelson and J. McVaugh, "The dynamics of rotor-bearing systems using finite elements," *Journal of Engineering for Industry,* vol. 98, pp. 593-600, 1976.

[74] S. Garvey, "The vibrational behaviour of laminated components in electrical machines," in *Electrical Machines and Drives, 1989. Fourth International Conference on*, 1989, pp. 226-231.

[75] J. D. Ede, Z. Zhu, and D. Howe, "Rotor resonances of high-speed permanent-magnet brushless machines," *IEEE Transactions on Industry Applications,* vol. 38, pp. 1542-1548, 2002.

[76] "Magna-Tac E-645 Data Sheet," *http://www.beaconadhesives.com/TechSheets/e645tech.htm*.

[77] C. Zwyssig, S. Round, and J. Kolar, "Analytical and experimental investigation of a low torque, ultra-high speed drive system," in *Conference Record of the 2006 IEEE Industry Applications Conference Forty-First IAS Annual Meeting*, 2006, pp. 1507-1513.

[78] F. Lorenz, J. Rudolph, and R. Wemer, "Design of 3D printed High Performance Windings for switched reluctance machines," in *2018 XIII International Conference on Electrical Machines (ICEM)*, 2018, pp. 2451-2457.

[79] J. Dang, J. R. Mayor, S. A. Semidey, R. Harley, T. Habetler, and J. Restrepo, "Practical considerations for the design and construction of a high speed SRM with a flux-bridge rotor," in *2014 IEEE Energy Conversion Congress and Exposition (ECCE)*, 2014, pp. 3842-3849.

[80] J. Luomi, C. Zwyssig, A. Looser, and J. W. Kolar, "Efficiency optimization of a 100-W 500 000-r/min permanent-magnet machine including air-friction losses," *IEEE Transactions on industry applications,* vol. 45, pp. 1368-1377, 2009.

[81] "Round Litz Wire Data Sheet," *https://www.newenglandwire.com/products/litz-wire-and-formed-cables/round*.

[82] "Wire Gauge and Current Limits Including Skin Depth and Strength," *http://www.powerstream.com/Wire_Size.htm*.

[83] "PES Tutorial on Magnetic Materials," *https://www.pes.ee.ethz.ch/uploads/tx_ethpublications/APEC2012_MagneticTutorial.pdf*.

[84] S. Long, Z. Zhu, and D. Howe, "Vibration behaviour of stators of switched reluctance motors," *IEE Proceedings-Electric Power Applications,* vol. 148, pp. 257-264, 2001.

[85] S. Watanabe, S. Kenjo, K. Ide, F. Sato, and M. Yamamoto, "Natural frequencies and vibration behaviour of motor stators," *IEEE transactions on power apparatus and systems,* pp. 949-956, 1983.

[86] H. Le-Huy and P. Brunelle, "A versatile nonlinear switched reluctance motor model in Simulink using realistic and analytical magnetization characteristics," in *Industrial Electronics Society, 2005. IECON 2005. 31st Annual Conference of IEEE*, 2005, p. 6 pp.

[87] C. Zwyssig, S. D. Round, and J. W. Kolar, "An ultrahigh-speed, low power electrical drive system," *IEEE Transactions on Industrial Electronics,* vol. 55, pp. 577-585, 2008.

[88] C. Gong and T. Habetler, "Constant volts per hertz control of ultra-high speed switched reluctance machines," in *2017-43rd Annual Conference of the IEEE Industrial Electronics Society (IECON)*, 2017, pp. 1868-1873.

[89] G. Gallegos-Lopez, P. C. Kjaer, and T. J. Miller, "A new sensorless method for switched reluctance motor drives," *IEEE Transactions on Industry Applications,* vol. 34, pp. 832-840, 1998.

[90] C. J. Bateman, B. C. Mecrow, A. C. Clothier, P. P. Acarnley, and N. D. Tuftnell, "Sensorless operation of an ultra-high-speed switched reluctance machine," *IEEE Transactions on Industry Applications,* vol. 46, pp. 2329-2337, 2010.

[91] L. Xu and C. Wang, "Accurate rotor position detection and sensorless control of SRM for super-high speed operation," *IEEE Trans. Power Electron.,* vol. 17, pp. 757-763, 2002.

[92] D.-H. Lee and J.-W. Ahn, "A novel four-level converter and instantaneous switching angle detector for high speed SRM drive," *IEEE Trans. Power Electron.,* vol. 22, pp. 2034-2041, 2007.

[93] A. V. Radun, "High-power density switched reluctance motor drive for aerospace applications," *IEEE Trans. Ind. Appl.,* vol. 28, pp. 113-119, 1992.

[94] T. Wichert, "Design and construction modifications of switched reluctance machines," Ph.D. Thesis, Institute of Electrical Machines, Warsaw University of Technology, Poland, 2008.

[95] D.-H. Lee and J.-W. Ahn, "Performance of High-Speed 4/2 Switched Reluctance Motor," *Journal of Electrical Engineering and Technology,* vol. 6, pp. 640-646, 2011.

[96] S. H. Won, J. Choi, and J. Lee, "Windage loss reduction of high-speed SRM using rotor magnetic saturation," *IEEE Trans. Magn.,* vol. 44, pp. 4147-4150, 2008.

[97] J. Kim and R. Krishnan, "High efficiency single-pulse controlled switched reluctance motor drive for high speed (48k rpm) application: Analysis, design, and experimental verification," in *2008 IEEE Industry Applications Society Annual Meeting*, 2008, pp. 1-8.

[98] M. D. Bui, "Maximum torque control of a high speed switched reluctance starter/generator used in more/all electric aircraft," Ph.D Thesis, Technical University of Berlin, Germany, 2014.

[99] S. Kachapornkul, P. Somsiri, R. Pupadubsin, N. Nulek, and N. Chayopitak, "Low cost high speed switched reluctance motor drive for supercharger applications," in *2012 15th International Conference on Electrical Machines and Systems (ICEMS)*, 2012, pp. 1-6.

[100] S. R. MacMinn and W. D. Jones, "A very high speed switched-reluctance starter-generator for aircraft engine applications," in *Proceedings of the IEEE 1989 National Aerospace and Electronics Conference (NAECON)* 1989, pp. 1758-1764.

[101] S. D. Calverley, G. Jewell, and R. Saunders, "Design of a high speed switched reluctance machine for automotive turbo-generator applications," SAE Technical Paper 0148-7191, 1999.

[102] C. A. Ferreira, S. R. Jones, W. S. Heglund, and W. D. Jones, "Detailed design of a 30-kW switched reluctance starter/generator system for a gas turbine engine application," *IEEE Trans. Ind. Appl.,* vol. 31, pp. 553-561, 1995.

[103] H. J. Brauer and R. W. De Doncker, "Thermal modeling of a high-speed switched reluctance machine with axial air-gap flow for vacuum cleaners," in *Proceedings of the 2011-14th European Conference on Power Electronics and Applications (EPE 2011)*, 2011, pp. 1-10.

[104] E5 Optical Kit Encoder [Online]. Available: http://www.usdigital.com/products/e5

[105] P. Laurent, M. Gabsi, and B. Multon, "Sensorless rotor position analysis using resonant method for switched reluctance motor," in *1993 IEEE Industry Applications Society Annual Meeting*, 1993, pp. 687-694.

[106] S. Kozuka, N. Tanabe, J. Asama, and A. Chiba, "Basic characteristics of 150,000 r/min switched reluctance motor drive," in *2008 IEEE Power and Energy Society General Meeting-Conversion and Delivery of Electrical Energy in the 21st Century*, 2008, pp. 1-4.

[107] C. Gong, T. Habetler, J. Restrepo, and B. Soderholm, "Direct position control for ultra-high speed switched reluctance machines based on non-contact optical sensors," in *2017 IEEE International Electric Machines and Drives Conference (IEMDC)*, 2017, pp. 1-6.

[108] J.-W. Ahn, S.-J. Park, and D.-H. Lee, "Novel encoder for switching angle control of SRM," *IEEE Trans. Ind. Electron.,* vol. 53, pp. 848-854, 2006.

[109] Resolver [Online]. Available: https://en.wikipedia.org/wiki/Resolver_(electrical)

[110] Resolver vs encoder [Online]. Available: https://www.motioncontroltips.com/faq-why-are-so-many-designers-replacing-resolvers-with-encoders/

[111] M. Ehsani and B. Fahimi, "Elimination of position sensors in switched reluctance motor drives: state of the art and future trends," *IEEE Trans. Ind. Electron.,* vol. 49, pp. 40-47, 2002.

[112] EE-SY310/-SY410 Datasheet [Online]. Available: http://omronfs.omron.com/en_US/ecb/products/pdf/en-ee_sy310_410.pdf

[113] C. Gong and T. Habetler, "Electromagnetic design of an ultra-high speed switched reluctance machine over 1 million rpm," in *2017 IEEE Energy Conversion Congress and Exposition (ECCE)*, 2017, pp. 2368-2373.

[114] 100,000 rpm switched reluctance motor [Online]. Available: https://youtu.be/yd-5vlgyPdY

[115] D. E. Cameron, J. H. Lang, and S. D. Umans, "The origin and reduction of acoustic noise in doubly salient variable-reluctance motors," *IEEE Trans. Ind. Appl.,* vol. 28, pp. 1250-1255, 1992.

[116] R. S. Colby, F. M. Mottier, and T. J. Miller, "Vibration modes and acoustic noise in a four-phase switched reluctance motor," *IEEE Trans. Ind. Appl.,* vol. 32, pp. 1357-1364, 1996.

[117] M. Anwar and I. Husain, "Radial force calculation and acoustic noise prediction in switched reluctance machines," *IEEE Trans. Ind. Appl.,* vol. 36, pp. 1589-1597, 2000.

[118] J. O. Fiedler, K. A. Kasper, and R. W. De Doncker, "Calculation of the acoustic noise spectrum of SRM using modal superposition," *IEEE Trans. Ind. Electron.,* vol. 57, pp. 2939-2945, 2010.

[119] C. Lin and B. Fahimi, "Prediction of radial vibration in switched reluctance machines," *IEEE Trans. Energy Convers.,* vol. 28, pp. 1072-1081, 2013.

[120] C. Lin and B. Fahimi, "Prediction of acoustic noise in switched reluctance motor drives," *IEEE Trans. Energy Convers.,* vol. 29, pp. 250-258, 2014.

[121] F. L. Dos Santos, J. Anthonis, F. Naclerio, J. J. Gyselinck, H. Van der Auweraer, and L. C. Góes, "Multiphysics NVH modeling: Simulation of a switched reluctance motor for an electric vehicle," *IEEE Trans. Ind. Electron.,* vol. 61, pp. 469-476, 2014.

[122] C. Gong, S. Li, T. Habetler, and P. Zhou, "Acoustic Modeling and Prediction of Ultra-high speed Switched Reluctance Machines Based on Finite Element Analysis," in *2019 IEEE International Electric Machines and Drives Conference (IEMDC)*, 2019, p. in press.

[123] C. Gong, S. Li, T. Habetler, J. A. Restrepo, and B. Soderholm, "Direct Position Control for Ultrahigh-Speed Switched-Reluctance Machines Based on Low-Cost Nonintrusive Reflective Sensors," *IEEE Trans. Ind. Appl.,* vol. 55, pp. 480-489, 2019.

[124] J.-P. Hong, K.-H. Ha, and J. Lee, "Stator pole and yoke design for vibration reduction of switched reluctance motor," *IEEE Trans. Magn.,* vol. 38, pp. 929-932, 2002.

[125] A-weighting [Online]. Available: https://en.wikipedia.org/wiki/A-weighting

[126] C. Gong, S. Li, and T. Habetler, "Practical Considerations in the Design and Manufacture of Ultra-high Speed Switched Reluctance Machines over 1 Million

rpm," in *2019 IEEE International Electric Machines and Drives Conference (IEMDC)*, 2019, p. in press.

[127] Newway Air Bushings [Online]. Available: https://www.newwayairbearings.com/catalog/product/13mm-air-bushings/

# VITA

Cheng Gong was born in Shanghai, China in 1990. He received a Bachelor of Engineering degree from Shanghai Jiao Tong University, Shanghai, China, in 2012 and the dual Master of Engineering degree from Shanghai Jiao Tong University, Shanghai, China and Georgia Institute of Technology, Atlanta Georgia, USA, in 2015, both in Electrical Engineering.

Since January 2015, he has been working on the analysis, design and control of electric machines, as a Graduate Research Assistant in the electric power group of Georgia Institute of Technology. In summer 2017, he was invited as a visiting scholar in the Power Electronic Systems Lab, ETH-Zurich, Switzerland. In summer 2018, he worked as an R&D intern with ANSYS/Maxwell group in Canonsburg, PA.

His research interests include design, optimization and control of electric machines for different applications.